Mechanisms of Subcellular Organization in Bacteria

by

Christopher A. Azaldegui

A dissertation submitted in partial fulfillment
of the requirements for the degree of
Doctor of Philosophy
(Chemical Biology)
in The University of Michigan
2025

Doctoral Committee:

Professor Julie S. Biteen, Chair
Professor Matthew Chapman
Professor Anna K. Mapp
Associate Professor Anthony G. Vecchiarelli

Christopher A. Azaldegui

azaldegc@umich.edu

ORCID iD: 0000-0002-3889-2660

© Christopher A. Azaldegui 2025

All Rights Reserved

To my parents, Carmen and Wilfredo.

For all your dreams and sacrifices.

ACKNOWLEDGEMENTS

This dissertation is the culmination of years of support from a village of people.

First, I thank my research advisor, Prof. Julie Biteen, for all the support and mentorship she has given me over these years. I am grateful for the freedom she allowed me to pursue my curiosity and for pulling me back when I deviated from the path. I am eternally thankful for her kindness, her patience, her knowledge, and for her belief in me.

I also thank my co-advisor, Prof. Anthony Vecchiarelli. He generously provided his resources and time to guide my thesis work. I am grateful for his motivation and enthusiasm, which refreshed me when I was down. His moral and scientific support has been invaluable on this journey.

I thank Profs. Anna Mapp and Matthew Chapman for their insights and for pushing me to think beyond the boundaries of my thesis work. I am particularly grateful to Anna for her support since my undergraduate years and for showing me what could be.

I thank Prof. Peter Dahlberg and his lab for hosting me during my sabbatical and for providing stability during a chaotic time.

It has been a pleasure to share many hours with the members, past and present, of the Biteen and Vecchiarelli labs. I am thankful for their support, feedback, and encouragement over the years. I am particularly grateful to the 2525 crew: Ziyuan, Saaj, David, Xiaofeng, and Luis for the joy and laughs they brought to work. I want to mention and thank Anne, Lisa, and Joe for welcoming me into the Vecchiarelli Lab and teaching me biology. I also thank the people I worked closely with: Y, Lisa, Hema, and Claire. Our science discussions are some of my favorite moments in the PhD. Finally, I am grateful to Hannah, Ziyuan,

Saaj, Lisa, Kate, and Luis for their friendship outside of work.

This dissertation was possible in part by the administrative and financial support I received. I am grateful to the Program in Chemical Biology team for their help. I also want to thank the Rackham Graduate School and the Chemistry/Biology Interface Training Program for their financial support.

I would not be in this position without the support of people I met during my time at St. Edward's University. I am grateful to Prof. Toledo for opening the door to research and Prof. Raychelle Burks for teaching me how to do science. Both have been guiding lights on this journey. I must also thank the McNair Scholar's program for their support and preparation ahead of graduate school.

I thank all my friends for caring for me and bringing joy to my life. My friends from school, the climbing gym, and my travels have been with me through the worst and the best times. I particularly want to thank Shason, J'Reisz, and Sebastian for their friendship. The time spent with you all is time I hold dear.

I want to thank my family for their unconditional love and support. I thank my brother Sebastian for picking up the phone countless times and for his humor. I thank my mother, Carmen, and my father, Wilfredo, who have defined perseverance and hard work for me. Everything I achieve is because of them. Finally, I thank my best friend and partner Jordan for her love and the happiness she brings me. I am grateful for her companionship, our silly jokes, and her encouragement. I look forward to the next chapters of our life together.

TABLE OF CONTENTS

DEDICATION ii

ACKNOWLEDGEMENTS iii

LIST OF FIGURES x

LIST OF TABLES xii

LIST OF ABBREVIATIONS xiii

ABSTRACT xv

CHAPTER

I. Spatial Organization in Bacteria 1

1.1 Compartmentalization through bacterial organelles 1
1.1.1 Membrane-bound organelles 1
1.1.2 Membraneless organelles 2
1.1.3 Carboxysomes are the model BMC 2
1.2 Biomolecular condensates and their properties 3
1.2.1 Condensate formation processes 4
1.2.2 Observed properties of condensates 5
1.3 The roles of biomolecular condensates in bacteria 5
1.3.1 Bacterial ribonucleoprotein bodies organize mRNA decay 7
1.3.2 PopZ microdomains regulate asymmetric cell development 8
1.4 Active partioning in bacteria 9
1.4.1 ParA/MinD ATPases position cellular machinery 9
1.4.2 The ATPase cycle of ParA 10
1.5 Proposed mechanisms of ParA-mediated partioning 10
1.5.1 Mechanochemical coupled Brownian-ratchet 12
1.5.2 DNA-relay model 14
1.5.3 Hopping and relay model 15
1.6 Maintenance of carboxysome distribution system 16

1.7 Thesis outline . . . 18

II. Microscopy as a Tool to Study Spatial Organization in Bacteria . . . 20

2.1 Microscopy and bacteria . . . 20
2.2 Fluorescence microscopy . . . 21
2.2.1 The diffraction limit . . . 22
2.3 Single-molecule fluorescence microscopy . . . 23
2.3.1 Breaking the diffraction limit . . . 23
2.3.2 Active control mechanisms . . . 23
2.3.3 Single emitter super-localization . . . 23
2.4 Single-particle tracking and analysis . . . 25
2.4.1 Analysis of single-particle trajectories . . . 26
2.4.2 Analysis of single particle displacements . . . 27
2.5 Correlative light and electron microscopy . . . 28
2.5.1 Cryogenic electron microscopy . . . 29
2.5.2 Cryogenic electron tomography . . . 29
2.5.3 Super-resolution cryoCLEM . . . 30
2.5.4 Biosensor cryoCLEM . . . 30

III. An Experimental Framework to Assess Biomolecular Condensates in Bacteria . . . 34

3.1 Introduction . . . 34
3.2 Results . . . 38
3.2.1 Probing the liquid-like properties of foci formed by protein overexpression . . . 38
3.2.2 Using single-cell tunable expression to probe the formation of biomolecular condensates . . . 40
3.2.3 Probing the *in vivo* concentration dependence of biomolecular condensates . . . 45
3.2.4 Condensates coexist with a soluble phase . . . 47
3.2.5 Changes in cellular concentration, osmolarity, and temperature probe the reversibility of condensates . . . 51
3.2.6 Probing the dynamic rearrangement, confinement, and exchange of biomolecular condensates . . . 57
3.2.7 IbpA as a reporter to differentiate between condensates and aggregates . . . 62
3.3 Discussion . . . 66
3.4 Materials and Methods . . . 68
3.4.1 Bacterial strains, plasmids, and primers . . . 68
3.4.2 Growth conditions . . . 69
3.4.3 Total protein and immunoblot analyses . . . 71
3.4.4 Wide-field fluorescence and phase-contrast imaging . . . 73
3.4.5 Time-lapse videos of protein induction in *E. coli* BL21 . . . 73

3.4.6 DAPI staining . . . 74
3.4.7 Localized cell lysis . . . 74
3.4.8 Cellular shape change in *E. coli* BL21 . . . 75
3.4.9 Single-cell tunable induction of mCherry fusion focus . 75
3.4.10 Nucleoid compaction . . . 76
3.4.11 Focus reversibility in response to changes in concentration in *E. coli* MG1665 . . . 76
3.4.12 Osmotic Shock . . . 77
3.4.13 Temperature shift . . . 77
3.4.14 Fluorescence recovery after photobleaching (FRAP) . . 78
3.4.15 Imaging the IbpA protein with wide-field fluorescence microscopy . . . 78
3.4.16 Imaging the IbpA protein with 2D Structured illumination microscopy (SIM) . . . 79
3.4.17 Single-molecule fluorescence microscopy . . . 79
3.4.18 Single-molecule data analysis . . . 80
3.4.19 Measuring single-cell protein concentrations . . . 81
3.4.20 Image analysis . . . 83

IV. The McdA Kinetics and Mobility Drive Carboxysome Distribution in *Halothiobacillus neapolitanus* . . . 86

4.1 Introduction . . . 86
4.2 Results . . . 89
4.2.1 Carboxysomes are evenly distributed in *H. neapolitanus* 89
4.2.2 Carboxysomes are dynamic on the nucleoid . . . 89
4.2.3 Construction and characterization of functional McdA fluorescent fusions . . . 93
4.2.4 McdA forms gradients on the nucleoid . . . 96
4.2.5 McdA binding to DNA is ATP- and dimerization-dependent 96
4.2.6 McdA ATPase activity is triggered by DNA . . . 99
4.2.7 McdB stimulates the release of McdA from DNA without enhancing its ATPase activity *in vitro* . . . 102
4.2.8 Carboxysome localized McdB releases McdA from the nucleoid . . . 105
4.2.9 McdA dimers can diffuse while bound to the nucleoid . 110
4.2.10 McdA dynamics are consistent with regular positioning of α-carboxysomes . . . 113
4.3 Discussion . . . 115
4.3.1 BMC positioning may be dictated by their copy number and the cell geometry . . . 116
4.3.2 McdA release from DNA is not obligatorily coupled to ATP hydrolysis . . . 117

4.3.3 Diffusion on DNA by ParA dimers contributes to its flux control . . . 117
4.3.4 Brownian-ratchet models may explain differences between McdAB systems . . . 118
4.4 Materials and Methods . . . 119
4.4.1 Construct designs and cloning . . . 119
4.4.2 Media and growth conditions . . . 121
4.4.3 Making competent cells of *H. neapolitanus* c2 . . . 122
4.4.4 Transformation in *H. neapolitanus* . . . 122
4.4.5 Protein structure prediction and visualization . . . 122
4.4.6 Expression and purification of WT and mutants of *H. neapolitanus* McdA proteins . . . 123
4.4.7 Gel filtration assay . . . 123
4.4.8 DNA binding assay . . . 124
4.4.9 ATPase assay . . . 124
4.4.10 Fluorescence polarization assay . . . 125
4.4.11 Cleaning coverslips for fluorescence microscopy . . . 125
4.4.12 Widefield epifluorescence microscopy . . . 125
4.4.13 Nucleoid staining for live-cell imaging . . . 126
4.4.14 Image processing and analysis . . . 126
4.4.15 Single-molecule fluorescence microscopy . . . 130
4.4.16 Single-molecule data analysis . . . 131
4.4.17 Single-molecule time-lapse fluorescence microscopy . . . 133
4.4.18 Cumulative distribution function (CDF) analysis . . . 134
4.4.19 Single-molecule residence time *in vivo* . . . 134

V. Environmental Biosensors for Cryogenic Correlative Light and Electron Microscopy . . . 145

5.1 Introduction . . . 145
5.2 Results . . . 146
5.2.1 The molecular crowding sensor SED1 preserves its function at cryogenic temperatures . . . 146
5.2.2 Biosensor cryoCLEM of SED1 in S. cerevisiae reveals structural changes in response to osmotic stress . . . 150
5.2.3 pHRed preserves its pH sensing at cryogenic temperatures . . . 153
5.2.4 Cryogenic light microscopy of H. neapolitanus demonstrates pHRed as an unsuitable biosensor for cryoCLEM 157
5.2.5 pHmScarlet and pHluorin2 are alternative pH sensors for cryoCLEM . . . 157
5.2.6 MatryoshCaMP6s loses its calcium sensitivity at 77 K . 159
5.2.7 jREX-GECO1 preserves its calcium sensing at cryogenic temperatures . . . 160
5.3 Discussion . . . 163

5.4 Materials and Methods . . . 164
5.4.1 Protein Purification . . . 164
5.4.2 Fluorescence spectroscopy . . . 166
5.4.3 Cryogenic freezing of purified biosensors . . . 167
5.4.4 Production of strains . . . 167
5.4.5 Cell growth and sample preparation . . . 168
5.4.6 Cryogenic fluorescence microscopy . . . 169
5.4.7 Fluorescence image analysis . . . 170
5.4.8 Focused-ion beam milling . . . 171
5.4.9 Cryogenic electron tomography . . . 171

VI. Conclusions and Future Directions . . . 172

6.1 Introduction . . . 172
6.2 Biomolecular condensates in bacteria . . . 172
6.3 Spatial regulation of carboxysomes . . . 174
6.4 Biosensor cryoCLEM . . . 176
6.5 Contributions to other work . . . 177
6.6 Overarching Conclusions . . . 178

BIBLIOGRAPHY . . . 179

LIST OF FIGURES

Figure

1.1 Compartmentalization strategies in bacteria . . . 3
1.2 Properties of biomolecular condensates. . . . 6
1.3 Roles of condensates in bacteria. . . . 7
1.4 ParA ATPases position cellular machinery. . . . 11
1.5 Proposed models for ParA-mediated cargo partitioning. . . . 13
1.6 The McdAB system distributes carboxysomes in *S. elongatus*. . . . 17
2.1 Length-scales of microscopy . . . 21
2.2 Single-molecule localization microscopy . . . 24
2.3 Cryogenic correlative light and electron microscopy . . . 32
3.1 Framework to assess biomolecular condensates in bacteria . . . 36
3.2 Overexpression of mNG-McdB in *E. coli* BL21 . . . 39
3.3 Expression of mCherry fusion proteins . . . 42
3.4 Proteins that phase separate *in vitro* form foci above a quantifiable *in vivo* c_{sat} . . . 43
3.5 mCherry fusion proteins form cellular foci . . . 44
3.6 EMCCD calibration for photon counting . . . 46
3.7 Cells that form condensates maintain a soluble cytoplasmic fraction . . . 48
3.8 Normalized pixel intensity histograms and condensation coefficients of mCherry fusion proteins . . . 49
3.9 mCherry-McdB^{sol} condenses by repulsive interactions with the nucleoid 50
3.10 Changes in cell volume and temperature drive condensate reversibility . 53
3.11 Condensate reversibility through cell growth, division, and osmolarity shift . . . 56
3.12 FRAP in concert with single-particle tracking informs on the material state of foci in bacterial cells . . . 59
3.13 Diffusion coefficients of PAmCherry fusion proteins . . . 60
3.14 The nature of IbpA chaperone association with foci informs their material state *in vivo*. . . . 64
3.15 Nature of IbpA association with mCherry fusion foci by 2D SIM . . . 65
4.1 Carboxysomes in *H. neapolitanus* are distributed and their motion is consistent with regular positioning . . . 91
4.2 Distribution of distances between adjacent carboxysome foci . . . 92
4.3 Analysis of carboxysome and ParB foci diffusion . . . 92
4.4 Analysis of functional fluorescent fusions of McdA . . . 95

4.5 McdA forms gradients on the nucleoid . . . 97
4.6 Examination of bulk McdA localization . . . 98
4.7 Purification of *H. neapolitanus* His-SUMO-McdA . . . 99
4.8 McdA binds DNA in a ATP-dependent dimer state and its ATPase activity is triggered by DNA . . . 101
4.9 Biochemical analysis of McdA DNA binding mutant . . . 102
4.10 Carboxysome-localized McdB promotes release of McdA from DNA despite not stimulating its ATPase activity . . . 104
4.11 ATPase activity of McdA in the presence of excess McdB . . . 106
4.12 Diffusion analysis of single-molecule trajectories of McdA and its mutants collected with 20 ms camera integration . . . 107
4.13 Localization uncertainty associated with consecutive detections of single PAmCherry molecules in fixed *H. neapolitanus* cells . . . 108
4.14 McdA-mNG^{SW} colocalizes with McdB-bound carboxysomes . . . 109
4.15 Nucleoid-bound McdA dimers can diffuse . . . 113
4.16 Nucleoid-bound McdA-PAmCherry^{SW} dynamics are heterogenous . . . 114
4.17 *H. neapolitanus* cell and nucleoid lengths . . . 115
5.1 Experimental workflow for biosensor cryoCLEM . . . 147
5.2 SED1 maintains its crowding-sensing properties at cryogenic temperatures 149
5.3 Cryogenic ratiometric imaging of SED1 expressed in *S. cerevisiae* . . . 151
5.4 cryoCLEM of SED1 in *S. cerevisiae* . . . 152
5.5 pHRed maintains its pH-sensing properties at cryogenic temperatures . . . 155
5.6 pHRed is too dim for cryoCLEM . . . 156
5.7 Alternative pH sensors for cryoCLEM . . . 158
5.8 MatryoshCaMP does not sense calcium at cryogenic temperature . . . 161
5.9 jREX-GECO1 maintains its calcium-sending properties at cryogenic temperatures . . . 162

LIST OF TABLES

Table

3.1 Focus dissolution tracking analysis results 55
3.2 Apparent diffusion coefficients and weight fraction resulting from two-state Gaussian mixture fitting 61
3.3 Strain and plasmids used in this study 70
3.4 Primers used in this study 71
3.5 Reagents used in this study 72
3.6 Parameters used to detect fluorescent foci for classification 84
4.1 Summary of diffusion coefficients (Fast SPT) from Chapter 4 136
4.2 Summary of confinement radii (Slow SPT) from Chapter 4 137
4.3 Summary of diffusion coefficients (Slow SPT) from Chapter 4 138
4.4 Strains used in Chapter 4 139
4.5 Plamids used in Chapter 4 140
4.6 DNA oligonucleotides used in Chapter 4 141
4.7 Chemicals used in Chapter 4 143
4.8 Software used in Chapter 4 144
5.1 Plasmids used in this study 165
5.2 Strains used in this study 168
5.3 Fit parameters for biosensor calibration curve fitting 171

LIST OF ABBREVIATIONS

ATP Adenosine triphosphate

ATPase Adenosine triphosphotase

BR-body bacterial ribonucleoprotein body

BMC bacterial microcompartment

cryoCLEM cryogenic correlative light and electron microscopy

EMSA Electrophoretic mobility shift assay

FRAP fluorescence recovery after photobleaching

IBs Inclusion bodies

IbpA Inclusion binding protein A

IDR Intrinsically disordered region

LB Lysogeny broth

LLPS liquid-liquid phase separation

LoG Laplacian of Gaussian

mNG mNeonGreen

MSD mean squared displacement

McdA Maintenance of carboxysome distribution A

McdB Maintenance of carboxysome distribution B

msfGFP monomeric superfolder GFP

PA photo-activatable

PC Phase contrast

PSCP phase separation coupled to percolation

ROI region of interest

sCMOS scientific Complementary Metal-Oxide-Semiconductor

SMALL-LABS Single-Molecule Accurate LocaLization by LocAl Background Subtraction

SPT Single-particle tracking

SIM structured illumination microscopy

nsDNA non-specific DNA

ABSTRACT

Spatial organization is a key feature in all living organisms. Compartmentalization of enzymatic reactions enables efficient cellular metabolism, and intracellular transport ensures that molecular machinery localizes to the correct places at the correct times. Bacteria often lack the mechanisms employed by eukaryotic systems to achieve spatial organization, such as membrane-bound organelles and linear transport by motor proteins on filaments. Instead, bacteria utilize self-organizing protein systems to achieve compartmentalization and transport. This dissertation aims to understand the mechanisms used by bacteria for subcellular organization. Chapter 1 provides background on these organization strategies and highlights the specific systems investigated: biomolecular condensates and the positioning system of a bacterial microcompartment (BMC). Chapter 2 delineates the principles of single-molecule fluorescence microscopy, single-particle tracking (SPT), and cryogenic correlative light and electron microscopy (cryoCLEM).

To compartmentalize enzymatic reactions, bacteria have developed protein-based organelles such as BMCs and biomolecular condensates. Despite the growing literature describing condensate-forming bacterial proteins *in vitro*, their correlation to *in vivo* properties is lacking. To address this gap, I developed an experimental framework to assess biomolecular condensates in live bacterial cells in Chapter 3. I used quantitative fluorescence microscopy and single-molecule tracking to systematically examine the conditions for condensate formation, their reversibility, and the dynamics of their components. We also discovered that IbpA, an established marker for insoluble aggregates, localizes to condensates differently than aggregates. Our work distinguishes between the behaviors of

condensates and aggregates, demonstrating that condensates can reversibly form despite having different material states.

BMCs are also spatially organized in the cell. The most extensively studied BMC is the carboxysome, which selectively concentrates the enzyme ribulose-1,5-biphosphate carboxylase/oxygenase (RuBisCO) with carbon dioxide to efficiently catalyze carbon fixation in many autotrophic bacteria. Carboxysomes are positioned along the cell length by the Maintenance of carboxysome distribution (Mcd) system. McdA is a DNA-binding deviant Walker-like ATPase similar to the ParA/MinD ATPase family, which bacteria employ to organize crucial components like genetic material and cell division machinery. McdB is an adaptor protein that localizes to carboxysomes and connects them with McdA. While the functions of McdA and McdB are known, their positioning mechanism is unknown. In Chapter 4, I investigate the dynamics of carboxysomes and McdA by live-cell fluorescence microscopy, single-particle tracking, and biochemical assays. I show that McdA is a DNA-binding protein and that its kinetics and mobility drive the regular positioning of carboxysomes on the nucleoid. These results provide the first quantitative description of BMC positioning in bacteria.

cryoCLEM is an approach that couples the strengths of fluorescence and electron microscopy to provide molecular specificity to cellular structures. To extend these capabilities for a more comprehensive investigation of cellular structures, I develop biosensor cryoCLEM in Chapter 5. I identify fluorescent biosensors compatible with cryogenic conditions that report on molecular crowding, pH, and calcium to provide physiological context to the high-resolution cellular structures acquired by cryoEM.

Finally, in Chapter 6, I summarize the findings presented and provide future directions for each investigation. This dissertation deepens our understanding of spatial organization in bacteria and provides an imaging-based approach that can be implemented to obtain high-resolution structures with local environmental information.

CHAPTER I

Spatial Organization in Bacteria[1]

1.1 Compartmentalization through bacterial organelles

With the development of high-resolution microscopy techniques, it has become apparent that bacteria are not just mere bags of enzymes and instead, contain a highly organized cellular interior [1,2]. Among these spatial organization mechanisms, compartmentalization is key in providing physiological advantages to bacteria. Like their eukaryotic counterparts, bacteria also deploy organelles to achieve compartmentalization [3,4]. Here, I borrow from Greening and Lithgow and define an organelle as a subcellular structure with interior components distinct from its exterior and a defined boundary layer composed of lipids or proteins [4].

1.1.1 Membrane-bound organelles

Although limited, some examples of lipid-enclosed organelles are present in bacteria. One of the earliest discovered examples of a lipid-enclosed organelle is lipid bodies, which employ a lipid monolayer to sequester energy storage lipids and associated proteins [5]. Some membrane-bound organelles also accumulate metal ions for storage in ferrosomes or magnetoreception in magnetosomes [6–8]. Cyanobacteria have thylakoid membranes

[1]Section 1.3 and Figures 1.2 and 1.3 in this chapter were previously published in *Biophysical Journal*. Azaldegui, C.A., Vecchiarelli, A.G. and Biteen, J.S. The emergence of phase separation as an organizing principle in bacteria *Biophys. J.* **120**, 1123-1138 **(2021)** DOI: 10.1016/j.bpj.2020.09.023

which contain the light-harvesting proteins that drive the initial steps of photosynthesis [9, 10].

1.1.2 Membraneless organelles

Membraneless organelles are more widespread than membrane-bound organelles in bacteria. Mostly composed of protein molecules, these organelles typically use a protein shell as a boundary [4, 11]. The simplest form comes in encapsulin nanocompartments [11]. Encapsulin monomers self-assemble into spherical structures 20 – 40 nm in diameter and are diverse in their function, ranging from elemental storage to oxidative stress protection [12, 13]. The most widely studied class of protein-bound organelles are bacterial microcompartments (BMCs), which are much larger compared to encapsulin nanocompartments, generally ranging between 100 – 500 nm in diameter [14]. BMCs implement a multi-protein shell to encapsulate catabolic and anabolic pathways, improving the efficiency of enzymes by concentrating them with their substrates, preventing unfavorable or wasteful reactions, and/or sequestering toxic intermediates (Fig. 1.1a) [14–16]. Recently, bioinformatic analyses revealed 68 distinct BMC operon types across 45 bacterial phyla [17].

1.1.3 Carboxysomes are the model BMC

The most widely studied BMC is the carboxysome. Carboxysomes encapsulate the enzyme ribulose-1,5-biphosphate carboxylase/oxygenase (RuBisCO) together with its CO_2 substrate to enhance carbon fixation. Encapsulation of CO_2 favors this reaction pathway over the competitive substrate, O_2, which leads to wasteful photorespiration. Due to their role in optimizing the carbon fixation process, carboxysomes contribute significantly to global carbon fixation [18]. Since their discovery in the mid-20th century, carboxysomes have become the model BMC, with numerous studies focusing on their structure, assembly, and catalytic function [14, 19–22]. Beyond fundamental research, carboxysomes are

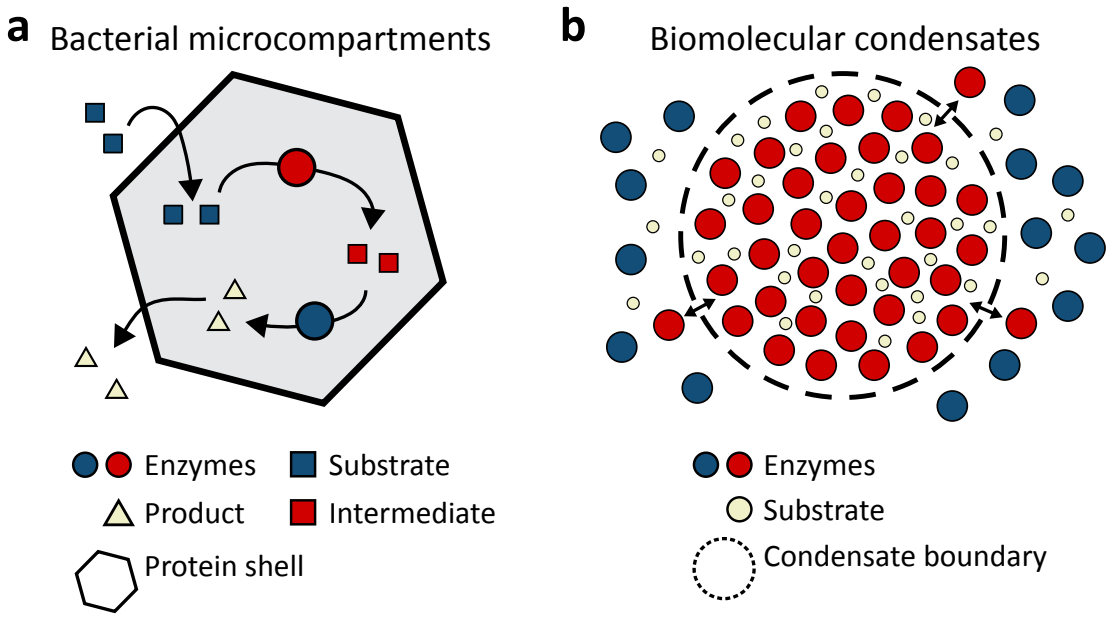


Figure 1.1: Compartmentalization strategies in bacteria. a. Diagram of a BMC. A protein shell encapsulates a specific set of enzymes and is selectively permeable to its substrates and products. **b**. Diagram of a biomolecular condensate. The region within the dashed line is the dense phase enriched with the red enzyme and its substrate. The exterior is the dilute phase which includes a mixture of enzymes (blue and red).

also of interest in biotechnology and synthetic biology as a potential means to improve carbon fixation in other organisms and for engineering in nanomedicine [14, 23–26].

Carboxysomes exist as either α or β types, sharing their carbon fixation function but differing in structural composition, assembly, and regulation [27–30]. Both types are found in cyanobacteria, while α-carboxysomes are widespread across other bacterial phyla and more closely resemble other types of BMCs [17,29]. Studying both carboxysome types has revealed differences and similarities that inform on the conserved properties of BMCs in general.

1.2 Biomolecular condensates and their properties

Biomolecular condensates are another type of membrane-less organelle. These structures are not enclosed by a membrane but enrich specific biomolecules, such as proteins and nucleic acids, at non-stoichiometric concentrations [31]. Importantly, unlike BMCs,

biomolecular condensates are not surrounded by an ordered protein shell. Instead, their boundary is defined by a density difference between the components within the organelle and its surroundings (Fig. 1.1b). Condensates are usually observed as droplets that exhibit liquid-like behaviors such as droplet fusion and relaxation into spherical shapes [31–35]. Due to their similarities to colloidal coacervate droplets, biomolecular condensates were proposed to assemble via similar phase separation processes [32, 34].

1.2.1 Condensate formation processes

Phase separation is a process in which molecules in a homogenous mixture separate into two distinct coexisting phases [36, 37]. For example, using the illustration in Figure 1.1b, the dense phase is enriched in the red macromolecule, while the dilute phase has a lower density of this macromolecule. Before phase separation, the macromolecules are well mixed with the solvent. When the system reaches a concentration at which the single-phase regime can no longer be maintained, the free energy of mixing becomes unfavorable, and the system favors separating the mixture into two separate phases. This critical concentration is known as the saturation concentration, c_{sat}. The c_{sat} for a specific mixture depends on all components present and can be altered by adjusting parameters that affect the thermodynamic stability of the system, such as temperature, ionic strength, and pH. After phase separation, the dilute phase becomes buffered to c_{sat}, while the concentration in the dense phase is referred to as c_{dense}.

Biological macromolecules can engage in both inter- and intra- molecular interactions. Therefore, an associative transition, known as percolation, can occur in addition to phase separation [38–41]. If the concentration at which percolation occurs in a system is higher than c_{sat}, both processes are coupled, resulting in a condensate volume characterized by a network of multivalent interactions among its components. This coupled process, called phase separation coupled to percolation (PSCP) [38–40], produces condensates that are viscoelastic in nature, meaning they exhibit time-dependent material properties. Given

that proteins and nucleic acids exhibit multivalent associations, it is more likely that they form condensates through PSCP rather than just liquid-liquid phase separation (LLPS).

1.2.2 Observed properties of condensates

In biological systems, several properties have been observed for condensates which can help differentiate them from other structures like protein aggregates, regardless of the underlying formation process. Importantly, the reversible formation of condensates when reaching c_{sat} has been demonstrated by titrating expression of condensate components or perturbing the system to shift the c_{sat} (Fig. 1.2a) [35, 42–44]. Both *in vitro* and *in cellulo*, condensates typically adopt a spherical shape through viscous relaxation to minimize surface area (Fig. 1.2b) [33, 35, 42, 43, 45]. The broad size distribution of condensates can be explained by the fusion events observed between them (Fig. 1.2c) [31, 33, 35]. Since many of these condensates have liquid-like properties, their components tend to remain mobile within the assemblies and can exchange with the surrounding dilute phase (Fig. 1.2d) [46]. While these behaviors are indicative of viscous fluids, the viscoelastic nature of condensates may manifest in a variety of material states [47–52], thus careful interpretation is necessary when assessing the nature of condensates [40, 53].

1.3 The roles of biomolecular condensates in bacteria

Several biomolecular condensates have been implicated in bacterial cell biology [39, 54]. For instance, prior to recruitment of its protein shell, carboxysomes are suggested to behave like condensates and may share similar assembly mechanisms [55–57]. Proteins involved in biofilm formation, heterochromatin regulation, transcription, cell division, active transport, among others, have been shown to form condensates *in vitro* [58–65]. Mutation of key residues underlying *in vitro* condensate formation also disrupts their respective cellular processes, suggesting condensate formation and/or phase transitions are important to their function. Below I describe two examples of well-characterized biomolecular

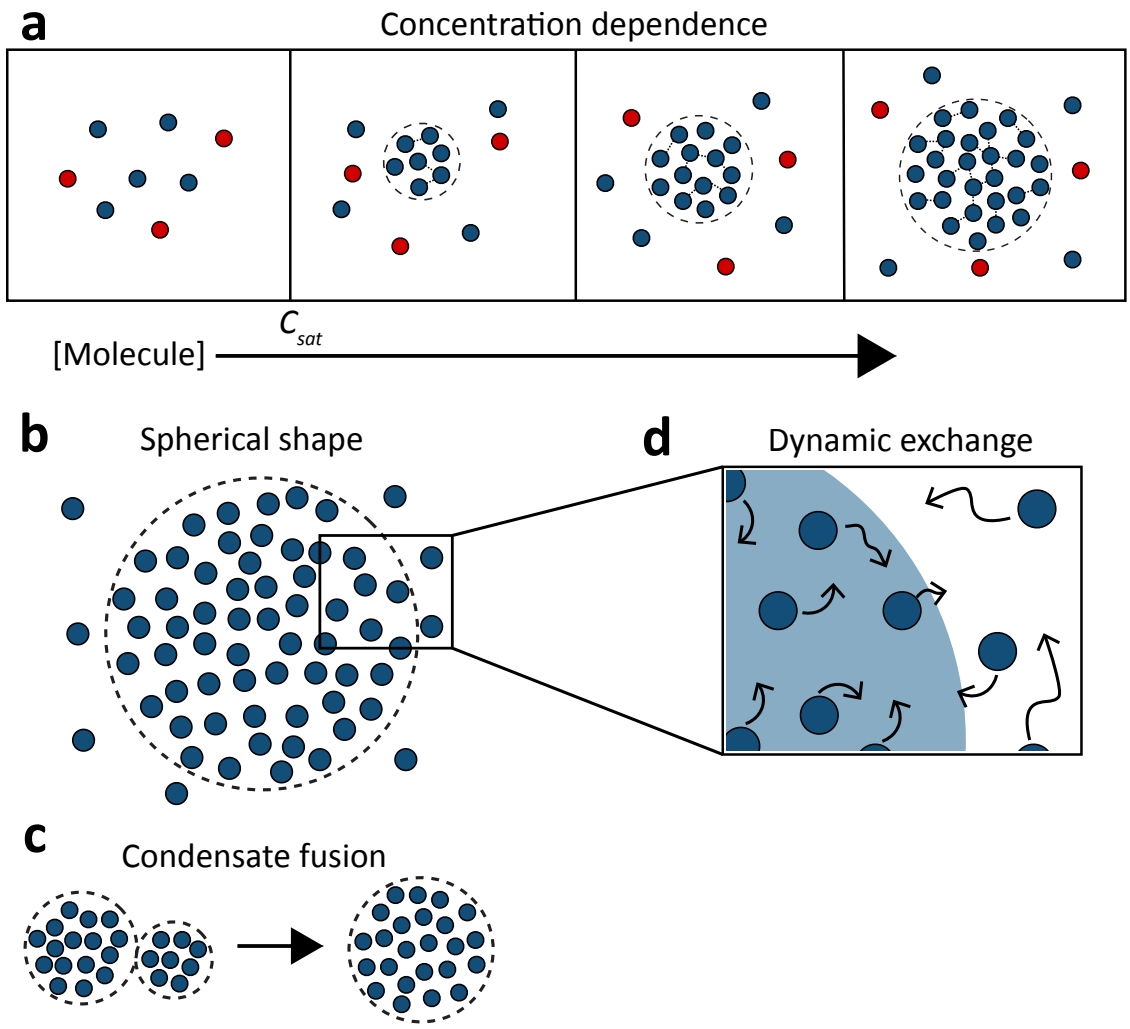


Figure 1.2: Properties of biomolecular condensates. **a**. Condensates can form via a concentration-dependent associative phase transition. Associations between condensate components (dotted lines) can result in emergent viscoelastic properties. Condensates with liquid-like behavior exhibit properties such as (**b**) relaxing into a spherical shape and (**c**) fusing into larger condensates. **d**. Condensate components can exchange between the dense and dilute phases.

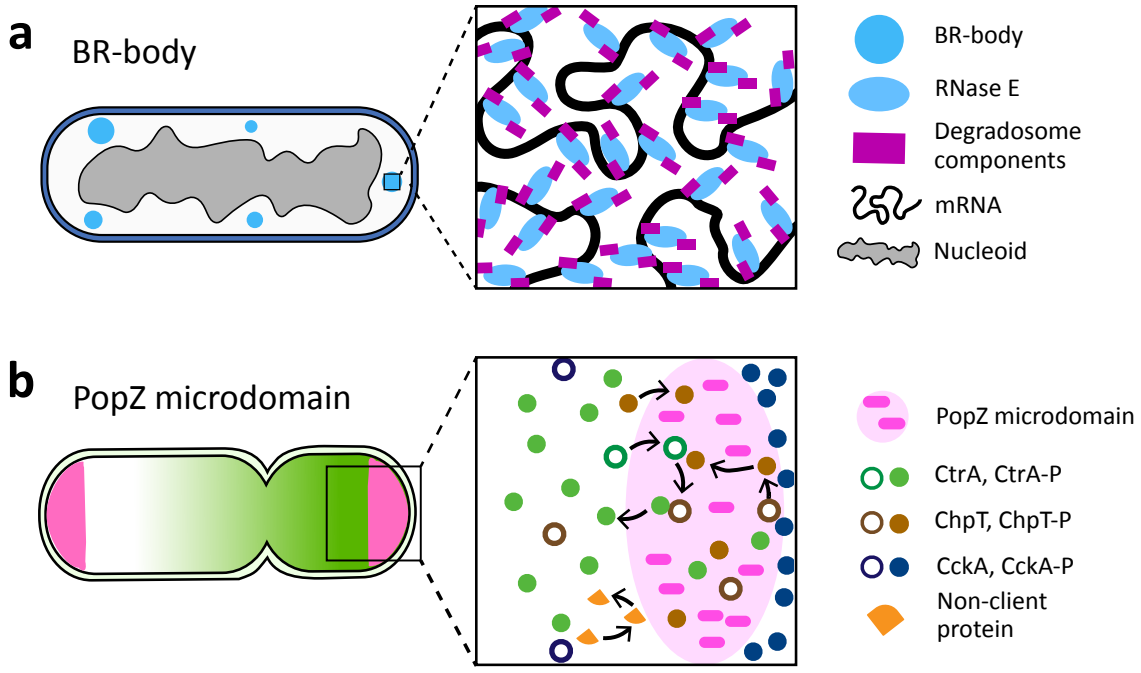


Figure 1.3: Roles of condensates in bacteria. a. BR-bodies are critical in the RNA decay pathway. **b**. PopZ microdomains play a role in the asymmetric development of *C. crescentus*.

condensates involved in mRNA regulation and asymmetric development in bacteria (Fig. 1.3).

1.3.1 Bacterial ribonucleoprotein bodies organize mRNA decay

The best characterized prokaryotic condensate to date is the bacterial ribonucleoprotein body (BR-body), which controls mRNA decay by locally concentrating the RNA degradosome proteins and their substrates (Fig. 1.3a) [66, 67]. In *Caulobacter crescentus*, this assembly is facilitated by RNase E, which uses its C-terminal domain (CTD) as a scaffold [68]. This essential domain for BR-body assembly is an IDR containing many RNA-binding sites [66, 68]. BR-bodies dynamically respond to decreases in translation levels by forming condensates that accelerate mRNA decay [67]. Condensate disassembly is promoted by mRNA cleavage, releasing mRNA fragments for other uses. For a more in-depth review of BR-body function and phylogenetic distribution, see Muthunayake et al. [69].

The BR-body function also shifts as a result of a transition in its material state. A recent

study from the Biteen and Schrader Labs found that RNase E dynamics within the BR-body become arrested upon stress [70]. This behavior correlates with a functional transition from mRNA decay to storage, allowing rapid regrowth once the stress is removed. While the specific molecular mechanism underlying this transition remains unknown, this finding exemplifies a stress response mechanism that enables bacteria to quickly recover once optimal growth conditions are restored.

1.3.2 PopZ microdomains regulate asymmetric cell development

The asymmetric bacterium *C. crescentus* has two distinct cell poles: the new swarmer pole and the old, stalked pole. The phosphorylated transcription factor CtrA (CtrA-P) plays a crucial role in establishing this functional asymmetry. Among the factors contributing to this gradient, the polar organizing protein PopZ is significant. After chromosome segregation, PopZ localizes to both cell poles, recruiting proteins to each. However, its effects differ at the two poles. At the swarmer pole, PopZ forms a microdomain essential for the polar localization of several proteins, including various phospho-signaling proteins (Fig. 1.3b) [71–73]. This pathway regulation by PopZ ultimately leads to differential gene expression between daughter cells and inhibits replication initiation in the swarmer cell [73, 74].

PopZ microdomains also play a role in stalked cell development and bacterial stress response. They recruit the condensate-forming, membrane-bound protein SpmX, which localizes a critical kinase DivJ, establishing another cellular asymmetry [75, 76]. *In vitro* reconstitution of PopZ and SpmX results in condensate formation, with mutations affecting their self-interaction activities influencing the diffusive properties within cellular condensates [77]. Because SpmX condensates slow DivJ diffusion, increasing its polar concentration, one function of the SpmX condensate is to enhance the density-dependent DivJ kinase activity under varying nutrient conditions. These two interacting condensates in *C. crescentus* robustly regulate the critical DivJ signaling reaction.

Recently, the molecular mechanisms behind PopZ condensate formation were dissected to modulate the properties of PopZ microdomains in cells [78]. This investigation demonstrated how bacteria tune the biophysical properties of their compartments to enhance cellular fitness. The findings also led to the development of an engineered module, named PopTag, that induces condensate formation when fused to other proteins. In Chapter 3, I describe how we implemented different versions of PopTag to systematically study the behavior of condensates within bacterial cells [79].

1.4 Active partioning in bacteria

Effective bacterial proliferation requires the faithful inheritance of cellular machinery by daughter cells after cell division. For components present in high copy numbers, passive diffusion is sufficient to evenly distribute the components across the mother cell such that equal amounts are inherited in both daughter cells. However, passive diffusion is inadequate for effectively partitioning components that are low in copy number. To overcome this challenge, bacteria have evolved active transport mechanisms, that differ from those used by eukaryotes, to achieve subcellular organization and ensure the appropriate inheritance of molecular machinery.

1.4.1 ParA/MinD ATPases position cellular machinery

One such mechanism is the active positioning by the ParA/MinD family ATPases. This family is responsible for the spatial regulation of various genetic- and protein-based cargos across the bacterial domain [80–85]. Their best-studied members are ParA and MinD, the namesakes of the family. ParA ATPases partition plasmids and segregate chromosomes before cell division, while MinD positions the divisome at the midcell plane, preventing asymmetric cell division. Many other ParA/MinD-like ATPases are found in prokaryotes, organizing protein-based complexes such as BMCs, flagella, chemotaxis clusters, and conjugation machinery.

The ParA/MinD ATPase family shares several key features. The primary identifier is the 'deviant' Walker A motif, KGGxxK[S/T], required for Adenosine triphosphate (ATP) binding and hydrolysis [83, 86, 87]. In a few cases, the signature lysine residue is found outside of the Walker A box [88, 89]. ParA/MinD ATPases form sandwich dimers and typically have their ATP hydrolysis activity stimulated by a matrix substrate (such as nucleoid-DNA or membrane-lipid) and/or the N-terminus of their partner protein [81, 90–98]. These ATPases use their C-terminal domain to bind their matrix substrate as ATP-bound dimers, employing an amphipathic helix for membrane binding (MinD-like) or a positively charged interface for non-specific DNA (nsDNA) binding (ParA-like) [99–101]. From here, I will focus on DNA partitioning by ParA to elaborate on its mechanism.

1.4.2 The ATPase cycle of ParA

The ATPase cycle of ParA results in dynamic patterning within the cell (Fig. 1.4a). For example, a plasmid-positioning ParA monomer binds ATP, to enable it to dimerize with another ATP-bound ParA. This dimerization prompts nonspecific binding to DNA. The partner protein, ParB, localized to the plasmid cargo, interacts with ParA, stimulating its release from DNA, typically through ATP hydrolysis. ParA can then exchange nucleotides and restart the cycle. Repeating this biochemical cycle results in cargo "pulling" by emergent ParA concentration gradients. For a single plasmid cargo, these dynamics position the plasmid at midcell as it continually follows the oscillating ParA gradients, resulting in oscillatory motion around this "home" position (Fig. 1.4b) [102–104]. When multiple plasmids are present, the interplay between ParA and ParB-bound plasmids positions them equidistantly at the quarter positions of the cell (Fig. 1.4c-d) [105–108].

1.5 Proposed mechanisms of ParA-mediated partioning

Despite a thorough understanding of ParA biochemistry, it remains unclear how ParA gradients "pull" plasmids to their correct positions. Over the last decade, it has become

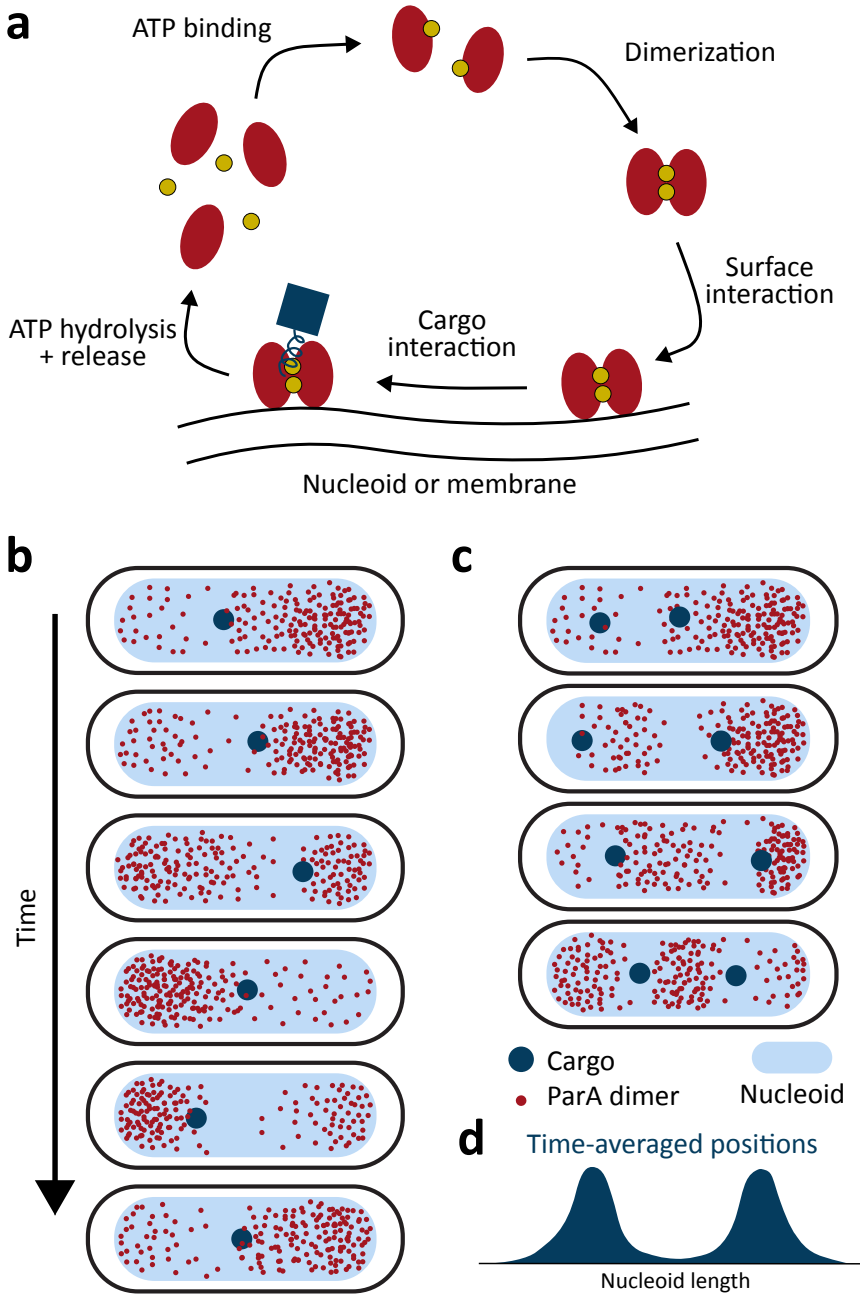


Figure 1.4: ParA ATPases position cellular machinery. a. Putative ATPase cycle of ParA ATPases (red). ParA binds ATP (gold) and dimerizes. A conformational change enables interaction with the DNA surface. Interaction with the cargo-localized partner protein, ParB (dark blue), stimulates ATP hydrolysis and release of ParA from the nucleoid. ParA-ParB interactions result in ParA gradients on the nucleoid that drive positioning of (**b**) one or (**c**) more cargo. **d**. In the latter case, the cargos are positioned at the quarter positions of the nucleoid.

evident that the combination of ParA biochemistry and intrinsic cargo diffusion is insufficient to explain the active partitioning of cargo and ParA patterning (Fig. 1.4b-c). To date, several models have been proposed that successfully reproduce cargo positioning [104, 109–116]. These models include a non-Brownian ParA-dependent force reminiscent of a Brownian ratchet-based mechanism. In this section, I will briefly describe the concept of a Brownian ratchet. Following that, I will illustrate the two most prominent models and introduce a more recent model which proposes a unified framework that captures the diversity of dynamics observed across ParA systems in different organisms.

To understand the concept of a Brownian ratchet, I borrow the explanation from Peskin et al. [117]. Consider a particle diffusing randomly in a one-dimensional path that is divided into intervals, with each interval representing a 'ratchet'. If the particle crosses the boundary of an interval from the left, it cannot move back in that direction. Although the particle has an intrinsic ability to step in either direction with equal probability, the ratcheting effect causes directed motion towards the right. In a biological context, this type of motion requires an environmental asymmetry (the ratchet) created by some energy input and intrinsic diffusion of the particle which allows it to process along this asymmetry [117, 118].

1.5.1 Mechanochemical coupled Brownian-ratchet

One prominent model for ParA-mediated cargo partitioning is the mechanochemical coupled Brownian-ratchet model (Fig. 1.5a). This model is based on measurements of directed motion by a ParB-decorated bead on a plasmid ParA-covered DNA carpet [109–111, 119–122]

In this model, ParB-stimulated ATP hydrolysis of ParA creates the asymmetry required to drive cargo motion. The elasticity of ParA-ParB bonds generates the mechanical force needed to 'pull' the cargo along the ParA concentration gradient, invoking a chemophoretic force proposed by Sugawara and Kaneko [115, 116]. Key aspects of this

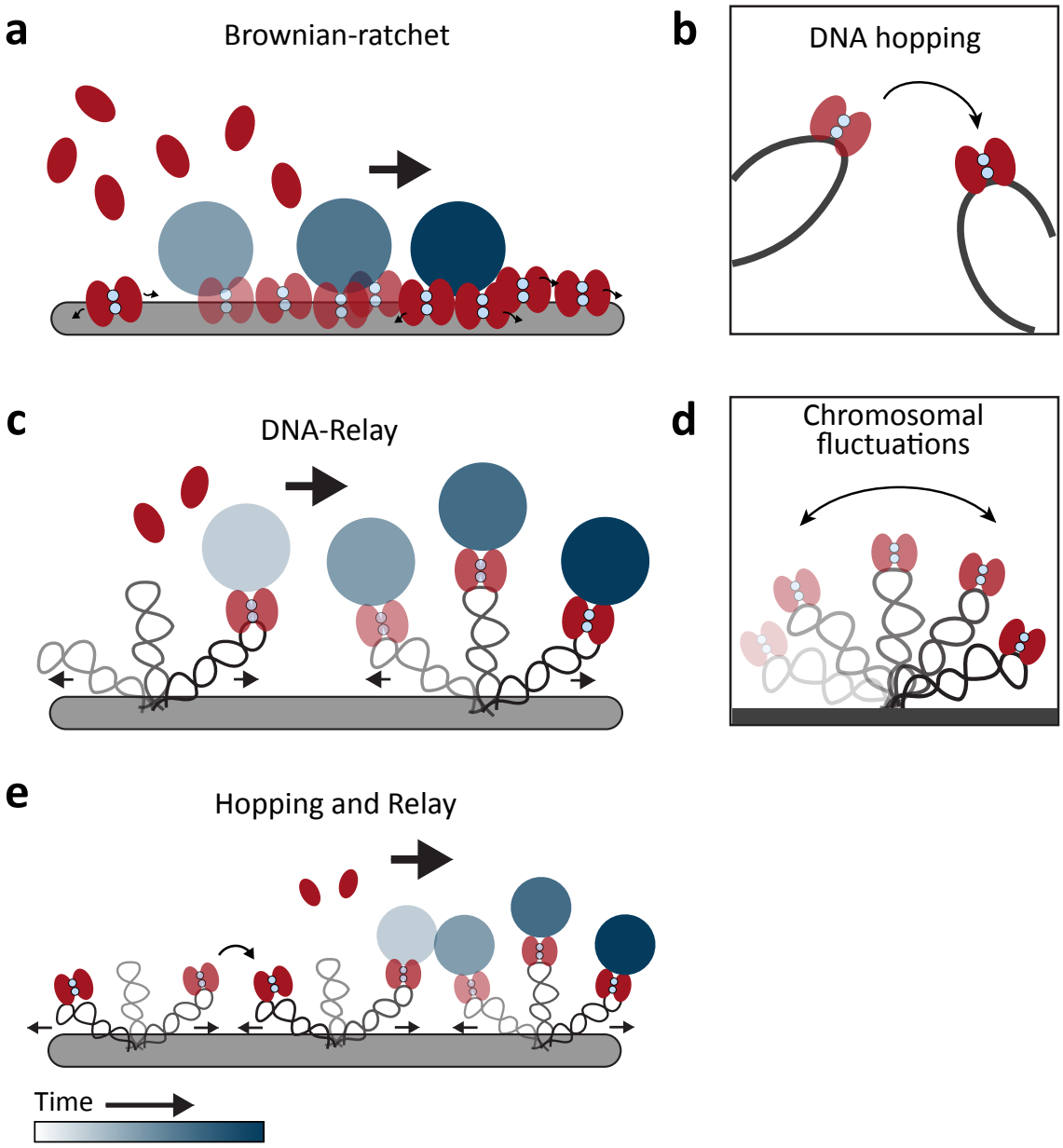


Figure 1.5: Proposed models for ParA-mediated cargo partitioning. **a**. The Brownian-ratchet model proposes that chemophoretic force driven by ParA-ParB interactions translocate the cargo in a directed fashion. **b**. Important to this model is the intersegmental transfer or hopping of ParA dimers on DNA, which helps maintain the protein gradient. **c**. The DNA-relay model proposes that the (**d**) elastic fluctuations of the chromosome enable the "relay" of cargo by ParA dimers bound to DNA. **e**. The Hopping and Relay model builds on the DNA relay model by including DNA hopping as an additional mechanism for ParA flux control on the nucleoid.

model include (1) quenching of intrinsic lateral diffusion by ParA-ParB tethers, creating a bias in the direction of motion, and (2) lateral diffusion of ParA on the nucleoid (Fig. 1.5b), which delays the rebinding of ParA behind the cargo, maintaining the directional gradient.

By varying the rate of cargo motion relative to the rate of replenishment of the ParA depletion zone the Brownian-ratchet model can reproduce different types of cargo dynamics and positioning observed in cells. These include pole-to-pole oscillations, local excursions or approximate positioning, diffusive, and stationary. It is still unclear how this model translates to three dimensions, as it usually assumes that cargos are confined to the nucleoid surface and inner membrane, particularly as nucleoids and chromosomes are partitioned within the nucleoid volume [123].

1.5.2 DNA-relay model

A robust investigation into the chromosomal ParAB system of *C. crescentus* argued for a DNA-relay model (Fig. 1.5c) [104, 112]. In this model, the elastic fluctuations of the chromosome (Fig. 1.5d) generate the translocating force that drives the directed motion of the cargo across the cell.

The authors proposed that the DNA-bound ParA dimer fluctuates in space as a result of the DNA elasticity, thereby generating a force that pulls the cargo and 'relays' it to another DNA-bound ParA dimer. This DNA-relay model contrasts with early versions of the Brownian ratchet model, which were based on a reaction-diffusion mechanism. This distinction lies in the fact that, without DNA-enabled ParA fluctuations, reaction-diffusion simulations cannot reproduce the experimental data.

Like the Brownian-ratchet model, the DNA-relay model also relies on ATP hydrolysis-induced ParA concentration gradients to achieve directed motion. The model was extended to scenarios with multiple cargos, resulting in an inverse relationship between the number of cargos and their degree of oscillation confinement [104].

1.5.3 Hopping and relay model

A recent study on the dynamics of F1 plasmid positioning in *E. coli* demonstrated that these plasmids are regularly positioned [124]. Since neither the Brownian-ratchet nor the DNA-relay models fully captured regular positioning, the authors proposed their own model extended from the DNA-relay model. This new model incorporated the concept of ParA flux balancing, which had previously been shown to result in regular positioning of ParA-regulated cargo [98, 114].

To produce ParA fluxes that capture regular positioning, the Hopping and relay model includes two key parameters (Fig. 1.5e): (1) the fraction of the nucleoid that DNA-bound ParA dimers explore before dissociating and (2) the ratio of the ParB-induced dissociation rate to the basal dissociation rate. The diffusive length scale required for regular positioning suggested that chromosome fluctuations were insufficient in driving this motion, therefore the authors included ParA dimer diffusion to extend the nucleoid-exploration length scale. By varying the mobility and kinetic parameters of ParA, the model reproduced all possible plasmid dynamics, including the transition of the pB171 plasmid dynamics from regular to oscillatory dynamics in longer cells.

A correlative analysis of ParA and plasmid dynamics revealed that ParA gradients flip between nucleoid lobes in response to nucleoid constriction and plasmid crossing between the lobes [125]. Incorporating cooperative DNA binding by ParA into the Hopping and Relay model effectively captured these gradient flips, further supporting the model's validity. Despite being based on the DNA-relay model, where the driving force is from DNA elasticity, the ParA fluxes that drive cargo motion are independent of the force's origin. While contributions from both ParA-ParB bond elasticity and DNA elasticity are likely, the specific degree of their respective contributions remains unclear.

1.6 Maintenance of carboxysome distribution system

Earlier, I introduced carboxysomes as a type of BMC that sequesters enzymes involved in carbon fixation. In the model organism *Synechococcus elongatus* PCC 7942, β-carboxysomes are evenly distributed across the cell to ensure faithful inheritance after cell division (Fig. 1.6). In 2010, a ParA-like ATPase was discovered to be responsible for this equidistant distribution [126]. Building on this finding, the Vecchiarelli Lab characterized the system further, identifying a partner protein and subsequently renaming the system to Maintenance of carboxysome distribution protein A (McdA) and protein B (McdB) [127]. Deletion of either or both proteins leads to the irregular distribution and aggregation of carboxysomes, which in turn results in decreased carbon fixation and inhibited cell growth [127, 128].

Initially, it was proposed that McdA distributes carboxysomes through a filament-based mechanism, similar to early models of ParA-mediated DNA segregation [126, 129]. However, the Vecchiarelli Lab refuted this model by characterizing the dynamics of McdA and McdB in *S. elongatus* [127]. They found that McdA preserves the nonspecific DNA-binding property of ParA ATPases and exhibits significantly higher ATPase activity (200-fold) compared to DNA-segregating ParA ATPases. This higher activity is potentially due to divergence from the deviant Walker A motif, where a serine replaces the signature lysine residue. Furthermore, McdA gradients oscillate on the nucleoid (Fig. 1.6a-b). These dynamics are driven by its interaction with McdB, which localizes to the carboxysomes (Fig. 1.6c) and stimulates McdA ATP hydrolysis *in vitro*. Based on these observations, the Vecchiarelli Lab proposed a Brownian-ratchet model to explain the distribution of β-carboxysomes in *S. elongatus* (Fig. 1.6d).

McdAB systems have been identified in various other organisms [130–132]. McdAB-like genes are present in all β-carboxysome-containing cyanobacteria but are notably absent in α-carboxysome-containing cyanobacteria [130]. A distinct McdAB system was later discovered in α-carboxysome-containing proteobacteria, in which species the McdA

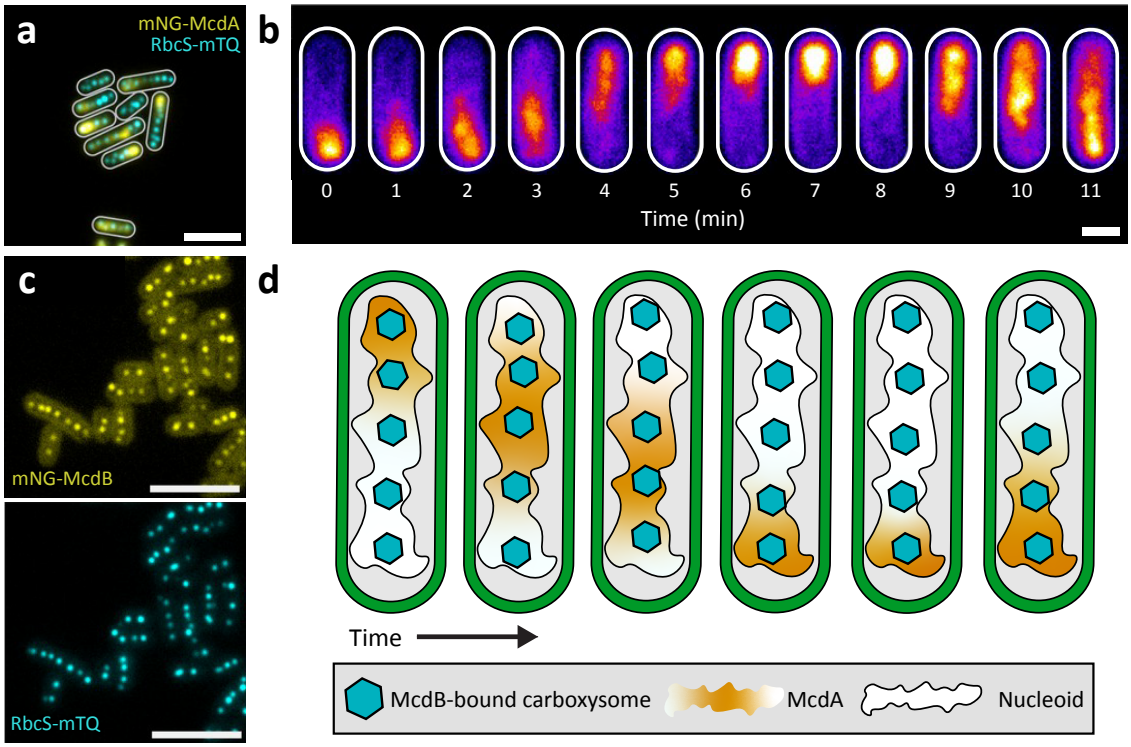


Figure 1.6: The McdAB system distributes carboxysomes in *S. elongatus*. **a**. McdA (yellow) is a ParA-like ATPase in *S. elongatus* PCC 7942 that distributes carboxysomes (cyan) on the nucleoid. Scale bar: 5 μm. **b**. McdA forms oscillating gradients on the nucleoid. Scale bar: 1 μm. **c**. McdB (yellow) is the partner protein that localizes the carboxysome cargo(cyan). Scale bar: 5 μm. **d**. Schematic of observed dynamics of carboxysomes and the McdAB system. Figures a-c were adapted from reference [127].

genes maintain the complete 'deviant' Walker A motif [131]. Using the model chemoautotrophic proteobacterium *Halothiobacillus neapolitanus*, the Vecchiarelli Lab demonstrated that α-carboxysome are indeed distributed by this newly identified McdAB system.

Despite the Brownian-ratchet model being proposed to explain β-carboxysome distribution in *S. elongatus*, it remains unclear whether it fully captures the dynamics of carboxysomes and McdA. Furthermore, *H. neapolitanus* has shorter cell lengths and a larger average carboxysome copy number (8 to 12), making α-carboxysomes more densely packed [133]. To address this knowledge gap, Chapter 4 quantitatively describes the dynamics of α-carboxysomes and McdA in *H. neapolitanus* to elucidate the underlying mechanism governing carboxysome distribution in bacteria.

1.7 Thesis outline

This dissertation focuses on the mechanisms of spatial organization in bacteria. In Chapter 1, I introduce key concepts relevant to this dissertation, beginning with compartmentalization mechanisms in bacteria, specifically emphasizing biomolecular condensates and their roles in spatial organization. I also discuss ParA ATPases, a family of proteins that partition bacterial subcellular machinery, highlighting the Maintenance of Carboxysome Distribution (Mcd) system, which is pertinent to both compartmentalization and active partitioning.

In Chapter 2, I outline the principles of single-molecule fluorescence microscopy and single-particle tracking, which are fundamental to the investigations presented here. Additionally, I cover the basic concepts of cryogenic correlative light and electron microscopy (cryoCLEM) and provide a proof-of-principle implementation of a fluorescent biosensor in the cryoCLEM workflow. The remainder of the dissertation is devoted to the completed investigations.

Chapter 3 describes an experimental framework to assess putative biomolecular condensates in bacteria. By combining quantitative fluorescence microscopy with single-

molecule tracking, I systematically probe various biomolecular condensates to understand their properties in living bacterial cells. My findings distinguish between the behavior of condensates and insoluble aggregates, demonstrating that condensates can reversibly form despite having different material states.

In Chapter 4, I report a mechanistic study of carboxysome positioning by the Mcd system. I analyze the motion of carboxysomes, implement biochemical assays, and employ live-cell single-molecule tracking to examine the kinetics and mobility of the carboxysome-positioning protein, McdA. My findings indicate that the kinetics and mobility of McdA drive the regular positioning of carboxysomes.

Chapter 5 details the development of a biosensor for cryoCLEM, a novel correlative technique that provides physiological context to cellular structures. I describe an optimized experimental workflow used to identify fluorescent biosensors for cryoCLEM and demonstrate their application in cellular experiments.

Finally, in Chapter 6, I summarize the findings from each chapter and propose future directions for each investigation. Overall, this dissertation deepens our understanding of spatial organization in bacteria and provides an imaging-based approach that can be implemented to obtain high-resolution structures with local environmental information.

CHAPTER II

Microscopy as a Tool to Study Spatial Organization in Bacteria

2.1 Microscopy and bacteria

Bacteria are generally very small (for instance, *E. coli* cells are a few μm in length and about 1 μm in diameter), making them impossible to see with the naked eye. A standard light microscope can resolve objects as small as 300 nm [134] (Fig. 2.1), making it useful for observing bacteria at the single-cell level or within populations. However, to dissect the molecular-scale and mesoscale subcellular organization mechanisms described in Chapter 1, the internal structure of bacterial cells must be visualized. Observing small structures (20 – 300 nm) is limited in light microscopy due to the wavelengths of visible light (400 – 750 nm) and the low absorption cross sections of biological samples. Electron microscopes can achieve higher resolution than light microscopes (down to 1 nm) but require cellular fixation and extensive sample preparation, making this technique incompatible with live-cell experiments. Fluorescence microscopy has helped overcome these limitations as it enables visualization of specific biomolecules with high sensitivity in a minimally invasive and live-cell compatible manner. Its implementation has resulted in key observations of internal structure and spatial organization in bacteria [135, 136].

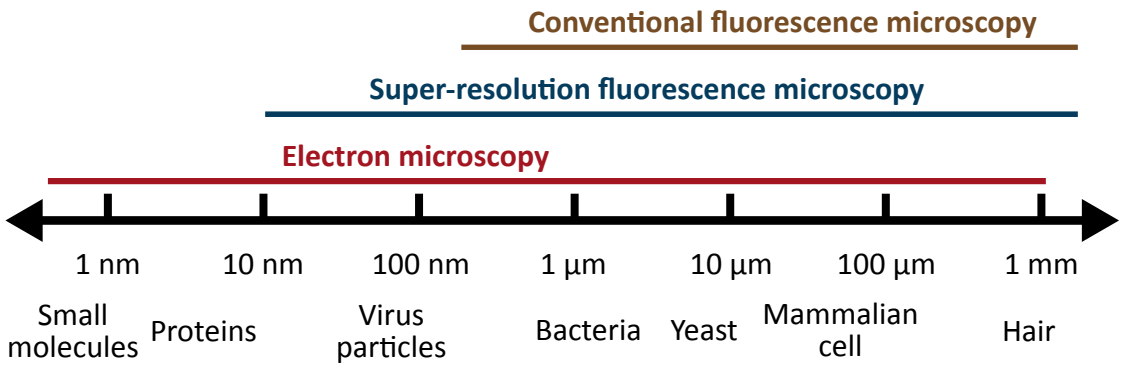


Figure 2.1: Length-scales of microscopy. Scales of conventional fluorescence microscopy, super-resolution microscopy, and electron microscopy compared to typical sizes of biomolecules, biomolecular assemblies, and organisms.

2.2 Fluorescence microscopy

In fluorescence microscopy, biomolecules of interest are attached to a fluorophore for visualization. Fluorophores are molecules that can absorb light of particular wavelengths and then emit photons with lower energy (higher wavelength) than those absorbed. Detection of the emitted photons against a dark background makes fluorescence microscopy a highly sensitive technique.

One approach for fluorescent labeling is by chemical conjugation of the target biomolecule with an organic fluorophore. Although this approach is often not ideal for live-cell experiments due to the limited dye permeability of the cell membrane and organelles, and the challenge of achieving specificity in labeling, advances in the field have facilitated this strategy through specific enzymatic conjugation, antibody labeling, and bio-orthogonal approaches [137–139].

As a result of the challenges of specifically labeling biological molecules with organic probes, alternative strategies abound. A popular approach for labeling proteins in cells is to fuse them to an intrinsically fluorescent protein [140, 141]. In this method, the gene that encodes the protein of interest is replaced with one that co-expresses a fluorescent protein, generating a chimeric fusion. Genetic encoding of the fluorescent probe elimi-

nates the need to deliver an extrinsic probe through the cell membrane, enabling specific labeling and live-cell compatibility. Despite avoiding a labeling step for every experiment, fluorescent proteins also have drawbacks. They are generally dimmer and less photostable compared to organic fluorophores [142]. Furthermore, they are much larger in size relative to organic dyes, requiring careful characterization of the fusion to ensure that protein function is preserved.

2.2.1 The diffraction limit

Conventional fluorescence microscopes are fundamentally limited. Visible light has a finite wavelength on the scale of a few hundred nanometers, making it impossible to focus it to an infinitesimal point or even to the size of an individual biomolecule 10 nm in size. As a result, even an infinitesimally small object will appear to have a finite size that depends on the specific optical configuration, limiting the resolution of any optical microscope to a few hundred nanometers. The diffraction pattern of an object is described by the point spread function (PSF) (Fig. 2.2a), which is represented by an Airy function in the x-y plane [143]. The best resolution attainable is described by the relationship below:

$$d = \frac{\lambda}{2NA} \tag{2.1}$$

where d is the minimum separation distance that can be resolved between two infinitesimally small objects (point emitters), λ is the emission wavelength of the point emitter, and NA is the numerical aperture of the objective. In fluorescence microscopes, d is limited to approximately 200 – 300 nm, a length scale two orders of magnitude larger than the size of an individual biomolecule and near the size of a bacterium itself, limiting the number of total resolvable molecules within a single cell. Ultimately, this limitation results in unresolvable (or blurred) structures and patterns within bacteria, as these structures are typically in the order of tens of nanometers in size (Fig. 2.2b).

2.3 Single-molecule fluorescence microscopy

2.3.1 Breaking the diffraction limit

Since the 1980s, scientists have made significant strides in the detection and visualization of individual molecules [144–151]. These efforts culminated in the development of single-molecule fluorescence microscopy, also known as single-molecule localization microscopy (SMLM) [152–155]. SMLM is an approach that circumvents the diffraction limit of conventional optical microscopy, enabling visualization of subcellular events in live cells with nanometer precision (10 – 30 nm). Breaking the diffraction limit by single-molecule fluorescence requires two key principles: (1) isolating an individual fluorescent emitter using an active control mechanism [156], and (2) using the PSF of the emitter to more precisely localize the emitter's position.

2.3.2 Active control mechanisms

Single-molecule detection requires that the concentration of emissive emitters in the system is limited. Therefore, active control mechanisms are employed to obtain isolated PSFs from individual molecules in each imaging frame [156, 158]. Some approaches for active control include photoactivation [159, 160], photo-switching [161], photo-induced blinking [162], and transient binding [155], which are utilized in methods like photoactivation localization microscopy (PALM), stochastic optical reconstruction microscopy (STORM), points accumulation in nanoscale topography (PAINT) and their variations.

2.3.3 Single emitter super-localization

Active control of fluorescence emission permits single-molecule detection; however, the emitter is still diffraction-limited and thus appears as a 300 nm-wide spot (Figure 2.2a). To localize a molecule with high precision, the intensity profile of the molecule can be approximated by a mathematical function (Fig. 2.2a) [145–147, 163, 164]. The precision of

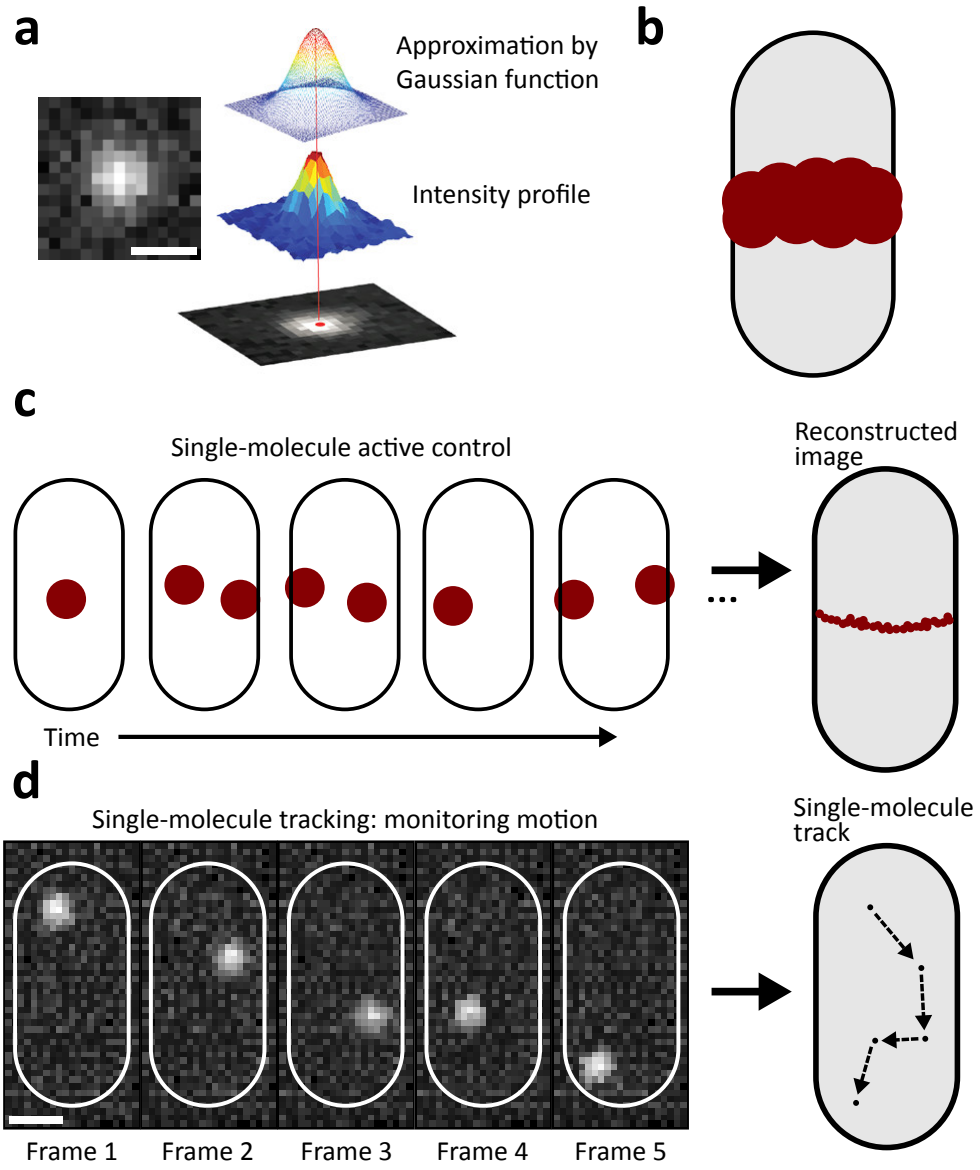


Figure 2.2: Single-molecule localization microscopy. a. The position of a fluorescent molecule can be localized by treating the molecule as a point source. The width of the intensity profile is defined by the point spread function (PSF) of the microscope (scale bar = 300 nm). The position of a single molecule (red point) is determined by fitting the intensity profile to a Gaussian function. The uncertainty in the position estimation (10 – 30 nm) is much smaller than the PSF width. Adapted from reference [157]. **b**. Cartoon of the diffraction-limited image of a structure that is smaller than the diffraction limit inside of a bacteria cell. **c**. Single molecules can be visualized via active control mechanisms. Iterative sampling of different molecules over time provides a list of localizations that can be used to reconstruct the super-resolution image of the structure in (**b**). **d**. The motion of each single molecule can be tracked across sequential imaging frames to generate a trajectory. Scale bar: 500 nm.

localization scales with the number of photons collected for that molecule in the imaging frame. Typical precisions are in the range from 10 to 40 nm, and can theoretically be improved with the collection of more photons [165, 166]. The precise positions of individual molecules across many frames are used to reconstruct a super-resolved image of a subcellular structure (Fig. 2.2c) [167].

In this dissertation, I used PALM to localize the position of various proteins within bacteria. I detected single molecules by using a photo-activatable (PA) fluorescent protein called photoactivatable mCherry 1 (PAmCherry) [168]. This variant of the mCherry fluorescent protein is initially in a dark state. Exposure to 406-nm light activates PAmCherry, converting it into its emissive state that absorbs green light. Iterations of this process allowed me to visualize a series of PAmCherry molecules one at a time and to localize my proteins of interest based on their fusion to PAmCherry.

2.4 Single-particle tracking and analysis

Because it combines high spatial resolution with temporal resolution in the ms range, single-molecule microscopy is a valuable tool for studying the motion and dynamics of specific molecules (Fig. 2.2d). Single-particle tracking (SPT) of molecules within cells provides critical insights into their functions. For instance, if a protein is rapidly moving and then stops at a specific location, this change may indicate a binding event or an interaction with another biomolecule. Although photobleaching of fluorophores limits trajectory lengths, collectively, many trajectories can reveal valuable information about the molecules, such as the presence of heterogeneous subpopulations within a cell or across different cells. Additionally, time-lapse imaging allows observation of single molecules' behavior over much longer periods by extending the photon budget of the fluorophore through intermittent excitation.

The concept of tracking can be extended beyond single molecules to larger protein complexes, such as bacterial organelles. These protein particles can be visualized with

conventional fluorescence microscopy as they are typically decorated with multiple fluorescent emitters, which increases their signal-to-noise ratio and reduces the rate of photobleaching due to a lower required excitation powers. Tracking particles such as bacterial microcompartments (BMCs) or condensates can provide information about their environment or the types of forces they experience within the cell [169].

2.4.1 Analysis of single-particle trajectories

Single-molecule trajectories can be analyzed to extract key parameters that describe the motion of a particle. These parameters help identify the type of motion a particle is undergoing and thus its potential biological activity. One important property is the diffusion coefficient, D, which characterizes the rate of diffusion for a particle in a solvent. According to the Einstein-Smoluchowski relation, the mean squared displacement (MSD or $\langle r^2 \rangle$) of a particle engaging in Brownian motion (random walk) during a time lapse, τ, is directly proportional to its diffusion coefficient, where n is the dimensionality of the motion [170].

$$\langle r^2(\tau) \rangle = 2nD\tau \tag{2.2}$$

Experimentally acquired trajectories are camera-based; therefore, modifications to this relationship (Equation 2.2) have been incorporated to account for motion blur and the associated localization error, σ (Equation 2.3) [171, 172].

$$\langle r^2(\tau) \rangle = 2n\left(D\tau + \sigma^2 - \frac{1}{3}D\tau\right) \tag{2.3}$$

The MSD vs. τ profile of a trajectory is linear only when a particle undergoes Brownian motion. However, biomolecules often deviate from this behavior and engage in anomalous diffusion [173]. Super-diffusion can result from active transport by linear motor proteins [174], while sub-diffusion can result from confinement or molecular crowding [175]. Both

of these motion types cause the MSD vs. τ profile to follow a power law [173]. The MSD function above can be modified to account for this behavior by including an anomalous diffusion scaling exponent, α. When a particle is subdiffusive, α is less than 1; conversely, when a particle is super-diffusive, α is greater than 1.

$$\langle r^2(\tau) \rangle = 2nD\tau^{\alpha} \tag{2.4}$$

Even if a single protein in the cytoplasm, molecules in bacteria cells will eventually experience the confinement of the bacterial cell, resulting in a plateau of the MSD vs. τ relationship. However, because these trajectories are often short in length (5 – 10 frames or 100 – 200 ms with a typical 20-ms camera frame integration time), they often do not capture this confined behavior. Furthermore, the limited length of trajectories means that fitting to the MSD vs. τ relationship should be done using the first few τ values to minimize the contribution of error to the MSD of a specific τ with fewer displacements [172].

2.4.2 Analysis of single particle displacements

A protein can transition between biochemical states. For example, a protein can be bound to DNA and then dissociate, causing a change in the apparent diffusion coefficient (D_{app}) of the particle from having a small D_{app} when bound to having a large D_{app} when it freely diffuses in the cytoplasm. These transitions highlight an important limitation of measuring the average diffusion coefficient of a trajectory by MSD fitting. If both behaviors are captured in a single trajectory, then this analysis approach averages two distinct behaviors into one value, resulting in an inaccurate representation of events.

An alternative approach is to analyze the distribution of squared displacements across many particles at different τ [169,176]. To determine the associated diffusion coefficient(s), one can fit the cumulative probability distribution (CPD) of squared displacements to Equation 2.5:

$$P\left(r^2,\tau\right) = 1 - \exp\left(\frac{-r^2}{\frac{8}{3}D\tau + 4\sigma^2}\right) \tag{2.5}$$

This model uses a simplified form of Equation 2.3 and is used if the data can be described by a single diffusion coefficient. Furthermore, this model can be expanded to include multiple diffusive states, for instance for two diffusive states:

$$P\left(r^2,\tau\right) = 1 - \left(\pi e^{\frac{-r^2}{\frac{8}{3}D_1\tau+4\sigma^2}} + (1-\pi)\, e^{\frac{-r^2}{\frac{8}{3}D_2\tau+4\sigma^2}}\right) \tag{2.6}$$

Here, π is the weight fraction of the population associated with the first state. While this analysis is powerful in recovering the heterogeneity within trajectories, it comes at the expense of losing spatial information.

2.5 Correlative light and electron microscopy

Live-cell fluorescence microscopy and single-molecule localization are powerful methods that enable real-time observations of protein dynamics. However, these techniques rely on specific labeling of biomolecules, which results in the loss of broader cellular context. Conversely, cryogenic electron microscopy (cryoEM) provides detailed cellular context with high spatial resolution but lacks the contrast necessary to identify specific biomolecules smaller than a few kilodaltons. The combination of both imaging techniques in correlative light and electron microscopy (CLEM) leverages the strengths of each method to overcome their respective weaknesses [177]. Through CLEM, it is possible to achieve both specific labeling and broader cellular context, providing a more comprehensive view of cellular structures.

In this section, I describe the basic principles of cryoEM, with a particular focus on electron tomography (cryoET). Following that introduction, I present the current state of the art in CLEM, specifically super-resolution cryoCLEM and biosensor cryoCLEM.

2.5.1 Cryogenic electron microscopy

CryoEM uses a transmission electron microscope (TEM) to visualize samples that are prepared and imaged under cryogenic conditions. Unlike optical microscopy, which relies on photons, TEM transmits a beam of accelerated electrons through a sample. Electrons have wavelengths much shorter than visible light, allowing for sub-nanometer resolution. Thus, cryoEM provides exceptionally high preservation of structural detail and the highest resolution in biological imaging.

CryoEM can determine angstrom-level structures of purified biomolecular complexes by analyzing thousands of copies using a method known as single-particle cryoEM [178, 179]. Additionally, cryoEM facilitates the study of cellular structures through cryogenic electron tomography (cryoET). CryoET generates three-dimensional (3D) tomographic reconstructions by imaging the same specimen from multiple angles [180, 181].

2.5.2 Cryogenic electron tomography

The three main goals of cryoET when imaging cells are: (1) to determine the overall cellular architecture of a biological specimen with nanometer resolution, (2) to identify biomolecules *in situ*, and (3) to determine the structures of these molecules within cells at the highest possible resolution [177].

Several steps are required to generate 3D renderings of cellular structures through cryoET [181]. First, cells are added to an electron microscope grid and plunge-frozen to vitrify the sample, preserving it in a near-native condition [182]. In cases where cells are too thick to image with TEM, focused-ion-beam (FIB) milling is performed to thin the samples down to lamellae which are a few hundred nanometers thick [183, 184]. These samples are then imaged on a TEM at cryogenic temperatures through a tilt-series acquisition (Fig. 2.3a). In this process, the sample is tilted between acquisitions to collect a series of 2D snapshots from different angles. This data is then reconstructed to generate a 3D rendering of the sample. The final step is segmentation, in which structures are manually

annotated to identify significant features such as filaments or compartments (Fig. 2.3a).

While cryoET excels at determining cellular architecture, achieving the other two goals is more challenging if the biomolecules cannot be identified. Given the limited contrast in tomograms, most biomolecules cannot be distinguished unless they assemble into large repetitive structures. As highlighted earlier, this limitation makes the co-implementation of fluorescence microscopy an invaluable tool in achieving the goals of cryoET.

2.5.3 Super-resolution cryoCLEM

CLEM has been broadly implemented to visualize specific structures at high resolution while maintaining cellular context [186–188]. However, the diffraction limit of conventional fluorescence microscopy has restricted its use in CLEM, as the resolution of the two methods differs significantly (Fig. 2.1). To overcome this obstacle, several studies have contributed to the development of super-resolution CLEM (SR-CLEM) [177, 189–195].

Significant challenges remain in achieving SR-cryoCLEM comparable to room temperature super-resolution microscopy. These challenges include maintaining the stability of cryogenic stages for cryogenic fluorescence microscopy to prevent devitrification from high laser powers, understanding the photophysics of fluorophores under cryogenic conditions, and accurately registering images [177].

2.5.4 Biosensor cryoCLEM

In addition to providing molecular specificity, fluorescent readouts can also provide physiological context through environmental sensing. Engineered fluorescent proteins with photophysical properties that respond to their environment have enabled biosensing in live cells and revealed insights about cell signaling pathways and organelle homeostasis [196].

To quantitatively measure an environmental observable, ratiometric fluorescent biosen-

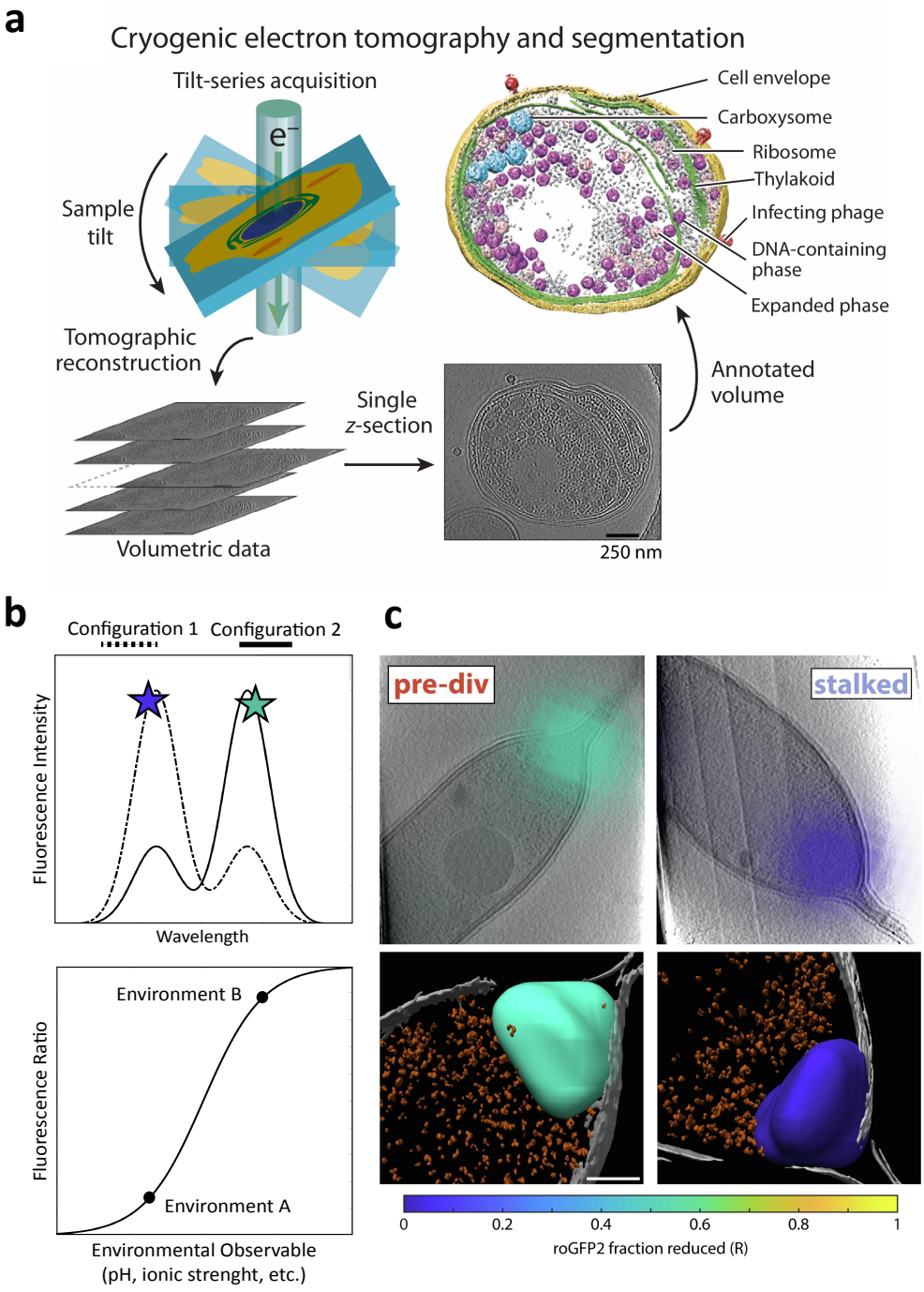

a
Cryogenic electron tomography and segmentation
Tilt-series acquisition
e⁻
Sample tilt
Tomographic reconstruction
Volumetric data
Single z-section
250 nm
Annotated volume
Cell envelope
Carboxysome
Ribosome
Thylakoid
Infecting phage
DNA-containing phase
Expanded phase
b
Configuration 1
Configuration 2
Fluorescence Intensity
Wavelength
Fluorescence Ratio
Environment B
Environment A
Environmental Observable
(pH, ionic strenght, etc.)
c
pre-div
stalked
0
0.2
0.4
0.6
0.8
1
roGFP2 fraction reduced (R)

Figure 2.3

Figure 2.3: Cryogenic correlative light and electron microscopy. a. Cryogenic electron tomography and segmentation. A plunge-frozen cell is imaged on an electron microscope through a series of tilts to acquire volumetric information. The images are then reconstructed into a 3D tomogram that is then annotated to identify structures of interest. Adapted from reference [177]. **b**. Principle of fluorescent biosensors. Top: the fluorescence spectrum of a biosensor changes based on the environment. Bottom: The fluorescence ratio of a sensor, based on differential excitation or emission, quantitatively reports on the environmental factor. **c**. roGFP2 was used to sense the oxidative state of the PopZ microdomain in C. crescentus. Top: Registered single Z-section of a 3D tomogram overlaid with the fluorescence ratio image in pre-divisional (left) and stalked (right) cells. Bottom: rendering of segmented PopZ microdomain color-coded by its fluorescence ratio. The ribosomes (orange) and cell membrane (gray) were also segmented. Adapted from reference [185].

sors can be designed. This type of biosensor usually has two excitation or emission maxima, with each being specific to an environmental condition. The ratio of the intensity between the two maxima can be used to quantitatively describe the environment around the biosensor (Fig. 2.3b). For example, consider a ratiometric biosensor that has two excitation peaks: a blue peak that is more responsive in oxidized environments and a red peak that dominates in reduced conditions. The biosensor signal then depends on its environment and the excitation wavelength used and will be independent of the total concentration of the biosensor. This property makes ratiometric biosensors more applicable than intensiometric biosensors, which only exhibit a brightness change rather than a spectral change.

In the context of cryoCLEM, fluorescent biosensors provide the physiological context often missed in structural studies. Recently, Perez et al. [185] identified roGFP2 as a fluorescent biosensor that preserves its photophysical sensing properties under cryogenic conditions and demonstrated its use by correlating the PopZ microdomain redox state to its structure at different developmental stages (Fig. 2.3c).

A critical step in the application of fluorescent biosensors in cryoCLEM is showing that their sensing behavior is maintained at cryogenic temperatures. In Chapter 5, I describe my work expanding the fluorescent biosensors toolkit to sense pH, calcium, and molecular

crowding in cryoCLEM experiments. This work was completed at SLAC National Lab in the lab of Dr. Peter Dahlberg.

CHAPTER III

An Experimental Framework to Assess Biomolecular Condensates in Bacteria[1]

3.1 Introduction

Though many cellular compartments and organelles use membranes to encapsulate their contents, biomolecular condensates concentrate proteins and nucleic acids without the use of a membrane [31, 197]. Condensates have been widely reported in eukaryotes [31, 198] and more recently in prokaryotic organisms [39, 54], and they have been linked to diverse biological processes important for cell function and physiology [53, 199]. Yet, how bacterial condensates maintain their structures, modulate their composition, and regulate internal biochemical reactions is largely unexplored. Our understanding of these questions has improved in eukaryotes [200], but the small size of bacteria has hindered *in vivo* measurements.

The term condensate is not supposed to prescribe a formation mechanism [31, 40].

[1]The work presented in this chapter was previously published in *Nature Communications*. *Hoang, Y, *Azaldegui, C.A., Dow, R., Ghalmi, M., Biteen, J.S., and Vecchiarelli, A.G. An experimental framework to assess biomolecular condensates in bacteria. *Nature Communications* **15**, 3222 **(2024)** DOI: 10.1038/s41467-024-47330-4.
Y.H., C.A.A., J.S.B, and A.G.V conceptualized the work. Y.H. and C.A.A. generated the strains. Y.H., C.A.A., R.D., and M.G. performed all bulk fluorescence microscopy experiments. C.A.A. performed all image analyses and quantification. Y.H. and R.D. performed biochemical assays. C.A.A. performed all single-molecule fluorescence experiments and analyses. Y.H. performed the 2D SIM imaging. Y.H., C.A.A., J.S.B, and A.G.V. wrote the manuscript.

However, condensate formation has been broadly attributed to phase separation [31, 53, 197] because of the liquid-like behavior observed in condensates in living cells and *in vitro* reconstitution. Importantly, condensates that are in a distinct phase from their surrounding environment can be considered as a result of phase separation if they exhibit three key characteristics: a difference in component densities between the two phases, dynamic exchange of components between the two phases, and the formation of a condensate upon reaching a saturation concentration, c_{sat} [40]. These observations have been made in eukaryotic cells [43, 201–205] and recently, super-resolution techniques have been implemented to probe sub-diffraction limited bacterial condensates *in vivo* [60, 67, 73, 77, 206–208]. However, the general use of these approaches remains limited. The growing number of bacterial systems with reported condensates makes it clear that these membraneless organelles play a key role in bacterial cell biology, making a unifying framework to understand their formation across systems necessary. It is therefore imperative that methods become widely available and flexible to study their formation in bacteria.

Here, we present an experimental framework (Fig. 3.1) to determine whether a bacterial biomolecular condensate forms through phase separation *in vivo*. We specifically examined Maintenance of carboxysome distribution protein B (McdB) from the cyanobacterium *Synechococcus elongatus* (*S. elongatus*) PCC 7942. Carboxysomes are carbon-fixing protein-based organelles that are subcellularly distributed in cyanobacterial cells as well as in some chemoautotrophs. Maintenance of carboxysome distribution B (McdB) is part of a two-protein system responsible for spatially organizing carboxysomes in the cell [127]. McdB associates with carboxysomes in a currently unknown manner, and acts as an adaptor, linking the carboxysome cargo to its positioning Adenosine triphosphotase (ATPase), called Maintenance of carboxysome distribution A (McdA). McdA forms dynamic gradients on the nucleoid in response to McdB-bound carboxysomes, distributing them across the length of the nucleoid. McdB robustly forms phase-separated droplets *in vitro*, and mutants that are unable to form condensates *in vitro* are also defective in carboxysome

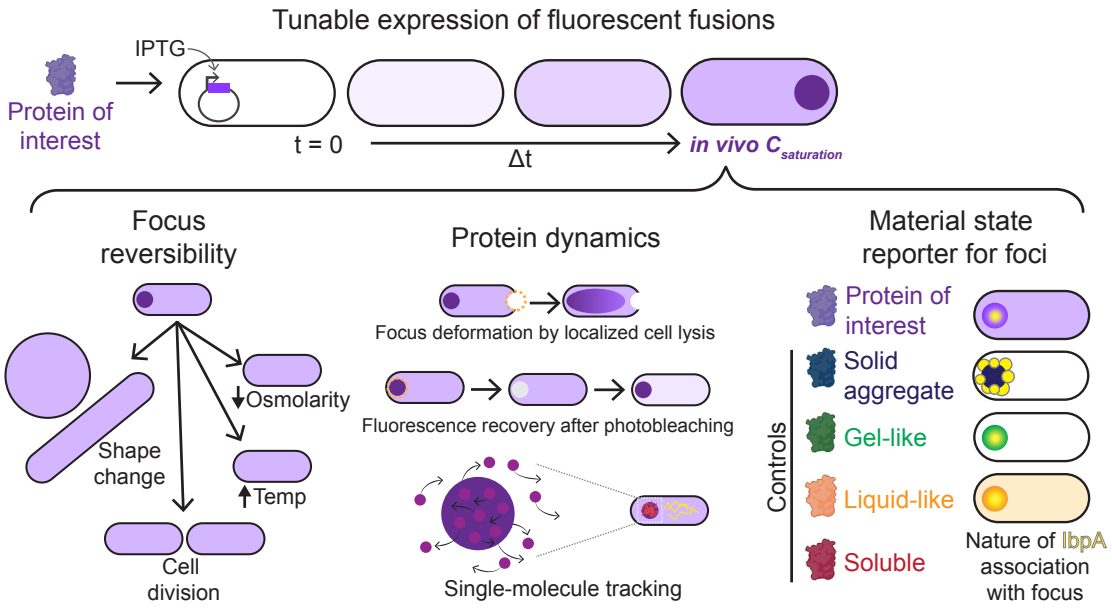


Figure 3.1: Framework to assess biomolecular condensates in bacteria. Proteins of interest or control proteins are inducibly expressed to form foci (dark purple circle) in *E. coli* (top). The *in vivo* saturation concentration ($c_{saturation}$) is quantified. The material state of each focus can be assessed: (Left) Condensates dissolve upon cell growth, cell division, cell shape change, temperature shift, or osmolarity shift, whereas insoluble aggregates remain intact. (Middle) Analysis of protein dynamics informs on the material properties of the focus. Dashed magenta circles: photobleached areas. (Right) The chaperone Inclusion binding protein A (IbpA) (yellow) surrounds insoluble aggregates but penetrates condensates.

positioning *in vivo* [65, 127, 130]. It remains to be determined if McdB forms condensates in its native host because McdB associates with carboxysomes, making it difficult to parse this association from its potential phase separation activity *in vivo*. Therefore, we developed and adapted a suite of molecular and cell biology methodologies along with super-resolution imaging techniques in *E. coli* to characterize the formation, solubility, and dynamic exchange of McdB condensates.

E. coli as the model system provides a wealth of molecular biology tools. It was also chosen over larger eukaryotic cells, such as yeast, because phase separation is influenced by crowding, and we required a cytoplasm representative of the environment for bacterial proteins. Finally, *E. coli* is also a pragmatic choice for the study of heterologously expressed bacterial proteins because it prevents associations with potential binding partners in the native host. For example, as noted above, in the native organism *S. elongatus*, McdB associates with carboxysomes, which complicates a reductionistic study of McdB phase separation *in vivo*.

Alongside McdB, we used well-established control proteins that form condensates [78] and insoluble aggregates [209, 210]. First, we probed the liquid-like properties of McdB condensates using switch-like expression assays. Next, we used single-cell tunable expression promoters to quantify the conditions for condensate formation and probed condensate reversibility. Moreover, we measured the dynamic exchange of condensate constituents and inferred the material properties of condensates with single-molecule tracking. Finally, we implemented the heat-shock chaperone IbpA as a molecular sensor that differentially associates with condensates and aggregates. Our framework ensures a low barrier to general applicability by users, consolidates an array of assays, and complements widely accessible methods with more advanced techniques such as super-resolution imaging and single-molecule tracking to validate method performance.

3.2 Results

3.2.1 Probing the liquid-like properties of foci formed by protein overexpression

Bacterial condensates have been mainly studied *in vitro*, and it is largely unexplored if these proteins form foci with liquid-like properties inside the cell. Overexpression and imaging of fluorescent fusions provide a quick and useful method for gaining insight into the material state of a bacterial focus. Therefore, we first overexpressed a fully functional mNeonGreen-McdB (mNG-McdB) fusion in *E. coli* BL21 cells and performed time-lapse fluorescence microscopy to investigate the behaviors of the McdB protein *in vivo*. Focus formation was observed in <1 h post-induction with IPTG at 25 °C (Fig. 3.2a and Supplementary Movie 1). DAPI staining of the nucleoid showed that these larger mNG-McdB foci were nucleoid-excluded (Fig. 3.2b). Strikingly, large mNG-McdB foci localized to the inner membrane near sites of local cell curvature (white arrows in Fig. 3.2a and Supplementary Movie 1). Together, we find that overexpressed mNG-McdB forms small foci that eventually become larger nucleoid-excluded structures. These structures appear to wet to the inner membrane and cause local changes in cell morphology.

A hallmark of phase-separated condensates is their responsiveness to changes in the cellular concentration. To probe the concentration dependency of mNG-McdB foci formation *in vivo*, we treated the cells with A22 which caused a rod-to-sphere transition and corresponding increase in cell volume. We also included a control protein that forms insoluble aggregates in *E. coli*, cI^{agg} [210]. The protein cI^{agg} is a truncated and mutated version of the Lambda cI repressor. During this transition, mNG-McdB foci dissolved towards a homogenous phase in the cytoplasm, while the aggregator control mNG-cI^{agg} maintained punctate foci in spherical cells (Fig. 3.2c, Supplementary Movie 2). We analyzed condensation in cells by normalizing all pixel intensities in single cells and calculating the fraction of pixels below a normalized intensity threshold of 50% [60, 211]. The condensation co-

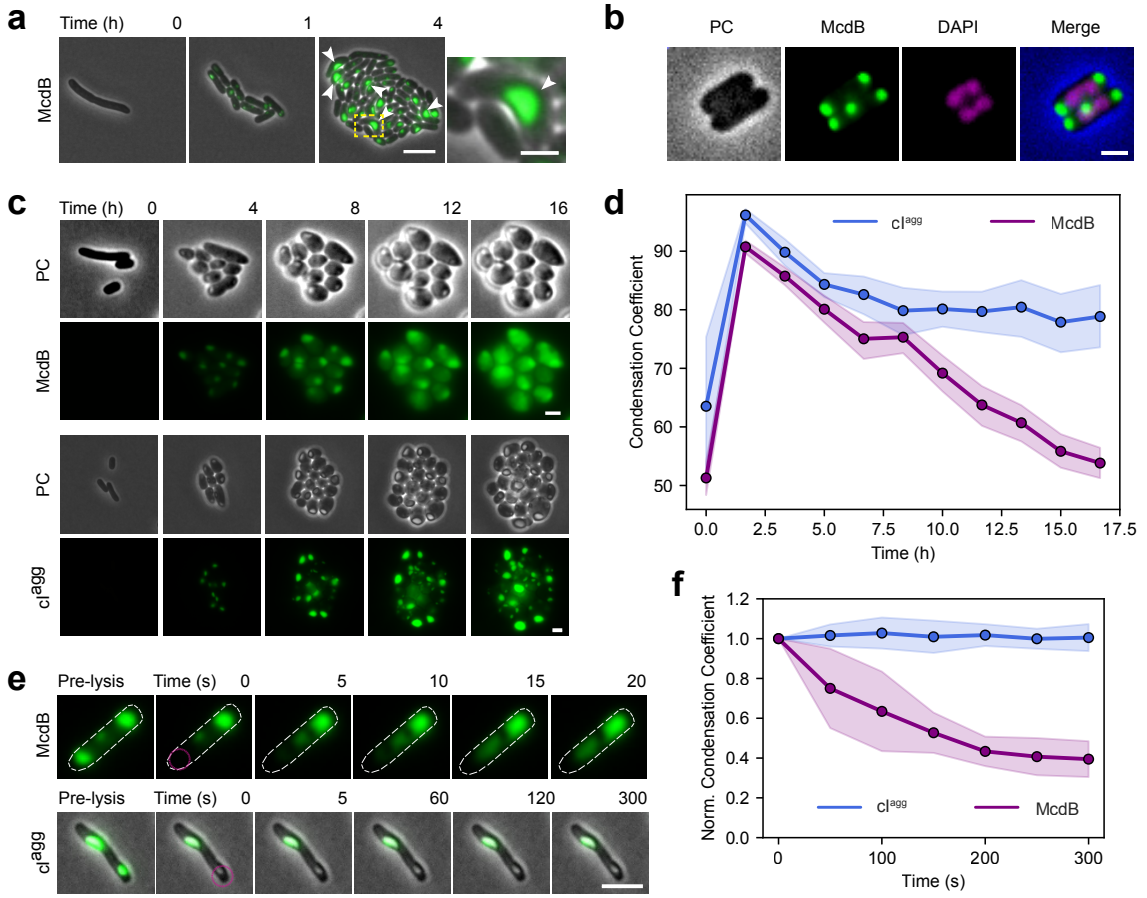


Figure 3.2: Overexpression of mNG-McdB in *E. coli* BL21. a. mNG-McdB forms foci. The phase contrast channel is shown in gray and the mNeonGreen (mNG) channel is in green. Images are representative of three biological replicates. White arrows highlight cells where McdB foci wet to the inner membrane inducing cell curvature. Scale bars: 5 µm. **b**. mNG-McdB foci are nucleoid-excluded. DAPI stain is shown in magenta. Scale bar: 1 µm. **c**. Effects of changing cell volume on focus stability. *E. coli* cell volume was increased by treating cells with the MreB inhibitor, A22 (10 µg/mL). Images were taken at 6 h post-treatment, when rod-shaped cells transitioned their morphology into round cells. Scale bar: 5 µm. **d**. Quantification of cells shown in (c). Solid lines and shading represent the mean condensation coefficient of a representative cell population (n > 10 cells) and its 95% confidence interval. An intensity threshold of I = 0.5 was used; a condensation coefficient of 50 is equivalent to a homogenous pixel intensity distribution. **e**. Localized lysis of the cell. One cell pole was lysed using a high-intensity laser, focused within the indicated magenta circle. Representative frames show solubilization of the opposing focus and shift of fluorescent signal to the opposite end. Scale bar: 1 µm. **f**. Quantification of three representative cells (n = 3) for each protein shown in (e). Solid lines and shading represent the mean condensation of three representative cells and the standard deviation. An intensity threshold of I = 0.1 was used.

efficients for both McdB and cI^{agg} peaked at about 2 h once fluorescent foci formed (Fig. 3.2d). However, mNG-McdB showed a dramatic decrease in its condensation coefficient towards a homogenous pixel intensity distribution. In contrast, the condensation coefficient of cI^{agg} remained high. The results show that McdB redistributed in cells undergoing shape changes, while cI^{agg} foci increased in size and with minimal fluorescence observed in the cytoplasm.

The drug-induced changes to cell volume were gradual and may have involved pleiotropic effects. Therefore, we developed an approach to probe the dynamic properties of mNG-McdB foci upon an instantaneous change in cell volume. In this localized-lysis method, a high-intensity laser was focused on one cell pole to lyse the cell. Localized lysis caused cell contents to unidirectionally rush out of the cell. Strikingly, upon cell lysis, the McdB focus dispersed towards the opposing open cell pole while the aggregator cI^{agg} focus remained the same (Fig. 3.2e and Supplementary Movie 3). The observed dynamics of McdB resemble the observed jetting of P granules under sheer stress [32]. Over the 300-second period, the condensation coefficient of McdB decreased by a factor of 2.5, whereas the condensation coefficient of cI^{agg} remained constant (Fig. 3.2f). Altogether, these results demonstrate that mNG-McdB foci in *E. coli* BL21 exhibit properties consistent with those of condensates.

3.2.2 Using single-cell tunable expression to probe the formation of biomolecular condensates

In eukaryotic cell biology, the majority of condensate studies perform *in vivo* measurements using ectopic overexpression [212], analogous to our overexpression assays (Fig. 3.2f). However, phase-separating systems are exceedingly sensitive to changes in concentration, and overexpression may introduce significant caveats in the extrapolation that a protein forms condensates when expressed at lower endogenous levels. We therefore set out to find additional metrics other than overexpression to support claims that a bacterial

focus is indeed phase-separated.

We turned to a single-cell tunable expression system to observe condensate formation during controlled protein expression. We fused the fluorescent protein mCherry to the N-terminus of McdB(*mCherry-mcdB*) and placed it under the control of an IPTG-inducible promoter on a pTrc99A expression vector (*pTrc99A-mCherry-mcdB*). Along with our protein of interest, we probed a series of well-established control proteins, all fused to mCherry. We switched from mNG to mCherry for our experiments in MG1665 because we later performed single-particle tracking of our protein set using PAmCherry. Therefore using mCherry for our wide-field fluorescence microscopy, instead of mNG, allowed for a reliable comparison with our single particle data. In addition, later experiments required our protein set to be co-imaged with an *E. coli* chaperone protein fused to monomeric superfolder GFP (msfGFP).

As above, the protein cI^{agg} is a truncated and mutated version of the Lambda cI repressor that is well-known to form insoluble aggregates in *E. coli* [210]. On the other hand, fluorescent protein fusions to PopTag proteins form condensates via phase separation with tunable material properties that depend on the length of the linker between PopTag and the fusion protein [78]. We engineered two versions of the PopTag fusion: $PopTag^{SL}$ with a short (six-amino acid) GS repeat linker (*pTrc99A-mCherry-L6-PopTag*) and $PopTag^{LL}$ with the native linker of the PopZ protein (78-amino acid) (*pTrc99A-mCherry-L78-PopTag*). Based on the linker lengths, $PopTag^{LL}$-mCherry condensates should be more fluid than $PopTag^{SL}$-mCherry condensates, the latter of which we expect to be more viscous or in a gel-like state [78]. Additionally, we probed a solubilized McdB mutant ($McdB^{sol}$), previously shown to be abrogated in its phase separation activity both *in vitro* and *in vivo* [65]. Finally, mCherry alone was used as a control for a completely soluble protein. None of the mCherry fusion proteins showed significant cleavage of the mCherry tag compared to mCherry alone when expressed with the pTrc99A promoter (Fig. 3.3). Therefore, mCherry fluorescence served as a reliable measure of protein expression and localization *in vivo*.

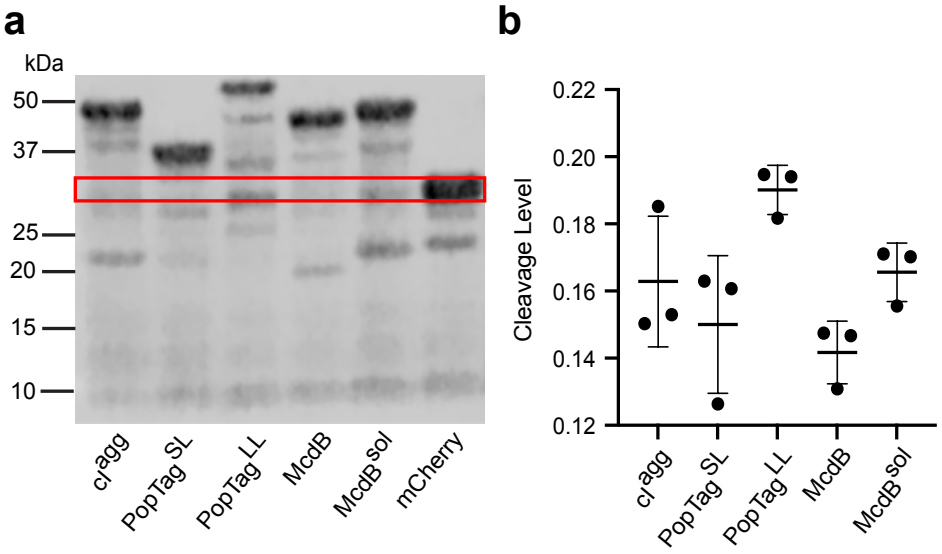


Figure 3.3: Expression of mCherry fusion proteins. *E. coli* MG1665 cells of indicated strains were induced with 1 mM IPTG for 2 h. **a**. Immunoblot analysis of mCherry fusion proteins. Representative immunoblots are shown. Red box shows the band at the mCherry size (28 kDa). Similar results were observed in three biological replicates. **b**. Cleavage level of mCherry fusion proteins. In each lane, the intensity of the band at the mCherry size was quantified and normalized to the total intensity of the respective lane. Error bars represent the standard deviation from the three biological replicates (n = 3).

Induced expression of these proteins in *E. coli* cells showed focus formation as a function of increasing protein concentration over time (Fig. 3.4a and b, Fig. 3.5). Within 1 h of expression, 80% of cI^{agg} and 60% of $PopTag^{SL}$ cells had a focus, while almost no foci were observed in $PopTag^{LL}$, McdB, and $McdB^{sol}$ cells (Fig. 3.4b). Past 1 h of expression, the percentage of cI^{agg} and $PopTag^{SL}$ cells with a focus slightly increased to reach about 90%. $PopTag^{LL}$ and McdB, on the other hand, showed a sharp increase to 90% and 80% respectively. $McdB^{sol}$ foci only became evident after 4 h of expression. Strikingly, a notable fraction of the fluorescence signal was localized to the cytoplasm of cells with a $PopTag^{SL}$, $PopTag^{LL}$, McdB, or $McdB^{sol}$ focus (Fig. 3.4a). The focus and the cytoplasmic fraction resemble the dense- and dilute-phases of a two-phase system, respectively. No notable fluorescence was in the cytoplasm of cI^{agg} cells.

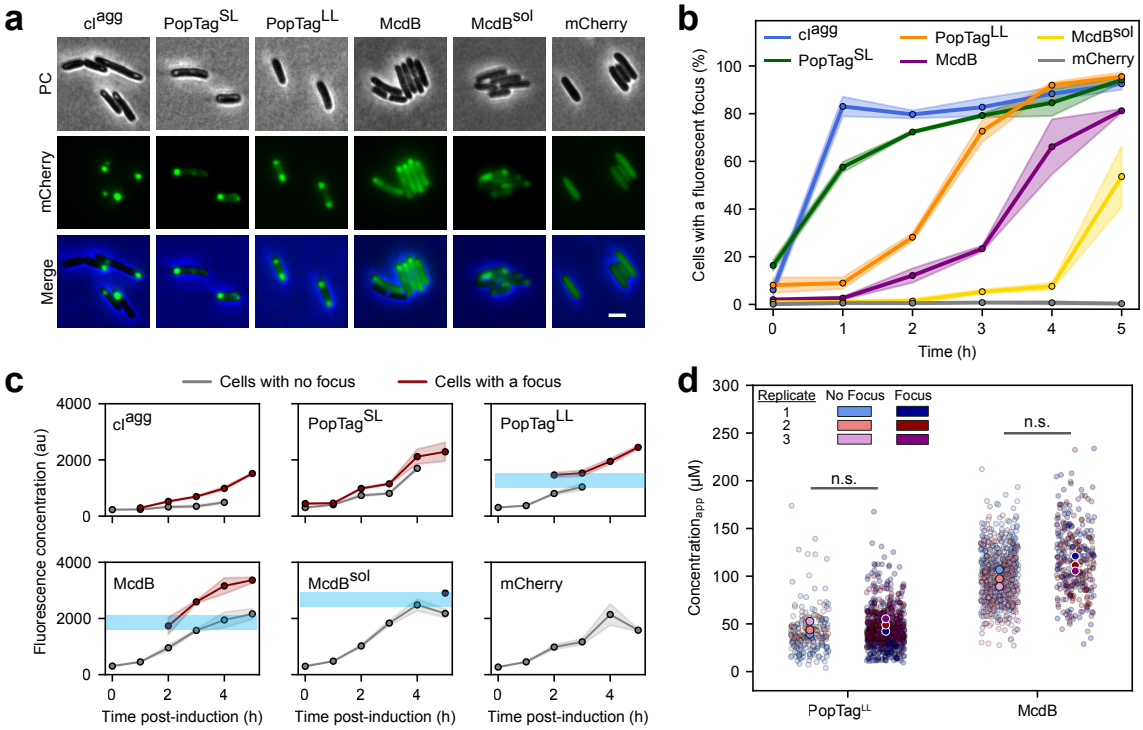


Figure 3.4: Proteins that phase separate *in vitro* form foci above a quantifiable *in vivo* c_{sat}. **a**. Representative images of mCherry fusion protein foci in *E. coli* at 4 h post-induction. Phase contrast (PC) (gray), mCherry channel (green), and merged images are shown. Images are representative of three biological replicates. Scale bar: 2 μm. **b**. Percent of cells with a focus over induction time. Solid lines and shading represent the average and standard deviation, respectively, over three biological replicates. $N > 100$ cells for each protein at each time point per replicate. **c**. Fluorescence concentrations of proteins at times post-induction in cells from (b). Cells were classified for the presence of a focus as in (b). Solid lines and shading represent the average and standard deviation, respectively, over three biological replicates. $N > 100$ cells for each protein at each time point per replicate. Each data point is shown if it totals at least 10% of the population at its corresponding time point. Light blue shading is added to highlight potential saturation concentration. **d**. Quantification of an apparent cellular c_{sat}. Cells are classified by the presence or absence of a focus. Data points correspond to individual cells. $N > 100$ cells for each protein per replicate. Two-sided Welch's t-test was done on the mean of the replicates. n.s. indicates no statistically significant difference between the samples.

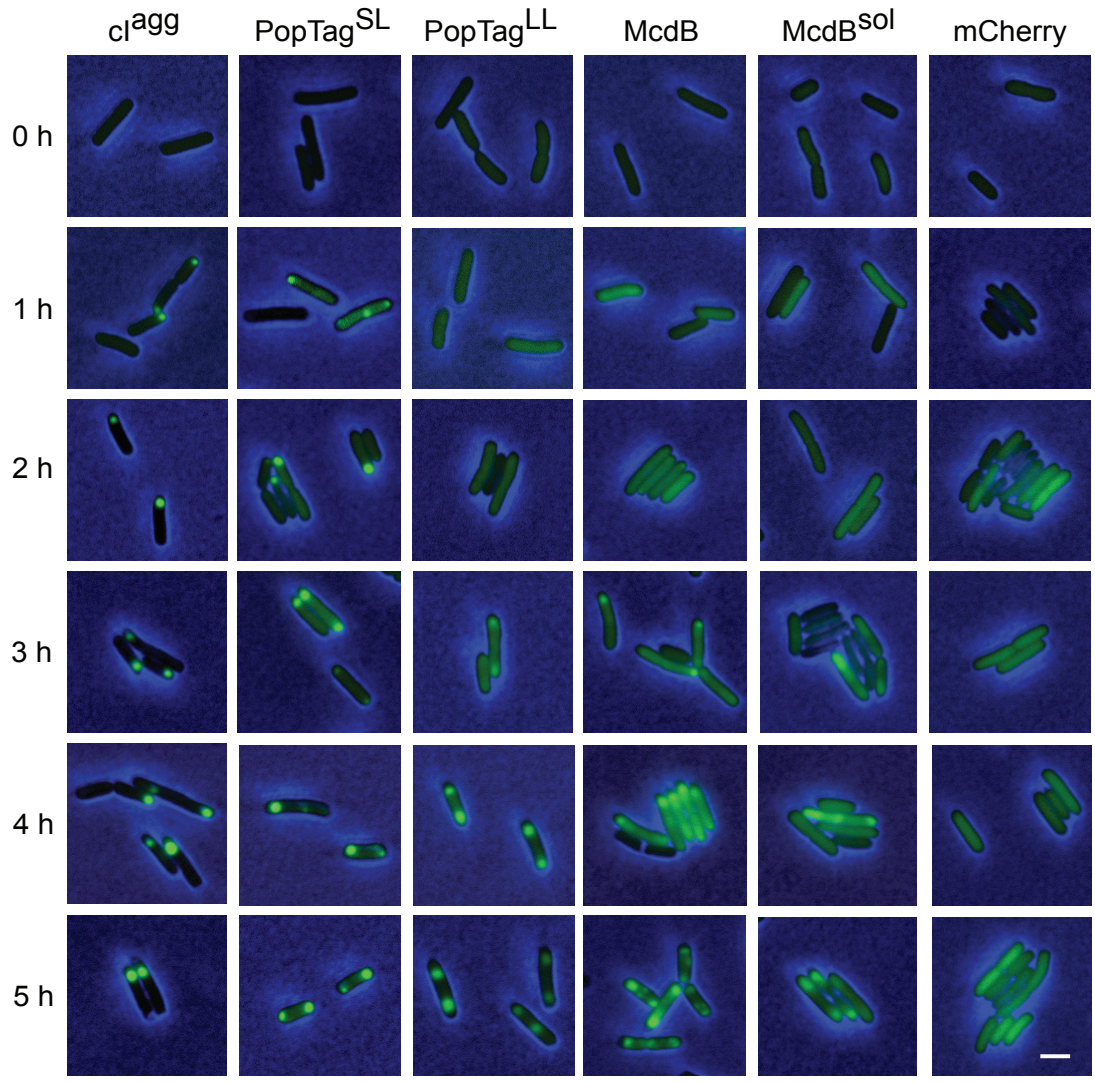


Figure 3.5: mCherry fusion proteins form cellular foci. Representative images of indicated mCherry fusion protein foci *E. coli* from 0 to 5 h post-induction. Phase contrast (blue) and mCherry (green) channels were merged. Images are representative of three biological replicates (n = 3). Scale bar: 1 μm.

3.2.3 Probing the *in vivo* concentration dependence of biomolecular condensates

We next determined the concentration dependence of focus formation among our protein set fused to mCherry. Cells were first categorized based on the presence or absence of a focus. We then plotted the fluorescence concentration of these cell types over the time course of protein expression (Fig. 3.4c). For cI^{agg}, cells lacking a focus displayed little to no fluorescence, while cells with a focus displayed a linear increase in concentration over time. The pattern for $PopTag^{SL}$ was similar to that of cI^{agg}, consistent with the previously established gel-like nature of $PopTag^{SL}$ condensates. In contrast, both $PopTag^{LL}$ and McdB displayed a relatively sharp fluorescence concentration boundary for focus formation. That is, cells without a focus displayed a fluorescence concentration at or below the concentration in cells displaying a focus. $McdB^{sol}$ foci also exhibited this concentration threshold, albeit foci were only observed at significantly higher concentrations 5 h post-induction.

Together, the data suggest that $PopTag^{LL}$ and McdB require a threshold concentration for focus formation, consistent with phase separation. To determine their apparent *in vivo* saturation concentrations ($c_{sat,\ app}$), we used quantitative fluorescence microscopy. We first determined the intensity of single mCherry molecules that were spatially isolated prior to photobleaching of fluorescence in the cell. These single-molecule localization images were quantified to measure the number of photons detected per molecule per imaging frame (Fig. 3.6). Next, we calculated the cellular concentration of mCherry-McdB by integrating the total cellular fluorescence intensity per imaging frame and dividing this value by the mCherry single-molecule intensity and the cellular volume. Cells were then classified by the presence or absence of a focus. After a 4-h induction, the average cellular concentration of mCherry-McdB was approximately 100 μM with no significant difference between cells without a detected focus (average cellular concentration of 98 ± 9 μM) and cells with a focus (113 ± 8 μM; Fig. 3.4d). This observation of condensates in cells with

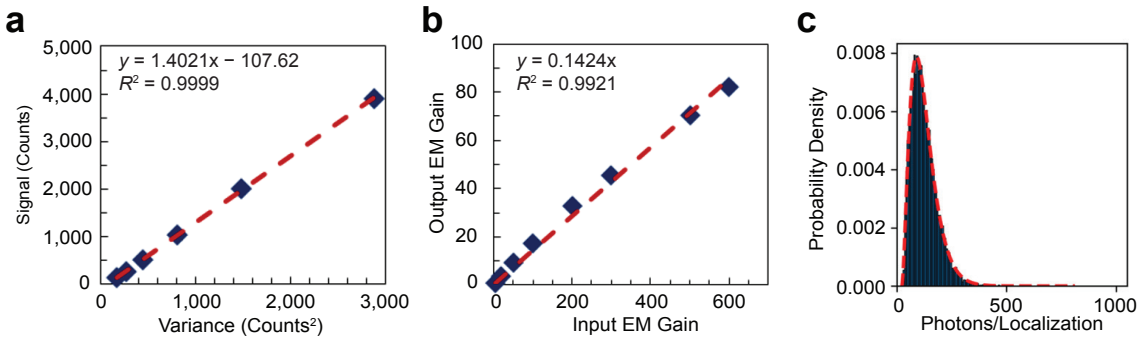


Figure 3.6: Electron-multiplying charge-coupled detector (EMCCD) calibration for photon counting. a. Signal variance versus signal average for different camera integration times. The data points correspond to the following camera integration times: 10, 20, 40, 80, 160, and 320 ms. The dashed red line is the linear regression. **b**. Electron multiplication conversion plot. The dashed red line is the linear regression constrained through the origin. **c**. Distribution of number of detected photons per localization per imaging frame for mCherry-McdB. Signal histogram was fit to a gamma distribution, determining a peak of 91.1 photons per localization at a 40-ms camera integration time. 35800 localizations were used to build the histogram.

a slightly higher total protein concentration is consistent with McdB undergoing a nearly immediate and concentration-dependent transition to form a focus. We performed the same analysis for cells expressing mCherry-PopTag^{LL}. The average cellular concentration of this fluid-condensate control was 45 ± 7 μM in cells without a focus while cells with a detected focus had an average concentration of 48 ± 7 μM (Fig. 3.4d). Together, the results provide a $c_{sat,\,app}$ at which condensates form; for mCherry-PopTag^{LL} and mCherry-McdB, we estimate the c_{sat} to be between 38 – 55 μM and 89 – 121 μM, respectively.

Full-length PopZ has a similar linker length as our mCherry-PopTag^{LL} fusion. *In vitro*, PopZ forms condensates at concentrations as low as 1 μM [78]. However, PopZ micro domains in its native host, *Caulobacter crescentus*, were estimated to be 50 μM at the cell poles. Therefore, our *in vivo* $c_{sat,\,app}$ of PopTag^{LL} is consistent with previously reported *in vivo* values [73, 78]. As for McdB, its cellular concentration in its native host, *S. elongatus*, has yet to be determined. *In vitro*, we have shown that McdB can form condensates at concentrations as low as 2 μM [65]. Here, we report estimates several fold higher than the *in vitro* c_{sat}. However, given that McdB associates with carboxysomes in *S. elongatus*,

we speculate that this association significantly increases the local concentration of McdB and/or drops the c_{sat} of McdB, which likely explains this discrepancy.

3.2.4 Condensates coexist with a soluble phase

A hallmark of phase separation is the existence of a soluble fraction in the cytoplasm. To quantify the ratio of mCherry protein fusion concentration in the focus (dense phase) to the concentration in the cytoplasmic fraction (dilute phase), the partitioning of each fusion was measured (Fig. 3.7a). The largest partitioning was measured for the aggregator control, cI^{agg}, in which there was no detectable fluorescent signal in the cytoplasm. The $PopTag^{SL}$ condensate control partitioned to a greater extent than the more fluid condensate control $PopTag^{LL}$. The partitioning of our protein of interest, McdB, was intermediate relative to the PopTags. The condensation coefficients determined by using the same dataset for each protein (Fig. 3.7b and 3.8) were consistent with the partition ratios (Fig. 3.7a).

To further inspect the partitioning of proteins to polar foci, we induced photoactivatable (PA) mCherry fusions of each protein and performed single-molecule localization super-resolution microscopy to generate normalized localization density heat maps (Fig. 3.7c). Consistent with our previous results, cI^{agg} had minimal localization density in the cytoplasm under all conditions, which suggests nearly all protein is recruited to the polar aggregate. On the other hand, the polar density of $PopTag^{SL}$ increased with increasing protein concentration, but these cells also maintained a protein fraction in the cytoplasm. Strikingly, $PopTag^{LL}$ and McdB displayed a transition between no induction and 2 h post-induction, indicative of focus formation. Intriguingly, $McdB^{sol}$, which does not form condensates *in vitro*, formed high-density regions at the poles; consistent with bulk fluorescence measurements (Fig. 3.4a). To abrogate phase separation in this $McdB^{sol}$ mutant, the net negative charge of its Intrinsically disordered region (IDR) was increased [65]. Therefore, we speculate that the localization pattern of the fluidized $McdB^{sol}$ condensate

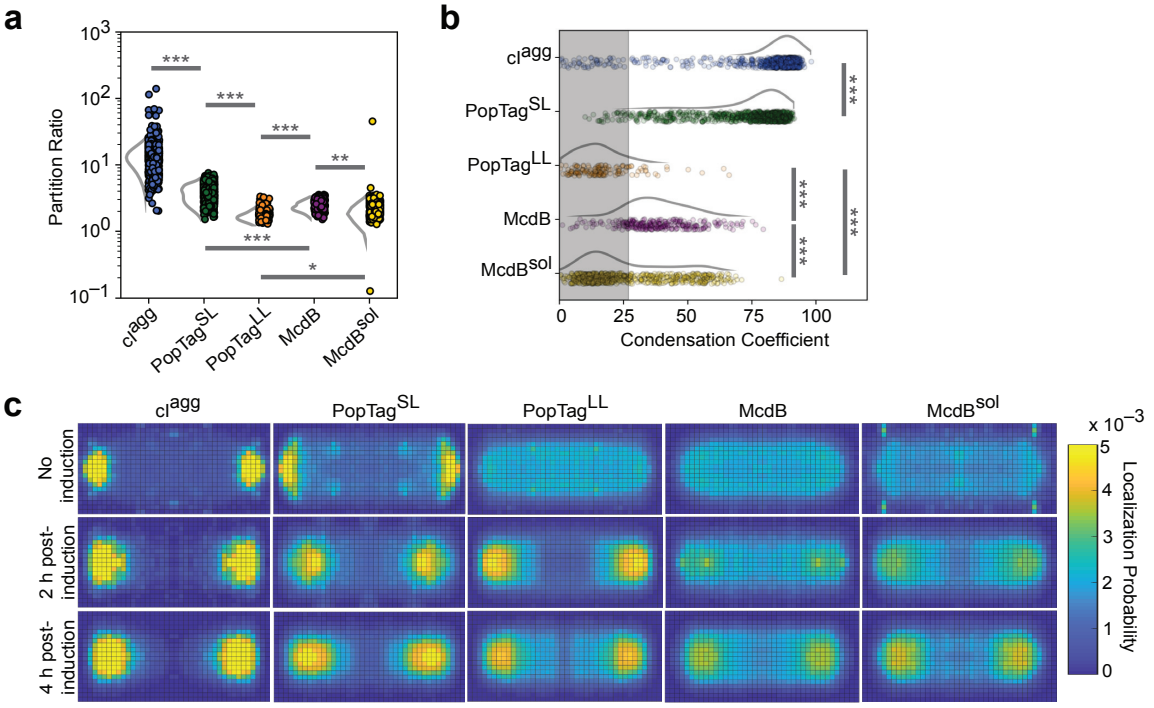


Figure 3.7: Cells that form condensates maintain a soluble cytoplasmic fraction. **a**. Partition ratios for specified mCherry fusions with detected foci (cI^{agg}, N = 995 cells; $PopTag^{SL}$, N = 939 cells; $PopTag^{LL}$, N = 147 cells; McdB, N = 341 cells; $McdB^{sol}$, N = 714 cells). **b**. Single-cell condensation coefficients for specified mCherry fusions with detected foci cI^{agg}, N = 1019 cells; $PopTag^{SL}$, N = 942 cells; $PopTag^{LL}$, N = 151 cells; McdB, N = 343 cells; $McdB^{sol}$, N = 717 cells. An intensity threshold I = 0.3 was used. Data points correspond to individual cells and were normalized the mean condensation coefficient of cells expressing mCherry only. The shaded region represents the measurement range for cells expressing a uniform mCherry signal. The curves next to the scatter plots were obtained via kernel density estimation. N values are the same as in (a). **c**. Normalized single-molecule localization 2D histograms. Single-molecule localizations of specified PAmCherry fusion proteins were collected, projected, and binned onto a normalized cell shape to generate the heat map. Localizations were collected from 30 cells or more per condition over three biological replicates. $^{*}p < 0.05$, $^{**}p < 0.01$, and $^{***}p < 0.001$ by two-sided Welch's t-test.

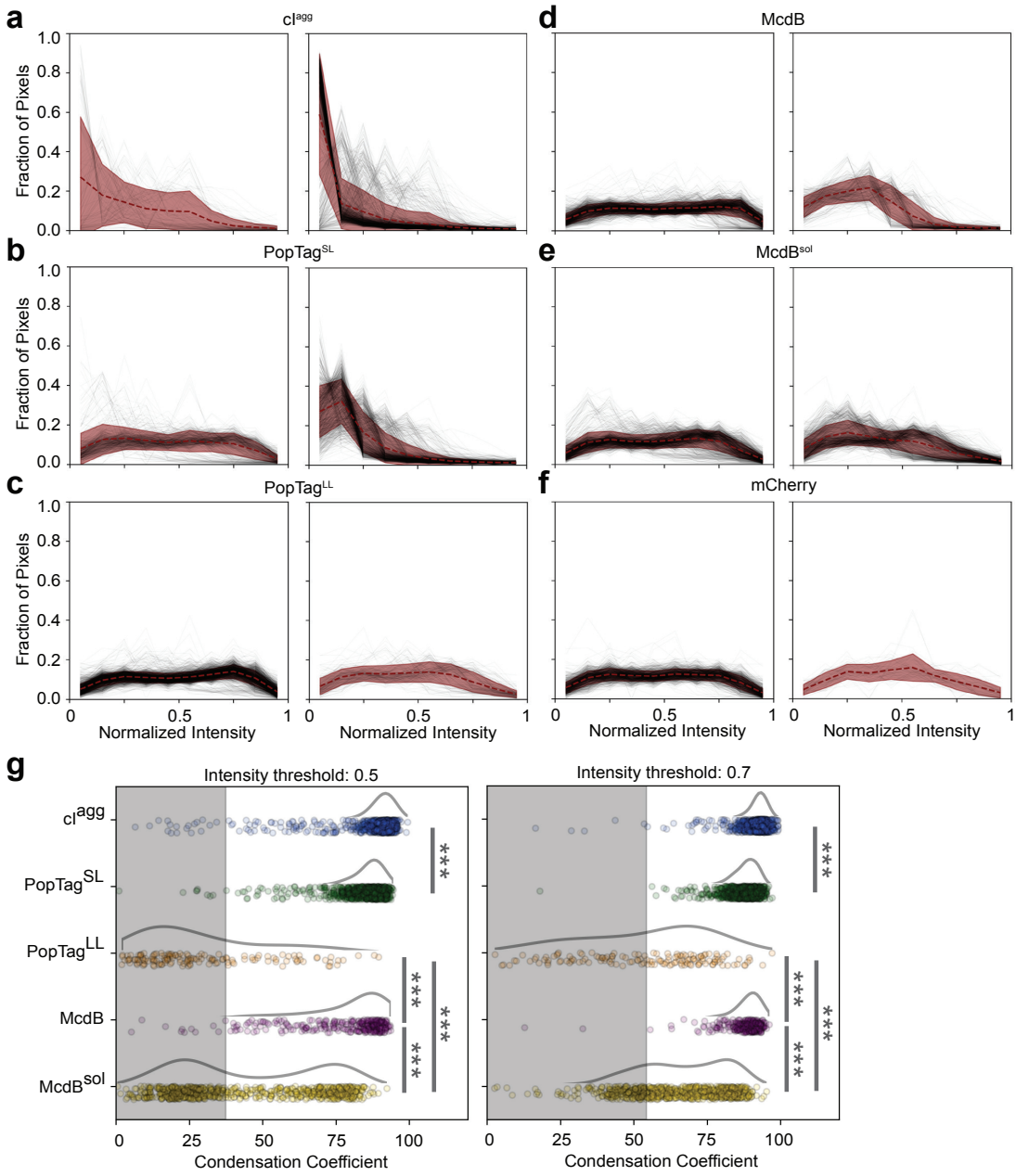


Figure 3.8: Normalized pixel intensity histograms and condensation coefficients of mCherry fusion proteins. a-f. Normalized pixel intensity histograms for cells with no detected focus (left) and a detected focus (right). Black lines represent individual cells. The red dashed line and shading are the average and standard deviation across cells for each plot. **g**. Quantification of condensation coefficients. Condensation coefficient plots for cells with a detected focus and threshold values of I = 0.5 and 0.7. Data points correspond to individual cells. The curves next to the scatter plots were obtained via kernel density estimation. The shaded region represents the measurement range for cells expressing a uniform mCherry signal. Analysis was done on $N > 900$ cells for each fusion over three biological replicates.

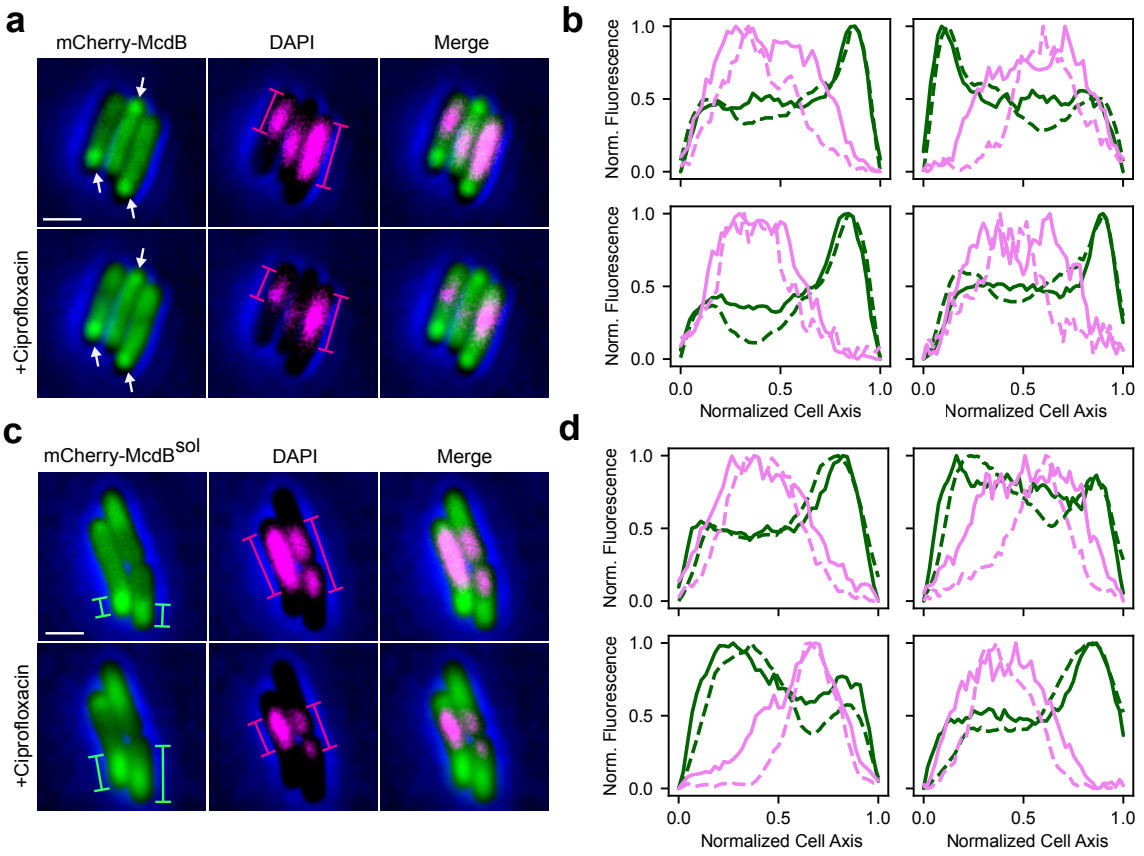


Figure 3.9: mCherry-McdB^{sol} condenses by repulsive interactions with the nucleoid. a. Representative images of mCherry-McdB foci in *E. coli* at 4 h post-induction (top). Cells were treated with ciprofloxacin (50 mM) for nucleoid compaction and stained with DAPI (2 µM) for nucleoid visualization (bottom). mCherry channel (green), DAPI (magenta), and merged images overlaid with Phase contrast (blue) are shown. White arrows highlight the mCherry-McdB foci that remained after nucleoid compaction. Magenta bars highlight the size of the nucleoid before and after ciprofloxacin treatment. **b**. Normalized profile lines along the normalized lengths of the long axes of four representative cells (n = 4) from the population shown in (a). Green and magenta lines represent the mCherry and DAPI signals, respectively. Solid lines and dashed lines represent the signal before and after ciprofloxacin treatment, respectively. **c**. Same as in (a) for mCherry-McdB^{sol} cells. Green bars indicate the length of the mCherry-McdB^{sol} foci before and after ciprofloxacin treatment. **d**. Same as in (b) for cells from the population shown in (c). Images are representative of three biological replicates. Scale bar: 1 µm.

is due to nucleoid exclusion by repulsive electrostatic interactions. Consistently, we found that the polar McdB^{sol} signal encroached throughout the cytoplasm as the nucleoid was compacted via drug treatment (Fig. 3.9 and Supplementary Movie 5).

Collectively, our results demonstrate the use of a tunable expression system that shows the concentration-dependent formation of condensates and exhibits a two-phase behavior, indicative of phase separation. Phase separation theory predicts that while many small condensates form at the initiation of phase separation, this number decreases, and the sizes of those that persist increase via coalescence [213, 214]. Our findings here are consistent with the expected final ground state being a single large condensate that coexists with a dilute phase. Some cells had foci at opposing poles (Fig. 3.2b). However, this can be attributed to the steric effects of nucleoid exclusion that prevent condensates from physically interacting and coalescing.

3.2.5 Changes in cellular concentration, osmolarity, and temperature probe the reversibility of condensates

A hallmark of condensates is reversibility in response to changes in protein concentration and chemical environment. We implemented several approaches to probe condensate reversibility of our protein set in *E. coli* cells. First, we set out to determine if dropping protein concentration below c_{sat} would dissolve condensates, thus demonstrating solubility as a driving force for condensate formation (Fig. 3.10a-f). Each protein was expressed via IPTG induction, and once foci formed, the inducer was removed from the media. Cells were then allowed to grow and divide, and in doing so, dilute the concentration of the mCherry fusion proteins. cI^{agg} foci remained at the pole from which they formed even as cells grew and divided over 10 h ($\geq$ 6 generations) (Fig. 3.10a-b and Supplementary Movie 6). This result shows no threshold concentration dependence in the formation and maintenance of cI^{agg} foci, and further supports its insolubility previously reported [210].

In contrast, PopTag^{SL}, PopTag^{LL}, and McdB foci all exhibited concentration-dependent

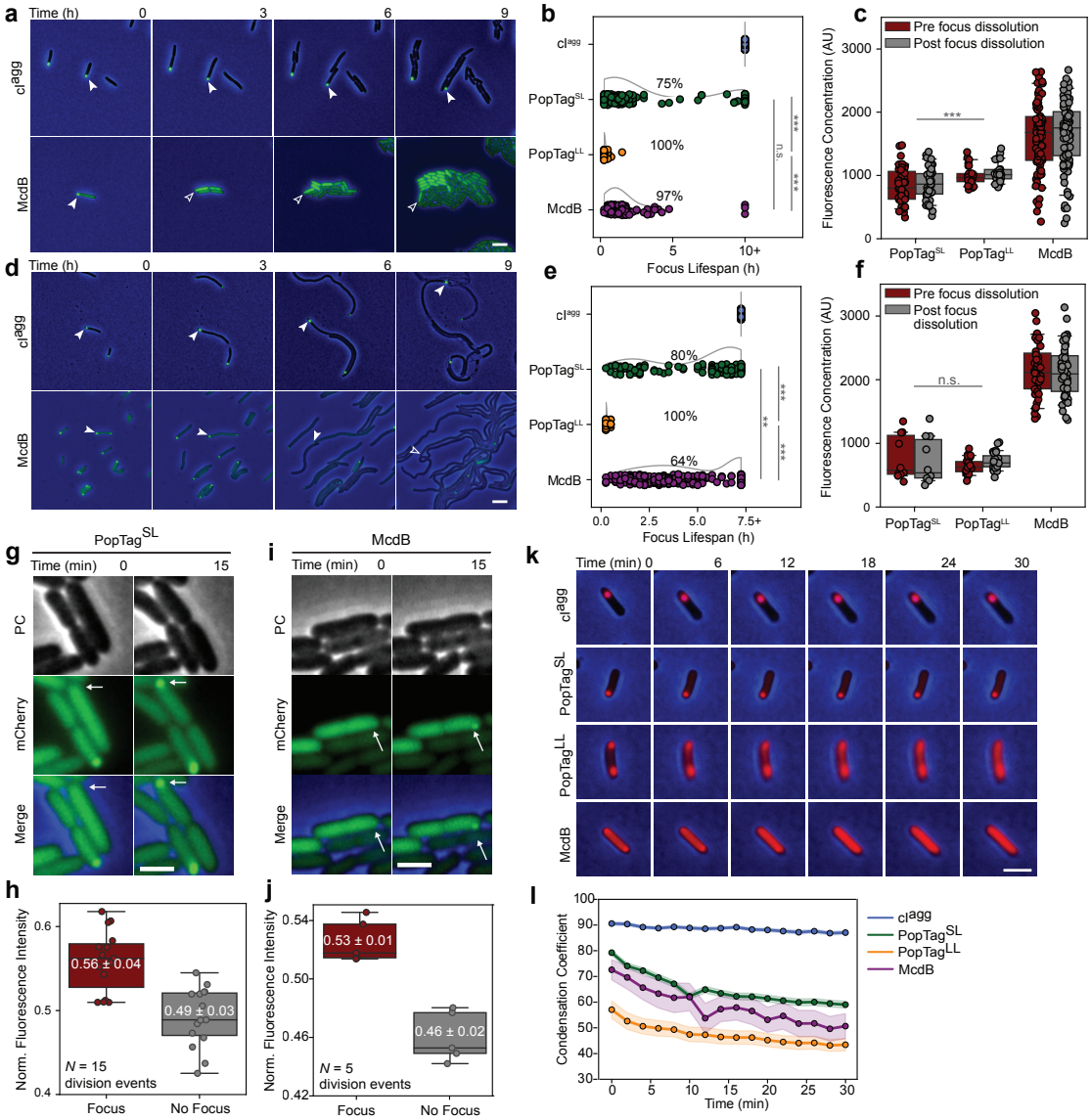

a
Time (h)
0
3
6
9
cIagg
McdB
b
cIagg
PopTagSL
PopTagLL
McdB
75%
100%
97%
n.s.
***
0
5
10+
Focus Lifespan (h)
c
Pre focus dissolution
Post focus dissolution
Fluorescence Concentration (AU)
3000
2000
1000
0
***
PopTagSL
PopTagLL
McdB
d
Time (h)
0
3
6
9
cIagg
McdB
e
cIagg
PopTagSL
PopTagLL
McdB
80%
100%
64%
***
**
***
0.0
2.5
5.0
7.5+
Focus Lifespan (h)
f
Pre focus dissolution
Post focus dissolution
Fluorescence Concentration (AU)
3000
2000
1000
0
n.s.
PopTagSL
PopTagLL
McdB
g
PopTagSL
Time (min)
0
15
PC
mCherry
Merge
i
McdB
Time (min)
0
15
PC
mCherry
Merge
k
Time (min)
0
6
12
18
24
30
cIagg
PopTagSL
PopTagLL
McdB
h
Norm. Fluorescence Intensity
0.6
0.5
0.4
0.56 ± 0.04
0.49 ± 0.03
N = 15
division events
Focus
No Focus
j
Norm. Fluorescence Intensity
0.54
0.50
0.46
0.42
0.53 ± 0.01
0.46 ± 0.02
N = 5
division events
Focus
No Focus
l
Condensation Coefficient
100
90
80
70
60
50
40
30
0
5
10
15
20
25
30
Time (min)
cIagg
PopTagSL
PopTagLL
McdB

Figure 3.10

Figure 3.10: Changes in cell volume and temperature drive condensate reversibility. The phase contrast (PC) channel is shown in blue or gray and the mCherry channel is in green. Sample size is shown in Table 3.1. Images are representative of four biological replicates. Scale bars: 1 μm **a**. Generational-dilution dissolves condensates. White arrows demarcate the cellular location of the same focus over time. Blank arrows demarcate the same cellular position now absent of a focus. **b**. Lifespan of protein foci during cell division. Data points correspond to individual foci. The curves next to the scatter plots are obtained via kernel density estimation. Percentages indicate the percent of foci that dissolved prior to the last frame in the data collection. Statistical analysis was performed on the lifespans of foci that dissolved. **c**. Fluorescence concentration of cells in the frames pre- (red) and post- (gray) the disappearance of a fluorescent focus. **d**. Cell elongation dissolves condensates. Same as in (a). **e**. Lifespan of protein foci during cell elongation. Same as in (b). **f**. Fluorescence concentration of cells in the frames pre- (red) and post- (gray) the disappearance of a fluorescent focus. Same as in (c). **g**. Focus reformation after cell division. White arrows demarcate the same cellular location before and after cell division. **h**. Quantification of daughter cells in (g). **j–l**. Same as in (g, h). **k**. Effects of temperature shift on focus stability. **j**. Quantification of (k). Condensation coefficient of cells over time using an intensity threshold $I = 0.5$. Colored solid lines and shading represent the average and 95% confidence interval, respectively, of at least 7 cells per sample at every time point. $^{***}p < 0.001$, $^{**}p < 0.01$, n.s. indicates no statistically significant difference between the samples by two-sided Welch's t-test. All box plots presented show the median, upper and lower quartiles, and the whiskers represent the 1.5 × interquartile range.

dissolution. Roughly 75% of PopTag^{SL} foci dissolved and had an average lifespan of 1.6 ± 2 h (Fig. 3.10a-b, Fig. 3.11a and Table 3.1). The generational dilution effect was more immediate with PopTag^{LL} (Fig. 3.11a), where all foci dissolved within 0.3 ± 0.2 h or roughly a single cell division event (Fig. 3.10b and Table 3.1). When compared to these controls, McdB focus dissolution mirrored that of the fluid PopTag^{LL} condensate, with approximately 97% of foci dissolving within 1.4 ± 1 h or within one to three cell divisions (Fig. 3.10a-b and Table 3.1). Indeed, most McdB foci dissolved following a single cell division event (Supplementary Movie 6). Furthermore, we measured the fluorescence concentration of cells that exhibited focus dissolution at the frames immediately preceding and immediately following the dissolution event (Fig. 3.10c, f). Consistent with our previous c_{sat} measurements, the average fluorescence concentration of McdB when foci dissolved was two-fold higher than cells expressing PopTag^{LL} (Fig. 3.10c). PopTag^{LL} having a higher fluorescence concentration than PopTag^{SL} when foci dissolved is also consistent with the

longer linker length increasing c_{sat} [78].

Intriguingly, some cells reformed McdB and PopTag^{SL} foci immediately after cell division (Fig. 3.10g-j). We hypothesized that this phenomenon was due to an asymmetric inheritance of protein upon cell division, which drove the concentration in one daughter cell above c_{sat}. Analysis of several division events for cells expressing McdB and PopTag^{SL} (see Methods) confirmed our hypothesis: most daughter cells that form foci have inherited more fluorescence signal than the other corresponding daughter cell (Fig. 3.10h and j).

We also probed condensate solubility by diluting protein concentration via an increase in cell length without cell division or further protein expression. *E. coli* cells were prepared as described above, but with the inclusion of the cell division inhibitor cephalexin. We expected similar trends for dilution via cell elongation as in cell division. Indeed all cI^{agg} foci were observed to persist throughout the experiment duration (> 7.5 h) (Fig. 3.10d-e and Supplementary Movie 7). Also consistent with the generational dilution experiment, approximately 80% of PopTag^{SL} foci dissolved during cell elongation; albeit with a slightly longer average focus lifespan (4.3 ± 2.3 h) (Fig. 3.10e, Fig. 3.11b and Table 3.1). The more fluid PopTag control, PopTag^{LL}, also readily dissolved with an average lifespan of 0.3 ± 0.1 h. Like PopTag^{SL}, McdB foci also exhibited an extended lifespan of 3.2 ± 1.6 h, compared to the generational dilution experiment. Moreover, only 64% of foci dissolved—a significant decrease compared to the generational dilution experiment. The reason for condensate persistence during cell elongation and not during cell division is unknown. However, we speculate that the altered cytoplasmic conditions (e.g. effective volume and crowding) of multi-nucleate elongated cells, compared to cells undergoing vegetative growth, play a role in the observed differences in focus dissolution. Consistent with this hypothesis, the fluorescence concentration of cells expressing PopTag^{LL} and McdB when foci dissolved during cell elongation (Fig. 3.10f) were shifted when compared to the generational dilution experiment (Fig. 3.10c).

Hyperosmotic stress is commonly used to induce condensate formation in eukary-

Table 3.1: Focus dissolution tracking analysis results

Figure	Protein	Number of foci tracked	Number of foci that dissolved	% of foci that dissolved	Lifespan of dissolved foci (h)
4a-b	cI^{agg}	93	0	0	na
4a-b	$PopTag^{SL}$	148	111	75	1.6 ± 2
4a-b	$PopTag^{LL}$	64	64	100	0.3 ± 0.2
4a-b	McdB	87	84	96.6	1.4 ± 1
4d-e	cI^{agg}	102	0	0	na
4d-e	$PopTag^{SL}$	119	95	75	4.3 ± 2.3
4d-e	$PopTag^{LL}$	35	35	100	0.3 ± 0.1

otic cells, via increases in the concentration of phase-separating proteins as well as the macromolecular crowding and the ionic strength of the cell. In bacteria, condensate formation and dissolution in response to changes in osmolarity have yet to be described to the best of our knowledge. We expressed each protein fused to mCherry, and once foci formed, the inducer was removed. Cells were then osmotically stressed at 300 mM NaCl for 15 min and allowed to recover for 15 min or 30 min prior to imaging (Fig. 3.11c-d). Immediately following osmotic upshift, cI^{agg} cells displayed slightly more foci, compared to untreated cells (Fig. 3.11c-d). Upon recovery, the foci number declined over time, but at a rate that matched untreated cells, showing this decrease was not due to a recovery from the osmotic upshift. On the other hand, cells expressing $PopTag^{SL}$, $PopTag^{LL}$, or McdB, all formed significantly more foci immediately following osmotic upshift, and upon recovery, foci count rapidly decreased to the level of untreated cells (Fig. 3.11d). The findings suggest that McdB and PopTag condensates are responsive to changes in osmolarity.

Finally, temperature is also a well-established modulator of protein phase separation. We hypothesized that increasing the temperature of cells with a preformed focus would influence condensates, while having little to no effect on insoluble aggregates. Cells expressing the mCherry fusions were induced to form foci, placed on ice to further cool the

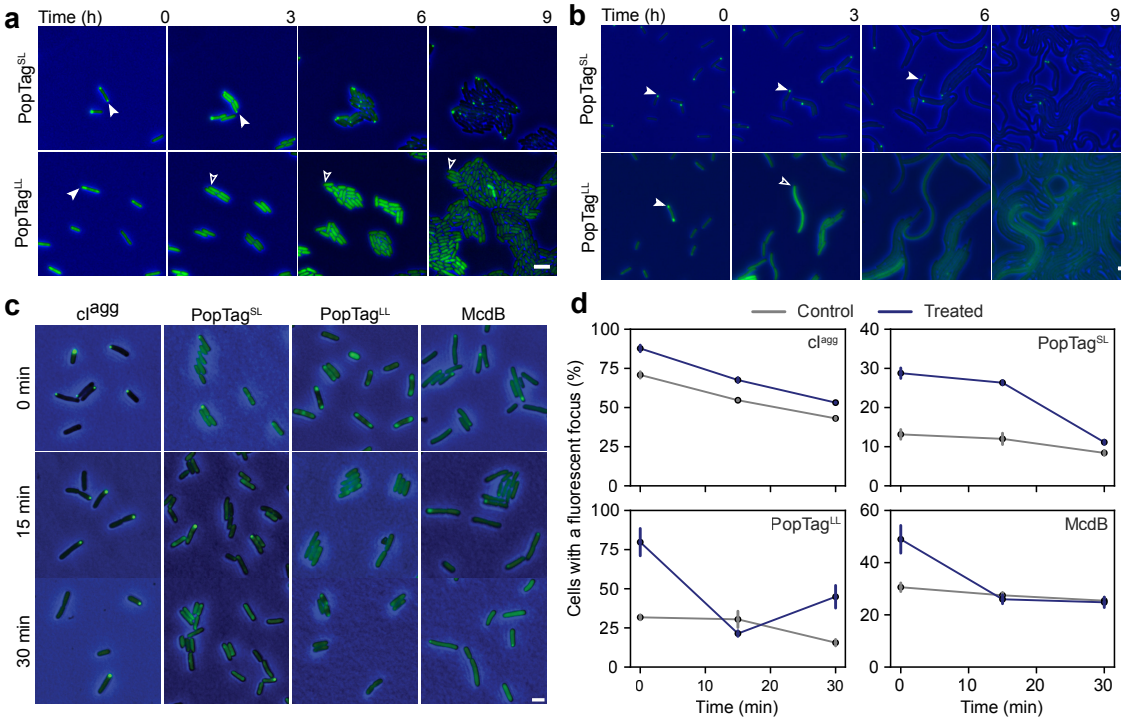


Figure 3.11: Condensate reversibility through cell growth, division, and osmolarity shift. a. Generational dilution dissolves phase-separated foci. The phase contrast channel (blue) and the mCherry channel (green) are merged for a-c. White arrows demarcate the same cellular location of the same focus over time. Blank arrows demarcate the cellular position now absent of a focus. Images are representative of four biological replicates. Scale bars: 2 μm. **b**. Cell elongation dissolves phase-separated foci. As in (a), except cells were treated with 10 μg/ml cephalexin to block cell division prior to spotting on agar pads. **c**. Cells osmotically shocked with 300 mM NaCl. The first row of panels shows cells treated cells prewash; 15 and 30 min are cells post-wash. Images are representative of three biological replicates. **d**. Percent of cells with a fluorescent focus for osmotically shocked cells shown in (c) and for untreated control cells from three biological replicates. Bars indicate the standard deviation across the replicates. $N > 50$ cells for each protein at each time point per replicate.

cells, and then imaged on a stage-top incubator set at 37 °C. As expected, cI^{agg} foci remained unchanged throughout the temperature increase (Fig. 3.10k-l). $PopTag^{SL}$ foci did not readily dissolve, but cells exhibited a gradual increase in the cytoplasmic fluorescence intensity. Consistently, the single-cell condensation coefficient for $PopTag^{SL}$ decreased over the temperature shift, indicating a transition in protein distribution in the cell (Fig. 3.10l). $PopTag^{LL}$ and McdB foci dissolved more readily towards a homogenous distribution (condensation coefficient = 50) (Fig. 3.10l). These results demonstrate that, unlike insoluble aggregates, phase-separated condensates are sensitive to temperature change, and the extent of responsiveness may correlate with the material properties of the condensate.

Together, using a series of reversal assays that probe the influences of protein concentration, osmolarity, and temperature, we observed focus dissolution and a corresponding turnover of protein into the cytoplasmic phase. The findings are consistent with the reversal to a one-phase system once the concentration has decreased below c_{sat}. These characteristics further support condensate formation by the PopTag fusions via phase separation and suggest a similar formation process for McdB condensates.

3.2.6 Probing the dynamic rearrangement, confinement, and exchange of biomolecular condensates

To probe the dynamic rearrangement of molecules within a focus and their exchange with the surrounding cytoplasm, we first implemented fluorescence recovery after photobleaching (FRAP) on the mCherry fusion foci. The aggregator control, cI^{agg}, exhibited no fluorescence recovery (Fig. 3.12a-b), supporting the static nature of the proteins within these aggregates and the absence of protein exchange with the cytoplasm. The PopTag fusions partially recovered to an extent consistent with their respective fluidity levels: $PopTag^{SL}$ and $PopTag^{LL}$ recovered to approximately 10% and 40%, respectively, of the initial fluorescence intensity (Fig. 3.12b). Recovery of McdB foci was once again similar to that of the fluid $PopTag^{LL}$ condensate. Taken together, the data suggest that McdB exhibits

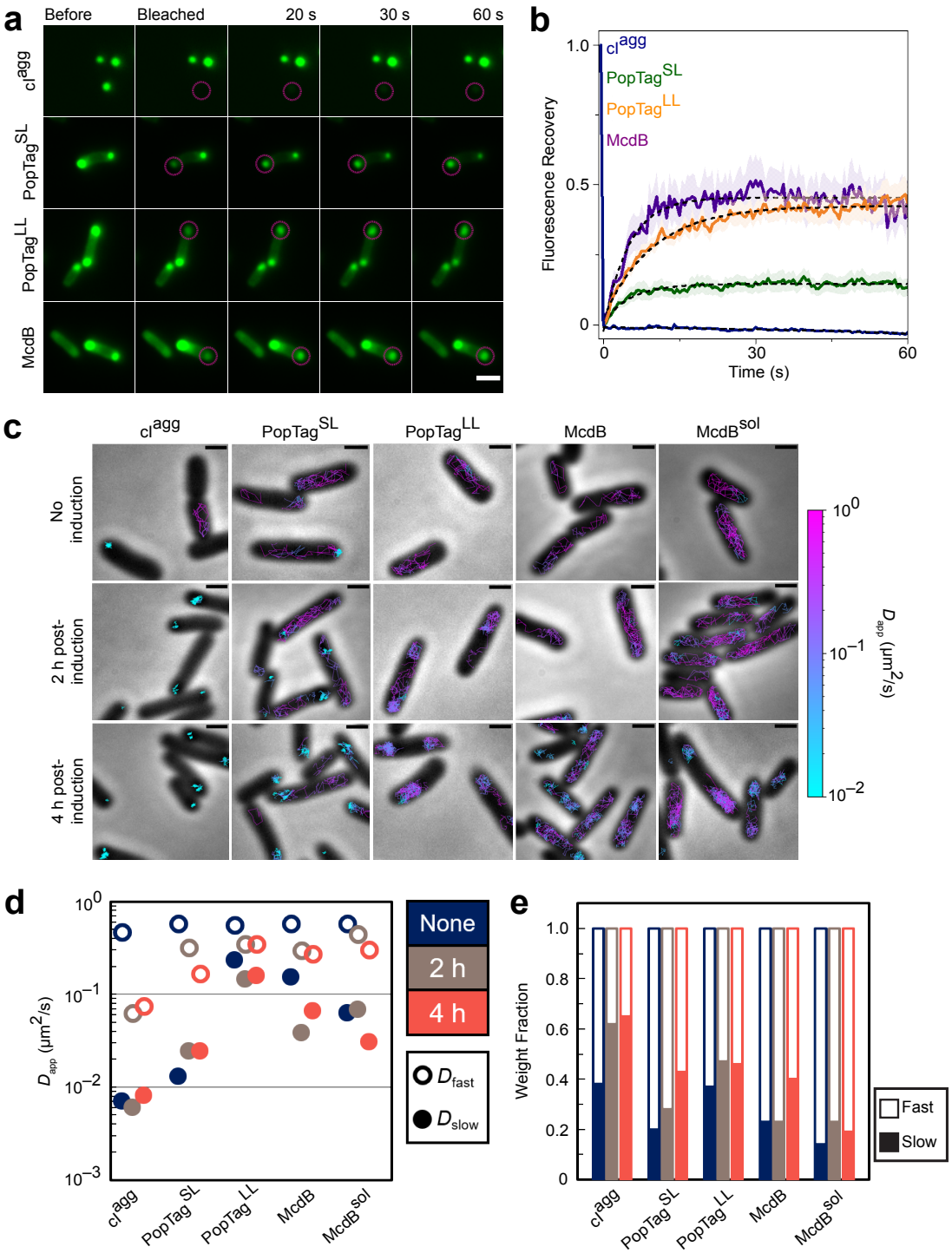

a
Before
Bleached
20 s
30 s
60 s
cIagg
PopTagSL
PopTagLL
McdB
b
cIagg
PopTagSL
PopTagLL
McdB
Fluorescence Recovery
1.0
0.5
0
0
30
60
Time (s)
c
cIagg
PopTagSL
PopTagLL
McdB
McdBsol
No induction
2 h post-induction
4 h post-induction
10^0
10^−1
10^−2
Dapp (μm2/s)
d
Dapp (μm2/s)
10^0
10^−1
10^−2
10^−3
None
2 h
4 h
Dfast
Dslow
cIagg
PopTagSL
PopTagLL
McdB
McdBsol
e
Weight Fraction
1.0
0.8
0.6
0.4
0.2
0
Fast
Slow
cIagg
PopTagSL
PopTagLL
McdB
McdBsol

Figure 3.12

Figure 3.12: FRAP in concert with single-particle tracking informs on the material state of foci in bacterial cells. a. Fluorescence recovery of mCherry-fusion proteins after photobleaching. Magenta circles indicate the FRAP region. Scale bar: 2 μm. **b**. Quantification of fluorescence recovery of mCherry fusion proteins. Shading represents the standard error of the mean. cI^{agg}: n = 14 foci; $PopTag^{SL}$: n = 12 foci; $PopTag^{LL}$: n = 14 foci; McdB: n = 10 foci. **c**. Representative single-molecule trajectories. Overlay of tracks, color-coded according to the track apparent diffusion coefficient, obtained from representative *E. coli* cells expressing PAmCherry fusion proteins. Scale bars: 1 μm. **d**. Diffusion coefficients of PAmCherry fusion proteins. The diffusion coefficients of the indicated PAmCherry fusions were obtained by fitting the histograms of the log diffusion coefficients of single tracks to a two-component Gaussian mixture model assuming that the fusion proteins are composed of a slow (closed circles) and fast (open circles) fraction. **e**. Weight fractions of mobility states of PAmCherry fusion proteins. Two-component Gaussian mixture fitting results show an increase in slow mobility fraction (solid bars) and a decrease in fast mobility fraction (empty bars) as protein concentration increases.

dynamics similar to that of the fluid $PopTag^{LL}$, while the minimal recovery of $PopTag^{SL}$ is consistent with its predicted gel-like state [78]. Given the limited number of pixels that make up the photobleached foci, we note that the fluorescence recovery contributions from internal rearrangements of molecules within a focus cannot be distinguished from the exchange of molecules with the surrounding milieu [212]. While FRAP is commonly used to determine if a compartment is liquid-like, this method is solely a measure of exchange dynamics, so FRAP alone is not a reliable "gold standard" measure of the material state of a focus.

Therefore, to further investigate the dynamics of our set of proteins both in the focus and in the cytoplasm, we implemented single-molecule localization microscopy and tracked the movement of individual molecules. We then determined the apparent diffusion coefficients (D_{app}) of the PAmCherry fusions to the screened proteins under different induction conditions by measuring the mean squared displacement (MSD) of individual trajectories as a function of time lag, τ. Prior to induction, low-level leaky expression of all fusions displayed a fast diffusive state ($D_{app,\ fast}$) (Fig. 3.13 and Table 3.2). Trajectory mapping back onto the cell showed the $D_{app,\ fast}$ population corresponds to free diffusion in the cytoplasm (Fig. 3.12c). cI^{agg} and $PopTag^{SL}$ also displayed a small population of nearly

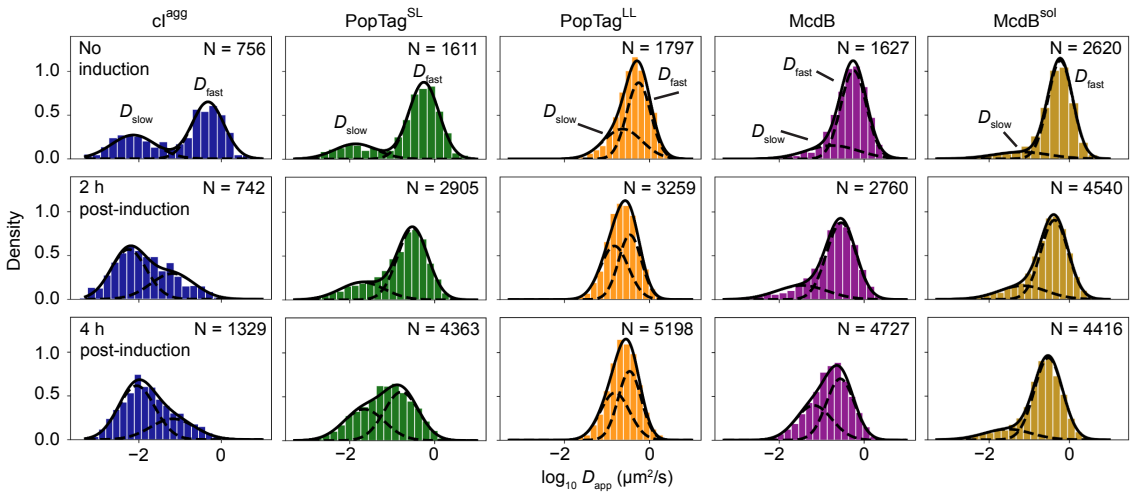


Figure 3.13: Diffusion coefficients of PAmCherry fusion proteins. Normalized log apparent diffusion coefficient histograms and two-component Gaussian mixture fit. The solid black line corresponds to the two-component Gaussian fit. The dashed black lines represent the Gaussian fit of each component which we refer to as $D_{app,\ slow}$ and $D_{app,\ fast}$. N indicates the number of trajectories analyzed for each protein per condition.

static molecules ($D_{app,\ slow}$) (Fig. 3.13 and Table 3.2), with trajectories that mapped to the cell poles (Fig. 3.12c). Upon induction, the near-static fraction of molecules increased for cI^{agg} and PopTag^{SL}, and became the dominant state for cI^{agg} (Fig. 3.13 and Table 3.2). A diffuse state, slower than free diffusion, also emerged for McdB, which mapped to the cell poles (Fig. 3.12c). The vast majority of McdB^{sol} molecules, on the other hand, remained in the fast diffusive state but remained nucleoid excluded (Fig. 3.12c); consistent with our wide-field microscopy of this fluidized McdB mutant (Fig. 3.9). PopTag^{LL} also exhibited nucleoid exclusion (Fig. 3.12c), despite remaining highly mobile. As stated earlier, we speculate that this behavior is caused by charge repulsion with the nucleoid.

By comparing the average mobility of $D_{app,\ slow}$ populations across all fusions, we find that cI^{agg} molecules within a focus were essentially static (Fig. 3.12d), consistent with being an aggregate. PopTag^{SL} molecules in foci displayed an intermediate mobility consistent with a gel or highly-viscous fluid state. All PopTag^{LL} molecules, on the other hand, essentially displayed a monomodal diffusive distribution across all induction conditions, consistent with this version of the PopTag being highly fluid. Finally, McdB displayed a

Table 3.2: Apparent diffusion coefficients and weight fraction resulting from two-state Gaussian mixture fitting (3.12c-e and 3.13).

Protein	Sample induction (100 µM)	$D_{app,slow}$ (µm²/s)	π_{slow}	$D_{app,fast}$ (µm²/s)	π_{fast}
cI^{agg}	None	0.007 ± 0.001	0.38 ± 0.02	0.467 ± 0.024	0.62 ± 0.02
	2 h	0.006 ± 0.001	0.62 ± 0.03	0.062 ± 0.006	0.38 ± 0.03
	4 h	0.008 ± 0.001	0.65 ± 0.03	0.074 ± 0.006	0.35 ± 0.03
$PopTag^{SL}$	None	0.013 ± 0.001	0.20 ± 0.01	0.572 ± 0.016	0.80 ± 0.01
	2 h	0.024 ± 0.002	0.28 ± 0.02	0.314 ± 0.010	0.72 ± 0.02
	4 h	0.023 ± 0.001	0.43 ± 0.02	0.165 ± 0.006	0.57 ± 0.02
$PopTag^{LL}$	None	0.234 ± 0.021	0.37 ± 0.04	0.559 ± 0.026	0.63 ± 0.04
	2 h	0.143 ± 0.006	0.47 ± 0.03	0.347 ± 0.008	0.53 ± 0.03
	4 h	0.158 ± 0.004	0.46 ± 0.03	0.347 ± 0.012	0.54 ± 0.03
McdB	None	0.153 ± 0.026	0.23 ± 0.05	0.576 ± 0.022	0.77 ± 0.05
	2 h	0.038 ± 0.005	0.23 ± 0.02	0.293 ± 0.006	0.77 ± 0.02
	4 h	0.065 ± 0.003	0.40 ± 0.02	0.268 ± 0.008	0.60 ± 0.02
$McdB^{sol}$	None	0.063 ± 0.017	0.14 ± 0.01	0.581 ± 0.010	0.87 ± 0.01
	2 h	0.068 ± 0.008	0.23 ± 0.01	0.437 ± 0.009	0.77 ± 0.01
	4 h	0.030 ± 0.003	0.19 ± 0.01	0.297 ± 0.003	0.81 ± 0.01

$D_{app,\ slow}$ state only slightly less mobile than the $D_{app,\ fast}$ population, consistent with a liquid-like condensate. Although our fluidized mutant, McdB^{sol}, displayed a D_{app} population similar to that of McdB, $D_{app,\ slow}$ was a minor fraction of the total population (Fig. 3.12e and Fig. 3.13).

A recent study that reports on the inhomogeneity of the bacterial cytoplasm finds slowed apparent protein diffusion at the cell poles compared to other regions of the *E. coli* cell [215]. The finding highlights the importance of comparative studies of in-focus diffusion measurements for foci occupying the same cellular location. It is likely that slowed protein diffusion contributes to condensate formation at cell poles. But, even if diffusion is slowed at the poles to some extent, our in-focus diffusion measurements are much slower and non-uniform across our protein set; supporting the conclusion that interactions involved in condensate formation further affect protein diffusion. Collectively, the data parse the dynamic exchange of molecules in foci and the surrounding cytoplasm, and delineate the spectrum of possible mobilities within a focus, thus allowing for inference of its material state.

3.2.7 IbpA as a reporter to differentiate between condensates and aggregates

The heat shock chaperone, IbpA, has been shown to colocalize with insoluble aggregates in *E. coli* [210]. We therefore initially thought that IbpA may work as an *in vivo* reporter that discriminates between aggregates and condensates, colocalizing with the aggregator control and not recognizing PopTag- or McdB-condensates. We expressed the mCherry fusion proteins under focus-forming conditions in an *E. coli* strain that expressed a chromosomal fluorescent reporter of IbpA (IbpA-msfGFP) and then observed colocalization patterns of the mCherry fusion proteins with IbpA. Unexpectedly, the IbpA foci strongly colocalized with all proteins surveyed (Fig. 3.14a), showing that IbpA does not specifically localize to misfolded protein aggregates in the cell as ascribed by current models [210]. Upon further investigation, we observed that the localization pattern of IbpA

association with the aggregate control versus the condensates was quantifiably different. We also found that IbpA appeared to coat, as opposed to penetrate, the cI^{agg} foci (Fig. 3.14a). Consistently, we quantified and compared the diameters of the IbpA signal projections relative to each mCherry fusion (Fig. 3.14b) and found that the IbpA signal was spread over a larger area than the cI^{agg} foci.

We extracted from the wide-field fluorescence data an intensity profile line plot of foci in both color channels. When normalized to the maximum intensity of the mCherry signal, we observed significant differences in the relative amounts of IbpA penetrating each of the mCherry fusion foci (Fig. 3.15a). On average, the max intensity of IbpA was 20 ± 9 % of that of cI^{agg} foci, while it was 58 ± 33, 188 ± 131, and 33 ± 35 % for $PopTag^{SL}$, $PopTag^{LL}$, and McdB foci, respectively. The limited amount of IbpA relative to cI^{agg} suggests that while IbpA can sense the aggregate, it cannot penetrate it well. In contrast, the higher amounts of IbpA in all other foci pointed to its ability to penetrate more fluid assemblies. This result demonstrates varying degrees of IbpA penetration within the corresponding mCherry fusion foci, which correlate well with their hypothesized material state. Together, the findings suggest a different pattern of colocalization of IbpA with the examined biomolecular condensates and aggregates.

To better resolve the colocalization patterns between IbpA and the mCherry fusion foci, we imaged cells under the same conditions as described earlier by structured illumination microscopy (SIM). With the increased resolution in both channels, the localization patterns of IbpA relative to the mCherry fusion foci were more easily observed (Fig. 3.15b). We registered the detected mCherry fusion protein foci at their center positions, normalized the intensities, and projected all detected focus images to produce an average image of each mCherry fusion protein focus. We observed that IbpA forms a rosette pattern around the mCherry-cI^{agg} foci, a punctate focus within mCherry-$PopTag^{SL}$ foci, and an amorphous focus pattern with mCherry-$PopTag^{LL}$ and mCherry-McdB (Fig. 3.15c). This result demonstrates that IbpA exhibits a different colocalization pattern with biomolec-

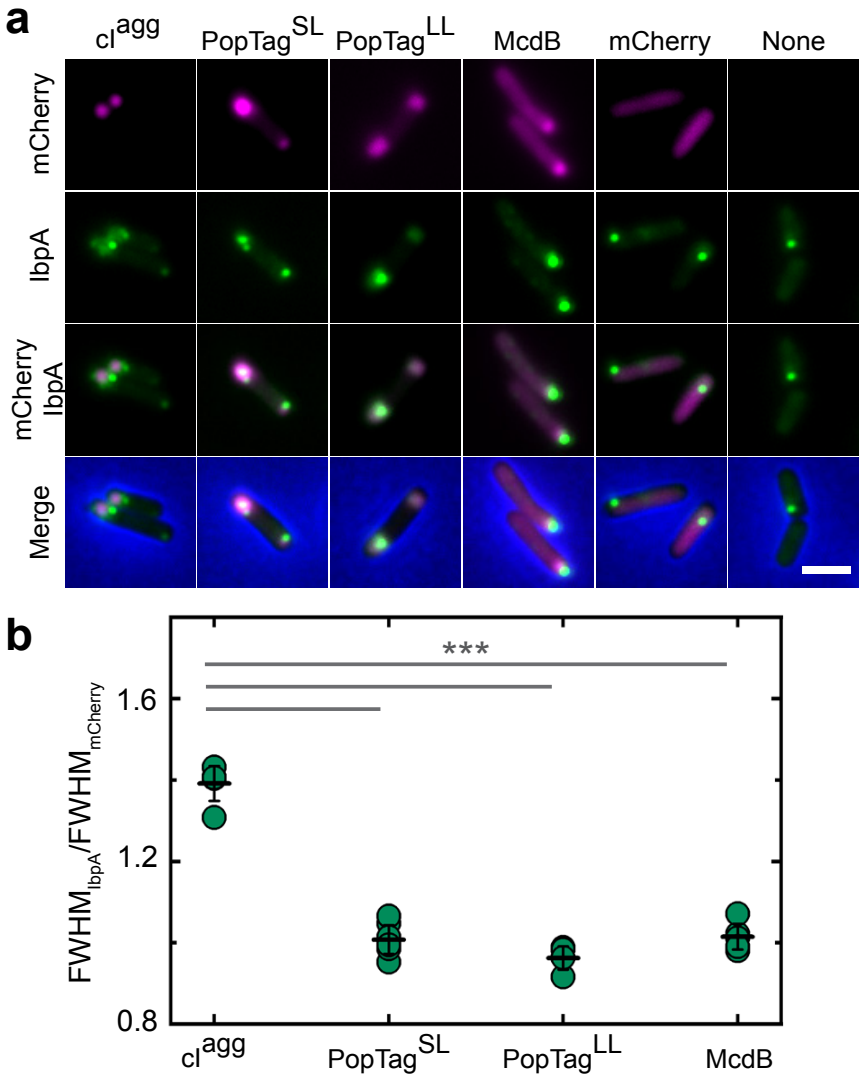


Figure 3.14: The nature of IbpA chaperone association with foci informs their material state *in vivo*. **a**. Wide-field fluorescence images of mCherry fusion foci (magenta) and IbpA-msfGFP foci (green). Phase Contrast is blue in the merge. Images are representative of three biological replicates. Scale bar: 2 µm. **b**. Quantification of the association of the foci of mCherry fusions and IbpA-msfGFP. Data points correspond to the ratio of the mean full-width at half maximum (FWHM) for the two channels ($FWHM_{IbpA}$ / $FWHM_{mCherry}$) for the sum projections of technical replicates (cI^{agg}: 5, $PopTag^{SL}$: 7, $PopTag^{LL}$: 4, McdB: 5) over three independent experiments. $n > 30$ foci for each protein per technical replicate. Black lines represent the mean ratio and the error bars represent the standard deviation. $^{***}p < 0.001$ by Welch's t-test.

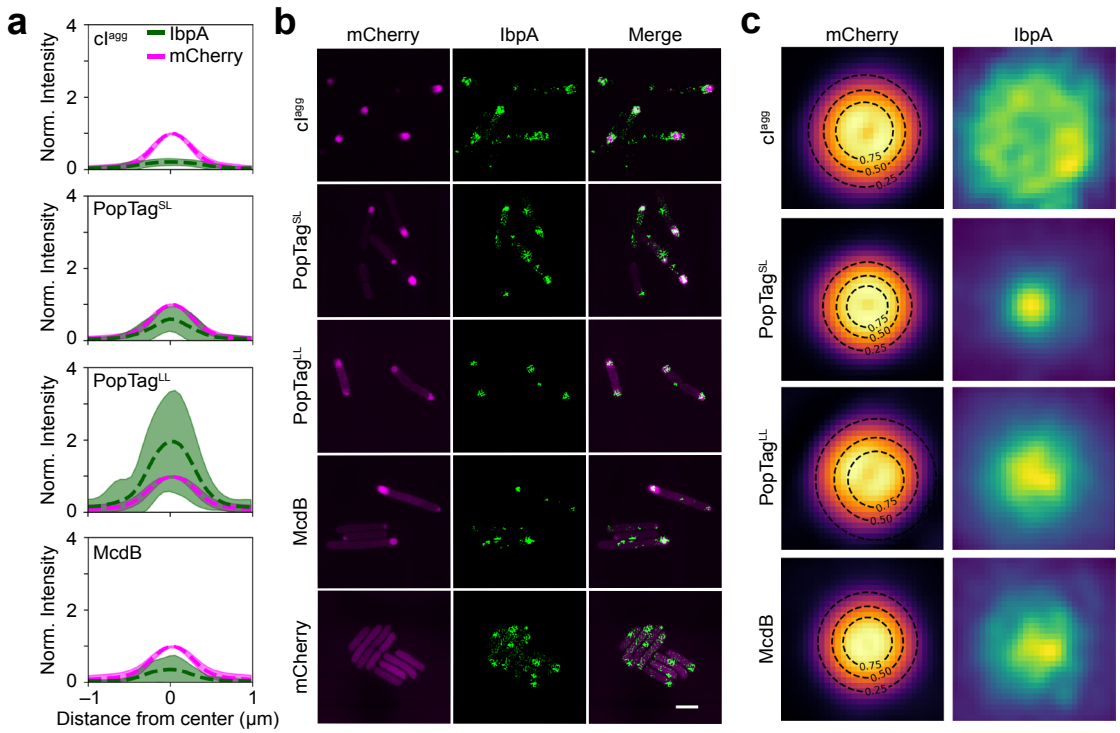


Figure 3.15: Nature of IbpA association with mCherry fusion foci by 2D SIM. a. Fluorescence intensity profile lines of mCherry fusion foci (magenta) and IbpA-msfGFP foci (green). Dashed lines and shading are the mean and standard deviation, respectively, of fluorescence intensities normalized to the mCherry signal. cI^{agg}: n = 348 foci; $PopTag^{SL}$: n = 540 foci; $PopTag^{LL}$: n = 547; McdB: n = 295 foci. **b**. 2D SIM images of mCherry fusion proteins foci (magenta) and IbpA foci (green) are shown. Images are representative of three biological replicates. Scale bar: 2 μm. **c**. Fluorescence projection images of mCherry fusion foci and local IbpA-msfGFP signal. Black dashed lines indicate the contour at 0.25, 0.50, and 0.75 of the 2D Gaussian fit amplitude surrounding the mCherry fusion focus. cI^{agg}: n = 84 foci; $PopTag^{SL}$: n = 506 foci; $PopTag^{LL}$: n = 457 foci; McdB: n = 217 foci.

ular condensates compared to aggregates and better penetrates more fluid condensates. These patterns serve as a proof of concept that IbpA serves as a reporter capable of differentiating between these macromolecular assemblies *in vivo*. Future studies will determine if other chaperones share this activity.

3.3 Discussion

In this study, we developed an experimental framework to assess the material state of fluorescent foci in bacteria; specifically, whether a focus can be described as a phase-separated condensate. When studying a new condensate, it is crucial to first determine the conditions under which it forms or dissolves. Inducer-controlled protein expression combined with quantitative fluorescence microscopy demonstrated general applicability in identifying the *in vivo* c_{sat} for condensate formation. Our results also indicate that i*in vivo* c_{sat} may vary within the cell population. Another critical metric is to determine the reversibility of a focus, as it is one of the hallmarks that distinguish condensates from aggregates. Our approaches for decreasing cellular protein levels below c_{sat}, via changes in cell shape, osmolarity, temperature, or generational dilution, provide accessible methods to probe the reversibility of condensate formation.

The dynamics of proteins inside a focus should then be determined by FRAP and single-molecule tracking. While FRAP is more accessible, it is challenging to collect data from a large number of cells. Single-molecule tracking experiments, on the other hand, enable the assessment of a large sample size and more in-depth analysis of protein dynamics within both the cytoplasm and the focus. However, the material state of a focus cannot be determined based on the diffusion coefficient alone. Even when the diffusion coefficient is relatively low, focus formation can still be reversible, as observed with the gel-like control protein in our study. Therefore, a combination of reversibility and dynamic assessments is essential to determine the material state of a focus in bacterial cells.

Finally, we identified the heat-shock chaperone, IbpA, as a molecular sensor that sur-

rounds solid aggregates but penetrates condensates. We demonstrated the versatility of these approaches by using focus-forming control proteins that span the spectrum of material states from a solid aggregate to a highly fluid condensate. When compared to these control proteins, we find that our protein of interest, McdB, robustly phase-separates into liquid-like condensates *in vivo*. As shown with the fluidized mutant of McdB, this framework can also be combined with mutagenesis studies to determine the regions and residues of a protein governing its material state and phase separation behavior in a bacterial cell.

Our framework overcomes current limitations in identifying the material state of a fluorescent focus and can be used to assess the phase separation activity of expressed recombinant proteins and bacterial Inclusion bodies (IBs). IBs are mesoscale protein aggregates, once strictly proposed as being composed of nonfunctional and misfolded proteins [216]. Phase separation has only recently been considered in the assembly and organization of IBs [217]. For example, several condensates have been shown to mature into gels and solid amyloids [197]. However, direct determination of whether a bacterial IB is a liquid, gel, solid, or a mixture of these states remains to be demonstrated.

Inclusion body binding protein A (IbpA) of *E. coli* belongs to the conserved family of ATP-independent small heat shock proteins, well-established in binding protein aggregates and driving them towards reactivation-prone assemblies [218–220]. As such, we presumed IbpA would serve as a molecular sensor that would selectively associate with protein aggregates, but not condensates. Instead, we found that IbpA surrounded protein aggregates and penetrated condensates. Moreover, the degree to which IbpA colocalized with condensates strongly correlated with increasing fluidity. Consistent with our findings, Yoo *et al.* recently showed that condensates are dispersed by chaperones far more rapidly than misfolded aggregates [221]. These findings warrant a reevaluation of the function of chaperone systems governing protein homeostasis and demonstrate the utility of IbpA, and potentially other chaperones, as molecular sensors for the material state

of fluorescent foci in bacteria.

The framework was built by contrasting the principles of aggregation versus phase separation behaviors of proteins. While not an exhaustive list, the approaches used here are highly accessible and probe several aspects of condensate assembly, maintenance, and dissolution. The framework is not without limitations. First, the approaches used here do not provide mechanistic insights into the process of phase separation, that is, whether condensate formation is driven purely by liquid-liquid phase separation (LLPS), phase separation coupled to percolation (PSCP), or phase separation coupled to other phase transitions (PS++) [40]. The current framework also does not include an assessment of the boundary between the dense and dilute phases, which is important in understanding the finite interfacial tension that hinders macromolecular transport across the boundary. Third, for broad use and accessibility, we developed the experimental framework using heterologous protein expression in *E. coli*, which may not accurately reflect the *in vivo* conditions of the native host. Finally, low-level leaky expression of inducible promoters may preclude the examination of proteins that phase separate at very low *in vivo* c_{sat}. Despite these limitations, this framework provides broad-use and systematic approaches that address ongoing debates over the rigor and standardization of phase separation assessments in bacterial cells.

3.4 Materials and Methods

3.4.1 Bacterial strains, plasmids, and primers

Strains, plasmids, and primers used in this study are listed in Tables 3.3 and 3.4. All constructs were made using Gibson assembly [222] from PCR fragments or synthesized dsDNA (Integrated DNA Technologies) and verified by Sanger sequencing. For example, plasmid pCA3 was generated from plasmid pTrc99A-*mCherry-cI78*^{EP} by replacing mCherry with PAmCherry. The PAmCherry fragment was generated using primers YH1

F and YH1 R. The plasmid pTrc99A-*mCherry-cI78*^{EP8} was amplified using YH2 F and YH2 R to generate the second fragment. The two fragments were then added to a Gibson assembly reaction to enzymatically join the overlapping DNA sequences. Other plasmids were generated using similar methods with primers indicated in Table 3.4. When relevant, homology regions for Gibson assembly are indicated in blue. Plasmids were introduced into their respective host strains by chemical transformation and selection for antibiotic resistance encoded by the plasmid. All plasmids are available on AddGene. The linker sequence used for PopTagLL was: DDAPAEPAAEAAPPPPPEPEPEPVSFDDEVLELTDPIAPEPELP-PLETVGDIDVYSPPEPESEPAYTPPPAAPVFDRD

3.4.2 Growth conditions

Lysogeny broth (LB) and AB media were used as either a broth or solid for culturing bacteria. LB medium was used to grow *E. coli* BL21 (AE) and overnight cultures of *E. coli* MG1665. The minimal AB medium was used when inducing protein expression in *E. coli* MG1665 to ensure protein expression reproducibility, as all the components are defined; as opposed to a complex medium such as LB [210, 223]. AB medium was supplemented with 0.2 % of a carbon source (glycerol for growth or glucose to also inhibit basal protein expression from the P_{trc} promoter), 0.2 % casamino acids, 10 µg/ml thiamine, and 25 µg/ml uracil [210]. *E. coli* was grown in a 15 ml tube overnight for approxiamtely 15 h in 5 ml of LB broth at 37 °C on an orbital shaker at 200–225 rpm. Exponential phase cultures were prepared by diluting overnight cultures 1:100 and further incubated until an OD600 of 0.2–0.6 was reached. When appropriate, the following chemicals were added to the medium at the indicated final concentrations: carbenicillin (100 µg/ml) for selecting the plasmids in culture, IPTG (0.1-1 mM) or L-arabinose (0.2 %) for protein induction. Reagents used are listed in Table 3.5.

Table 3.3: Strain and plasmids used in this study

Strains & Plasmids	Description	Source
Strains		
BL21 AE		
BL21 AI		
MG1655 Δ*lacY*		
MG1655 Δ*lacY ibpA-msfgfp*	MG1655 encoding a C-terminal fusion of IbpA to msfGFP	This study
Plasmids		
	pET-*mNeonGreen-mcdB*	This study
	pET-*His_6-mNeonGreen-mcdB*	This study
pYH79	pET-*His_6-mCherry-mcdB*	This study
pTrc99A-*mCherry-cI78^{EP8}*	pTrc99A expression vector allowing the inducible expression (P_{trc} promoter) of a N-terminal fusion of cI78^{EP8} (a mutagenized fragment of the lambda prophage repressor protein) to the mCherry fluorescent protein	[28]
pCA3	pTrc99A-PAmCherry- *cI78^{EP8}*	This study
pYH70	pTrc99A-*PAmCherry-mcdB*	This study
pYH71	pTrc99A-*mCherry-mcdB*	This study
pYH74	pTrc99A-*mNeonGreen-mcdB*	This study
pYH75	Ptrc99A-*mCherry-L6-PopTag*	This study
pYH76	Ptrc99A-*PAmCherry-L6-PopTag*	This study
pYH77	Ptrc99A-*mCherry*	This study
pYH78	Ptrc99A-*PAmCherry*	This study
pYH80	Ptrc99A-*mCherry-L78-PopTag*	This study
pYH88	trc99A-*PAmCherry-L78-PopTag*	This study
pYH86	Ptrc-*mCherry-mcdB^{sol}*	This study
pYH89	Ptrc-*PAmCherry-mcdB^{sol}*	This study

Table 3.4: Primers used in this study.

Primers	Description	Note
YH1 F	CACAGGAAACAGACCATGGCAGTGAGCAAGGGCGAGGAGG	To make pTrc99A-PAmCherry- *cI78*^{EP8} from pTrc99A-*mCherry-cI78*^{EP8}
YH1 R	CTGCTGCCGCTGCCGGATCCCTTGTACAGCTCGTCCATGC	
YH2 F	TGCCATGGTCTGTTTCCTGTG	
YH2 R	GGATCCGGCAGCGGCAGCAG	
YH3 F	CACAGGAAACAGACCATGGCAGTGAGCAAGGGCGAGGAGG	To make pYH70 from pYH71
YH3 R	CATGCTGCCGCTGCCGGATCCCTTGTACAGCTCGTCCATGC	
YH4 F	TGCCATGGTCTGTTTCCTG	
YH4 R	GGATCCGGCAGCGGCAGCATG	
YH5 F	AGGGATCCGGCAGCGGCAGCATGACTGACGCATTCGACCG	To make pYH71 from pTrc99A-*mCherry-cI78*^{EP8}
YH5 R	CTTGCATGCCTGCAGGTCGACTCACCAACCGTGCAGCTTG	
YH6 F	GCTGCCGCTGCCGGATCCCT	
YH6 R	GTCGACCTGCAGGCATGCAAG	
YH7 F	CACAGGAAACAGACCATGGCAGTGTCGAAAGGAGAAG	To make pYH74 from pYH71
YH7 R	CATGCTGCCGCTGCCGGATCCCTTGTATAATTCGTCCATC	
YH8 F	AGGGATCCGGCAGCGGCAGCATGGTCGCGGAACAACTTG	To make pYH75 from pYH74
YH8 R	GCATGCCTGCAGGTCGACTCATTAAGCTCCGCGACCACG	
YH9	GGATCCGGCAGCGGCAGCAT	To make pYH76 from pYH75
YH10	ATGCTGCCGCTGCCGGATCCCTTGTACAGCTCGTCCATGC	
YH11	GTCGACCTGCAGGCATGCA	To make pYH77 from pYH78

3.4.3 Total protein and immunoblot analyses

A 0.4-ml aliquot of *E. coli* cells (OD600: 0.2–0.4) was lysed using a Qsonica cupped-horn sonication system (20 cycles, 30 s on, 10 s off at 30% power) and centrifuged at 10,000 x g for 1 min at 4 °C. The protein content in the supernatant was measured using a Bradford assay kit according to the manufacturer's instructions. To prepare samples for immunoblot analysis, an equal volume of 2 x Laemmli sample buffer was added to *E. coli* culture prior to boiling 20 min. One microgram of total protein from each sample was loaded in each lane of a 4-12% Bis-Tris NuPAGE gel. Gels were transferred onto a mini-size polyvinylidene difluoride membrane using a Trans-Blot Turbo system (Table 3.5). The membrane was immunoprobed using a rabbit polyclonal antiserum against mCherry gifted by the Ming Li Lab at the University of Michigan (1:2000). The membrane was then incubated with the goat anti-rabbit IgG Secondary Antibody IRDye 800CW. Membrane signals were visualized and quantified using LI-COR Image Studio. The mCherry band of each lane was

Table 3.5: Reagents used in this study.

Reagent	Vendor	Catalog #	Use
4-12% Bis-Tris NuPAGE gel	Thermo Fisher Scientific	NP0323BOX	SDS-PAGE
Bradford assay kit	Bio-Rad Laboratories	5000006	To measure protein content
Carbenicillin	Thermo Fisher Scientific	MT46100RG	To select for the plasmid in culture
DAPI	Thermo Fisher Scientific	D1306	To label the nucleoid
Glucose	Thermo Fisher Scientific	15023021	As a carbon source and to inhibit protein expression from the P_{trc} promoter
Glycerol	Thermo Fisher Scientific	G334	As a carbon source for *E. coli* MG1665
Goat anti-rabbit IgG Secondary Antibody IRDye 800 CW	LI-COR	926-32210	For western blots
IPTG	Thermo Fisher Scientific	501126935	To induce protein expression
L-arabinose	Thermo Fisher Scientific	AC365181000	To induce protein expression
Mini-size polyvinylidene difluoride membrane	Bio-Rad	1704156	For protein transfer during western blots
Cephalexin	Thermo Fisher Scientific	AAJ6317206	To inhibit cell division
A22	Millipore Sigma	SML0471	As the MreB inhibitor, which converts rod-shaped into round cells
Casamino acids	Millipore Sigma	65072-00-6	For AB medium
Thiamine	Millipore Sigma	T4625-5G	For AB medium
Uracil	Millipore Sigma	66-22-8	For AB medium
UltraPure agarose	Invitrogen	16500100	For agar pads
Ciprofloxacin	Thermo Fisher Scientific	AAJ6131714	To compact the nucleoid

normalized to the total intensity of the lane to calculate the cleavage level of mCherry fusion proteins.

3.4.4 Wide-field fluorescence and phase-contrast imaging

Wide-field fluorescence and phase-contrast imaging were performed using a Nikon Ti2-E motorized inverted microscope controlled by the NIS Elements software with a SOLA 365 LED light source, a 100x objective lens (Oil CFI Plan Apochromat DM Lambda Series for Phase Contrast), and a Photometric Prime 95B back-illuminated sCMOS camera or Hamamatsu Orca-Flash 4.0 LTS camera. Fusions to mNeonGreen (mNG) were imaged using a "YFP" filter set (C-FL YFP, Hard Coat, High Signal-to-noise, Zero Shift, Excitation: 500/10 nm, Emission: 535/25 nm, Dichroic mirror: 515 nm). Fusions to msfGFP were imaged using a "GFP" filter set (C-FL GFP, Hard Coat, High Signal-to-noise, Zero Shift, Excitation: 436/10 nm, Emission: 480/20 nm, Dichroic mirror: 455 nm). DAPI fluorescence was imaged using a "DAPI" filter set (C-FL DAPI, Hard Coat, High Signal-to-noise, Zero Shift, Excitation: 350/25 nm, Emission: 460/25 nm, Dichroic mirror: 400 nm). mCherry was imaged using a "Texas Red" filter set (C-FL Texas Red, Hard Coat, High Signal-to-Noise, Zero Shift, Excitation: 560/20 nm, Emission: 630/37.5 nm; Dichroic Mirror: 585 nm).

3.4.5 Time-lapse videos of protein induction in *E. coli* BL21

Gene *mNG-mcdB* and *mNG-cI*^{agg} were cloned into the multiple cloning site of the vector pET11a to create the pJB37 and pYH73 plasmids respectively, used for inducible expression under the control of a bacteriophage T7 promoter. pJB37 and pYH73 were transformed into BL21 (AE) cells and a 5 ml overnight culture containing 100 µg/ml of carbenicillin in LB medium was grown at 37 °C with shaking at 225 rpm. The overnight culture (50 µl) was used to inoculate 5 ml of LB supplemented with 100 µg/ml of carbenicillin in a 15 ml tube. The cells were grown at 37 °C with shaking at 225 rpm to an OD600 of 0.2–0.6. Protein expression was then induced by the addition of 1 mM IPTG and 0.2% arabinose

solution to the tube. Cells (2 µl) were spotted on a 1 cm diameter pad made of 1.5% UltraPure agarose in LB and supplemented with 1 mM IPTG and 0.2% arabinose. After 2 min, the cell-containing side of the pad was flipped onto a 35 mm glass-bottom dish and mounted onto the stage of a Nikon Ti2-E motorized inverted microscope controlled by NIS Elements software with a SOLA 365 LED light source, a 100 x objective lens (Oil CFI Plan Apochromat DM Lambda Series for Phase Contrast), and a Photometrics Prime 95B back-illuminated scientific Complementary Metal-Oxide-Semiconductor (sCMOS) camera. mNG was imaged using the "YFP" filter set (see above). An image series was captured every 1 min for 4 h.

3.4.6 DAPI staining

E. coli BL21 (AE) cells with plasmid pJB37 were induced with 1 mM IPTG and 0.2% arabinose as described in the "Time-lapse videos of protein induction in *E. coli* BL21" section. DAPI (Table 3.5) was added to the exponentially growing culture at a final concentration of 2 µM. Cells were incubated in DAPI for 15 min at 25 °C before imaging, without rinsing. DAPI was imaged using the "DAPI" filter set (see above).

3.4.7 Localized cell lysis

pJB37 was transformed into BL21 (AE) cells, and a 10 ml overnight culture containing 100 µg/ml of carbenicillin was grown at 20 °C with shaking at 225 rpm. The overnight culture (0.5 ml) was used to inoculate 50 ml of LB supplemented with 100 µg/ml of carbenicillin in a 250 ml baffled flask. The cells were grown at 37 °C with shaking at 225 rpm to an OD600 of 0.5. The flasks were plunged into an ice bath for 2 min. Protein expression was then induced by the addition of 1 mM IPTG and 0.2% arabinose solution to the flask. Flasks were then returned to the shaker with incubation temperature set to 16 °C. Cells were then grown overnight with shaking at 225 rpm (approximtely 6 h induction). Cells (2 µl) were spotted on a 1 cm diameter pad made of 1.5% UltraPure agarose in LB. After

2 min, the cell-containing side of the pad was flipped onto a 35 mm glass-bottom dish and mounted onto the stage of a Nikon Ti2-E motorized inverted microscope controlled by NIS Elements software with a SOLA 365 LED light source, a 100 x objective lens (Oil CFI Plan Apochromat DM Lambda Series for Phase Contrast), and a Photometrics Prime 95B back-illuminated sCMOS camera. mNG-McdB was imaged using the "YFP" filter set (see above). A region of interest (0.5 μm diameter) was drawn at one cell pole and used as the target for a 405 nm laser pulse (1 sec at 50 mW), which caused localized cell lysis. An image series was captured every 500 ms for 60 s.

3.4.8 Cellular shape change in *E. coli* BL21

E. coli BL21 (AE) cells with plasmid pJB37 and pYH73 were induced with 1 mM IPTG and 0.2% arabinose as described in the "Time-lapse videos of protein induction in *E. coli*BL21" section. The MreB inhibitor A22 (10 μg/ml, Table 3.5) was added to the exponential phase cultures at time t = 0. The cultures were then incubated at 37 °C with shaking at 225 rpm for 6 h. Images were taken at 6 h post-treatment with the "YFP" filter set (see the "Wide-field fluorescence and phase-contrast imaging" section).

3.4.9 Single-cell tunable induction of mCherry fusion focus

Gene *mCherry-cI*^{agg}, *mCherry-PopTag*^{SL}, *mCherry-PopTag*^{LL}, *mCherry-mcdB*, *mCherry-mcdb*^{sol}, and *mCherry* were cloned into the multiple cloning site of the vector pTrc99A to create the pTrc99A-*mCherry-cI78*^{EP8}, pYH75, pYH80, pYH71, pYH86, and pYH77 plasmids respectively. The above plasmids were transformed into MG1665 cells and a 5 ml overnight culture containing 100 μg/ml of carbenicillin in AB medium (with 0.2% glycerol as the carbon source) was grown at 37 °C with shaking at 200 rpm. The overnight culture (50 μl) was used to inoculate 5 ml of AB (with 0.2% glycerol as the carbon source) supplemented with 100 μg/ml of carbenicillin in a 15 ml tube. The cells were grown at 37 °C with shaking at 200 rpm to an OD600 of 0.2–0.6. 500 μM of IPTG was added to the exponential phase cul-

ture to induce fluorescent fusion protein expression. After each hour, 2 μL of the MG1665 culture were spotted on an agarose round pad. The pads were prepared by dissolving Ultrapure agarose in AB to a final concentration of 1.5%. A series of images were taken with the "Texas Red" filter set (see the "Wide-field fluorescence and phase-contrast imaging" section) every 1 h for 5 h.

3.4.10 Nucleoid compaction

E. coli MG1665 with pYH86 plasmid was induced with 1 mM IPTG for 2 h. Cells were then stained with 2 μM DAPI and spotted on an agarose pad containing 50 μM of ciprofloxacin (Table 3.5). A series of images were taken with the "Texas Red" and "DAPI" filter sets (see the "Wide-field fluorescence and phase-contrast imaging" section) every 15 min for 7 h.

3.4.11 Focus reversibility in response to changes in concentration in *E. coli* MG1665

E. coli MG1665 with pTrc99A-*mCherry-cI78*^{EP8}, pYH75, pYH80, pYH71, pYH86, and pYH77 plasmids were induced with 1 mM IPTG for 2 h. The cells were then washed three times with 10 X volume of fresh AB media supplemented with 0.2% glucose and incubated for 30 min at 25 °C before imaging. After 30 min, 2 μL of the MG1665 culture was spotted on an agarose round pad. The pads were prepared by dissolving Ultrapure agarose in AB to a final concentration of 1.5% (the AB medium contains 0.2% glucose and 10 μg/ml cephalexin when specified). A series of images were taken with the "Texas Red" filter set (see the "Wide-field fluorescence and phase-contrast imaging" section) every 15 min for 15 h.

3.4.12 Osmotic Shock

E. coli MG1665 cells with pTrc99A-*mCherry-cI78*^{EP8} and pYH75 plasmids were induced with 50 μM IPTG for 1 h. *E. coli* MG1665 cells with pYH80 and pYH71 plasmids were induced with 200 μM IPTG for 2 h. After a significant fraction of cells (>20%) displayed foci, samples were washed three times with a 10 × volume of fresh AB media supplemented with 0.2% glucose and 300 mM KCl and incubated for 15 min at 37 °C with shaking. Control cells were also washed three times with a 10 × volume of fresh AB media supplemented with 0.2% glucose, but without KCl, and incubated at 37 °C with shaking. Cells (2 μl) were then spotted on a 1 cm diameter agarose pad. After 2 min, the cell-containing side of the pad was flipped onto a 35 mm glass-bottom dish and mounted onto a stage-top incubator. Images were captured with the "Texas Red" filter set (see the "Wide-field fluorescence and phase-contrast imaging" section). Cells treated with KCl were then subjected to another three washes with a 10 × volume of fresh AB media supplemented with 0.2% glucose, but without KCl, to visualize the focus dissolution. These cells, along with control cells that received no KCl treatment, were imaged as described above at 15 and 30 min following the osmotic upshift.

3.4.13 Temperature shift

E. coli MG1665 with pTrc99A-*mCherry-cI78*^{EP8}, pYH75, pYH80, pYH71, pYH86, and pYH77 plasmids were induced with 200 μM IPTG for 2 h. The cells were then washed three times with 10 × volume of fresh AB media supplemented with 0.2% glucose and incubated for 1 h on ice. Cells (2 μl) were then immediately spotted on a 1 cm diameter agarose pad. After 2 min the cell-containing side of the pad was flipped onto a 35 mm glass-bottom dish and mounted onto a stage-top incubator with temperature control. The stage-top temperature was set up at 37 °C. An image series was captured with the "Texas Red" filter set (see the "Wide-field fluorescence and phase-contrast imaging" section) every 1 min for 30 min to observe focus dissolution.

3.4.14 Fluorescence recovery after photobleaching (FRAP)

E. coli MG1665 with pTrc99A-*mCherry-cI78*^{EP8}, pYH75, pYH80, and pYH71 plasmids were induced with 1 mM IPTG for 2 h. FRAP was performed after cells were washed with fresh AB media supplemented with 0.2% glucose and incubated for 30 min. A Nikon Ti2-E motorized inverted microscope controlled by NIS Elements software with a SOLA 365 LED light source, a 100 x objective lens (Oil CFI Plan Apochromat DM Lambda Series for Phase Contrast), and a Photometrics Prime 95B back-illuminated sCMOS camera were used to do FRAP experiments. Control images were taken before bleaching, then the regions of interest (foci) were bleached with a laser at 405 nm and 30% power (15 mW). A series of images was captured every 500 ms for 60 s after bleaching. More than ten different region of interest (ROI) were chosen per sample. Image analysis was performed using ImageJ. The background signal was subtracted from the bleached focus and an unbleached focus within the cell. The resulting focus signal was normalized such that the pre-bleach signal is one and the first frame post-bleaching is zero.

3.4.15 Imaging the IbpA protein with wide-field fluorescence microscopy

The plasmids pTrc99A-*mCherry-cI78*^{EP8}, pYH75, pYH80, pYH71, and pYH77 plasmids were transformed into *E. coli* MG1665 that expresses IbpA-msfGFP by its native promoter. A 5 ml overnight culture containing 100 μg/ml of carbenicillin in AB medium (with 0.2% glycerol as the carbon source) of each strain was grown at 37 °C with shaking at 200 rpm. The overnight culture (50 μl) was used to inoculate 5 ml of AB (with 0.2% glycerol as the carbon source) supplemented with 100 μg/ml of carbenicillin in a 15 ml tube. The cells were grown at 37 °C with shaking at 200 rpm to an OD600 of 0.2–0.6. 1 mM of IPTG was added to the exponential phase culture to induce fluorescent fusion protein expression for 2 h. 2 μL of the MG1665 cultures were spotted on an agarose round pad. The pads were prepared by dissolving Ultrapure agarose in AB to a final concentration of 1.5%. Images were taken with the "GFP" and "Texas Red" filter set (see the "Wide-field fluorescence and

phase-contrast imaging" section) at 2 h post-induction.

3.4.16 Imaging the IbpA protein with 2D Structured illumination microscopy (SIM)

Agarose pads with induced MG1665 cells were prepared as in the "Imaging the IbpA protein with wide-field fluorescence microscopy" section. SIM images were acquired on a Nikon N-SIM system equipped with a Nikon SR HP Apo TIRF 100× 1.49NA objective, a Hamamatsu ORCA-Flash4.0 camera (65 nm per pixel), and 488 nm and 561 nm lasers from a Nikon LU-NV laser launch. Cells were identified using DIC to avoid photobleaching. For each 2D-SIM image, nine images were acquired in different phases via the built-in 2D SIM modes. Super-resolution image reconstruction was performed using the Nikon Elements SIM module.

3.4.17 Single-molecule fluorescence microscopy

Cells expressing protein fusions to PAmCherry of a plasmid with the P_{trc} inducible promoter were grown in 3 ml of LB medium in a culture tube for approximately 14 h, with shaking at 225 rpm at 37 °C. The following day, cells were diluted 1:100 into 3 ml of fresh AB medium supplemented with 0.2% glucose or glycerol and grown to OD600 0.3 before imaging either as is ("no induction" condition) or inducing with 100 μM IPTG ("inducing" condition). After a 2 or 4-h induction, cells were washed three times with 1 ml of AB medium supplemented with 0.2% glucose. All "no induction" and "inducing" cells were resuspended in M9 medium supplemented with 0.2% glucose for imaging. Agarose pads were made at 2% (w/v) with M9 minimal medium supplemented with 0.2% glucose. An aliquot of 2.5 μl of cells was loaded onto an agarose pad and sandwiched between two coverslips. Cells were imaged at room temperature with a 100 × 1.40 numerical aperture oil-immersion objective. A 406 nm laser (Coherent Cube 405–100; 0.2 W/cm^2) was used for PAmCherry photoactivation and a 561 nm laser (Coherent-Sapphire 561–50: 88.4 W/cm^2)

was used for imaging. Given the difference in protein expression level, 200–400 ms activation doses were used for cells not induced and 50 ms activation doses were used for the 2 h induction sample. The 4 h sample had many preactivated molecules and molecules activated spontaneously without activation via 405 nm laser, which limited our ability to confidently localize single molecules. To reduce the number of molecules per imaging frame, an initial 405 nm laser activation (10–15 s) was followed by photobleaching through illumination with a 561 nm laser with the same power density as above for 15–20 min or until spatially resolved single molecules were observed. The fluorescence emission was filtered to eliminate the 561 nm excitation source and imaged at a rate of 40 ms/frame using a 512 × 512-pixel Photometric Evolve EMCCD camera.

3.4.18 Single-molecule data analysis

Phase-contrast microscopy images were used to segment bacterial cells (see Image analysis for details) prior to localization and tracking. Single molecules were detected and localized with a 2D Gaussian fitting by the Single-Molecule Accurate LocaLization by LocAl Background Subtraction (SMALL-LABS) algorithm [224] and connected into trajectories using the Hungarian algorithm [225]. Localization heat maps (Fig. 3.4f) were made by normalizing the segmented cells and rotating them onto their long axes, followed by projection, binning, and symmetrization of the single-molecule localizations onto the normalized cell [226, 227].

Only single-molecule trajectories with a minimum of six steps were used for trajectory analysis. To extract the apparent diffusion coefficient for each trajectory, a modified version of the diffusion model (Equation 2.1) [171] was fit to the MSD as a function of time lag, τ, over the time interval $40 \leq \tau \leq 200$ ms. The modified diffusion model was used to account for motion blur due to averaging the true position of a molecule over the time of a single acquisition frame [171].

$$\text{MSD} = (8/3)D_{app}\tau + 4\sigma^2 \tag{3.1}$$

In this case, D_{app} is the apparent diffusion coefficient, τ is the time lag, and σ describes the localization precision. Only fits with $R^2 \geq 0.7$ were kept. The log distribution histograms of the D_{app} were each fit to a two-state Gaussian mixture to determine the D_{app} and the associated weight fraction for the slow and fast diffusion modes (Fig. 3.13, Table 3.2).

3.4.19 Measuring single-cell protein concentrations

To determine the average number of photons detected from a single mCherry molecule per imaging frame, cells expressing the indicated mCherry fusion proteins were grown in 3 ml of AB medium supplemented with 0.2% glucose to OD 0.3 and washed once in 1 ml of M9 minimal medium prior to imaging. Cells were pre-bleached with a 561-nm laser until only a few isolated molecules were observed. Images were then recorded at 40 ms exposure with a 561 nm laser (110.5 W/cm^2) and an input EM gain of 600 (NIS-Elements software setting). Single molecules were detected as described earlier. The number of photons detected per single molecule per imaging frame was obtained by calculating the integrated intensity counts of the 2D Gaussian fit from the localization step48, which was then converted into the number of photons using the following camera calibrations.

The conversion gain (number of photoelectrons per fluorescence intensity count) calibration was performed as described in a Teledyne Photometrics Technical Note [228]. Briefly, multiple images of a white business card were acquired for 10-, 20-, 40-, 80-, 160-, and 320 ms exposure times with no electron multiplication (EM) gain. To account for the camera bias, 100 frames were acquired with nominally 0 ms exposure and a shuttered camera path. The average of these 100 frames was subtracted from every subsequently analyzed image. A plot of the mean signal of the image for each exposure time versus the variance of the same image gives a straight line with a slope that equals the conversion

gain (Fig. 3.6a). Pixel-to-pixel nonuniformity effects were removed by recording two images at each exposure time [229]. The conversion gain of our camera was found to be 1.40 electrons per intensity count.

To determine the EM gain (the number of electrons per photoelectron), two images were recorded: one long-exposure image (1 s) with no EM gain and one short-exposure image (10 ms) with an arbitrary EM gain. The bias was subtracted from both images. The EM gain multiplication factor is the factor difference in signal per time unit between the corrected images. We repeated this procedure for various software setting EM gains and found a linear fit in the range of 5–600 input EM gain with a conversion factor of 0.15 between nominal EM gain and output EM gain (Fig. 3.6b).

To calculate the number of photons from the fluorescence image, we therefore multiplied the intensity counts recorded by the conversion gain of 1.40 and divided this quantity by the input EM gain multiplied by the EM gain conversion factor of 0.15. The distribution of photons per molecule per imaging frame was fit to a Gamma distribution resulting in a peak of approximately 90 photons per molecule per imaging frame (Fig. 3.6c).

To determine the apparent cellular concentration of mCherry-McdB and mCherry-PopTag^{LL} when foci are present, cells expressing these proteins were grown and prepared as described above. The mCherry-McdB strain was induced with 1 mM IPTG for 2 h prior to imaging and the mCherry-PopTag^{LL} was induced with 100 μM IPTG for 2 h prior to imaging. Cells were imaged with a 561 nm laser (110.5 W/cm^2) at 20 ms exposure and 10x (NIS-Elements software setting) EM gain. To minimize the effect of photobleaching on the photon counting measurement, image acquisition was started prior to laser illumination.

The brightest five frames in the movie were averaged to determine the cell brightness before photobleaching. The integrated total fluorescence emission within a cell is linearly related to the total quantity of McdB or PopTag^{LL} molecules per cell: this intensity value was divided by the number of photons per mCherry molecule per imaging frame to obtain the McdB or PopTag^{LL} copy number per cell. To determine the cellular concentration of the

proteins, the volume of the cell was estimated by modeling it as a cylinder with spherical caps [230].

3.4.20 Image analysis

Cell segmentation was performed with the Cellpose [231] and Omnipose [232] packages in Python. To train the Cellpose model optimally for bacterial cell morphology, 26 raw phase contrast images of cells were manually annotated. To segment the cells using the trained model, a Gaussian blur (standard deviation of Gaussian = 0.066 μm) was applied to the bacterial cell phase-contrast images, and the blurred cells were segmented. Cells touching the borders of the image were ignored. Erroneous segmentations were manually corrected using the Cellpose GUI or excluded from further analysis.

To calculate the condensation coefficient of a cell, the fluorescence intensity in each pixel in a cell was corrected for background by subtracting the median value of all pixels in an image outside of the cell regions and normalized by the minimum and maximum pixel intensity values in the corresponding cell (Equation 2.2)

$$I_{\mathrm{n}} = (I - I_{\mathrm{min}})/(I_{\mathrm{max}} - I_{\mathrm{min}}) \tag{3.2}$$

These normalized pixel intensities were then binned to generate histograms that represent the localization pattern for each protein [60, 211, 233] (Fig. 3.4a–f).

Next, cells were classified by the presence or lack of a focus. An ROI was defined for each cell using the segmentation phase mask. Each ROI was applied a Gaussian blur (SD = 0.066 μm) and normalized using (Equation 2.2). Next, foci were detected by generating a binary image where only pixels above a specified intensity threshold were assigned a non-zero value. The putative foci were then filtered by intensity, area, and eccentricity (see Table 3.6 for parameters used). Homogeneously distributed protein mCherry or cells without a detected focus display a flat distribution whereas the strongly clustered protein $\mathrm{cI}^{\mathrm{agg}}$ displays a strongly left-skewed distribution (Fig. 3.8a–f). To quantify the differences

Table 3.6: Parameters used to detect fluorescent foci for classification.

Protein	*norm_thresh*	*eccent_thresh*
cI^{agg}	0.55	0.85
$PopTag^{SL}$	0.65	0.85
$PopTag^{LL}$	0.75	0.85
McdB	0.8	0.85
$McdB^{sol}$	0.75	0.85
mCherry	0.75	0.85

between the proteins measured, we calculated the fraction of pixels with a normalized intensity below a threshold value, $I < 0.3$, 0.5, and 0.7, for each cell (Fig. 3.8g). These values were then normalized to the condensation coefficient distribution of mCherry as our experimental representative of a homogenous distribution (Fig. 3.7b). Condensation coefficients calculated for cells in the A22 treatment (Fig. 3.2c-d), localized lysis (Fig. 3.2e-f), and temperature shift (Fig. 3.10k-l) experiments were not normalized to a homogenous mCherry-only sample.

Foci partition ratios were calculated from cells with a detected focus as the ratio of the average background-corrected pixel intensity within a focus to the average background-corrected pixel intensity of the cells excluding the focus region. For cells with two or more detected foci, the average intensity of all foci was used for the ratio. Fluorescent foci were tracked during the reversibility experiment for images acquired over the course of bacterial cell division events or during cell elongation with cephalexin treatment as described above. Because the increased cell density over the imaging period causes cells to move out of focus and prevents accurate quantification of the data, we stopped our analysis at 10 and 7.25 hrs, for the generational dilution and cephalexin treatment, respectively. We detected fluorescent foci by the Laplacian of Gaussian (LoG) method in TrackMate [234] using an estimated blob diameter of 600 nm and a quality threshold of 80 for cI^{agg}, $PopTag^{SL}$, $PopTag^{LL}$, and 225 for McdB. Spot detections were subsequently

linked to generate trajectories using the Simple Lap Track option with a maximum linking distance of three pixels (198 nm), a maximum gap-closing distance of 3 pixels (198 nm), and a maximum gap of 2 frames (30 min). The following trajectory filters were used: (i) only trajectories present in the first frame were tracked in subsequent frames, (ii) trajectories of foci in cells that move out of the field of view during the movie were excluded, (iii) false positive detections in the first frame were removed, and (iv) trajectories of foci in cells that did not grow (cephalexin treatment) or divide (generational dilution) were excluded. Erroneous trajectories were removed from further analysis. Cells that exhibited focus dissolution over the imaging period were then segmented at the frames adjacent to the dissolution event. We then measured the mean fluorescence intensity of the cell in both frames (Fig. 3.10c and f). Focus lifespans were calculated for foci that dissolved prior to the end of the imaging period. See Table 3.1 for statistical details.

For cells that reformed a fluorescent focus after cell division, we segmented the mother cell in the preceding frame and the two daughter cells. The total fluorescence intensity of each daughter cell was then normalized to that of the mother cell (Fig. 3.10h–j).

Images of dual-color labeled cells expressing msfGFP-IbpA and mCherry fusion proteins were analyzed by detecting fluorescent foci in the mCherry channel using an intensity-based threshold of 30% of the maximum intensity in the image. mCherry fusion protein spot detections were subsequently filtered based on a minimum area threshold of 4 pixels and an eccentricity threshold of 0.75. The centroid of these spots was used to define the center of a 23 × 23 pixel ROI. This ROI was then used to analyze the IbpA channel. First, an intensity profile was collected using the centroid of the ROI as the center point for both channels and subsequently normalized to the max intensity values in the mCherry channel. Next, the normalized ROIs for each channel were averaged to generate the projection images (Fig. 3.15c). The resulting intensity patterns for both channels were then fit with a 2D Gaussian to measure the full width at half max (FWHM) of the intensity. Finally, we calculated the ratio of $\mathrm{FWHM}^{\mathrm{IbpA}}/\mathrm{FWHM}^{\mathrm{mCherry}}$.

CHAPTER IV

The McdA Kinetics and Mobility Drive Carboxysome Distribution in *Halothiobacillus neapolitanus*[1]

4.1 Introduction

Efficient cellular metabolism is achieved by compartmentalizing enzymatic reactions. Prokaryotes achieve this process by using bacterial microcompartments (BMCs), ubiquitous organelles that encapsulate metabolic pathways within a protein-based shell [14, 17, 20]. The most extensively studied BMC is the carboxysome, which selectively concentrates the enzyme ribulose-1,5-biphosphate carboxylase/oxygenase (RuBisCO) with CO_2 to efficiently catalyze carbon fixation in many autotrophic bacteria [21,27]. Carboxysomes exist as either α and β types, differing in structural composition, assembly, and regulation [27, 29, 30, 235]. Both types are found in cyanobacteria, while α-carboxysomes are also widespread across other bacterial phyla and more closely resemble other types of BMCs [17,29]. Therefore, understanding α-carboxysome regulation is crucial for compre-

[1]The work presented in this chapter is in preparation as a manuscript by Azaldegui, C.A., Swasthi, H.M, Pulianmackal, L.T., Rivett, H.R., Vecchiarelli, A.G., and Biteen, J.S.
C.A.A. designed, performed and analyzed experiments (live-cell ensemble and single-molecule imaging), produced cell strains, interpreted results, and wrote the manuscript. H.M.S designed, performed and analyzed experiments (protein purification, ATPase assays, EMSA, fluorescence polarization). L.T.P produced cell strains. H.R. performed and analyzed experiments (single-molecule imaging). A.G.V. provided expertise in the design biochemical experiments, interpreted results and wrote the manuscript. J.S.B. provided expertise in the design of live-cell imaging experiments, designed experiments, interpreted results and wrote the manuscript.

hending broader BMC biology.

An important aspect of carboxysome regulation is their spatial organization within the cell. In *Synechococcus elongatus* PCC 7942, β-carboxysomes are positioned along the nucleoid by the Maintenance of Carboxysome Distribution (Mcd) system, consisting of McdA and McdB [126, 127, 132]. McdA is a DNA-binding deviant Walker-like ATPase similar to the ParA/MinD ATPase family that bacteria employ to organize genetic- and protein- based cellular complexes [80, 84, 85]. McdB is an adaptor protein that localizes to carboxysomes and connects them with McdA [65, 127, 236]. The interaction between McdA and McdB creates McdA gradients on the nucleoid, positioning carboxysomes and ensuring their even inheritance after cell division [126–128].

Recently, we identified an α-McdAB system in *Halothiobacillus neapolitanus*, which positions α-carboxysomes and is widely encoded in α-carboxysome-containing proteobacteria [131]. Unlike β-McdA, α-McdA preserves the full deviant Walker A box and is predicted to be structurally homologous with typical ParA ATPases [81, 131]. α-McdAB-like sequences within and near operons of other types of BMCs suggest that *H. neapolitanus* α-McdAB can be used as a model for BMC spatial regulation in general [131]. While the functions of *H. neapolitanus* α-McdAB are known, the biochemical properties of α-McdA and its positioning mechanism remain elusive.

Carboxysomes have been proposed to be positioned through a similar mechanism to that used by ParAB, which partition plasmids and chromosomes: ParA binds DNA non-specifically in its ATP-bound dimer state, and ParB binds to a specific DNA sequence (*parS*) to form a nucleoprotein complex. ParB stimulates the ATPase activity of ParA, displacing it from the nucleoid and creating gradients that stably position evenly spaced cargo within cells (e.g., one copy at mid-cell, two copies at quarter positions). This positioning pattern is referred to as regular positioning [114, 115].

Several Brownian-ratchet models have been proposed to explain ParA-mediated cargo positioning [104, 109, 110, 112, 120, 122–124]. In all models, ParA gradients on the nucleoid

drive cargo movement but differ in their proposals of gradient formation and how it results in cargo motion [118]. The most prevalent model is the mechanochemical Brownian-Ratchet model, which argues that a chemophoretic force drives persistent cargo motion through ParA-ParB bonds [109, 110, 120, 122]. In this model, the DNA-ParA-ParB dissociation kinetics and ParA diffusion on the nucleoid drive the gradient formation that guides cargo movement. Another possibility is the DNA-Relay model, which proposes that the elasticity of the chromosome drives cargo movement [104, 112]. Similar time-averaged cargo positions emerge from DNA-relay, however, the cargo oscillate around this 'home' position instead of being stably positioned there. An extension of this model, called the Hopping and Relay model, added the Brownian-ratchet's nucleoid-bound diffusion by ParA to capture all cargo positioning behaviors (regular positioning, approximate positioning, and oscillations) [124]. In contrast to the copy number of genetic cargo which range from 1 to sometimes 4 copies, the carboxysome copy number usually ranges from 4 up to 16 [133], thus carboxysomes are a unique cargo among ParA-mediated positioning systems. Whether the models decribed can explain carboxysome and BMC positioning in general remains unclear.

Here, we combined biochemical assays, quantitative fluorescence microscopy, and *in vivo* single-molecule imaging to advance our understanding of α-McdAB-mediated carboxysome distribution in *H. neapolitanus*. We found that α-carboxysomes are dynamic and evenly distributed by McdA gradients on the nucleoid. Additionally, we discovered that the α-McdA ATPase activity is stimulated by DNA rather than its partner protein, α-McdB, making it unique among ParA/MinD ATPases. On the other hand, α-McdB does promote α-McdA release from DNA, suggesting that ATP-hydrolysis and DNA release are not strictly coupled. Finally, we found that nucleoid-bound α-McdA dimers can diffuse. Our results are consistent with Brownian-ratchet models for ParA-mediated cargo positioning, extending these models to a protein-based cargo, and suggest that the biochemical properties of ParA ATPases are tailored to the positioning needs of their cargo. These find-

ings have broader implications for the spatial regulation of protein-based organelles that are positioned by ParA-like ATPases.

4.2 Results

4.2.1 Carboxysomes are evenly distributed in *H. neapolitanus*

To quantify the α-carboxysome (carboxysome hereafter) distribution in *H. neapolitanus*, we imaged fluorescently labeled carboxysomes (CbbS-mTurquoise2) (Figure 4.1a). We calculated carboxysome density as the number of carboxysome foci per cell length (Figure 4.1b). We measured 2.7 ± 0.6 foci/μm length of the cell (mean ± standard deviation, SD, N = 1061 cells) (Figure 4.1b). In contrast, Δ*mcdA* cells had reduced carboxysome density of 0.8 ± 0.2 foci/μm (N = 1106 cells) (Figure 4.1b), indicating aggregation of carboxysomes at the cell poles (Figure 4.1a). We also quantified carboxysome distribution by measuring the spacing between carboxysome foci and their nearest neighbor focus (Figure 4.2). In WT cells, carboxysome foci were on average 0.31 ± 0.14 μm apart (N = 3477 foci), while in Δ*mcdA* cells with more than one focus, these were spaced by 1.15 ± 0.4 μm (N = 500 foci), which represents nucleoid excluded foci. Notably, carboxysome foci appeared staggered in WT cells ((Figure 4.1a); white arrows); a feature also observed in *S. elongatus* cells with higher carboxysome numbers [127], which may be due to the McdAB system maximizing inter-carboxysome spacing.

4.2.2 Carboxysomes are dynamic on the nucleoid

Next, we investigated whether carboxysome mobility is consistent with any positioning type. Using time-lapse fluorescence microscopy at 1-second intervals, we tracked carboxysome motion inside live *H. neapolitanus* cells (Figure 4.1c) (see Methods). In Δ*mcdA* cells, carboxysomes form static aggregates at cell poles, serving as an immobile control (Figure 4.1c). We fit the mean squared displacement (MSD) of each track across various

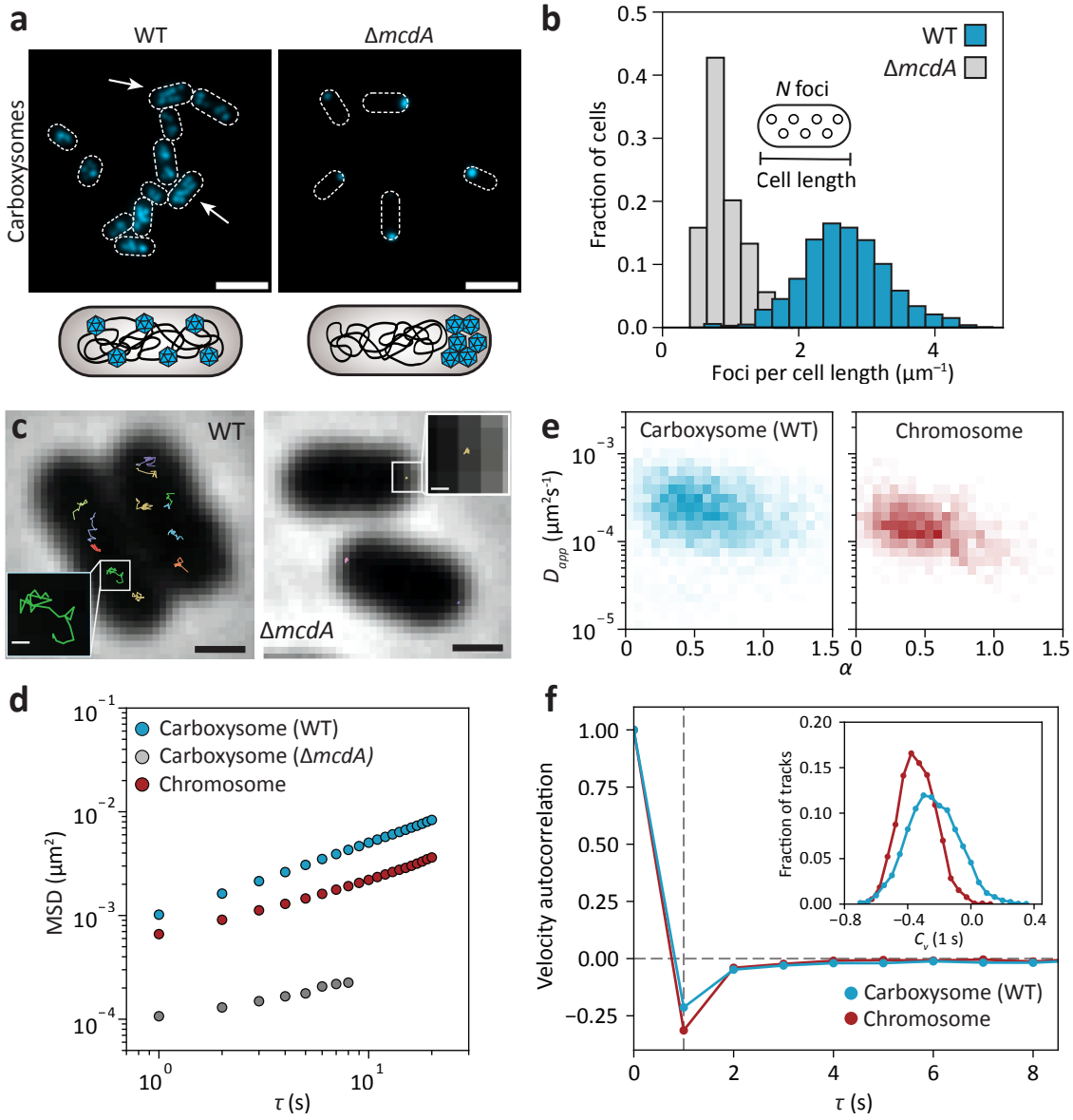

a
WT
ΔmcdA
Carboxysomes
b
WT
ΔmcdA
N foci
Cell length
Fraction of cells
Foci per cell length (μm⁻¹)
c
WT
ΔmcdA
d
Carboxysome (WT)
Carboxysome (ΔmcdA)
Chromosome
MSD (μm²)
τ (s)
e
Carboxysome (WT)
Chromosome
D_app (μm²s⁻¹)
α
f
Velocity autocorrelation
Fraction of tracks
C_v (1 s)
Carboxysome (WT)
Chromosome
τ (s)

Figure 4.1

Figure 4.1: Carboxysomes in *H. neapolitanus* are distributed and their motion is consistent with regular positioning. a. Representative fluorescence images of wildtype (WT, left) and Δ*mcdA* (right) *H. neapolitanus* cells (white dashed outlines) expressing the carboxysome marker, CbbS-mTurquoise2 (cyan). White arrows: cells with hexagonally packed carboxysomes. Scale bars: 2 μm. **b**. Distributions of cellular carboxysome focus density in WT (N = 1061 cells) and Δ*mcdA* (N = 1106 cells) from two independent datasets. **c**. Representative trajectories of single carboxysome particles in WT (top) and ΔmcdA (bottom) cells. Scale bars: 500 nm. Insets: Zoom-in of carboxysome trajectory. Scale bars: 50 nm. **d**. Population average mean squared displacement (MSD) curves for carboxysome trajectories in WT (N = 3630 trajectories) and Δ*mcdA* (N = 1896 trajectories) cells and ParB-mNG foci (N = 1284 trajectories), from at least two independent datasets per sample. **e**. 2D histograms of the D_{app} and α exponent for the trajectories of carboxysomes in WT cells (N = 3680 trajectories) and ParB-mNG foci (N = 1304 trajectories). **f**. Average velocity autocorrelation function of carboxysome trajectories (N = 3680 trajectories) from WT cells and ParB-mNG foci (N = 1579 trajectories) as a function of lag time, τ. The vertical dashed line at τ = 1 s demarcates the sampling time of the experiment. Inset shows the distribution of velocity autocorrelation values (C_v) at 1 s.

time lags (τ) to the diffusion model MSD = $4D_{app}\tau^{\alpha}$, where D_{app} is the apparent diffusion coefficient of the particle, and α is the anomalous diffusion exponent. For WT cells, D_{app} was $(2.4 \pm 0.05) \times 10^{-4}$ μm^{2}s^{-1}, an order of magnitude higher than the immobile carboxysome foci in Δ*mcdA* cells (Figures 4.1d and 4.3). Notably, a subpopulation of carboxysomes in Δ*mcdA* cells had faster diffusion with D_{app}, $(0.23 \pm 0.02) \times 10^{-4}$ μm^{2}s^{-1}, which we interpret as individual carboxysomes diffusing at the cell pole.

Furthermore, carboxysomes generally have $\alpha < 1$ (Figure 4.1e), indicating subdiffusive motion. We hypothesized that this behavior represents carboxysomes tethered to DNA via McdA-McdB interactions [127, 131]. To test if α correlates with the elastic behavior of chromosomes [112, 175, 237]), we tracked the chromosomal partition complex by imaging ParB-mNeonGreen (ParB-mNG) in *H. neapolitanus* under the same conditions. ParB-mNG foci also showed subdiffusive behavior (Figure 4.1e), but with a tighter α distribution centered approximately at 0.4, consistent with chromosomal locus behavior in *Escherichia coli* and *Vibrio cholerae* [175, 237]. A small subset of the ParB-mNG foci had a larger α, which may represent freer chromosomal movements [238] or segregating chromosomes as many of the cells imaged had two ParB-mNG foci. Both ParB-mNG foci and carboxysomes have

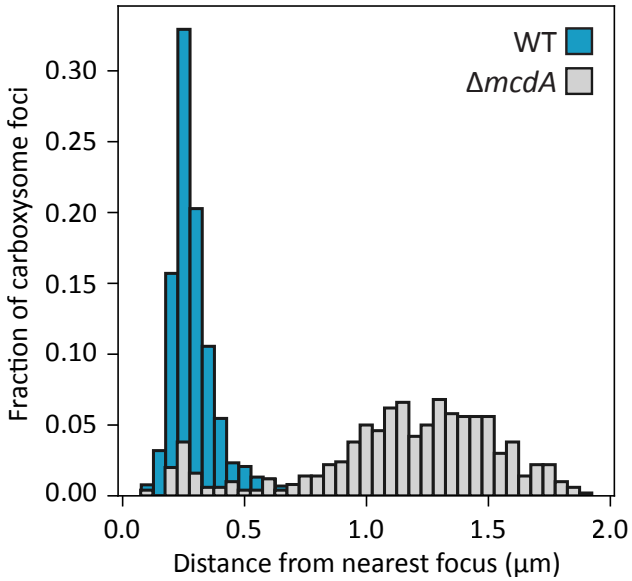
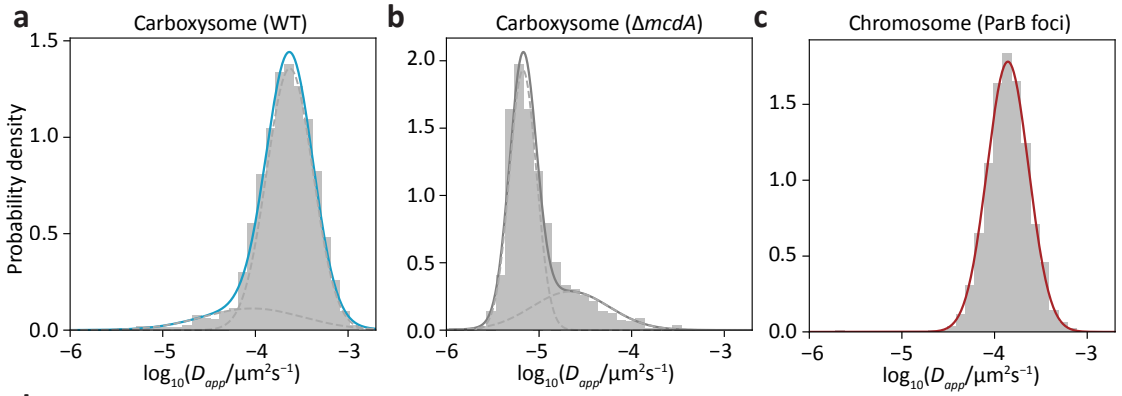


Figure 4.2: Distribution of distances between adjacent carboxysome foci. Histogram of the distance between a carboxysome focus and its nearest neighbor in WT (N = 3477 foci) and Δ*mcdA* (N = 500 foci) cells.



d

	D_{app} (μm²s⁻¹)	Fraction	D_{app} (μm²s⁻¹)	Fraction
Carboxysome (WT)	(1.04 ± 0.14) × 10⁻⁴	17 ± 5%	(2.40 ± 0.05) × 10⁻⁴	83 ± 5%
Carboxysome (Δ*mcdA*)	(0.07 ± 0.01) × 10⁻⁴	73 ± 2%	(0.23 ± 0.02) × 10⁻⁴	27 ± 2%
Chromosome (ParB foci)	(1.4 ± 0.02) × 10⁻⁴	100%		

Figure 4.3: Analysis of carboxysome and ParB foci diffusion. Probability density distributions of apparent diffusion coefficients, D_{app}, for carboxysome foci in (**a**) WT (N = 2746 trajectories), (**b**) Δ*mcdA* cells (N = 1896 trajectories), and (**c**) ParB-mNG foci (N = 1314 trajectories) based on tracks collected from 1-s timelapse imaging. Also shown in each plot is the D_{app} fit by a one or two-state Gaussian Mixture Model (GMM) (solid line). Dashed lines represent the fits of the individual states. **d**. Values for D_{app} and population fraction % are the mean ± SD from 100 bootstrapped samples.

a negative velocity autocorrelation at a 1-second timescale (Figure 4.1f), representative of the viscoelastic cytoplasm [239]. The absence of oscillatory behavior or random diffusion of carboxysomes and the ParB partition complex suggests elastic behavior of both cargo, consistent with other reports of ParA-mediated positioning [114, 124]. However, ParB-mNG foci have a stronger negative autocorrelation (Figure 4.1f), likely due to greater elastic effects from the chromosome.

Together, our results show that carboxysome are dynamic and their motion correlates with the chromosome demonstrating that they are positioned on the nucleoid. The faster mobility of carboxysomes (Figure 4.1d-f) relative to the chromosome suggests additional factors are at play. For instance, β-carboxysomes in *S. elongatus* are confined in motion but move towards regions of increased McdA concentrations on the nucleoid [126, 127, 240] suggestive of a chemophoretic force by a McdA gradient on the nucleoid [109, 110, 116, 120]. Other possibilities include intrinsic carboxysome diffusion if untethered from the nucleoid and DNA-based cargo relaying [104, 112].

4.2.3 Construction and characterization of functional McdA fluorescent fusions

To investigate the driving factor for carboxysome dynamics, we sought to visualize α-McdA (McdA hereafter) *in vivo*. We constructed a PAmCherry-McdA (PAmC-McdA) fusion with a GSGSGS linker, replacing the native *mcdA* gene. Carboxysome localization served as the phenotypic indicator of McdA function (Figures 4.1a and 4.4a-b). Unlike the *S. elongatus* homolog [127], this N-terminal fusion caused carboxysomes to form a single focus that was randomly positioned along the cell length, suggesting that PAmC-McdA can load carboxysomes onto the nucleoid but not distribute them (Figure 4.4c). We also generated a C-terminal McdA-PAmC fusion, commonly used in functional ParA fluorescent fusions [112, 129, 241], which caused the carboxysomes to aggregate at the cell poles (Figure 4.4d).

In some cases, fluorescent proteins have been fused internally to target bacterial pro-

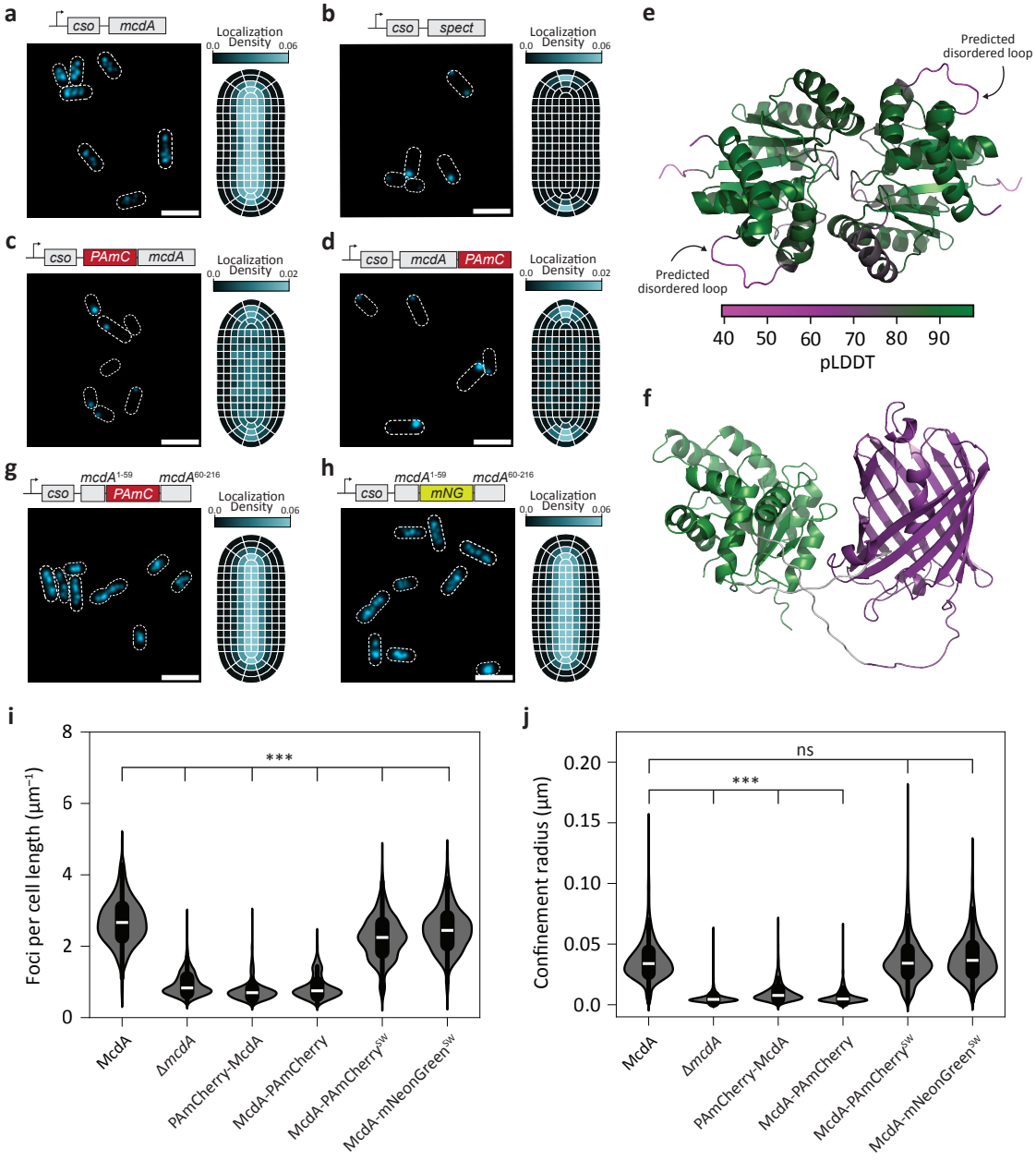

a
cso
mcdA
Localization Density
0.0
0.06
b
cso
spect
c
cso
PAmC
mcdA
0.02
d
cso
mcdA
PAmC
e
Predicted disordered loop
Predicted disordered loop
40 50 60 70 80 90
pLDDT
f
g
mcdA1-59
mcdA60-216
cso
PAmC
h
mNG
i
Foci per cell length (µm⁻¹)
***
McdA
ΔmcdA
PAmCherry-McdA
McdA-PAmCherry
McdA-PAmCherrySW
McdA-mNeonGreenSW
j
Confinement radius (µm)
ns
***

Figure 4.4

Figure 4.4: Analysis of functional fluorescent fusions of McdA. a-d. Representative images of carboxysome localizations in (**a**) WT, (**b**) Δ*mcdA*, (**c**) PAmCherry-McdA, and (**d**) McdA-PAmCherry cells. The carboxysome signal (cyan) is from CbbS-mTQ. Dashed white outlines demarcate the cell outlines. Scale bars: 2 μm. Gene constructs (top) within the carboxysome (*cso*) operon. (Right) Carboxysome localization density heatmaps for each strain. (**a**) N = 1061 cells, (**b**) N = 1106 cells, (**c**) N = 632 cells, (**d**) N = 494 cells. **e**. McdA homodimer structure generated with AlphaFold2 (AF2). Color scale indicates the predicted Local Distance Difference Test (pLDDT). **f**. AlphaFold2-generated structure of McdA monomer (green) fused to PAmCherry (violet) in the sandwich orientation. **g-h**. Representative cellular carboxysome localization for (**g**) McdA-PAmCherry^{SW} and (**h**) McdA-mNeonGreen^{SW} fusions. Content as in (**a-d**). (**g**) N = 987 cells, (**h**) N = 1052 cells. Scale bars: 2 μm. **i**. Number of carboxysome foci per unit of cell length for each strain. McdA N = 1061 cells, Δ*mcdA* N = 1106 cells, PAmCherry-McdA N = 871 cells, McdA-PAmCherry N = 683 cells, McdA-PAmCherry^{SW} N = 1623 cells, McdA-mNeonGreen^{SW} N = 1052 cells. **j**. Confinement radius for carboxysome trajectories in each strain. McdA N = 3680 foci, Δ*mcdA* N = 1896 foci, PAmCherry-McdA N = 950 foci, McdA-PAmCherry N = 1217 foci, McdA-PAmCherry^{SW} N = 2355 foci, McdA-mNeonGreen^{SW} N = 2781 foci. White line is the median and the black core is the interquartile range. *** denotes p-value < 0.001 by Kruskal-Wallis' test. ns denotes $p > 0.05$: McdA-PAmCherry^{SW} $p = 0.54$, McdA-mNeonGreen^{SW} $p = 0.23$. Statistical tests were done on the mean of means from 10 bootstraps randomly sampling 100 data points.

teins without perturbing function [242–245]. We examined the predicted AlphaFold2 (AF2) structure of McdA [81] and identified a disordered region with low prediction confidence between residues 55 and 64 (Figure 4.4e). Only residue Q62 within this loop is predicted to be functionally significant, and the loop is not conserved among other ParA/MinD models, suggesting it is not critical for ParA/MinD function. We inserted PAmCherry and mNeonGreen between McdA residues 59 and 60, flanking them with GSGSGS linkers to create the sandwich (SW) fusions *mcdA-PAmC^{SW}* and *mcdA-mNG^{SW}* (Figure 4.4f). Complementation of these fusions in Δ*mcdA* cells restored carboxysome distribution (Figure 4.4g-h), but with a slightly reduced carboxysome density. Indeed, cells with McdA-PAmC^{SW} and McdA-mNG^{SW} had 2.2 ± 0.6 and 2.4 ± 0.6 carboxysome foci per micron cell length, respectively, compared to 2.7 ± 0.6 foci/μm in unlabeled McdA cells (Figures 4.1b and 4.4i). Carboxysome also had comparable mobility across all functional strains, further supporting the functionality of the McdA sandwich fusions (Figure 4.4j).

4.2.4 McdA forms gradients on the nucleoid

We studied the spatial distribution and dynamics of McdA by time-lapse fluorescence imaging. Imaging McdA-mNG^{SW} on a time scale similar to that of carboxysomes did not show pole-to-pole oscillations as in *S. elongatus* (Figure 4.5a-b). Instead, the McdA-mNG^{SW} proteins form high-density regions on the nucleoid, resulting in short-scale gradients along the cell length (Figures 4.5a-b and 4.6a). This behavior is similar to that of *E. coli* F plasmid ParA [123, 125, 246]. We determined that these high-density regions were due to the binding of McdA to DNA by imaging McdA[K20A]-mNG^{SW}, which contains a mutation that inhibits DNA binding in other ParA-like proteins by inhibiting ATP binding [92]. This mutant was homogeneously distributed, consistent with cytoplasmic localization and lack of DNA binding (Figures 4.5a-b and 4.6b).

Although binding of DNA by McdA enables the formation of these gradients, depletion of McdA on the nucleoid by McdA-McdB interactions [127, 247] and stimulation of ATP hydrolysis may also influence the distribution of McdA, as is the case for a majority of ParA/MinD partner proteins [80]. We imaged McdA-mNG^{SW} in Δ*mcdB* cells and observed dynamics similar to WT cells (Figures 4.5a-b and 4.6c). This result indicates that McdA can form gradients on the nucleoid independent of its association with McdB, suggesting differences in the biochemical properties of McdA relative to typical ParA ATPases.

4.2.5 McdA binding to DNA is ATP- and dimerization-dependent

Building on the *in vivo* observations of McdA, we next investigated the biochemical properties of McdA *in vitro*. We purified recombinant *H. neapolitanus* McdA and McdB from the soluble fraction of *E. coli* lysates. We fused a SUMO tag [248] to the N-terminus of McdA (*his-SUMO-mcdA*), which significantly increased its solubility (Figure 4.7). Without ATP, His-SUMO-McdA elutes as a single species in size-exclusion chromatography (Figure 4.8a), consistent with a McdA monomer. With ATP, the peak of the His-SUMO-McdA elution shifted and broadened (Figure 4.8a), indicating the presence of multiple species;

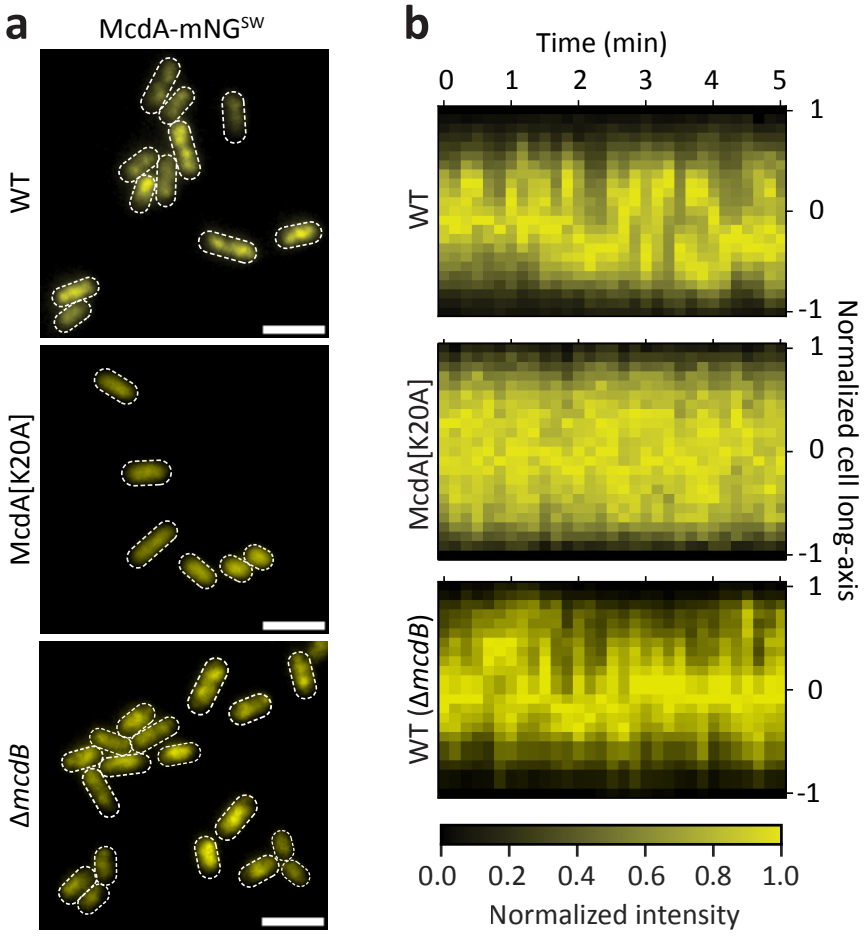


Figure 4.5: McdA forms gradients on the nucleoid. a. Representative images of McdA-mNG^{SW} in WT and Δ*mcdB* cells, respectively, and McdA[K20A]-mNG^{SW}. Dashed white lines are the cell outlines. Scale bars: 2 μm. **b**. Representative normalized kymographs across the long-axis of WT and Δ*mcdB* cells expressing McdA-mNG^{SW}, and McdA[K20A]-mNG^{SW} in WT cells.

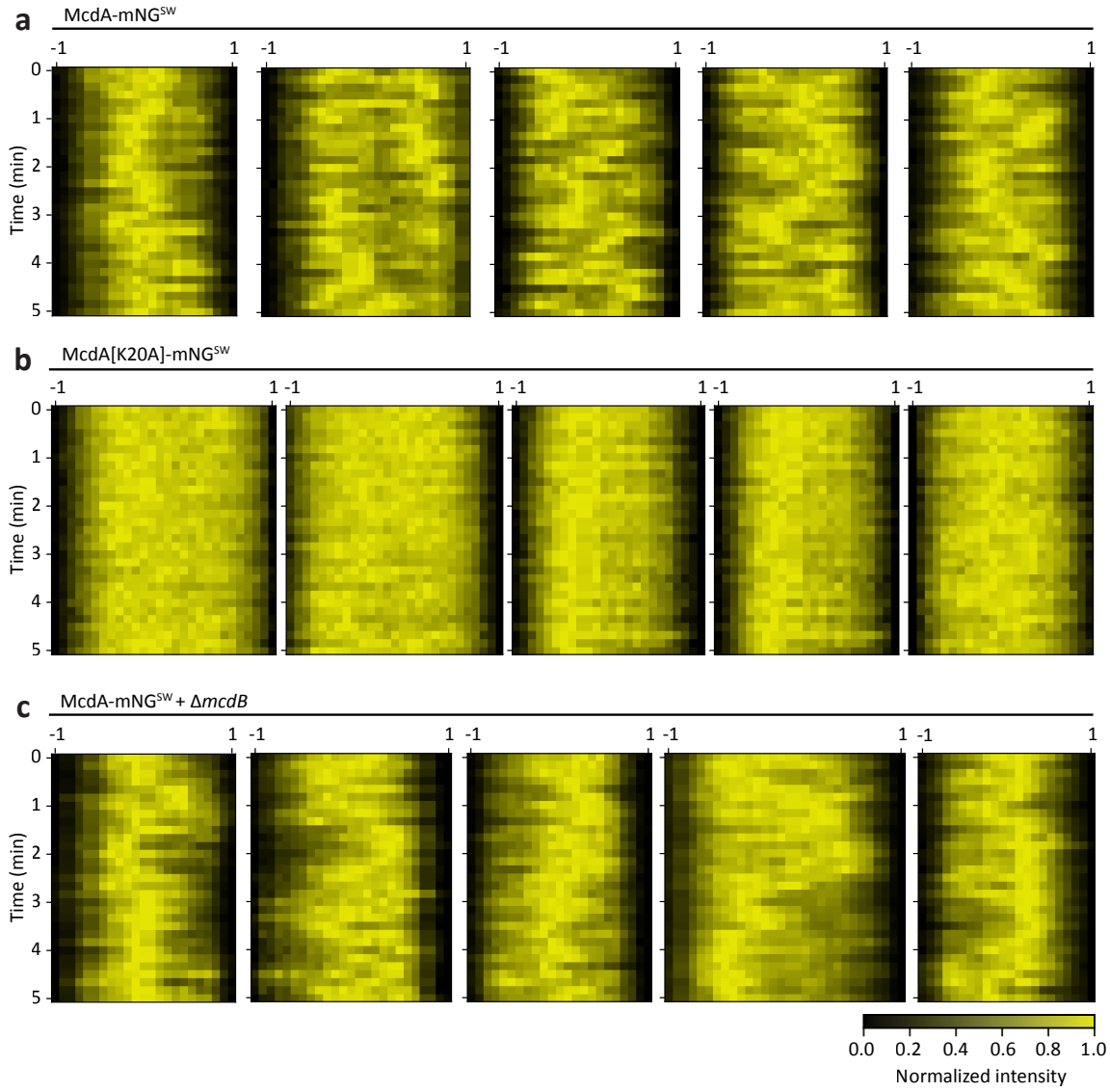


Figure 4.6: Examination of bulk McdA localization. Kymographs for a McdA-mNG^{SW} in (**a**) WT cells, (**b**) McdA[K20A]-mNG^{SW} in WT cells, and (**c**) McdA-mNG^{SW} in Δ*mcdB* cells. Time-lapse frames were collected every 10 seconds for 5 minutes. Profiles are normalized to the maximum and minimum intensities within the corresponding timepoint.

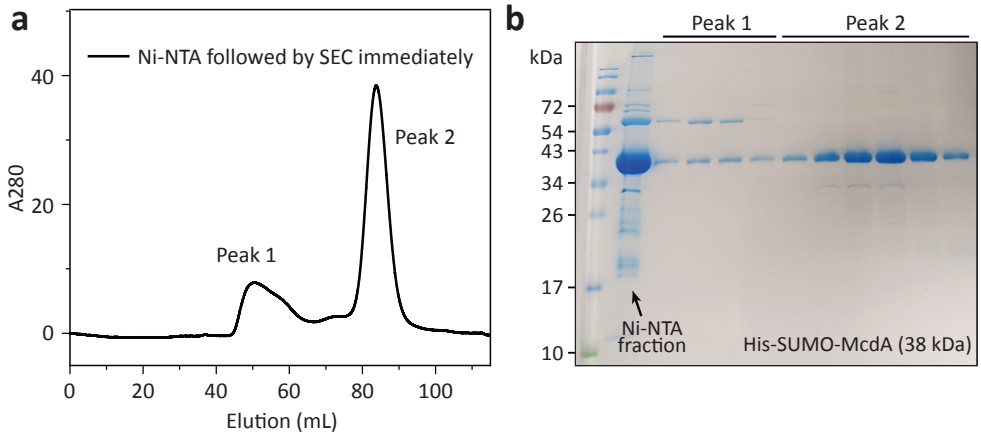


Figure 4.7: Purification of *H. neapolitanus* His-SUMO-McdA. a. Chromatogram of size exclusion column of His-SUMO-McdA. Peaks represent the eluting populations. **b**. SDS-PAGE of elution fractions collected from (**a**) Peak 2 depicts a pure band at 38 kDa consistent with His-SUMO-McdA.

likely the monomer and the ATP-dependent dimer form. The His-SUMO-α-McdA[K20A] mutant eluted as a single narrow peak with and without ATP, matching the WT peak in the absence of ATP (Figure 4.8a). These results show that McdA can dimerize upon ATP binding *in vitro*.

Next, we probed the DNA-binding activity of McdA by an Electrophoretic mobility shift assay (EMSA). Adding His-SUMO-McdA to nonspecific DNA (nsDNA) in the presence of ATP, but not ADP, caused a change in EMSA that correlates with the concentration of His-SUMO-McdA, demonstrating ATP-dependent DNA binding (Figure 4.8b). His-SUMO-McdA [K20A] did not change DNA mobility (Figure 4.8b), indicating that the nonspecific DNA binding activity of McdA depends on ATP binding and subsequent dimerization.

4.2.6 McdA ATPase activity is triggered by DNA

S. elongatus β-McdA has strong ATPase activity, which we posed is due to its unique Walker A motif (SGGxxGKT) which differs from α-McdA and typical ParA ATPases (KGGxxGKT) [89, 127, 131]. This difference prompted us to test whether α-McdA acts as a robust ATPase like β-McdA [127] or a poor ATPase like typical ParA ATPases [96, 98, 112,

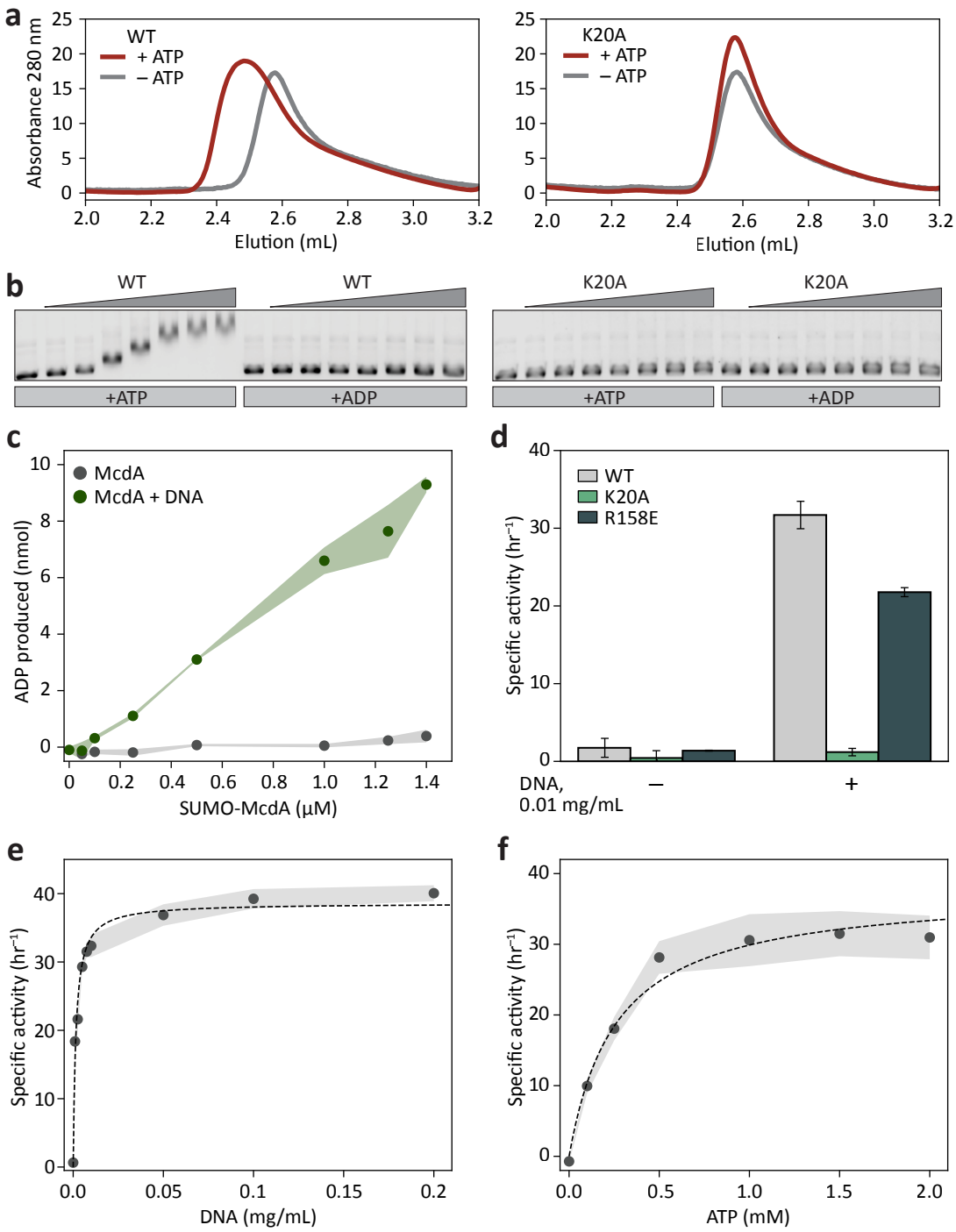

a
Absorbance 280 nm
WT
+ ATP
– ATP
Elution (mL)
K20A
+ ATP
– ATP
Elution (mL)
b
WT
WT
K20A
K20A
+ATP
+ADP
+ATP
+ADP
c
McdA
McdA + DNA
ADP produced (nmol)
SUMO-McdA (μM)
d
WT
K20A
R158E
Specific activity (hr⁻¹)
DNA, 0.01 mg/mL
–
+
e
Specific activity (hr⁻¹)
DNA (mg/mL)
f
Specific activity (hr⁻¹)
ATP (mM)

Figure 4.8

Figure 4.8: McdA binds DNA in a ATP-dependent dimer state and its ATPase activity is triggered by DNA. a. Gel filtration analysis of purified His-SUMO-McdA (left) and His-SUMO-McdA[K20A] (right) in the presence and absence of ATP. **b**. Electrophoretic mobility shift assay (EMSA) with increasing concentrations (0, 0.5, 1, 2.5, 5, 10, 12.5, 14 μM) of His-SUMO-McdA (left) and His-SUMO-McdA[K20A] (right). 1mM of ATP or ADP was used. **c**. ATPase activity of His-SUMO-McdA in the presence and absence of DNA (0.1 mg/mL). ATP was kept fixed at 1 mM. nmol of ADP produced in reaction after 2 hr. Shading represents the SEM of three independent experiments. **d**. Effect of DNA on ATPase activities of McdA, McdA[K20A], and McdA[R158E]. Error bars are the error on the linear regression of the mean ADP production rate (nmol hr^{-1}) vs. McdA (nmol) from three independent experiments. **e**. Specific activity of His-SUMO-McdA (concentration fixed at 1.0 μM) measured as a function of DNA concentration (0-0.2 mg/mL). Shading represents the SEM of three independent experiments. Michaelis-Menten equation fit to the data (black dashed line) gives K_{DNA} = 1.5 μg/mL and V_{max} = 38.6 h^{-1}. **f**. Specific activity of His-SUMO-McdA (concentration fixed at 1.0 μM) as a function of ATP (0-2 mM) with fixed DNA concentration (0.01 mg/mL). Michaelis-Menten equation fit to the data (black dashed line) gives K_M = 262 μM and V_{max} = 37.7 h^{-1}.

249]. Unlike S. elongatus β-McdA, His-SUMO-McdA has a low specific activity of 1.7 h^{-1} (Figure 4.8c-d). However, the addition of nsDNA significantly increased His-SUMO-McdA specific activity to 31.7 h^{-1} (Figure 4.8c-d), with maximum activity of k_{cat} = 38.6 h^{-1} and a half saturating DNA concentration K_{DNA} = 1.5 μg/mL (Figure 4.8e). The rate also depends on ATP concentration (K_M = 262 μM; Figure 4.8f). His-SUMO-McdA[K20A] had neglible ATPase activity in the presence and absence of DNA as it does not bind ATP (Figure 4.8d). The large fold-change in ATPase activity of McdA in the presence of DNA is unusual for ParA/MinD ATPases, which generally have less than two-fold enhancements [96, 98, 127, 249].

To test if direct DNA binding stimulates the ATPase activity of McdA, we mutated a residue near its C-terminus identified by AF2 modeling and thermodynamic calculations [81]. Mutation R158E forms an ATP-dependent dimer like WT McdA (Figure 4.9a), but with reduced DNA binding as it only shifted nsDNA at high protein concentrations (Figure 4.9b), highlighting the importance of this residue for DNA binding [100]. His-SUMO-McdA[R158E] also had enhanced ATPase activity in the presence of DNA, although with specific activity of 21.8 h^{-1}, which is lower than WT McdA (Figure 4.8d),

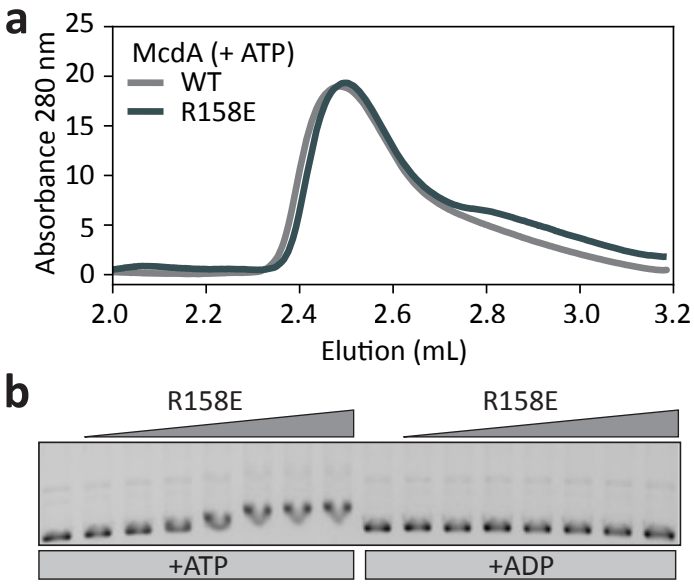


Figure 4.9: Biochemical analysis of McdA DNA binding mutant. a. Gel filtration analysis of purified His-SUMO-McdA and His-SUMO-McdA[R158E] in the presence of ATP. **b**. EMSA with increasing concentrations (0, 0.5, 1, 2.5, 5, 10, 12.5, 14 μM) of His-SUMO-McdA[R158E]. 1mM of ATP or ADP was used.

showing a direct correlation between DNA binding affinity and ATPase activity. Collectively, our data show that McdA non-specifically binds to DNA upon ATP binding and subsequent dimerization, consistent with putative models of the biochemical cycle of ParA ATPases [92, 98, 112, 129]. Additionally, the ATPase activity of α-McdA is stimulated by binding to DNA, suggesting that DNA binding may facilitate a conformational change in α-McdA that switches it to an ATP hydrolysis-competent form.

4.2.7 McdB stimulates the release of McdA from DNA without enhancing its ATPase activity *in vitro*

The activity of ParA ATPases is typically stimulated by their partner protein [96, 241, 249], therefore we tested whether the ATPase activity of McdA was further enhanced by its partner protein, McdB. Surprisingly, McdB lowered His-SUMO-McdA ATPase activity (Figure 4.10a). Because McdB is concentrated at the carboxysomes [127, 236], we tested whether high McdB concentrations (up to 40:1 molar ratios) are needed for stimulation,

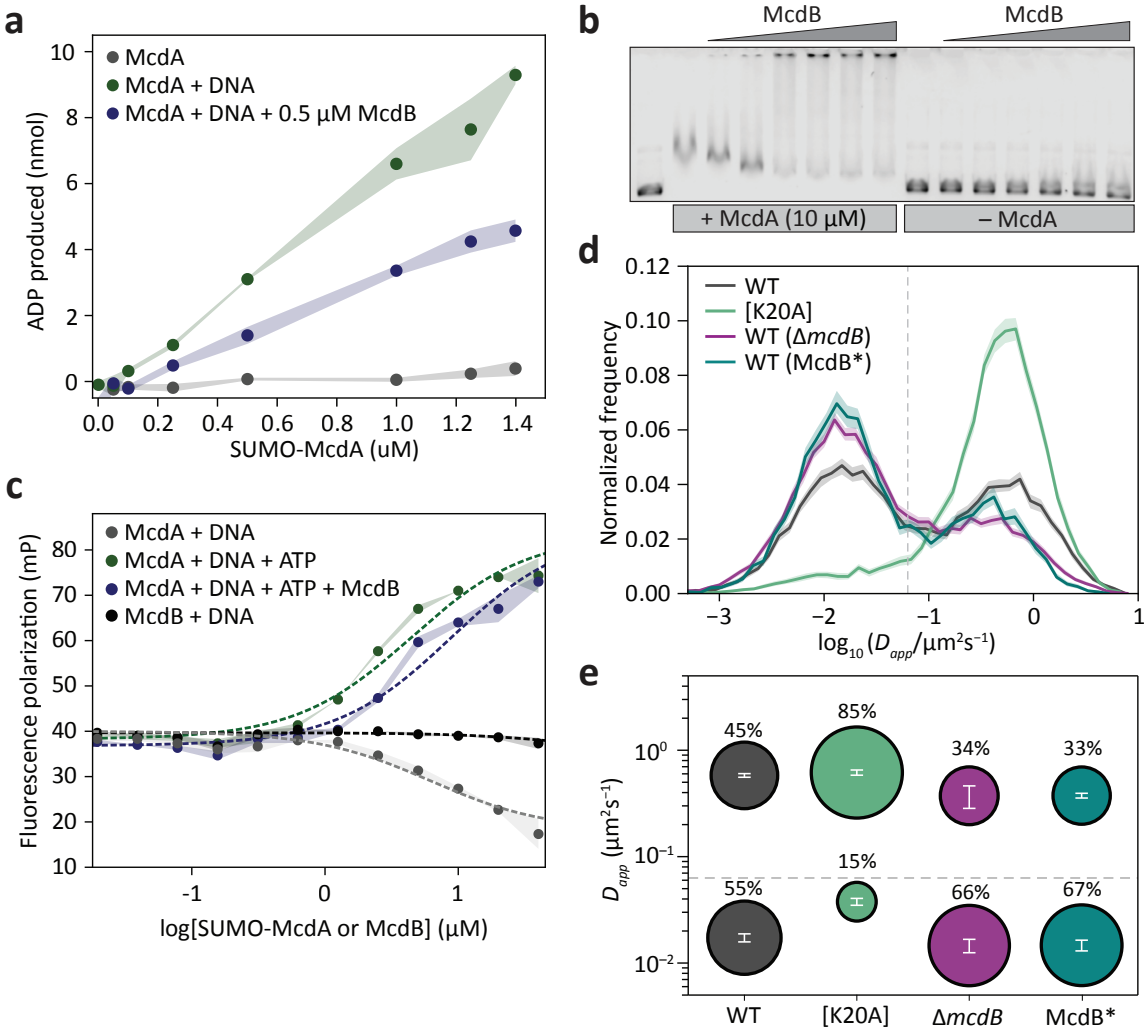

a
McdA
McdA + DNA
McdA + DNA + 0.5 µM McdB
ADP produced (nmol)
SUMO-McdA (uM)
b
McdB
McdB
+ McdA (10 µM)
– McdA
c
McdA + DNA
McdA + DNA + ATP
McdA + DNA + ATP + McdB
McdB + DNA
Fluorescence polarization (mP)
log[SUMO-McdA or McdB] (µM)
d
WT
[K20A]
WT (ΔmcdB)
WT (McdB*)
Normalized frequency
log10 (Dapp/µm²s⁻¹)
e
45%
85%
34%
33%
15%
55%
66%
67%
Dapp (µm²s⁻¹)
WT
[K20A]
ΔmcdB
McdB*

Figure 4.10

Figure 4.10: Carboxysome-localized McdB promotes release of McdA from DNA despite not stimulating its ATPase activity. a. ATPase activity of His-SUMO-McdA with DNA (0.1 mg/mL) and McdB (0.5 μM). His-SUMO-McdA with and witout DNA is the same as Figure 4.8c. ATP was kept fixed at 1 mM. nmol of ADP produced in reaction after 2 hr. Shading represents the SEM of three independent experiments. **b**. EMSA with increasing concentrations of McdB (0.5, 1, 2.5, 5, 10, 12.5 μM) in the presence and absence of McdA (10 μM). First lane is DNA only. Second lane is DNA + McdA (10 μM). 1 mM ATP was present in all lanes. **c**. Binding curves of His-SUMO-McdA with DNA in the presence and absence of McdB (1 μM) probed by fluorescence polarization assays. Dashed lines are fits to a hyperbolic binding model. Shading represents the SD of three independent experiments. **d**. Distributions of the apparent diffusion coefficients, D_{app}, of McdA-PAmCherry^{SW} in WT cells (11,115 tracks from 335 cells over 4 independent experiments), McdA[K20A]-PAmCherry^{SW} in WT cells (8176 tracks from 149 cells over 3 independent experiments), McdA-PAmCherry^{SW} in Δ*mcdB* cells (13,787 tracks from 531 cells over 5 independent experiments), and McdA-PAmCherry^{SW} in McdB[W94G] cells (6,138 tracks from 480 cells over 2 independent experiments). Only tracks with ≥ 5 localizations are included. Lines and shaded regions represent the mean ± 95% CI from 100 bootstraps. The dashed gray line is the theoretical lower bound for D_{app} based on localization uncertainty from a fixed sample (Figure 4.13). **e**. Bubble plot showing the apparent diffusion coefficients and associated population percentages for each of the two states fit to a Gaussian Mixture. Error bars are the standard deviations from independent experiments.

but found a McdB-dependent ATPase activity decrease (Figure 4.11).

Since DNA stimulates the ATPase activity of McdA, we tested whether McdB affected the binding of McdA to DNA. Using an EMSA with His-SUMO-McdA and McdB, we observed that at low McdB concentrations (< 4:1 McdA:McdB molar ratios), McdB released McdA from DNA (Figure 4.10b). At higher McdB concentrations (> 2:1 McdA:McdB molar ratios), we detected a higher-order nucleoprotein complex which we interpret as a DNA-McdA-McdB complex (Figure 4.10b). McdB did not associate with the DNA substrate in the absence of McdA (Figure 4.10b). To measure the kinetics of McdA binding to DNA in the presence of McdB, we monitored the fluorescence polarization of a Cy5-labeled double-stranded DNA oligo (Figure 4.10c). In the precense of ATP, McdA readily bound to DNA with a equilibrium dissociation constant (K_d) of 4.47 ± 0.01 μM. The addition of McdB increased the K_d to 8.83 ± 0.87 μM, indicating that McdB reduces the binding affinity of McdA to DNA. This effect may be due to McdB promoting McdA release from DNA or

inhibiting binding of McdA to DNA. In the either case, a decreased DNA binding affinity may explain the reduced ATPase activity of McdA as they are positively correlated (Figure 4.8).

We conclude that unlike typical ParA/MinD systems, McdB does not enhance the ATPase activity of McdA, but does interact with McdA to facilitate its release from DNA. This result contrasts typical ParA systems, wherein partner proteins greatly stimulate ParA ATPase activity, which is thought to be coupled to release from the nucleoid [96, 98, 112, 241, 249, 250]. Instead, McdA reaches similar ATPase activity upon DNA binding alone, and McdB facilitates McdA release without further stimulating its ATPase activity.

4.2.8 Carboxysome localized McdB releases McdA from the nucleoid

Considering the effect of McdB on McdA complex assembly and release from DNA *in vitro* (Figure 4.10b), we explored whether these activities were preserved *in vivo*. Although bulk imaging data (Figure 4.5) do not portray the associations between McdA and McdB, we cannot exclude their contribution. To resolve the effects of this interaction with improved sensitivity, we measured the dynamics of McdA at a higher spatial-temporal resolution using live-cell PALM and single-molecule tracking [251] in *H. neapolitanus*. A two-state Gaussian Mixture Model fit well to the D_{app} distribution of McdA-PAmC^{SW} trajectories from WT cells (Figures 4.10d-e and Figure 4.12, Table 4.1). The two diffusive states comprised 55 ± 5% and 45 ± 5% of the population, respectively: an immobile state (D_{app} = 0.017 ± 0.001 μm^{2}s^{-1}) slower than our theoretical lower bound of detection (D_{app} = 0.063 μm^{2}s^{-1}, Figure 4.13), and a mobile state (D_{app} = 0.58 ± 0.02 μm^{2}s^{-1}), consistent with the free diffusion of McdA. This bimodal D_{app} distribution is similar to that of F plasmid ParA-mEos2 in *E. coli* [123].

To determine whether the slow state represents α-McdA binding to DNA, we tracked α-McdA[K20A]-PAmC^{SW}, the monomeric mutant with inhibited DNA binding, expecting a significant reduction in the slow state population. Fitting the D_{app} distribution of

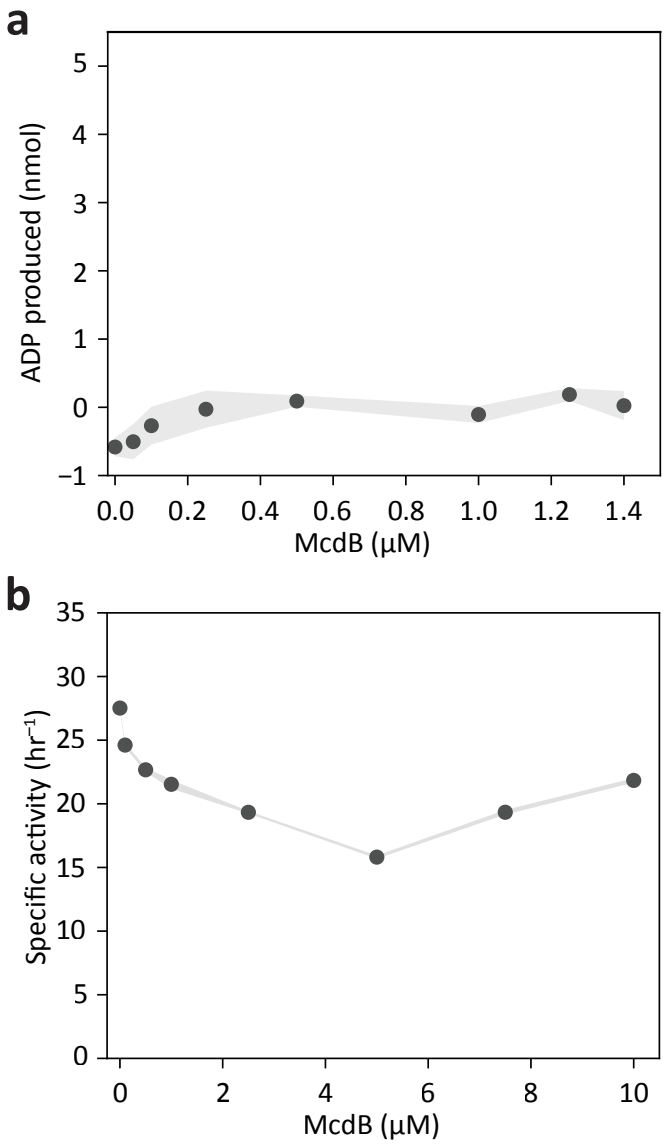


Figure 4.11: ATPase activity of McdA in the presence of excess McdB. a. ATPase activity of McdB with DNA (0.1 mg/mL). ATP was kept fixed at 1 mM. nmol of ADP produced in reaction after 2 hr. Shading represents the SEM of three independent experiments. **b**. Specific activity of His-SUMO-McdA (concentration fixed at 0.25 μM) measured as a function of McdB concentration (0-1.4 μM). Shading represents the error on the linear regression of the turnover rate (nmol ADP produced/hr vs. nmol McdA)

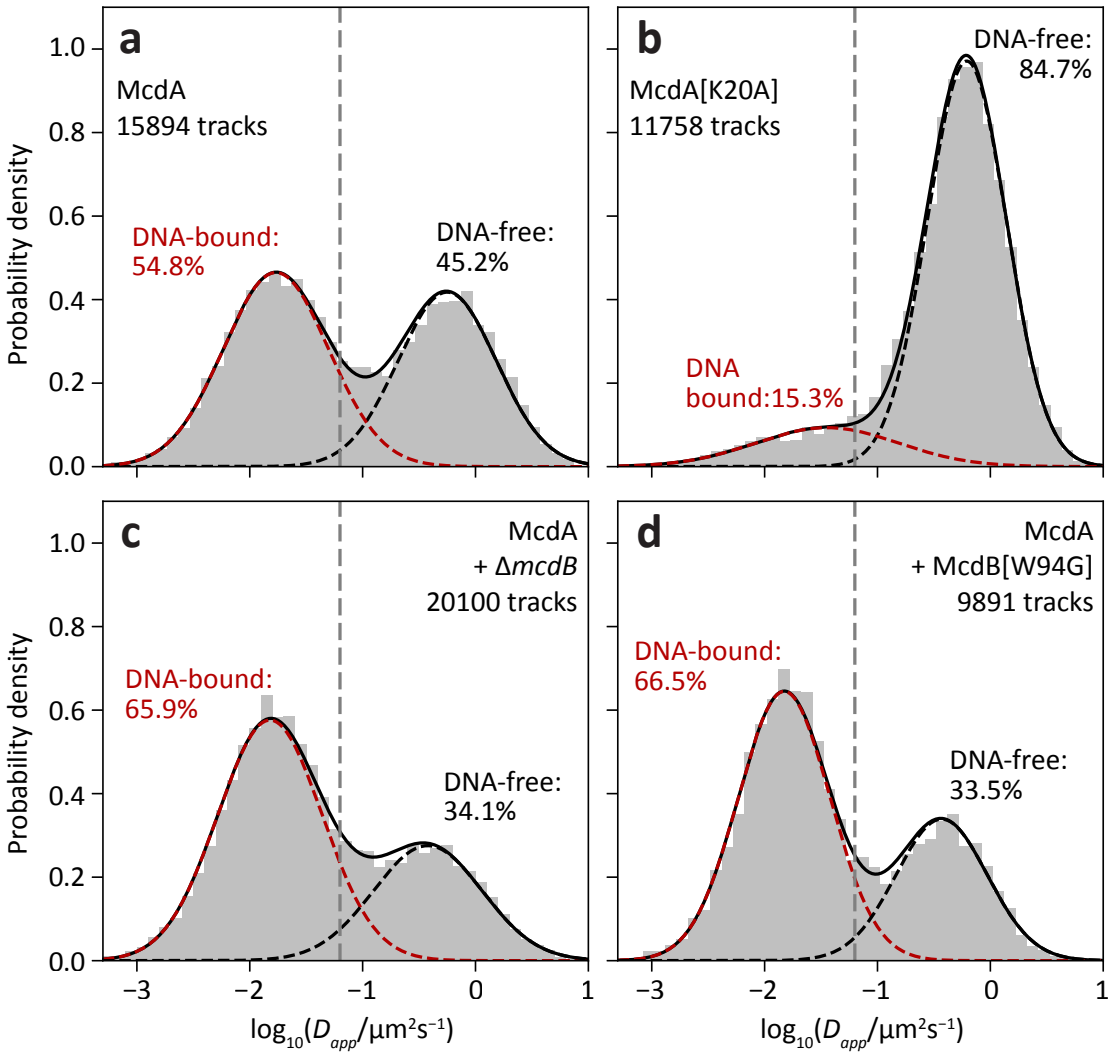


Figure 4.12: Diffusion analysis of single-molecule trajectories of McdA and its mutants collected with 20 ms camera integration. Probability density distributions of apparent diffusion coefficients, D_{app}, for (**a**) McdA-PAmCherry^{SW} in WT cells, (**b**) McdA[K20A]-PAmCherry^{SW}, (**c**) McdA-PAmCherry^{SW} in Δ*mcdB* cells, and (**d**) McdA-PAmCherry^{SW} in McdB[W94G] cells based on tracks collected with 20-ms camera integration times for all strains imaged in this study. Also shown in each plot is the D_{app} fit by a two-state GMM (solid black line). Colored dashed lines represent the individual states of the GMM fit colored-coded by the assigned biological state. Only tracks ≥ 5 frames are included. Data are from three or more biological replicates for each strain. The dashed gray line is the theoretical lower bound for D_{app} based on localization uncertainty from a fixed sample (Figure 4.13).

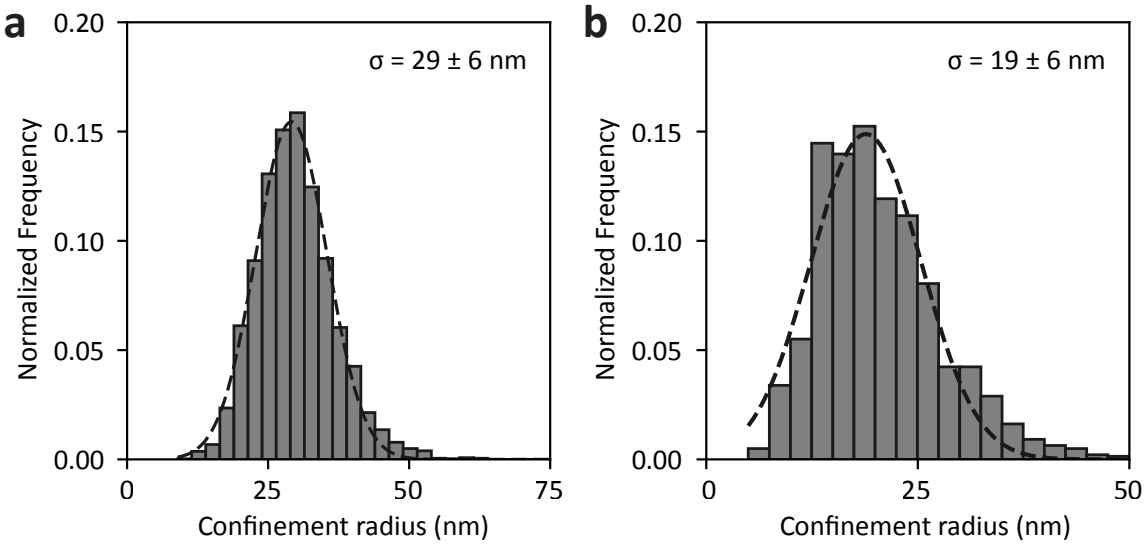


Figure 4.13: Localization uncertainty associated with consecutive detections of single PAmCherry molecules in fixed *H. neapolitanus* cells. Single molecules were imaged with (**a**) 20 ms and (**b**) 80 ms camera integration. The confinement radii of tracks with ≥ 5 frames were calculated by averaging the distance of every localization to the centroid (average position) of the track. Also shown is the Gaussian model fit (dashed line) of the confinement radius histogram.

α-McdA[K20A]-PAmC^{SW} resulted in two states comprising 15 ± 2% and 85 ± 2% of the population, respectively (Figures 4.10d-e and Figure 4.12, and Table 4.1): a slow state (D_{app} = 0.038 ± 0.003 μm^{2}s^{-1}) and a dominant fast state with similar diffusion to McdA-PAmC^{SW}, D_{app} = 0.62 ± 0.03 μm^{2}s^{-1}. This shift in the D_{app} distribution indicates an increase in the free population of McdA[K20A]-PAmC^{SW} consistent with its *in vitro* DNA-binding deficiency (Figures 4.5 and 4.8). We infer that the slow state represents weak and transient associations between monomeric McdA[K20A]-PAmC^{SW} and DNA

To measure the effect of McdB on McdA dynamics, we tracked McdA-PAmC^{SW} in Δ*mcdB* cells. Similar to WT cells, McdA-PAmC^{SW} in Δ*mcdB* cells showed two states with diffusion coefficients, 0.014 ± 0.002 μm^{2}s^{-1} and 0.37 ± 0.09 μm^{2}s^{-1} (Figure 4.10d-e, Table 4.1). However, the immobile population increased to 66 ± 6%, indicating a 20% enrichment of DNA-bound McdA-PAmC^{SW} molecules in the absence of McdB, consistent with *in vitro* results showing McdB promotes His-SUMO-McdA release from DNA (Figure 4.10b). Given that most McdB molecules are carboxysome-associated [236], we investigated whether

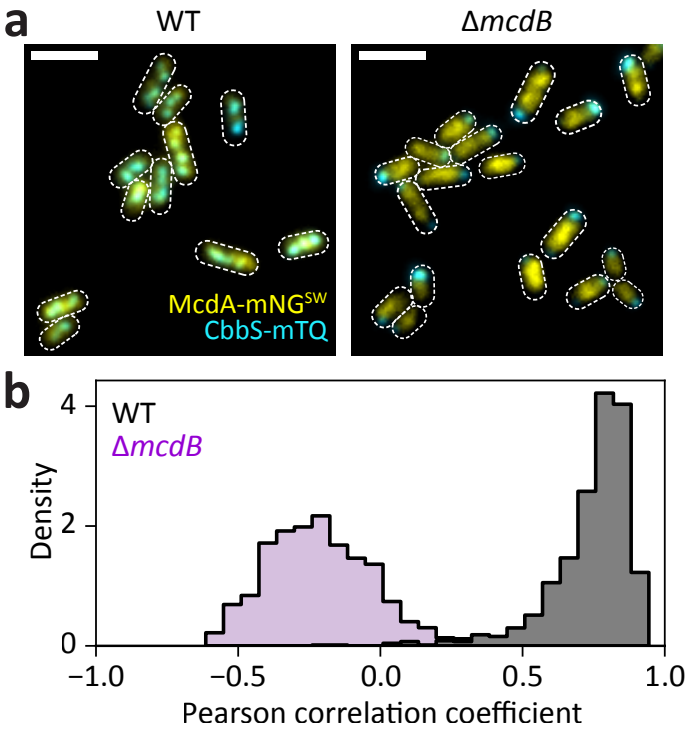


Figure 4.14: McdA-mNG^{SW} colocalizes with McdB-bound carboxysomes. a. Representative merged images of McdA-mNG^{SW} (yellow) and carboxysomes (CbbS-mTQ; cyan) in WT and Δ*mcdB* cells. Scale bars: 2 μm. **b**. Distribution of single-cell Pearson correlation coefficients for WT (N = 1126) and Δ*mcdB* (N = 954) cells.

the spatial distribution of McdB influences the dynamics of McdA. We tracked McdA-PAmC^{SW} in the presence of McdB[W94G] (McdB*), a mutant that does not associate with carboxysomes and is diffuse in the cytoplasm [236]. Since the N-terminus of McdB is predicted to associate with McdA [80] and the W94G mutation is at the C-terminus of McdB [236], we hypothesized this McdB* could still interact with McdA. This mutation resulted in an McdA diffusion profile similar to Δ*mcdB* cells (Figures 4.10d-e and Figure 4.12, Table 4.1) showing that, under physiological conditions, McdB needs to be localized at carboxysomes to promote the release of McdA from DNA. It is also possible that, upon interacting with carboxysomes, McdB adopts a different conformation that enables its activity [81].

Together, our data indicates that McdB facilitates McdA release from DNA *in vivo*, consistent with ParA/MinD family partner proteins which stimulate the release of their cognate ATPases from the positioning matrix. Relative to other ParAB systems, McdB has a lower effect on the release of McdA from DNA (Figure 4.10c), which may result in an increased McdA concentration near carboxysomes. Indeed, McdA-mNG^{SW} strongly colocalizes with carboxysomes (PCC = 0.75 ± 0.15) in WT cells (Figure 4.14). This colocalization suggests an high number of tethers between carboxysome-localized McdB and McdA on the nucleoid which may explain the motion of carboxysomes on the nucleoid.

4.2.9 McdA dimers can diffuse while bound to the nucleoid

In addition to the ratio of dissociation rates, the diffusive length scale of ParA dimers on the nucleoid is proposed to influence cargo dynamics [114, 124, 252]. This length scale, *s*, is determined by the diffusion coefficient of the nucleoid-bound ParA dimers, D_h, and its basal dissociation rate, k_{off}: $s = \sqrt{2D_{\mathrm{h}}/k_{\mathrm{off}}}$. DNA-bound diffusion by ParA dimers has been measured in *Caulobacter crescentus* [253] and on DNA carpets [120], and inferred from chromosome elasticity [104, 112] (Figure 4.15a). However, the elastic DNA fluctuations occur on length scales too short to explain all positioning behavior, thus ParA dimers can

extend this length scale by hopping between DNA strands (Figure 4.15a) [110, 111, 124].

To determine if nucleoid-bound McdA dimers still diffuse, we extended our single-molecule imaging camera integration time to 80 ms, biasing our detection to only slower McdA-PAmC^{SW} molecules. Plotting the trajectory MSD versus time lag for nucleoid-bound McdA-PAmC^{SW} revealed trajectories with heterogenous behavior (Figure 4.16a). For this reason, we extracted diffusion coefficients from the cumulative distribution function (CDF) of McdA-PAmC^{SW} dimer squared displacements (τ = 80 ms) (Figure 4.16b) [176]. The CDF was best fit by a two-state model, indicating two dynamic states for nucleoid-bound McdA-PAmC^{SW}. Molecules in the slower state were immobile based on our measurable lower bound (D_{app} < 0.0025 μm^{2}s^{-1}; Figure 4.13).

To elucidate a biological explanation for the diffusive states of nucleoid-bound McdA, we extended the observation period by adding a 140-ms dark time delay between imaging frames and tracked McdA-PAmC^{SW} as well as ParB-mNG foci as a chromosome marker. We found that the confinement radius of McdA-PAmC^{SW} in WT (47.0 ± 3.8 nm) and Δ*mcdB* (57.7 ± 4.7 nm) cells is greater than ParB-mNG foci (28.5 ± 0.9 nm) indicating nucleoid-bound McdA has a greater mobility than the chromosome itself (Figure 4.15b, Table 4.2). Indeed, the mobile state D_{app} of nucleoid-bound McdA-PAmC^{SW} (1.1 ± 0.1 × 10^{-2} μm^{2}s^{-1}) is higher than that of ParB-mNG foci (2.3 ± 0.2 × 10^{-3} μm^{2}s^{-1}) (Figures 4.15c and 4.16c, Table 4.3), suggesting that McdA dimer diffusion results in nucleoid exploration length scales greater than those possible by chromosomal fluctuations. Moreover, the D_{app} of ParB-mNG foci correlates with the immobile state of McdA-PAmC^{SW} implying that this population represents McdA-PAmC^{SW} stably bound to a DNA strand. Notably, the immobile fraction of McdA-PAmC^{SW} is enriched in WT cells compared to Δ*mcdB* cells (Figure 4.15d, Table 4.3), suggesting that McdA diffusion on the nucleoid is inhibited by interactions with carboxysome-localized McdB. In the mechanochemical Brownian-ratchet model, diffusing nucleoid-bound ParA dimers stop moving upon binding to the ParB partition complex providing a tether which quenches orthogonal diffusion of the cargo [110, 111]

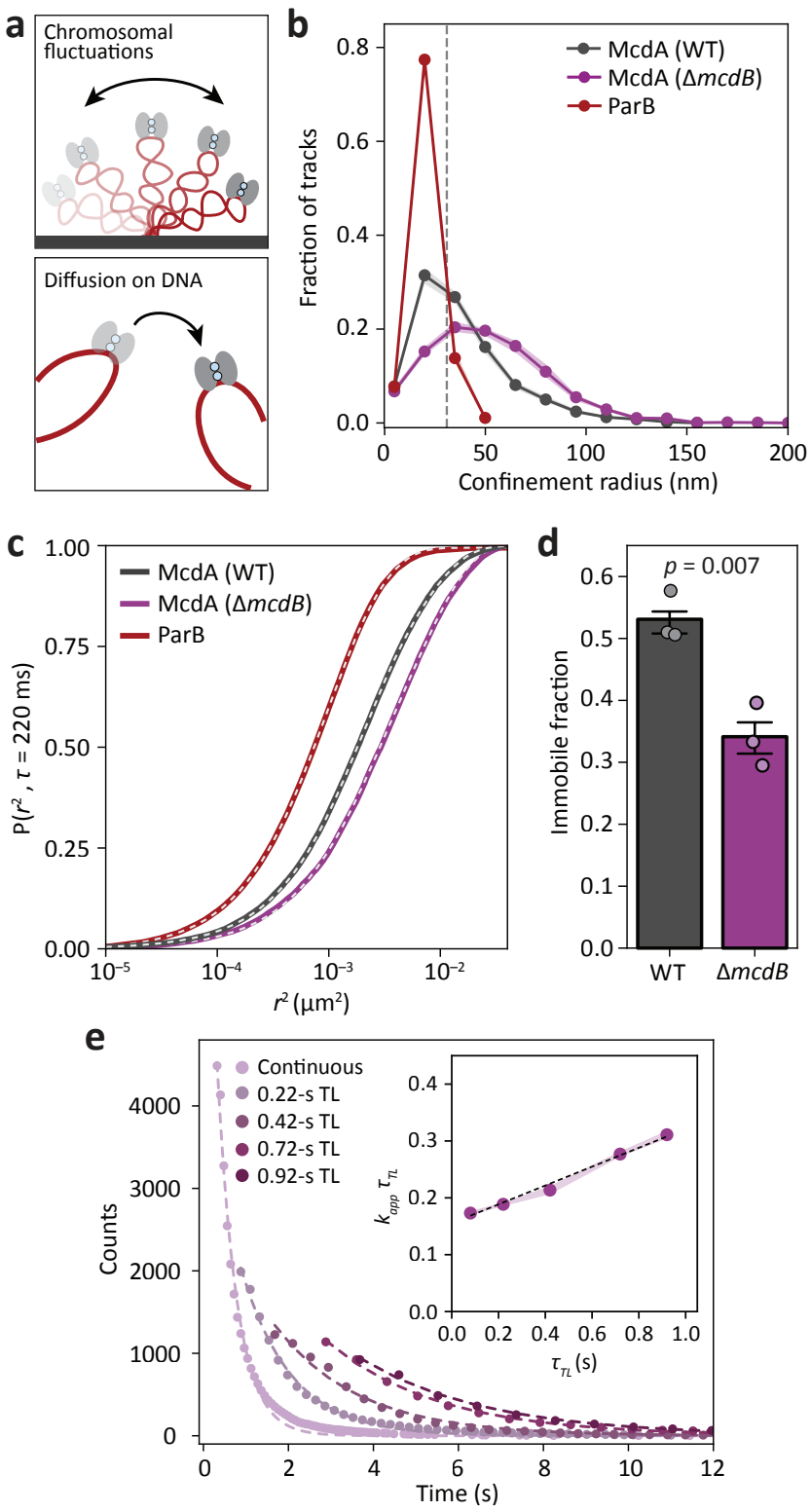

a
Chromosomal fluctuations
Diffusion on DNA
b
McdA (WT)
McdA (ΔmcdB)
ParB
Fraction of tracks
Confinement radius (nm)
c
McdA (WT)
McdA (ΔmcdB)
ParB
P(r², τ = 220 ms)
r² (μm²)
d
p = 0.007
Immobile fraction
WT
ΔmcdB
e
Continuous
0.22-s TL
0.42-s TL
0.72-s TL
0.92-s TL
Counts
Time (s)
k_app τ_TL
τ_TL (s)

Figure 4.15

Figure 4.15: Nucleoid-bound McdA dimers can diffuse. a. Diagram of possible mechanisms for the motion of nucleoid-bound McdA dimers (red): the chromosomal DNA (gray) may fluctuate elastically (top), the McdA dimers may hop from one DNA strand to another (bottom). **b**. Confinement radius distributions for McdA-PAmCherry^{SW} in WT (N = 2366 tracks) and Δ*mcdB* (**N** = 2054 tracks) cells and ParB-mNG (N = 950 tracks). Solid lines and shaded regions represent the mean ± 95% CI from 100 bootstrapped samples of the pooled datasets from 3 independent experiments. McdA-PAmCherry^{SW} tracks with confinement radii up to 0.031 μm (dashed gray line) are considered immobile. **c**. CDF of squared displacements from three pooled datasets of each strain. Dashed line is the two-state model fit (see Methods). **d**. Bar plot showing the immobile fraction (D_{app} < 0.0025 μm^{2}s^{-1}) for McdA-PAmCherry^{SW} in WT and Δ*mcdB* cells. Data points are the fit results from independent experiments and the error bars represent the standard deviation across the experiments. p-value is from a Welch's t-test. **e**. Raw survival of fluorescent 'on' times for McdA-PAmCherry^{SW} in Δ*mcdB* cells across different time-lapse conditions (Continuous, N = 4487 tracks; 0.22 s, N = 1990 tracks; 0.42 s, N = 1227 tracks, 0.72 s; N = 1139 tracks; 0.92 s, N = 924 tracks). Dashed lines are fits by an exponential decay model with one apparent rate constant (see Methods). Inset: Apparent rate constant, k_{app}, as a function of the time-lapse condition, τ_{TL}. Shading is the error on the fit of the exponential decay model. Dashed line is the linear fit used to extract k_{off}.

To experimentally determine the nucleoid exploration length scale, we also measured the *in vivo* basal dissociation rate, k_{off} with single-molecule time-lapse imaging. We measured an α-McdA-PAmC^{SW} dissociation rate of k_{off} = 0.166 ± 0.007 s^{-1} and an average residence time of 6.02 ± 0.24 s (Figure 4.15e), resulting in a length scale, s = 0.364 μm. Strikingly, the rate of DNA release by α-McdA-PAmC^{SW} is significantly faster (15-fold) than the ATP turnover rate of His-SUMO-α-McdA (0.011 s^{-1}) (Figure 4.8c-d). This result indicates that DNA release by α-McdA is not obligatorily coupled to ATP hydrolysis, consistent with increased His-SUMO-α-McdA release from DNA in the presence of α-McdB without enhanced ATP hydrolysis.

4.2.10 McdA dynamics are consistent with regular positioning of α-carboxysomes

In the Hopping and Relay model, regular positioning is possible if the s, diffusive length scale, is greater than $L/2n$, where L is the nucleoid length and n is the number of cargo. Using the measured *in vivo* k_{off} and $D_{h,\,app}$, we calculated s = 0.364 μm for α-McdA dimers.

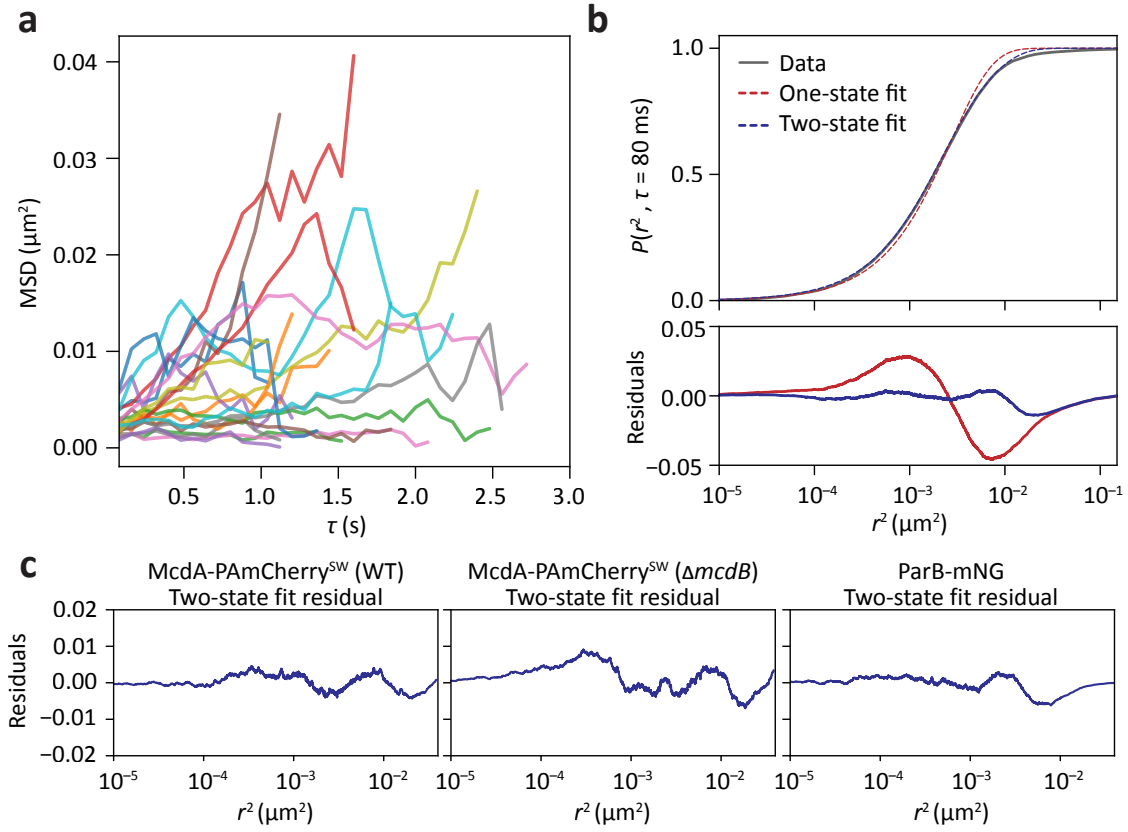


Figure 4.16: Nucleoid-bound McdA-PAmCherry^{SW} dynamics are heterogenous. a. MSD vs. τ curves for 20 randomly sampled McdA-PAmCherry^{SW} trajectories from Δ*mcdB* cells imaged continuously at 80-ms integration times. Curves show immobile, mobile, and switching behavior. **b**. Top: CDF of displacements with τ = 80 ms for McdA-PAmCherry^{SW} trajectories in Δ*mcdB* cells (N = 4487 tracks across three datasets). One-state (red dashed line) and two-state (blue dashed line) models were fit to the CDF (see Methods). Bottom: Residuals for the one-state (red line) and two-state (blue line) fits. **c**. Residuals for the two-state fits of McdA-PAmCherry^{SW} trajectories collected from WT (left) and Δ*mcdB* (center) cells and ParB-mNG foci (right) at 80 ms integrations and 140 ms dark-time delays.

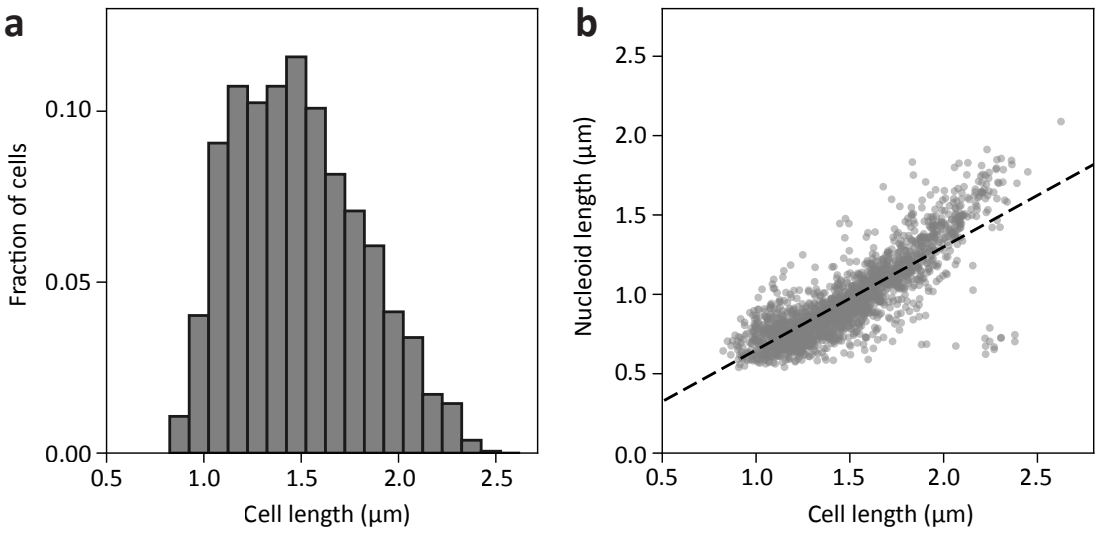


Figure 4.17: *H. neapolitanus* cell and nucleoid lengths. a. Distribution of WT cell lengths (N = 1864 cells). The average cell length is 1.49 ± 0.33 μm. **b**. Relationship between cell and nucleoid lengths (N = 1864 cells). Each point is an individual cell. Dashed line represents a linear relationship in the data of $L_{nucleoid} = 0.65L_{cell}$.

In *H. neapolitanus*, the average cell length is 1.5 μm (Figure 4.17a), the nucleoid length is 65% of the cell length (Figure 4.17b), and there are 2.7 carboxysome foci per micron cell length (Figure 4.1b), thus the average $L/2n$ = 0.120 μm. Considering the McdA DNA binding kinetics with and without α-McdB (Figure 4.10c), the experimentally determined s places α-McdAB-positioned cargo within the regular positioning regime of the Hopping and Relay model, further supported by our observations of α-carboxysome dynamics *in vivo* (Figure 4.1).

4.3 Discussion

In this study, we characterized the dynamics of α-carboxysomes and their positioning system, α-McdAB, using complementary *in vitro* and *in vivo* approaches. Overall, our findings support regular spacing of α-carboxysomes by McdA gradients, demonstrate novel biochemical properties of McdA which enable its positioning of a large number of carboxysomes in the cell, and are consistent with Brownian-ratchet models for ParA-mediated cargo positioning.

4.3.1 BMC positioning may be dictated by their copy number and the cell geometry

α-carboxysomes are regularly distributed in *H. neapolitanus* cells, supporting the proposed anti-aggregation function of McdAB systems [132]. The McdAB system keeps carboxysomes spaced apart on the nucleoid, ensuring their even inheritance after chromosome segregation and cell division. This same positioning mechanism may also govern β-carboxysome distribution in *S. elongatus* PCC 7942. β-carboxysomes are mobile on the nucleoid and biased to their 'home' positions [126, 127, 240]. β-carboxysomes only deviate from this behavior when they come into proximity with oscillating β-McdA gradients, where they are drawn towards the incoming or departing wave [127]. This movement pattern suggests that β-carboxysome motion is influenced by the incoming β-McdA flux.

At low carboxysome copy number (1—2), β-McdA gradients drive directed motion of β-carboxysomes towards oscillatory behavior. However, at the usual copy numbers (3-8), carboxysomes more closely resemble regular positioning, suggesting that carboxysome motions is dependent on their copy in the cell. Indeed, ParA ATPases may be capable of modulating cargo positioning based on the density of cargos. This effect was observed for a single pB171 plasmid, which transitions from regular positioning to oscillations at longer cell lengths but reverts back to regular positioning when two plasmids are present [103, 124]. Regular positioning seems to be the preferred positioning type among ParA ATPases, particularly in systems with high cargo densities [124, 127]. For instance, at high cargo concentrations, β-carboxysomes adopt a similar hexagonal arrangement to α-carboxysomes, thereby maximizing the distances between adjacent carboxysomes [127, 128].

Other BMC types are also positioned in the cell. For example, the 1,2-propanediol (1,2-PD) utilization microcompartments (Pdu BMC) are distributed along the cell length in *Salmonella enterica* serovar Typhimurium [254–257]. McdAB-like sequences have been found within and near the operons of these and other BMCs, often in bacterial pathogens

[131, 258, 259]. These shared characteristics make carboxysomes an important model system for general BMC spatial regulation, and call for further study of these unexplored BMCs.

4.3.2 McdA release from DNA is not obligatorily coupled to ATP hydrolysis

In classical ParA ATPase models, the release of ParA dimers from DNA is tightly coupled to ParB-stimulated ATP hydrolysis [92, 129]. ATP hydrolysis destabilizes the dimers, causing them to release as monomers. Stochastic models use these hydrolysis rates to model ParA dissociation kinetics from DNA [109, 110, 112, 124]. However, our data contradict this model: the dissociation rate of α-McdA (0.166 ± 0.007 s^{-1}) is 15-fold faster than its ATP hydrolysis rate (0.011 s^{-1}), and α-McdB stimulates α-McdA dissociation without enhancing ATP hydrolysis. This accelerated DNA dissociation relative to ATP hydrolysis is also seen in the plasmid partitioning ATPases SopA and P1 ParA [119, 120]. While ATP hydrolysis does result in DNA release, we propose that release from DNA can occur independently of ATP hydrolysis.

4.3.3 Diffusion on DNA by ParA dimers contributes to its flux control

Along these lines, we found that α-McdA dimers diffuse on the nucleoid with D_{app} = 1.1 x 10^{-2} $\mu m^2 s^{-1}$, much faster than the range enabled by chromosome fluctuations (Figure 4.15). This behavior can be explained by α-McdA dimers transiently dissociating from one DNA strand and hopping to another without hydrolyzing ATP (Figure 4.15a). Such diffusion of DNA-bound dimers has been measured for other ParA ATPases [93, 98, 119, 120, 253].

In *C. crescentus*, intermittent DNA binding by chromosome-segregating ParA establishes the gradient necessary for directional transport [253]. Similarly, ATPases like PomZ and MipZ, which position division machinery in *Myxococcus xanthus* and *C. crescentus*, respectively, are mobile even in their ATP hydrolysis-incompetent forms [93,98], supporting

ATP-hydrolysis-independent diffusion. Single SopA-GFP molecules show intersegmental hopping on DNA carpets in flow cells, though at a faster rate (0.9 $\mu m^2 s^{-1}$) than in living cells [120]. This discrepancy is likely due to the lower DNA concentration in flow cells, allowing SopA-GFP dimers to diffuse over longer distances before rebinding DNA, an effect that would be limited in the crowded cellular environment.

The ubiquity of DNA-bound diffusion highlights its role in dictating the flux of ParA ATPases. The concept of ParA 'flux balancing' has been argued as a mechanism for regular positioning of cargo [98, 114]. In the case of PomXYZ in *Myxococcus xanthus*, the imbalance in PomZ ATPase dimers (ParA) flux on either side of the PomXY cluster (cargo), drives the PomXY cluster towards mid-cell, the location where PomZ fluxes balance [98]. Since cargo need to 'feel' the disparity of incoming ParA flux, nucleoid bound ParA dimers must sufficiently diffuse to interact with the cargo. Otherwise, a ParA dimer that binds far from the cargo will never interact with it, resulting in ParA flux balance with the cargo at non mid-cell locations [124]. When cargo copy is drastically increased, like in the carboxysome system which can have an excess of a dozen carboxysomes, the required diffusive length scale for McdA dimers decreases as they are more likely to encounter carboxysomes. Consistent with this model, the diffusive length scale of α-McdA dimers is 0.364 μm, while the average distance between carboxysomes is 0.31 μm (Figure 4.2). Thus, α-McdA dimers are always able to find a carboxysome to interact with. We propose this mechanism allows α-McdAB to count and position carboxysomes effectively.

4.3.4 Brownian-ratchet models may explain differences between McdAB systems

The mechanochemical Brownian-ratchet and the Hopping and Relay models capture various observed cargo dynamics and may also explain the various patterns seen in different ParA ATPases, including McdAB. For example, α-McdA forms short-scale gradients on the nucleoid (Figure 4.2), rather than the large ParA gradients that often the span of

the nucleoid length [103, 104, 112, 114, 129] likely due to the shorter distances between carboxysomes. These gradients or flux imbalances may arise as the system responds to stochastic dissociations of McdA (caused by DNA-stimulated ATP hydrolysis or McdB association) from the nucleoid leading to the segregation of proximal carboxysomes from one another [110, 114, 124].

Although β-carboxysomes are also likely regularly positioned, the emergence of pole-to-pole oscillations of β-McdA remains unclear. One possibility is that *S. elongatus* polyploidy influences β-McdA dynamics. A recent study showed that ParA collectively migrates (flips) between constricted nucleoid lobes due to plasmid crossing to the half with more ParA [125]. We speculate that the rapid movement of β-McdA from one pole to another may result from sequential flips across each chromosome. Future work will further dissect these properties of the β-McdAB system—and how they relate to the α-McdAB system—in *S. elongatus*.

In conclusion, this study has uncovered key properties of the McdAB system that is responsible for positioning α-carboxysomes. Our data demonstrate that the dynamics of α-carboxysomes and α-McdA align with Brownian-ratchet models. Crucial to this finding was the integration of *in vitro* biochemical assays and live-cell single-molecule imaging, showcasing the effectiveness of these complementary approaches in elucidating molecular mechanisms in bacteria. While our focus was on α-carboxysomes, we anticipate that our results will be relevant to the spatial organization of other BMCs.

4.4 Materials and Methods

4.4.1 Construct designs and cloning

Strains, plasmids, and oligos used in this study are listed in Tables 4.4, 4.5, and 4.6, respectively. All constructs were generated using Gibson Assembly or site-directed mutagenesis (SDM) (NewEngland Biolabs Q5 Hot Start High-Fidelity; Cat. M0494S) and verified

by sequencing. Fragments for assembly were synthesized by polymerase chain reaction (PCR) or ordered as gBlocks (IDT). Constructs contained flanking DNA that ranged from 750 to 1100 bp in length upstream and downstream of the targeted insertion site to promote homologous recombination into the target genomic locus. Cloning of plasmids was performed in chemically competent *E. coli* Top 10 or Stellar cells (Takara Bio).

To prevent phenotype recovery by the presence of the native unlabeled McdA, all *mcdA* fusion plasmids were transformed into a *H. neapolitanus* Δ*mcdA* strain (AGV_Hn100) [131] or a Δ*mcdAB* strain (AGV_Hn432), unless otherwise noted. The mutants were selected by plating on S-6 agar plates supplemented with the appropriate antibiotic. All fusions were verified by PCR and by visualization of fluorescence signal by microscopy.

The Δ*mcdAB* background strain (AGV_Hn432) was used to transform fluorescent fusions of McdA for complementation. Strain AGV_Hn432 was constructed as follows. The sequence encoding plasmid pLT90 was amplified by PCR from pLT104 ([131] using the primer pair Pterin_rev/Hn0910_fwd. This step removed the *mcdB* gene (Hn0911) from pLT104. pLT90 was then transformed into AGV_Hn2 and selected by spectinomycin resistance to generate AGV_Hn432.

The strain AGV_Hn321 was used to induce the expression of McdB-PAmCherry determine the localization uncertainty of PAmCherry molecules in fixed *H. neapolitanus*. This strain was constructed by amplifying a fragment from pLT17 [131] using primer pair ptrc_backbone_rev/mcdB_CO_fwd and the *PAmCherry* fragment with primer pair PAmCherry _fwd/rev. The plasmid pLT67 was produced by Gibson assembly of the two fragments. pLT67 was then transformed in AGV_Hn2 and selected by kanamycin resistance to generate AGV_Hn321.

The strains AGV_Hn404 and AGV_Hn518 were native fluorescent fusions of McdA at its N- and C-terminus, respectively. The plasmid encoding PAmCherry-McdA (pLT79) was produced by Gibson assembly of the PAmCherry-McdA fragment amplified by primer pair PAmCherry_fwd/mcdA_CO_rev with the backbone amplified by primer pair Hn_0913_rev

/mcdA-mcdB-CO_fwd. The plasmid encoding McdA-PAmCherry (pLT87) was produced by Gibson assembly of the PAmCherry fragment amplified by primer pair GSGx9-PAmCherry_fwd/pamcherry_rev_2 with the backbone amplified by primer pair PAmCherry-mcdB/GSGx9_mcdA_rev from pLT79. Both plasmids were transformed into AGV_Hn2. The mutants were selected by plating on S-6 agar plates supplemented with 25 μg/mL of chloramphenicol.

The native sandwich fusions of McdA in strains AGV_Hn532 (mNeonGreen) and AGV_Hn431 (PAmCherry) were used for bulk imaging and single-molecule tracking of McdA, respectively. First, the sequence encoding the *PAmCherry* fragment with flanking GSGSGS linker sequences was amplified with primer pair GSGSGS_PAmCherry_fwd/rev. The PAmCherry fragment was then inserted in between the codon sequences encoding *mcdA* residues 59 and 60, amplified by primer pair GS_mcdA_fwd/Hn0912_GS_rev, by Gibson assembly to produce pLT94. The gene sequence for *mcdB* was included downstream of *mcdA*, followed by a chloramphenicol resistance cassette. The *cso* promoter was duplicated downstream of the resistance cassette to maintain faithful expression of the rest of the operon. To produce pCA2 (*mcdA-mNeonGreen*^{SW}) the backbone from pLT94 was amplified using primer pair GS_mcdA_fwd_2/Hn0912_GS_rev and Gibson assembled with a *mNeonGreen* fragment amplified by primer pair GS-mNG_fwd/mNG-GS_rev. To prevent phenotype recovery by the presence of the native unlabeled McdA, *mcdA* fusion plasmids were transformed into a Δ*mcdA* strain (AGV_Hn100) [131]. The mutants were selected by chloramphenicol resistance.

4.4.2 Media and growth conditions

All mutants described in this study were constructed using WT *Halothiobacillus neapolitanus* (Parker) Kelly and Wood (ATCC 23641) purchased from ATCC. Cultures were grown in ATCC Medium 290: S-6 medium for *Thiobacilli* [260] and incubated at 30 °C while shaken at 130 RPM in air supplemented with 5% CO_2, unless otherwise stated. Strains

were preserved at -80 °C in 10% DMSO.

4.4.3 Making competent cells of *H. neapolitanus* c2

H. neapolitanus competent cells were produced as previously reported [81]. Briefly, 0.5 L of culture was grown to an OD of 0.03 – 0.07. Cultures were harvested by centrifugation at 5000 × g for 20 min at 4 °C. Pellets were resuspended and washed twice with 250 mL of ice-cold nanopore water. All wash centrifugation steps were performed at 3000 × g for 30 min at 4 °C. The final pellet after washing was resuspended in 2 mL of ice-cold nanopore water. Competent cells were used immediately or frozen at -80 °C for future use. Frozen competent cells were thawed at 4 °C before use.

4.4.4 Transformation in *H. neapolitanus*

50 – 100 µL of competent cells were mixed with 5 – 7 µL of plasmid DNA (0.5 – 3 µg) and incubated on ice for 5 min. The mixture of competent cells and DNA was then transferred to a tube containing 5 mL of ice-cold S-6 medium without antibiotics and incubated on ice for 5 min. Transformations were recovered for 18 – 22 h while shaken at 130 rpm, at 30 °C in air supplemented with 5% CO2. Clones were selected by plating on S-6 plates with appropriate antibiotics. Colonies were restreaked once or twice. Restreaked colonies were verified for mutation by PCR and fluorescence microscopy.

4.4.5 Protein structure prediction and visualization

Protein structures were predicted using the ColabFold [261] implementation of AlphaFold2 [262]. Molecular graphics and protein structure analyses were performed in PyMOL.

4.4.6 Expression and purification of WT and mutants of *H. neapolitanus* McdA proteins

Chemicals used in this study are listed in Tables 4.7

Wild-type and mutant *H. neapolitanus* McdA proteins were expressed with an N-terminal His-SUMO tag in *E. coli* BL21(DE3) using a pET15b vector. The overnight culture was grown in LB media supplemented with 100 µg/mL carbenicillin. 1% of the overnight culture was transferred into 1 L of fresh LB media. Protein expression was induced with 100 µM IPTG when the OD_{600} of the culture reached 0.5-0.7. Cultures were incubated at 16 °C for 16 hours following induction. Cells were harvested by centrifugation and pellets were stored at -80 °C. The cell pellet was resuspended in 30 mL of lysis buffer: 50 mM Tris, 1 M KCl pH 8, 10% glycerol, 5 mM β-mercaptoethanol (BME), 1 protease inhibitor tablet (Thermo-Fisher). 30 mg of lysozyme was added to the resuspended pellet, and the suspension was incubated on ice for 10 minutes. Cells were disrupted by sonication using 10-second pulses (on) followed by 20-second intervals (off) at 50% power for 10 minutes. The lysate was centrifuged at 15,000 x g for 30 minutes at 4 °C and the supernatant was filtered through a 0.45 µm filter. The filtered lysate was loaded onto a 5 mL HisTrap HP column (Cytiva) pre-equilibrated with Buffer A (50 mM Tris, 1 M KCl pH 8, 10% glycerol, 5 mM BME). The column was washed with 5-column volumes of 5% Buffer B (50 mM Tris, 1 M KCl, 500 mM imidazole pH 8, 10% glycerol, 5 mM BME). The protein was eluted using a 5-100% gradient of Buffer B on an AKTA Pure system. Pooled fractions were injected onto a HiLoad 16/600 Superdex 200 pg column (GE Healthcare Life Sciences) equilibrated with Buffer A. Peak fractions were concentrated and filtered through a 0.45 µm filter and stored at -80 °C.

4.4.7 Gel filtration assay

50 µL samples of SUMO-Hn McdA or its mutants (at approximately 50 µM) with and without 1 mM ATP were incubated at room temperature before injecting into a Su-

perdex 200 5/150 GL column (GE Healthcare Life Sciences). For reactions without ATP, the column was equilibrated with 50 mM Tris-HCl (pH 8), 1 M KCl, 10% glycerol, 5 mM β-mercaptoethanol (BME), 5 mM $MgCl_2$ and for reactions with ATP the column was equilibrated with 50 mM Tris-HCl (pH 8), 1 M KCl, 10% glycerol, 5 mM BME, 5 mM $MgCl_2$, 1 mM ATP. The flow rate was set to 0.17 mL/min, and elution profiles were monitored by measuring absorbance at 280 nm.

4.4.8 DNA binding assay

Electrophoretic mobility shift assays (EMSAs) were performed in a final reaction volume of 10 µL using 50 mM Tris, 1 M KCl pH 8, 10% glycerol, 5 mM BME, 5 mM $MgCl_2$ buffer. The DNA substrate was pUC19 plasmid (10 nM). SUMO-Hn McdA or its mutants were incubated with the DNA for 30 minutes at 23°C in the presence of either 1 mM ATP or 1 mM ADP, at the indicated protein concentrations. Where applicable, McdB was added at the specified concentrations. Following incubation, 1 µL of DNA loading dye was added to each reaction. Samples were then loaded onto a 1% agarose gel prepared in TAE buffer with ethidium bromide and run at 100 V for 60 minutes. After electrophoresis, the gel was visualized using a Li-Cor Odyssey imager.

4.4.9 ATPase assay

ATPase assays were performed in a buffer containing 50 mM Tris, 1 M KCl pH 8, 10% glycerol, 5 mM BME, 5 mM $MgCl_2$ buffer, and 0.1 mg/ml sonicated salmon sperm DNA (unless otherwise specified). The reaction mixture, at the indicated protein concentration, was incubated at room temperature for 10 minutes. Following incubation, 10 µL of the reaction mixture was combined with 80 µL of EnzChek phosphate release assay (ThermoFisher Scientific) solution and further incubated for 5 minutes at room temperature. To initiate the ATPase reaction, 10 µL of 10 mM ATP was added to the mixture, which was then transferred to a 96-well plate. The plate was continuously shaken, and

absorbance at 360 nm was measured every 2.5 minutes for 160 minutes using a TECAN Infinite M200 Pro plate reader. ATP hydrolysis was quantified by comparing the absorbance data to a phosphate standard curve. ATP turnover was determined by linear regression of free phosphate produced vs. time up to 2 hours. Specific activities were determined by linear regression of ATP turnover (in nmol h^{-1}) vs. McdA concentration (in nmol). ATP turnover linear regressions were weighted by the error (SD) of three replicates, and specific activity linear regressions were weighted by the error on fit from the ATP turnover linear regression.

4.4.10 Fluorescence polarization assay

Polarization assays were performed in a buffer containing 50 mM Tris, 1 M KCl pH 8, 10% glycerol, 5 mM BME, 5 mM $MgCl_2$ buffer, and 100 nM of a Cy5 conjugated DNA primer dimer. The reaction mixture, at the indicated protein concentration, was incubated at room temperature for 10 minutes. Polarization data was collected using standard protocols. Polarization traces for each sample were fit to a hyperbolic binding model using a weighted least sqaures regression. Errors equal to 0 were set 0.01 to prevent division by zero.

4.4.11 Cleaning coverslips for fluorescence microscopy

For widefield epifluorescence microscopy, 35-mm glass-bottomed dishes (MatTek, Cat. P35G-1.5-14-C) were rinsed with 70% ethanol and dried in an oven at 30 °C. For single-molecule imaging, large (35 × 50mm) and small (25 × 25 mm) coverslips (Fisherbrand) were plasma etched in argon for 15 min.

4.4.12 Widefield epifluorescence microscopy

All live-cell microscopy was performed using exponentially growing cells. 2 – 4 µL of cells were spotted onto a pad of 2% UltraPure agarose (Invitrogen, Cat. 16500) + S-6 and

imaged on a 35-mm glass-bottomed dish (MatTek, Cat. P35G-1.5-14-C). All fluorescence and phase contrast imaging were performed using a Nikon Ti2-E motorized inverted microscope controlled by NIS Elements software. The microscope was equipped with a SOLA 365 LED light course, a 100× oil immersion objective lens (Oil CFI Plan Apochromat DM Lambda Series for Phase Contrast), and a Hamamatsu Orca Flash 4.0 LT + sCMOS camera. CbbS-mTurquoise2 (CbbS-mTQ) labeled carboxysomes were imaged using a "CFP" filter set (C-FL CFP, Hard Coat, High Signal-to-Noise, Zero Shift, Excitation: 436/20 nm [426-446 nm], Emission: 480/40 nm [460-500 nm], Dichroic Mirror: 455 nm). ParB-mNG, mNG-FliN , and McdA-mNGSW were imaged using a "YFP" filter set (C-FL YFP, Hard Coat, High Signal-to-Noise, Zero Shift, Excitation: 500/20 nm [490-510 nm], Emission: 535/30 nm [520-545 nm], Dichroic Mirror: 515 nm). DAPI-stained nucleoids were imaged using a "DAPI" filter set (C-FL DAPI, Hard Coat, High Signal-to-Noise, Zero Shift, Excitation: 350/50 nm [325-375 nm], Emission: 460/50 nm [435-485 nm], Dichroic Mirror: 400 nm). Samples were imaged for 1-1.5 hr before loading a new sample.

4.4.13 Nucleoid staining for live-cell imaging

A sample of 100 µL culture was stained with DAPI at a final concentration of 10 µM for 10 – 15 min immediately prior to imaging. 4 µL of stained cells were then loaded onto a 2% UltraPure agarose pad. The DAPI signal was captured with a 200 ms camera integration time.

4.4.14 Image processing and analysis

Software used in this study are listed in Table 4.8 and available in the Biteen Lab Github repository: https://github.com/BiteenMatlab

Cell registration: Image stacks were drift-corrected using a custom Python script: cell_registration.py. First, the phase contrast images were registered to the first frame in the stack using cross-correlation (skimage.feature.register_translation and skimage.transform.warp).

If the stack contained multi-channel data, the shifts used for the phase contrast images were applied to all other time-corresponding frames in other channels. The registered stacks were then saved as separate TIFF stacks.

Cell segmentation: Drift-corrected phase contrast images were used for cell segmentation via the Omnipose [232] package in Python. A custom Python script was implemented for batch segmentation: PhaseMasks_omni.py. Prior to segmentation, a Gaussian blur (SD of Gaussian = 1 pixel; skimage.filters.gaussian) was applied to the images. The bact_phase pre-trained model was used for segmentation. Cells touching the borders of the image were ignored, segmented objects smaller than 50 pixels were removed, and erroneous segmentations were manually corrected using the Omnipose GUI or excluded from further analysis if cell boundaries were not clear from the phase image. Resulting phase masks were used for subsequent single-cell analyses.

Carboxysome focus detection: To measure the number of foci per cell length, the cell length was first measured from the phase masks. Carboxysome foci were detected using a custom Python script: detect_carboxysomes.py: first, the phase masks were used to individually analyze every cell in the field of view. The fluorescent signal in each cell was then sharpened using the scikit-image [263] function skimage.filters.unsharp_mask; this step was followed by a Gaussian blur (skimage.filters.gaussian). Using this preprocessed image, carboxysome foci were detected with the Laplacian of Gaussian (LoG) algorithm (skimage.feature.blob_log). To reduce effects of overlapping carboxysome PSFs and improve detection, analysis was performed on image stacks that captured carboxysome separation due to their motion. All preprocessing and detection were performed on all frames within a time-lapse image stack. The frame with the highest number of detected foci was used for further analysis. In this chosen frame, putative foci signals were fit to a 2D Gaussian for subpixel localization. Carboxysome foci with a SD on the 2D Gaussian fit less than 1 pixel (66 nm) were excluded. Nearest neighbor distances between adjacent carboxysome foci was determined using the custom function nearest_neighbor. The number of carboxysome

foci localized in a cell was normalized to the length of that cell.

Carboxysome and chromosome tracking: Time-lapse fluorescence microscopy was used to measure the motion of carboxysome foci and the chromosome (ParB-mNG foci) we used. The signal was collected with 200-ms exposures and a dark-time delay of 800 ms. The image stack length was optimized for each sample: 10 frames for Δ*mcdA*, PAmcherry-McdA, and McdA-PAmcherry, and 25 – 31 frames for all other strains. Tracking of drift-corrected image stacks was done with the TrackMate [234] plugin in Fiji. Fluorescent spots were detected with LoG (radius = 3 pixels or 198 nm) using subpixel localization. Localizations were then linked with the LAP tracker method using a maximum linking length of 2 pixels (132 nm) and no gaps allowed. To remove erroneous trajectories due to mis-linking of proximal or overlapping foci, only trajectories with length equal to the imaging collection period were used for MSD analysis. Each trajectory was analyzed independently to extract a trajectory-average apparent diffusion coefficient, D_{app}, and the anomalous diffusion exponent α. The mean squared displacement, $\langle r^2 \rangle$, as a function of time lag (nτ), where n is an integer and τ is the 1 s time between frames, was calculated for up to the first 20 τ. The first 8 τ of the resulting curve were fit to Equation 4.1 using weighted non-linear least squares (scipy.optimize.curve_fit). The following bounds were placed on the fit parameters: D_{app} [0, infinity]; α [0, 2]. The distribution D_{app} was then fit to a GMM (sklearn.mixture.GaussianMixture) with one or two components, which provides the average D_{app}, the standard deviation, and the population weight associated with each component.

$$\langle r^2 (\tau) \rangle = 4 D_{\text{app}} \tau^{\alpha} \tag{4.1}$$

For velocity autocorrelation function (VACF) analysis, the same trajectory length thresholds described above were used. The VACF was calculated using Equation 4.2 and normalized to τ (0 s).

$$C_v^{\delta}(\tau) = \langle v(t+\tau) \cdot v(t) \rangle \tag{4.2}$$

$$v(t) = \frac{1}{\delta}\left[r(t+\delta) - r(t)\right], \delta = 1 \text{ s} \tag{4.3}$$

For confinement radius analysis, the same trajectory length thresholds were used. First, the average position of the track was calculated by averaging the xy coordinates. The average of the difference between this position and the track coordinates gives the confinement radius.

Carboxysome localization heatmaps: A custom Jupyter notebook was used to perform this analysis: Spydeymaps_carboxysomes_multi.ipynb. The localization coordinates of detected carboxysome foci and cell phase masks were used to make localization density heatmaps with the spideymaps tool in Python. First, the colicoords [264] package was used to convert the Cartesian coordinates of each cell into cellular coordinates that better describe the rod-shaped cell geometry. Then, cells were rotated and scaled to generate a uniform coordinate plane for all cells in a population. Localizations were binned and symmetrized across the x and y axes. Localization counts and associated bin areas were summed across all cells and the summed localizations count were divided by the summed area to calculate the localization density (counts per pixel^2). Spydeymaps package can be found in the Biteen Lab Github repository: https://github.com/BiteenMatlab/spideymaps

Kymographs: Time-lapse fluorescence microscopy image stacks of phase contrast (200 ms exposure) and mNG (2 s exposure) were collected at 10 s intervals and drift corrected as above. The corrected phase contrast image was opened in Fiji and a line was manually drawn along the long axis of a cell. The multi-kymograph tool was used to extract the intensity profile with a 9-pixel (594 nm) width. The resulting kymograph was saved as a TIFF file. For visualization, norm_kymographs.py script was used. The intensity profile at each timepoint of the kymograph is normalized to the minimum and maximum intensity

values within the corresponding time point, thus the values are normalized to 0 and 1. This post-processing removed the effects of photobleaching in the visualization of McdA-mNG.

Colocalization analysis: Single-cell Pearson correlation analysis was performed on corresponding CbbS-mTQ and McdA-mNG channels.

Nucleoid morphology: The cell phase masks were used to determine the pixel intensities within the inner rim of the cell boundary (skimage.segmentation.find_boundaries). The distribution of the single cell inner rim pixel intensities were fit to a Gaussian distribution (lmfit.Model.fit) to determine the average intensity of the cytoplasmic region of the cell. This intensity was subtracted across all pixels in the cell. A Gaussian blur (SD of Gaussian = 1 pixel (66 nm); skimage.filters.gaussian) was applied to the background subtracted image. Next, the nucleoid region was detected using Yen's thresholding (skimage.filters.threshold_yen) [265]. The length of the nucleoid is the length of the long-axis of the segmented region.

4.4.15 Single-molecule fluorescence microscopy

Cells expressing native protein fusions to PAmCherry were inoculated into S-6 medium and grown with shaking (130 rpm) at 30 °C, and in air supplemented with 5% CO_2 for 30 – 36 h before back diluting 1:100-200 in 5 mL of fresh S-6 medium. Cells were then grown under the same conditions for 18 – 24 h. Prior to imaging, 1 – 1.5 mL of cells were harvested by centrifugation at 5000 × g for 5 min and resuspended in 10 – 20 µL of fresh S-6 medium. Agarose pads were made at 2% (w/v) with S-6 medium without thiosulfate. An aliquot of 2 µL of cells was loaded onto an agarose pad and sandwiched between two coverslips. Samples were allowed to equilibrate on the stage top for 10 – 15 min prior to image collection. Cells were imaged at room temperature with a custom-built microscope equipped with a 100×, 1.40 numerical aperture oil-immersion objective. For fast single-molecule tracking experiments, 100 – 200 ms doses of 405-nm laser (Coherent Cube 405-100; 2 W/cm^2) were

used for PAmCherry photoactivation and a 561-nm laser (Coherent-Sapphire 561-50; 300 W/cm^2) was used for imaging. The laser power densities were determined by measuring laser power at the sample plane. The fluorescence emission was passed through a tri-band dichroic mirror and emission filter and 4000-6000 frames were collected at a rate of 50 Hz using a 512 × 512-pixel Photometrics Evolve EMCCD camera. Samples were imaged for 1-1.5 hr before loading a new sample.

4.4.16 Single-molecule data analysis

Phase-contrast microscopy images were used to segment bacterial cells (see Image Analysis section for details) prior to single-molecule localization and tracking. Image stacks with drift were excluded from analysis. Single molecules were detected and localized using the SMALL-LABS package in MATLAB [224]. Photoactivation by 406 nm light excites CbbS-mTQ, therefore an intensity-based threshold was set on the mean intensity of each frame to exclude the photoactivation frames from localization analysis. Putative single molecules were identified as non-overlapping punctate spots if an area of 8 × 8 pixels had pixel intensities above the 98th percentile intensity of the frame. Localization was done by fitting the putative single molecule spot to a 2D Gaussian; 'good' localization conditions were defined by a spot width = 7 pixels (343 nm), a tolerance threshold of 2.5 on the SD of the 2D Gaussian fit, and fit error ≤ 0.065 [224]. Good localizations were then assembled into trajectories via the Hungarian algorithm [225] using a maximum step size of 0.980 μm. Trajectories of at least 5 frames in which the molecule was localized in more than 50% of the frames and for which there were no more than three consecutive dark frames (in which no molecule was localized) were allowed.

Each trajectory was analyzed independently to extract a trajectory-average apparent diffusion coefficient, D_{app}, and the associated localization uncertainty, σ. The mean squared displacement, $\langle r^2 \rangle$, as a function of time lag (nτ), where n is an integer and τ is the 20 ms time between frames, was calculated for up to the first 4 τ (20 − 80 ms) and fit

with a weighted least-squares fit (scipy.optimize.curve_fit) to Equation 4.4. The slope of this curve is proportional to D_{app} according to a modified version of the diffusion model in two dimensions (Eq. 4.4). The modified diffusion model was used to account for motion blur due to averaging the true position of a molecule over the time of a single acquisition frame (Berglund, 2010). The following bounds were placed on the fit parameters: D_{app} [0, infinity]; σ [0, infinity]. Trajectories with an $R^2 \leq 0.2$ threshold were excluded from further analysis. The distribution D_{app} was then fit to a GMM (sklearn.mixture.GaussianMixture) with two components, which provides the average D_{app}, the standard deviation, and the population weight associated with each component. Bootstrap analysis was performed by randomly sampling the dataset with repetition to generate a set with sample size equal to that of the original. Reported means and standard deviations are from independent experiments (Table S1)

$$\langle r^2(\tau)\rangle = \frac{8}{3} D_{app}\tau + 4\sigma^2 \tag{4.4}$$

Estimation of localization uncertainty: To estimate the localization precision of immobile PAmCherry molecules in *H. neapolitanus* under the imaging conditions used, we performed the same single-molecule experiments with fixed cells. *H. neapolitanus* cells containing PAmCherry-McdB molecules expressed off an inducible promoter were induced with 0.5 mM IPTG for 3 h. Fixation was achieved by harvesting 1.5 mL of culture, concentrating the cells to 20 µL, and adding formaldehyde:PBS to a final concentration of 2.5% (v/v). The sample was then incubated at room temperature for 10 min before storing at 4 °C for 18 h. Imaging, localization, and tracking were done using the conditions described for 20 ms and 80 ms imaging. The confinement radii for tracks with at least five frames were calculated. The radius distribution was fit to a Gaussian function (Eq. 4.5) (lmfit.Model.fit) where r is the confinement radius, σ is the localization uncertainty, and ω is the standard deviation associated with σ. Analysis resulted in an uncertainty of 29 ± 6 nm for 20 ms imaging and 19 ± 6 nm for time-lapse (Figure 4.13).

$$p(r) = A \exp\left(\frac{-(r-\sigma)^2}{2\omega^2}\right) \tag{4.5}$$

4.4.17 Single-molecule time-lapse fluorescence microscopy

Single-molecule time-lapse experiments were performed as described above but with some modifications. Camera exposure times were increased to 80 ms to bias the detection to slow McdA-PAmCherry^{SW} molecules (i.e., the subset of molecules bound to DNA). Imaging was done with continuous acquisition or with an added dark-time delay between frames (140, 340, 640, and 840 ms). The 561-nm excitation power was lowered to 100 W/cm^2 to reduce the rate of photobleaching. Localization and tracking of PAmCherry constructs were performed with SMALL-LABS. SMALL-LABS parameters were modified to identify single molecules more strictly and prevent localizations of blurred molecules. The tolerance threshold was decreased to 1.75 on the SD of the 2D Gaussian fit, and the error on the fit was changed to ≤ 0.125. For the continuous imaging dataset, the max localization linking distance was set to 8 pixels (392 nm), and a maximum of 1 dark frame gap was allowed. The localization linking distance for each time-lapse experiment was determined by calculating the maximum possible squared displacement given the measured diffusion coefficient of the mobile state from the continuous imaging dataset: 0.018 ± 0.004 μm^{2}s^{-1} and the time-lapse, τ, between frames. A one-pixel (49 nm) buffer was added to account for noise. Imaging of ParB-mNG foci was performed on the same microscope setup as PAmCherry imaging. Here, all ParB-mNG molecules were excited simultaneously as there is no photoactivation mechanism. To maintain a comparable localization uncertainty, ParB-mNG molecules were excited with 2.0 W/cm^2 of 488-nm light. A total of 50 frames was collected using 80-ms camera integration times and a 140 ms dark-time delay. Localization and tracking were performed with TrackMate. Fluorescent spots were detected with LoG (radius = 6 pixels or 294 nm) using subpixel localization. Localizations were then linked with the LAP tracker method using a maximum linking length of 5 pixels

(245 nm) and no gaps allowed since the focus signal was stable throughout the imaging period. Confinement radius analysis was performed as above using the entire trajectory length for tracks with at least 4 localizations.

4.4.18 Cumulative distribution function (CDF) analysis

Trajectories were filtered to a minimum length of 4 localizations and at most 1 gap between frames. The squared displacement, r^2, was calculated for consecutive localizations within a trajectory (τ = 220 ms). The cumulative probability of the squared displacements in the observation period τ, $P(r^2, \tau)$, was generated from the pool of squared displacements across multiple tracks for each construct replicate by counting the number of squared displacements less than or equal to r^2 normalized by the sample size. The CDF of r^2 was fit to analytical functions (Eqs. 4.6 and 4.7) (lmfit.Model.fit) describing the diffusive processes with one or two dynamics states. D_1 and D_2 are the diffusion coefficients for the different states, and π describes the relative fraction between the states. Here, the D_1 term is assumed to be immobile and was constrained to a max value of 0.0024 $\mu m^2 s^{-1}$, the theoretical diffusion coefficient lower bound based on the uncertainty. The minimum for the D_2 term (mobile) was constrained to the same value. The error term is $4\sigma^2$, with σ = 0.019 μm, which was obtained as described above (Figure 4.13). Based on the calculated residuals, the two-state model resulted in the best fit (Figure 4.16).

$$\text{(One-state) } P\left(r^2, \tau\right) = 1 - \exp\left(\frac{-r^2}{\frac{8}{3}D\tau + 4\sigma^2}\right) \tag{4.6}$$

$$\text{(Two-state) } P\left(r^2, \tau\right) = 1 - \left(\pi e^{\frac{-r^2}{\frac{8}{3}D_1\tau + 4\sigma^2}} + (1-\pi)\, e^{\frac{-r^2}{\frac{8}{3}D_2\tau + 4\sigma^2}}\right) \tag{4.7}$$

4.4.19 Single-molecule residence time *in vivo*

The residence time of McdA binding to DNA was attained by analyzing the single-molecule time-lapse datasets as previously described [266] based on modeling the binding

as a direct two-component association/dissociation reaction: AB ↔ A + B. The measured residence time of each McdA-PAmCherry^{SW} molecule is estimated from the lifetime of the tracked fluorescence signal. k_{app} is obtained by fitting the survival curve (lmfit.Model.fit), P (Eq. 4.8), of the measured residence times, $\tau_{measured}$, to a single exponential decay function:

$$P = A \exp\left(-k_{app} \cdot \tau_{measured}\right) \tag{4.8}$$

Under the experimental conditions, the measured apparent dissociation rate, k_{app}, contains contributions from the true dissociation rate, k_{diss}, and the photobleaching rate of the PAmCherry label, $k_{bleaching}$. The $k_{bleaching}$ was measured by collecting data at multiple delay times, τ_{delay}, while maintaining a constant camera integration time, τ_{int}, to keep $k_{bleaching}$ constant for the different time delays, $\tau_{TL} = \tau_{int} + \tau_{delay}$. The residence time, $\tau_{measured} = n\tau_{TL}$, was determined by measuring the length, n, of each trajectory with 1 gap allowed. The true dissociation rate, k_{diss}, was estimated from a linear regression (scipy.optimize.curve_fit) of the two-term relationship:

$$k_{app}(\tau_{TL}) = k_{diss}\tau_{TL} + k_{bleaching}\tau_{int} \tag{4.9}$$

The linear regression was weighted by the uncertainty of each data point. Uncertainty values of each point are the error on the exponential fit for each time lapse. The error on the linear regression is the uncertainty on k_{diss}.

Table 4.1: Apparent diffusion coefficients, D_{app}, from two-state Gaussian Mixture fitting of data shown in Figures 4.10 and 4.12.

Sample	***N* tracks**	**Slow (%)**	D_{app} **(μm^{2}s^{-1})**	**Slow (%)**	D_{app} **(μm^{2}s^{-1})**
WT (rep 1)	4525	46.1	0.017	53.9	0.558
WT (rep 2)	3481	55.9	0.017	44.1	0.598
WT (rep 3)	4222	61.4	0.015	38.6	0.557
WT (rep 4)	3666	56.1	0.019	43.9	0.607
ΔmcdB (rep 1)	4166	60.8	0.012	39.2	0.244
ΔmcdB (rep 2)	3829	65.9	0.017	34.4	0.386
ΔmcdB (rep 3)	2652	63.1	0.012	36.9	0.316
ΔmcdB (rep 4)	4855	63.3	0.016	36.7	0.508
ΔmcdB (rep 5)	4598	76.9	0.016	23.1	0.412
[K20A] (rep 1)	4403	16.7	0.037	83.3	0.569
[K20A] (rep 2)	2915	12.2	0.035	87.8	0.635
[K20A] (rep 3)	4440	17.0	0.042	83.0	0.649
McdB[W94G] (rep 1)	4364	65.5	0.013	34.5	0.394
McdB[W94G] (rep 2)	5527	67.5	0.016	32.5	0.355

Table 4.2: Confinement radii for data shown in Figure 4.15.

Sample	***N* tracks**	**Confinement radius (nm)**
ParB (rep 1)	225	29.5
ParB (rep 2)	325	28.6
ParB (rep 3)	400	27.4
WT (rep 1)	898	46.6
WT (rep 2)	561	51.9
WT (rep 3)	907	42.6
ΔmcdB (rep 1)	956	51.2
ΔmcdB (rep 2)	470	62.4
ΔmcdB (rep 3)	564	59.5

Table 4.3: Apparent diffusion coefficients, D_{app}, from CPD fitting of data shown in Figures 4.15 and 4.16.

Sample	TL (ms)	N displacements	Immobile (%)	D_{app} (μm^2/s)	Mobile (%)	D_{app} (μm^2/s)
ΔmcdB (rep 1)	80	12641	62.8	1.9×10^{-3}	37.2	2.4×10^{-2}
ΔmcdB (rep 2)	80	13078	48.4	1.0×10^{-7}	51.6	1.5×10^{-2}
ΔmcdB (rep 3)	80	11818	50.0	1.7×10^{-4}	50.0	1.6×10^{-2}
WT (rep 1)	220	8768	57.7	1.0×10^{-7}	42.3	8.4×10^{-3}
WT (rep 2)	220	5198	51.0	1.0×10^{-4}	49.0	8.6×10^{-3}
WT (rep 3)	220	6192	50.6	1.0×10^{-7}	49.4	6.9×10^{-3}
ΔmcdB (rep 1)	220	7493	33.3	1.0×10^{-7}	67.7	8.7×10^{-3}
ΔmcdB (rep 2)	220	4037	39.6	8.7×10^{-4}	60.4	1.2×10^{-2}
ΔmcdB (rep 3)	220	3665	29.5	9.0×10^{-5}	70.5	1.1×10^{-2}
ParB-mNG (rep 1)	220	10465	30.5	4.1×10^{-4}	69.5	2.2×10^{-3}
ParB-mNG (rep 2)	220	15791	51.2	4.6×10^{-4}	48.8	2.5×10^{-3}
ParB-mNG (rep 3)	220	19506	51.9	3.9×10^{-4}	48.1	2.0×10^{-3}

Table 4.4: Strains used in Chapter 4.

Strain	Genotype	Source
AGV_Hn2	*Hn::cbbS-mTQ*	[131]
AGV_Hn14	*Hn::parB-mNG*	[81]
AGV_Hn100	*Hn::cbbS-mTQ::* Δ*mcdA*	[131]
AGV_Hn321	*Hn::cbbS-mTQ:: pTrc-PAmCherry-mcdB*	This study
AGV_Hn431	*Hn::cbbS-mTQ:: mcdA-PAmCherry*^{SW}	This study
AGV_Hn432	*Hn::cbbS-mTQ::* Δ*mcdAB*	This study
AGV_Hn441	*Hn::cbbS-mTQ:: mcdA-PAmC*^{SW} + Δ*mcdB*	This study
AGV_Hn481	*Hn::cbbS-mTQ:: mcdA[K20A]-mNG*^{SW}	This study
AGV_Hn498	*Hn::cbbS-mTQ:: mcdA-mNG*^{SW} + Δ*mcdB*	This study
AGV_Hn404	*Hn::cbbS-mTQ:: PAmC-mcdA*	This study
AGV_Hn518	*Hn::cbbS-mTQ:: mcdA-PAmC*	This study
AGV_Hn532	*Hn::cbbS-mTQ:: mcdA-mNG*^{SW}	This study
AGV_Hn537	*Hn::CbbS-mTQ:: mcdA[K20A]-PAmC*^{SW}	This study
AGV_Hn554	*Hn::CbbS-mTQ:: mcdA-PAmC*^{SW} *+ mcdB[W94G]*	This study

Table 4.5: Plasmids used in Chapter 4.

Plasmid name	Relevant genetic elements	Source
For constructing *H. neapolitanus* strains		
pLT04	*Hn0910-0911_specR_Hn0913-0914*	[131]
pLT17	*pTrc-mNeonGreen-mcdB-kanR*	[131]
pLT67	*pTrc-PAmCherry-mcdB-kanR*	This study
pLT79	*native-PAmCherry-mcdA-mcdB-chlR*	This study
pLT87	*native-mcdA-PAmCherry-mcdB-chlR*	This study
pLT90	*Hn0910_specR_Hn0913-0914*	This study
pLT94	*native-mcdA$^{1\text{-}59}$-PAmCherry-mcdA$^{60\text{-}216}$-mcdB-chlR*	This study
pLT103	*native-mcdA$^{1\text{-}59}$-PAmCherry-mcdA$^{60\text{-}216}$-chlR*	This study
pLT104	*native-mcdA$^{1\text{-}59}$[K20A]-PAmCherry-mcdA$^{60\text{-}216}$-mcdB-chlR*	This study
pCA2	*native-mcdA$^{1\text{-}59}$-mNeonGreen-mcdA$^{60\text{-}216}$-mcdB-chlR*	This study
pCA3	*native-mcdA$^{1\text{-}59}$-mNeonGreen-mcdA$^{60\text{-}216}$-chlR*	This study
pCA4	*native-mcdA$^{1\text{-}59}$[K20A]-mNeonGreen-mcdA$^{60\text{-}216}$-mcdB-chlR*	This study
pCA31	*native-mcdA$^{1\text{-}59}$-PAmCherry-mcdA$^{60\text{-}216}$-mcdB[W94G]-chlR*	This study
For transformation into *E. coli* BL21 (DE3)		
pJB26	*pET11b::hisx6-sumo-mcdB-ampR*	[65]
pAV96	*pET15b::hisx6-Hn_0912-GFP-ampR*	This study
pHS02	*pET15b::hisx6-SUMO-mcdA-ampR*	This study
pHS06	*pET15b::hisx6-SUMO-mcdA[K20A]-ampR*	This study
pHS08	*pET15b::hisx6-SUMO-mcdA[R158E]-ampR*	This study
For EMSA		
pUC19		New England Biolabs (Cat. # N3041S)

Table 4.6: DNA oligonucleotides used in Chapter 4.

Oligo name	Sequence (5' to 3')	Purpose
ptrc_backbone _rev	ATGTTTTTCCTCCTTGTGTGAA ATTGTTAT	To make pLT67
mcdB_CO_fwd	ATGACGAATCTGGAAGACAAA	To make pLT67
PAmCherry_fwd	GTGAGCAAGGGCGAGGAG	To make pLT67, pLT79
PAmCherry_rev	CTTGTACAGCTCGTCCATGC	To make pLT67
Hn_0913_rev	TGTTATCCTCCTCGCCCTTGCTC ACGGCGT TAGCTATACTTGGCG	To make pLT79
mcdA/mcdB_CO _fwd	TCTTAAATGAAGTCATCCCATCA TGACGAATCTGGAAGACAAATT ATCA	To make pLT79
mcdA_CO_rev	CATGATGGGATGACTTCATTTAA GATC	To make pLT79
GSGx9-PAmCh erry_fwd	ATCAGGTGGCGGTGGCGGTGGT GGCGGTGGTGTGAGCAAGGGC GAGGAG	To make pLT87
pamcherry_rev_2	TTTGTACAGCTCGTCCATGCC	To make pLT87
PAmCherry_mcdB	CCGGCGGCATGGACGAGCTGTAC AAATGA CTAATTTAGAAGATAA ACTGAGTG	To make pLT87
GSGx9_mcdA_rev	GCCACCACCGCCACCGCCACCTG ATCCTG ACGGGATAACCTCGTTA AG	To make pLT87
Pterin_rev	TTAGCTATACTTGGCGGCCAAG	To make pLT90
Hn0910_fwd	GTCAAACTATGAACCCAGCGAC	To make pLT90
GS/mcdA_fwd	GTACAAGGGTTCTGGTAGTGGAT CTGAC GCTCAAGTCCCCGTC	To make pLT94
Hn0912_GS_rev	TGCTCACTGATCCTGATCCTGAA CCCG CCTCTTTGCTTCCCCA	To make pLT94, pCA2, pCA3, pCA4
GSGSGS_PAmCh erry_fwd	GGTTCAGGATCAGGATCAGTGAG CAAGGGCGAGGAG	To make pLT94
GSGSGS_PAmCh erry _rev	AGATCCACTACCAGAACCCTTGT ACAGCTCGTCCATGC	To make pLT94
delmcdB_fwd	GTTATCCCGTCATGATTTTGTCC GAACATCGCGAATTACG	To make pLT103
delmcdB_rev	TCATGACGGGATAACCTCGTTAA GG	To make pLT103
SDM_McdA_K20A _fwd_long	AAAGGTGGCTGTGGCGCCACGA CC	To make pLT104, pCA4

mcdA_K20R _rev_long	GCCACAGCCACCTTTGAGGTTG GCGACA	To make pLT104, pCA4
GS-mNG_fwd	GGTTCAGGATCAGGATCAATGG TGTCGAAAGGAGAAGAAG	To make pCA2, pCA3
mNG-GS_rev	AGATCCACTACCAGAACCCTTG TATAATTCGTCCATCCCC	To make pCA2, pCA3
GS_mcdA_fwd_2	GGTTCTGGTAGTGGATCTGACG CTCAAGTCCCCGT	To make pCA2, pCA3
1_His SUMO Forward	CTTTAAGAAGGAGATATACATA TGGGCAGTAGCCACCATC	To make pHS02
2_SUMO w Hn-McdA tail Reverse	GCTTTATTGCTGGCCATGCCCC CGATCTGTTCACGGTGTG	To make pHS02
3_SUMO tail w Hn McdB backbone Forward	GTGAACAGATCGGGGGCATGGC CAGCAATAAAGCATTTAC	To make pHS02
4_RBS His pET15b backbone Reverse	CTACTGCCCATATGTATATCTCC TTCTTAAAGTTAAAC	To make pHS02
30_Hn-McdA K20A Forward	TGGTTGTGGTgcgACCACCATTAG	To make pHS06
31_Hn-McdA K20A Reverse	CCTTTCAGATTTGCAACTG	To make pHS06
36_Hn-McdA R158E Forward	CGCAATGACCgaaGCAATGCAGAC	To make pHS08
37_Hn-McdA R158E Reverse	CTACGCGGTTCGGTCTGATTCAG	To make pHS08

Table 4.7: Chemicals used in Chapter 4.

Chemical	Source	Catalog number
4',6-diamidino-2-phenylindole (DAPI), dihydrochloride	ThermoFisher Scientific	D1306
Isopropylthio-β-galactoside (IPTG)	ThermoFisher Scientific	15529019
EnzChek Phosphatase Assay Kit	ThermoFisher Scientific	E12020

Table 4.8: Software used in Chapter 4.

Program / library /script	**Package**	**Source**
Fiji	imagej.net/software/fiji	[267]
Trackmate	imagej.net/plugins/trackmate	[234]
MATLAB (2023b)	mathworks.com/products/new_products/release2023b.html	Mathworks
ColabFold	colab.research.google.com/github/sokrypton/ColabFold/blob/main/AlphaFold2.ipynb	[261]
PyMOL	pymol.org (v 3.0.1)	Schrodinger, Inc.
Python 3	python.org (v 3.12.5)	Python Software Foundation
Scikit-image	scikit-image.org	[263]
Scikit-learn	scikit-learn.org/stable	[268]
Matplotlib	matplotlib.org	[269]
Scipy	scipy.org	[270]
Seaborn	seaborn.pydata.org	[271]
Pandas	pandas.pydata.org	[272]
LMFIT	lmfit.github.io/lmfit-py	[273]
Omnipose	github.com/kevinjohncutler/omnipose	[232]
Spydeymaps	github.com/BiteenMatlab/spideymaps	Biteen Lab
PhaseMasks_omni.py	Cell segmentation by Omnipose; script for batch processing	This study
cell_registration.py	To drift correct image stacks. Requires specific package versions: scikit-image 0.16.2, numpy 1.18.5	This study
detect_carboxysomes.py	To localize carboxysome foci, determine their nearest neighbor distance, and measure the associated cellular morphology	This study
Spideymaps_carboxysomes_multi.ipynb	To make the carboxysome localization heatmaps.	This study
norm_kymographs.py	To normalize kymographs	This study
nucleoid_morphology.py	To segment nucleoid regions and measure the associated cellular morphology	This study
SMALLLABS_main_acti.m	To localize and track single molecules with activation frames excluded	This study

CHAPTER V

Environmental Biosensors for Cryogenic Correlative Light and Electron Microscopy[1]

5.1 Introduction

Fluorescence microscopy is a powerful approach for observing biological macromolecules. However, this imaging modality relies on the specific labeling of biomolecules, often resulting in the loss of the broader cellular context. Conversely, cryogenic electron tomography (cryoET) provides detailed cellular context with high spatial resolution but lacks the contrast necessary to identify specific biomolecules smaller than a few hundred kilodaltons [180, 181]. The combination of both imaging techniques in cryogenic correlative light and electron microscopy (cryoCLEM) leverages the strengths of each method to overcome their respective weaknesses [177, 189, 193, 274, 275]. Through CLEM, it is possible to achieve both specific labeling and broader cellular context. Despite these benefits, cryoCLEM lacks contextual physiological information, such as ion or metabolite concentrations, which would aid in the interpretation of the high-resolution snapshots provided

[1]The work presented in this chapter was done in the lab of Dr. Peter Dahlberg at Stanford University and SLAC National Lab. The data is in preparation for a manuscript by Azaldegui, C.A., Perez, D., Dwyer, W., Summers, J.A., Rui, Y., Mak, C.A., Byrne, J.A., Vecchiarelli, A.G., Biteen, J.S., Dinneny, J.R., and Dahlberg, P.D.
C.A.A. prepared the high-pressure frozen samples. C.A.A. and P.D.D prepared cellular samples for cryoCLEM and performed EM imaging. C.A.A., D.P., and P.D.D. performed all cryogenic spectroscopy and light microscopy and related analyses. C.A.A., W.D., and P.D.D. analyzed EM data. J.A.S and C.A.M. purified protein samples. C.A.A., J.A.B., and Y.R. produced strains used in this work.

by cryoCLEM (Fig. 5.1a).

Fluorescent protein engineering has led to the development of genetically encoded biosensors that report on a variety of cellular analytes [196, 276]. Fluorescent protein- and dye-based biosensors have been previously implemented in cryoCLEM to identify functional cellular states, but there are limited examples in the literature [185, 277, 278]. For example, roGFP2, a redox-sensitive derivative of green fluorescent protein (GFP), was identified as a suitable redox state reporter for cryoCLEM [185]. This demonstration of roGFP2 highlights the potential for ratiometric fluorescent biosensors to provide specificity and physiological information in high-resolution cellular structures.

Here, we expand the available suite of fluorescent biosensors for cryoCLEM. Specifically, we identify ratiometric biosensors that report on molecular crowding, pH, and calcium — environmental factors that play critical roles in cellular processes [279–281]. We developed an optimized identification process that involves initial validation of sensor function at cryogenic temperature, calibration of the sensor at cryogenic conditions, and subsequent cryoCLEM of cellular samples containing these sensors (Fig. 5.1b). Using this workflow, we identify and implement a molecular crowding sensor to show osmotic stress-induced structural changes in *Saccharomyces cerevisiae*. We also identify several pH and calcium sensors that function at cryogenic temperatures and calibrate their response at 77 K to demonstrate their dynamic range.

5.2 Results

5.2.1 The molecular crowding sensor SED1 preserves its function at cryogenic temperatures

First, we aimed to measure osmotic fluctuations, which are among the most common physicochemical changes that cells experience, by identifying a sensor responsive to the effects of osmotic stress. Osmotic fluctuations can be intrinsic to the cell physiology — for

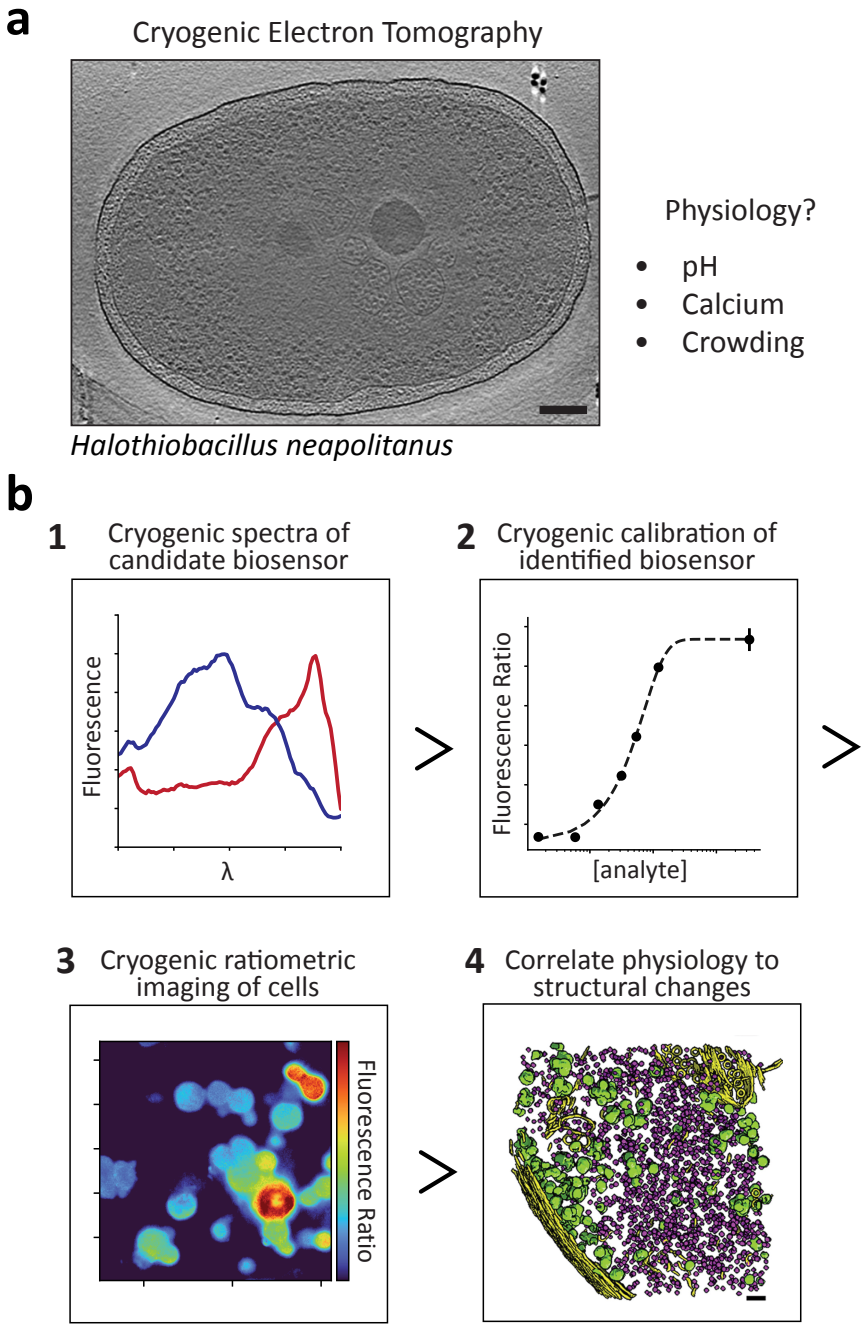


Figure 5.1: Experimental workflow for biosensor cryoCLEM. a A z-slice of a tomographic reconstruction of an *H. neapolitanus* cell. **b**. Biosensor cryoCLEM workflow: 1: Validate the biosensor for function by measuring its spectral properties in cryogenic conditions. 2: Calibrate the biosensor on a cryogenic light microscope. 3: Perform cryogenic ratiometric imaging in vitrified cells expressing the biosensor. 4: Perform electron tomography and analysis to correlate structures with the ratiometric readouts of the biosensor.

instance, the metabolite content changes throughout the cell cycle, and ion channel activity alters intracellular ionic concentrations [282, 283]. External osmotic stresses can also affect osmotic balance. For example, a decrease in external water content can drive intracellular water out of the cell, leading to increased cellular solute concentrations, molecular crowding, and viscosity [279, 284, 285]. We therefore investigated the applicability of a molecular crowding biosensor, Sensor Expressing Disorder Protein 1 (SED1), under cryogenic conditions to ultimately measure osmotic stress responses of cells in cryoCLEM.

SED1 is a Förster Resonance Energy Transfer (FRET)-based biosensor that links two FRET-compatible fluorescent proteins by an intrinsically disordered linker that is sensitive to osmotic changes [286]. The FRET donor is the cyan fluorescent protein (CFP), mCerulean3, and the FRET acceptor is the yellow fluorescent protein (YFP), mCitrine (Fig. 5.2a). Excitation at 410 nm results in a broad emission spectrum which is the sum of the CFP and YFP emission spectra; which peak at 475 nm and 530 nm, respectively (Fig. 5.2b). The linker (AtLEA4-5) is derived from a group 4 Late Embryogenesis Abundant (LEA) protein from Arabidopsis thaliana. In high-salt or crowded environments, AtLEA4-5 folds in a manner that brings the CFP and YFP into close proximity, enhancing the SED1 FRET efficiency which results in an intensity increase of YFP emission peak and a decrease in the CFP emission peak.

We validated the response of purified SED1 at room temperature (RT) and cryogenic temperature (77 K) under two crowding conditions: 0% and 10% PEG4000. The emission of SED1 excited at 410 nm was collected from 425 – 650 nm. At RT and in the absence of crowder, the ratio of fluorescence intensity at the peak wavelengths of YFP (525 nm) and CFP (470 nm) was approximately 0.8 (Fig. 5.2b). Addition of 10% PEG4000 results in an increase of the YFP/CFP ratio to 1.0 (Fig. 5.2b). At 77 K, the YFP/CFP ratio is 1.2 in the absence of crowder, and it increases to 2.1 when crowder is present (Fig. 5.2c). SED1 is even more sensitive to crowding at 77 K than at RT, though the mechanism of this enhanced sensitivity is unclear. Fluorophores are more photostable and have an increased photon

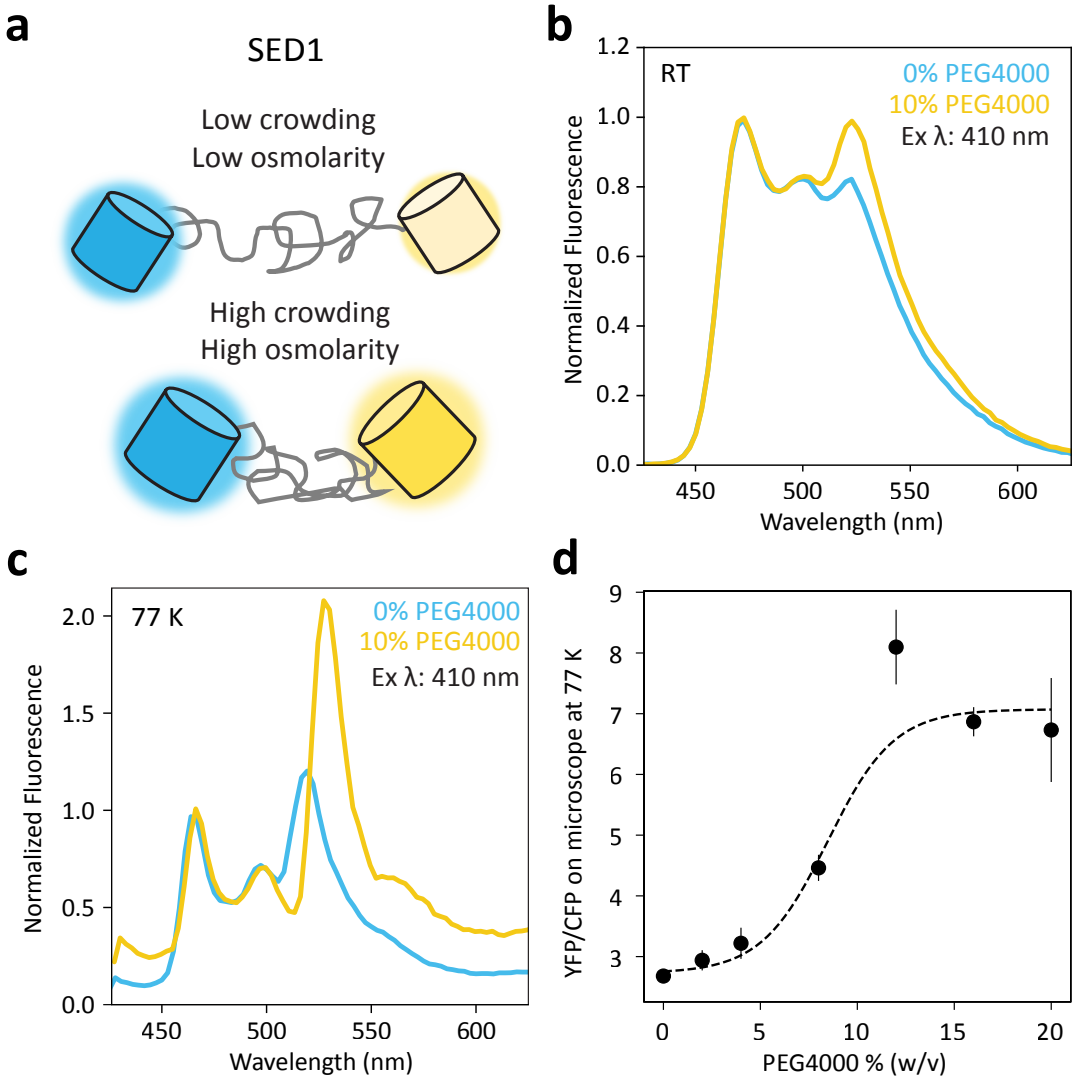


Figure 5.2: SED1 maintains its crowding-sensing properties at cryogenic temperatures. a. SED1 is a FRET-based biosensor. Upon high crowding or osmolarity, the IDR linker of SED1 folds, leading to higher FRET efficiency between the two fluorescent proteins. Cyan: mCerulean3. Yellow: mCitrine. Gray: AtLEA4-5. **b-c**. Emission spectra of SED1 at (**b**) room temperature (RT) and (**c**) 77 K with and without PEG4000. Each spectrum is normalized to the mCerulean3 emission peak: 471 nm at RT and 465 nm at 77 K. **d**. Calibration curve of vitrified SED1 measured on a microscope at 77 K. Each point on the calibration is the average of at least 5 ratiometric measurements for each condition. The error bars represent the standard error on the mean (SEM). The dashed line is the fit to a continuous logistic function.

yield at cryogenic temperatures [287–291]. However, we reason that the changes in the relative CFP and YFP emission intensity may be caused by two effects. First, improved spectral overlap between donor and acceptor; and second, a stabilized folded conformation due to hindered motion at 77 K and the annealing of the structures during freezing to conformations of local energetic minima. At RT, conformational fluctuations may lower the average FRET response of SED1. Regardless of the mechanism, our results demonstrate that SED1 is a highly sensitive sensor for molecular crowding at cryogenic temperatures.

Next, we calibrated the response of SED1 under different crowding conditions at 77 K. To generate vitrified samples of SED1, we high-pressure froze purified SED1 in the presence of 0 – 20% PEG4000 on gold planchettes. High-pressure freezing was performed instead of more traditional plunge freezing to avoid effects of the air-water interface that would not be present in plunge frozen cellular samples. These planchettes were then loaded onto a cryogenic light microscope and excited with 425-nm light, and emission was collected in two spectral windows: 450 – 480 nm and 525 – 565 nm. The fluorescence ratio (YFP/CFP) between the two windows has a sigmoidal relationship with the concentration of PEG4000 (Fig. 5.2d). Notably, at lower PEG4000 concentrations (< 10%), this relationship resembles the reported response of SED1 at RT [286]. At higher PEG4000 concentrations, the measurements are noisier, likely due to observed droplet-like assemblies of SED1, suggesting that SED1 may phase separate into condensates under these conditions.

5.2.2 Biosensor cryoCLEM of SED1 in S. cerevisiae reveals structural changes in response to osmotic stress

Having demonstrated SED1 as a suitable crowding sensor under cryogenic conditions, we implemented it in yeast cells to correlate mesoscale structural perturbations with osmotic stress. *S. cerevisiae* cells expressing cytoplasm-localized SED1 were treated with 1 M NaCl for 10 minutes or left untreated before plunge-freezing on finder grids. Cryogenic

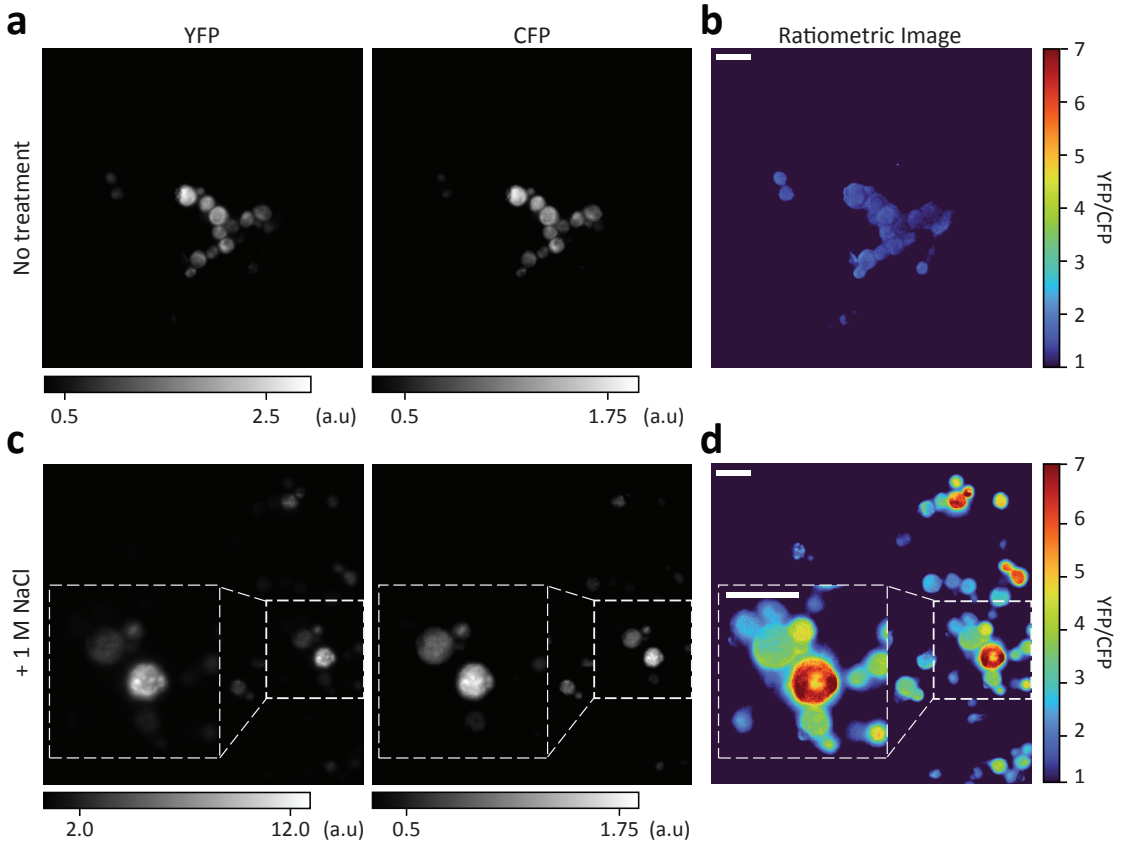


Figure 5.3: Cryogenic ratiometric imaging of SED1 expressed in *S. cerevisiae*. **a**. Fluorescence images of vitrified *S. cerevisiae* expressing SED1 at emission wavelengths of 545 ± 20 nm (YFP; left) and 465 ± 15 nm (CFP; right). **b**. Ratiometric image (YFP/CFP) of the images in (**a**). **c**. Same as in (**a**) but treated with 1 M NaCl. **d**. Ratiometric image (YFP/CFP) of the images in (**c**). Scale bars: 10 μm.

light microscopy of these samples was performed using the same excitation and emission collection conditions as above.

In the untreated sample (Fig. 5.3a-b), the fluorescence signal in the two channels was comparable, resulting in cellular YFP/CFP ratios less than 2. Notably, the ratiometric signal was homogenous across the cells in the sample (Fig. 5.3b). In contrast, SED1 YFP emission doubled in the treated cells 5.3c), resulting in YFP/CFP ratios greater than 3 (Fig. 5.3d). There was also an apparent heterogeneity in the ratiometric measurements between cells in the treated sample. As the YFP/CFP ratio in the untreated sample was uniform, we reason that the ratio heterogeneity in the treated sample stems from differential osmotic stress response within the sample, rather than intrinsic variability in the sensor response.

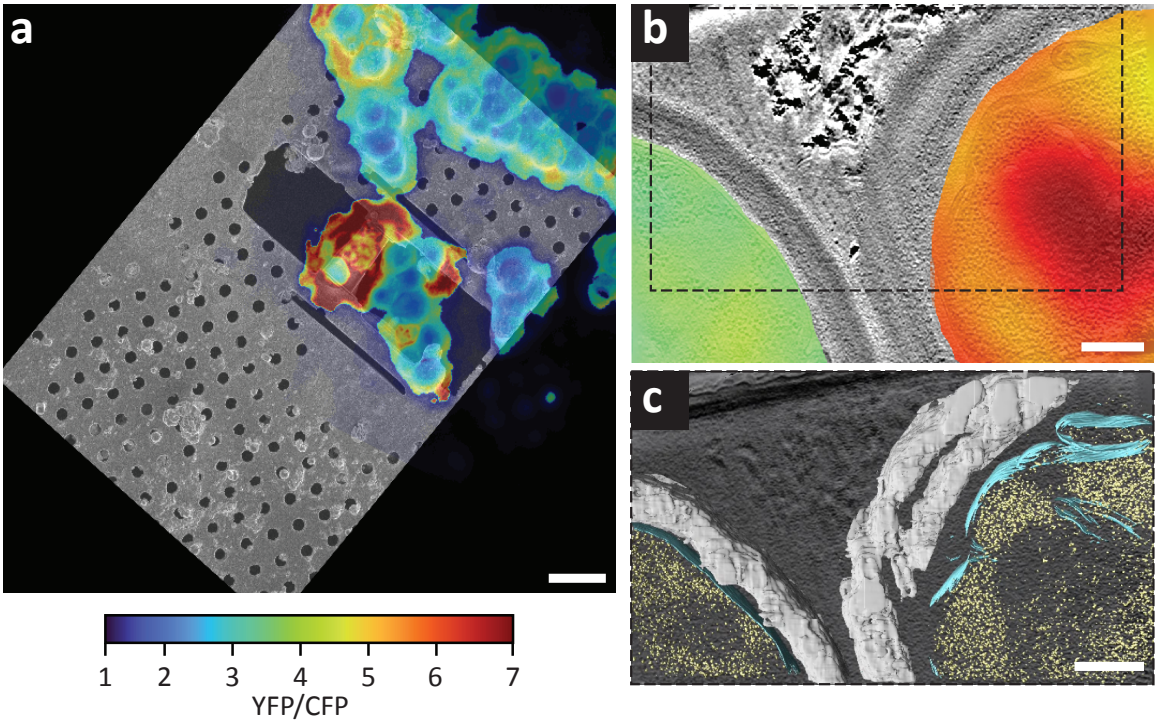


Figure 5.4: cryoCLEM of SED1 in *S. cerevisiae*. **a**. Electron micrograph (gray) overlaid with a registered ratiometric image color-coded by the YFP/CFP ratio. Scale bar: 10 µm. **b**. Electron tomogram reconstruction z-slice (gray) overlaid with the registered ratiometric image color-coded by YFP/CFP ratio. Dashed-line box highlights the segmented region shown in (**c**). Scale bar: 1 µm. **c**. Segmentation of the tomogram in (**b**) showing the cell wall (gray), membrane (blue), and ribosomes (gold). Scale bar: 1 µm.

To determine whether differences in the osmotic stress response correlate with changes in mesoscale structure, we prepared the treated *S. cerevisiae* cells for cryoET. Thin yeast lamellae were generated by focused ion beam (FIB) milling on a cryogenic dual-beam system. We targeted adjacent cells with different ratiometric responses for milling by cross-referencing with the cryogenic fluorescence images (Fig. 5.4a). We loaded the milled samples into a cryogenic electron microscope for tomography, recorded tilt series of several cells, including the cells show in Figure 5.4a-b, and reconstructed their 3D volumes. Registered fluorescence ratio images on their corresponding z-slice of the tomographic reconstruction depict fluorescence signal within the cytoplasmic region of the S. cerevisiae cells (Fig. 5.4b) showing a good agreement between the imaging modalities. We then segmented and annotated the tomographic reconstructions to identify recognizable mesoscale structures such as the cell wall, cell membrane, and ribosomes (Fig. 5.4c). Strikingly, the cell with a YFP/CFP ratio of 5.5, corresponding to crowding levels equivalent to approximately 10% PEG4000 *in vitro*, had structural perturbations. For instance, there were noticeable deformations to the cell wall and membrane in addition to a detachment of the membrane from the cell wall. These observations contrast with the adjacent cell, which had a ratio of approximately 4 and retained its membrane integrity. The correlation of cellular structure with the molecular crowding levels of the cells highlights structural differences between adjacent cells that are treated uniformly, providing additional context for structural differences that would otherwise remain elusive in origin.

5.2.3 pHRed preserves its pH sensing at cryogenic temperatures

Another key physiologically relevant environmental factor is pH. Intracellular pH modulates protein structure and function and plays important roles in membrane transport, energy production, and organelle homeostasis [280]. While typically buffered to a pH of 7.2-7.4, living cells can exhibit pH fluctuations due to their cell cycle or in response to external environmental changes. Notably, certain disease states are associated with al-

tered cellular pH levels [292–294]. Eukaryotes also compartmentalize different chemical environments within organelles, such as the lysosome, which has a relatively low pH (pH < 5), and the mitochondria, which maintains a pH of 8 within its lumen. Variable pH in organelles may be observed in prokaryotes as well; for example, carboxysomes are proposed to have a more acidic internal environment compared to the surrounding bacterial cytoplasm [295–297]. Given the central roles of pH in organelle homeostasis, we explored the applicability of pH sensors for cryoCLEM.

We first tested the pH sensor, pHRed, which emits at 610 nm and has two excitation maxima dependent on chromophore protonation (Fig. 5.5a-b) [298]. In acidic conditions, pHRed has an excitation peak at 585 nm, while in basic conditions, an excitation peak at 440 nm emerges. We tested the response of purified pHRed at RT and 77 K at two distinct pH levels, pH 5.5 and pH 9. Notably, pHRed was visually dim in solution and required an additional 594 longpass emission filter to improve the signal-to-noise ratio (SNR). The excitation spectra of pHRed behaved as expected at RT (Fig. 5.5b). At 77 K, pHRed exhibited a similar response but with notably narrowed linewidths. At pH 5.5, there were two prominent and narrow excitation peaks at 414 nm and 578 nm, with the 578 nm peak resulting in two-fold greater emission than the 414 nm peak (Fig. 5.5c). The inverse occurred at pH 9, with the 414 nm excitation having two-fold greater emission than the 578 nm peak. This result indicates that pHRed preserves its pH sensitivity at 77 K.

Next, we calibrated vitrified pHRed on a cryogenic light microscope. We imaged high-pressure frozen samples of pHRed in buffer solution ranging from pH 5.5-9 using interleaved excitation with 425 nm and 561 nm light. The resulting fluorescence ratios of 425/561 nm displayed a clear relationship with pH (Fig. 5.5d).

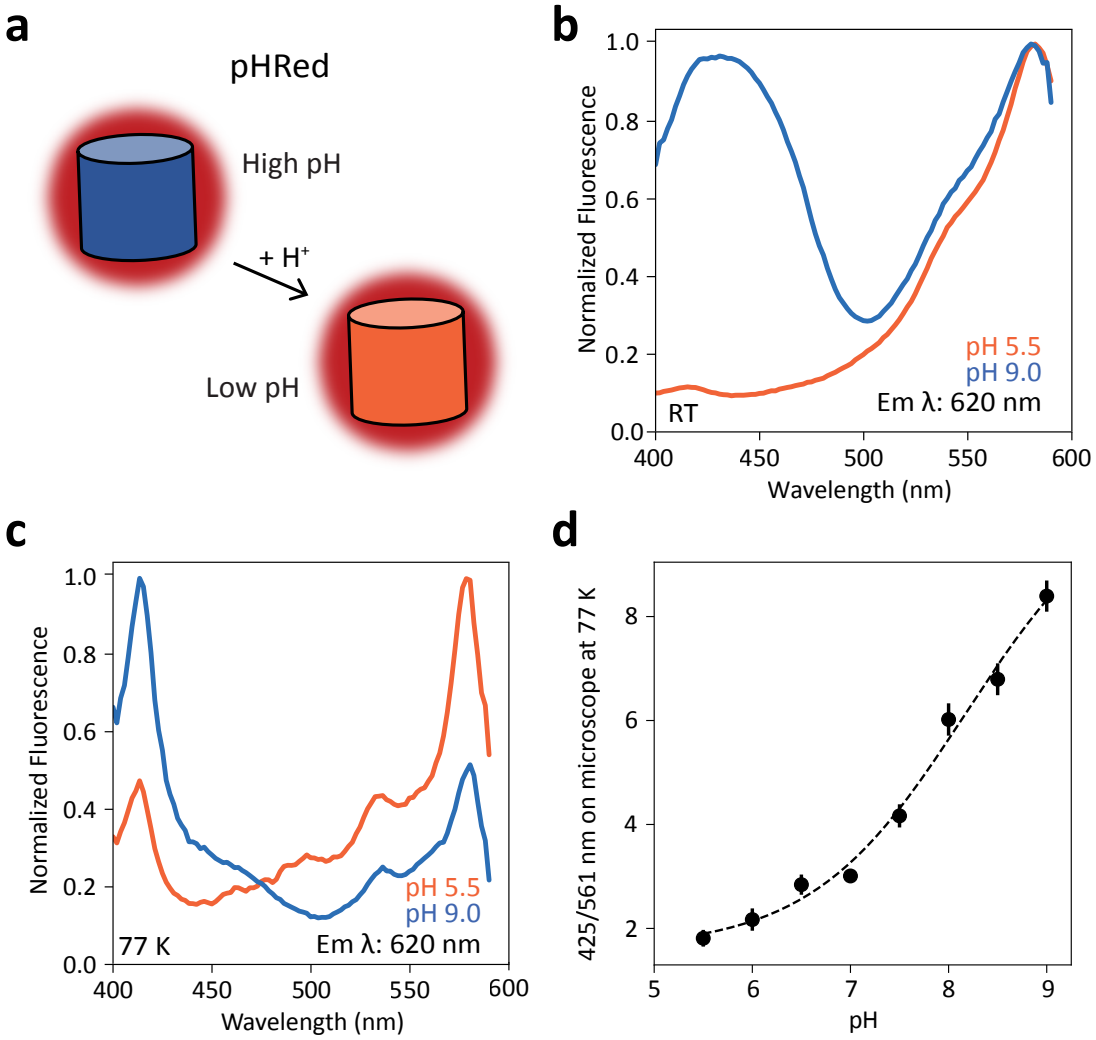


Figure 5.5: pHRed maintains its pH-sensing properties at cryogenic temperatures. a. pHRed excitation profile responds to the pH of its environment. **b-c**. Excitation spectra of pHRed in pH 5.5 and pH 9 at (**b**) RT (**c**) 77 K. Emission was collected at 620 nm. Each spectrum was normalized independently. **d** Calibration curve of vitrified pHRed measure on a microscope at 77 K. Each point on the calibration is the average of at least 5 ratiometric measurements for each condition. The error bars represent the SEM. The dashed line represents the fit of a continuous logistic function.

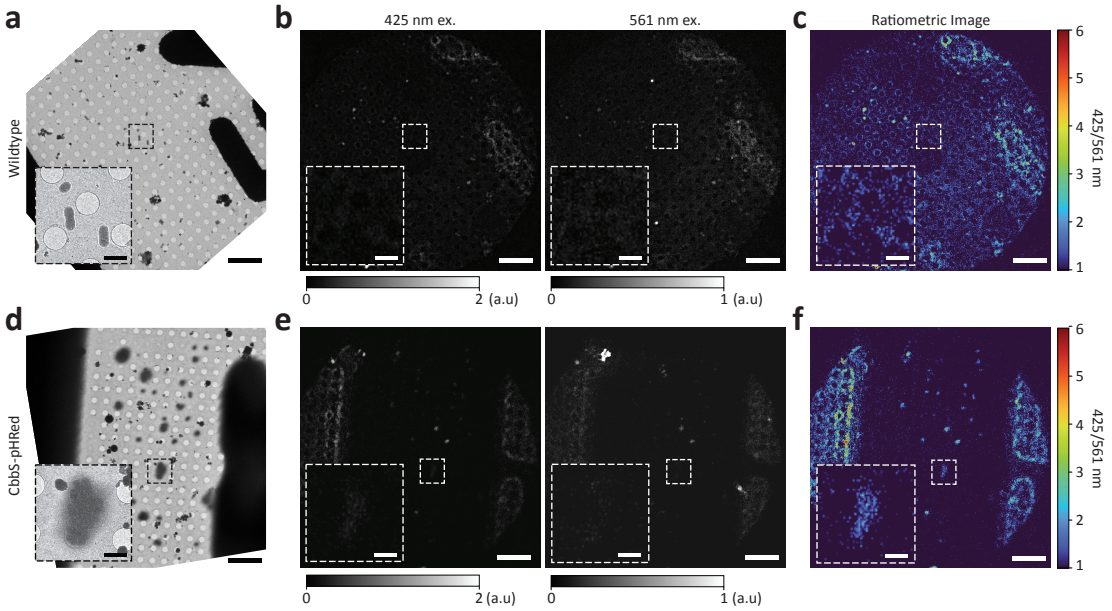


Figure 5.6: pHRed is too dim for cryoCLEM. a. Low-magnification electron micrograph of vitrified wildtype *H. neapolitanus* cells. **b**. Cryogenic fluorescence images of the same grid square from (**a**) with 425 nm (left) and 561 nm (right) excitation. **c**. Ratiometric image (425/561 nm) of images in (**b**). **d**. Low-magnification electron micrograph of vitrified wildtype *H. neapolitanus* cells expressing CbbS-pHRed. **e**. Cryogenic fluorescence images of the same grid square from (**d**) with 425 nm (left) and 561 nm (right) excitation. f Ratiometric image (425/561 nm) of images in (**e**). Scale bars: 10 µm. Inset scale bar: 2 µm.

5.2.4 Cryogenic light microscopy of H. neapolitanus demonstrates pHRed as an unsuitable biosensor for cryoCLEM

The internal pH of carboxysomes affects the kinetics of the enzymes it encapsulates, making pH regulation critical for carbon fixation. A lower pH (< 7.2) is proposed to drive the equilibrium from permeabilized HCO_3^- to $CO2_2$, which can then be fixed into organic carbon by RuBisCO [295, 296]. Moreover, carboxysomes are structurally heterogeneous, displaying variations in size, composition, and the packing of their encapsulated enzymes [299, 300]. Here, we used pHRed to explore whether there is a correlation between carboxysome structure and pH. We labeled the small subunit of RuBisCO (CbbS) with pHRed to specifically target it to the carboxysome lumen in *H. neapolitanus* cells.

Given our previous observation that pHRed is a dim emitter, we prepared vitrified samples of both wildtype- and CbbS-pHRed- containing *H. neapolitanus* cells to verify the SNR of pHRed *in situ* (Fig. 5.6). In wild-type cells, we found no cellular pHRed signal discernable from background sample fluorescence, as confirmed by correlating cell locations with a low-magnification electron micrograph (Fig. 5.6a-b). Consistent with the lack of signal, the 425/561 nm signal ratio was uniform across the grid. Cells containing CbbS-pHRed were identified but had a poor signal-to-noise (Fig. 5.6d-e), resulting in ratiometric measurements below the dynamic range of the pHRed calibration (Fig. 5.6f). Due to these limitations, we concluded that pHRed is too dim for effective use in cryoCLEM and explored two alternative pH sensors: pHmScarlet and pHluorin2.

5.2.5 pHmScarlet and pHluorin2 are alternative pH sensors for cryoCLEM

pHmScarlet is derived from the stable, red fluorescent protein, mScarlet-I [301]. At pH 8, pHmScarlet has an excitation maximum at 561 nm; decreasing pH results in decreased emission measured at 612 nm (Fig. 5.7a-b). This fluorescent protein also exhibits a pH-dependent change in its excitation maximum, shifting from 561 nm at pH 8-10 to approximately 500 nm below pH 7. This shift suggests that pHmScarlet could function as

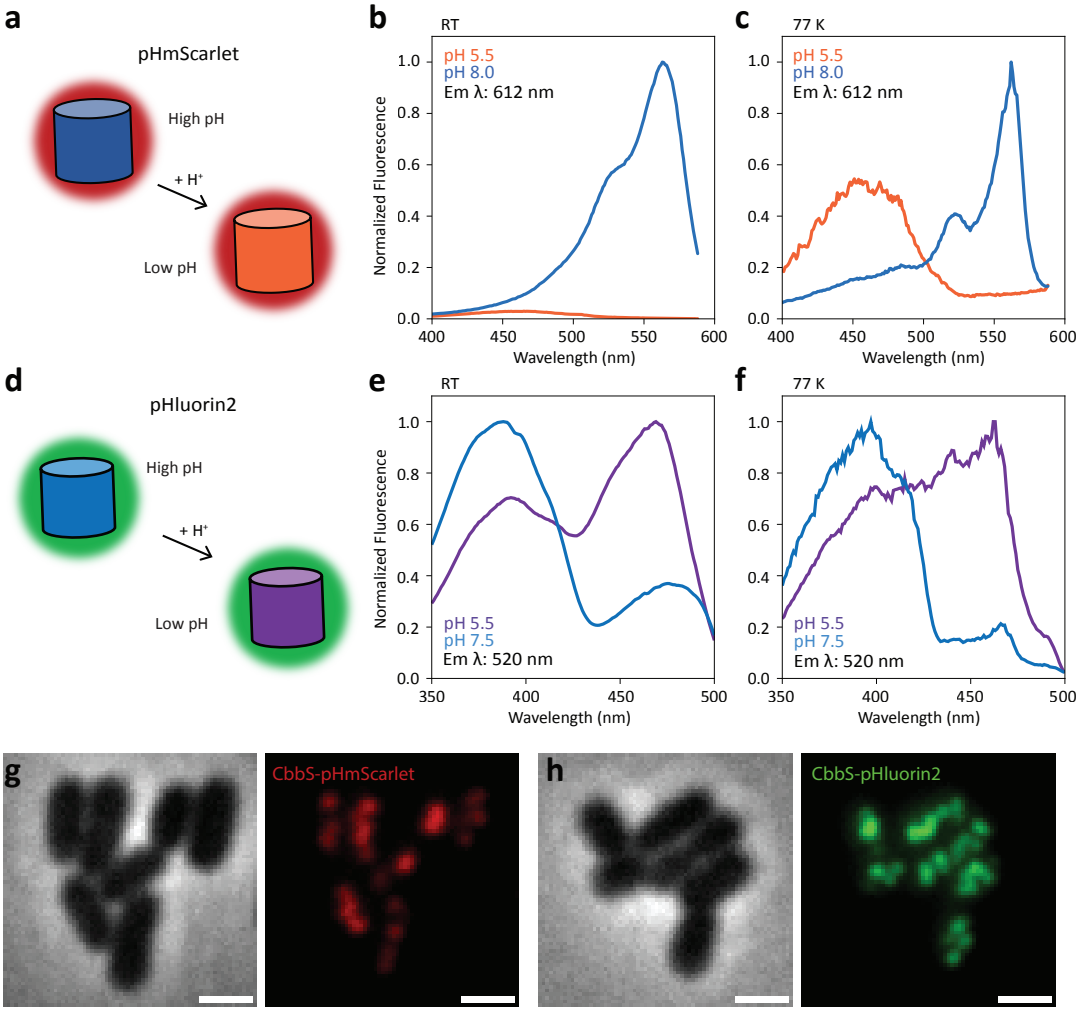


Figure 5.7: Alternative pH sensors for cryoCLEM. a. pHmScarlet excitation profile responds to the pH of its environment. **b-c**. Excitation spectra of pHmScarlet at pH 5.5 and pH 8 at (**b**) RT and (**c**) 77 K. Emission was collected at 612 nm. Each spectrum was normalized independently. **d**. pHluorin2 excitation profile responds to the pH of its environment. **e-f**. Excitation spectra of pHluorin2 at pH 5.5 and pH 7.5 at (**e**) RT and (**f**) 77 K. Emission was collected at 612 nm. Each spectrum was normalized independently. **g-h**. Phase contrast (left) and fluorescence (right) images of *H. neapolitanus* cells expressing (**g**) CbbS-pHmScarlet (red) and (**h**) CbbS-pHluorin2 (green). Scale bars: 1 µm.

a ratiometric biosensor. At 77 K, the 561 nm peak was preserved at pH 8. However, at pH 5.5, the excitation peaked at 455 nm (Fig. 5.7c), consistent with the reported change in absorption. The increased excitation at the blue wavelengths makes pHmScarlet a promising ratiometric fluorescent reporter of pH.

pHluorin2 is pH-sensitive green fluorescent protein with a bimodal excitation spectrum (Mahon 2011). At high pH, pHluorin2 excitation is maximized at its 395 nm peak, while at low pH, its 475 nm excitation peak dominates (Fig. 5.7d). As expected, the RT excitation spectra of pHluorin2 at pH 5.5 and 7.5 mirrored the reported behavior (Fig. 5.7e). At 77 K, pHluorin2 preserved its spectral differences in either pH (Fig. 5.7f), demonstrating its potential use for cryoCLEM.

To test the applicability of pHmScarlet and pHluorin2 for cellular cryoCLEM, we generated *H. neapolitanus* strains expressing CbbS-pHmScarlet or CbbS-pHluorin2 (Fig. 5.7g-h). We verified that these fusions do not disrupt carboxysome function by RT fluorescence imaging. The fluorescence signal from both strains displayed puncta distributed in the cell, representative of CbbS recruitment to carboxysomes. This observation is consistent with previous functional fluorescent fusions of CbbS (CbbS-mTurquoise2) [81,131]. Future work will focus on cryogenic calibration of pHmScarlet and pHluorin2, and ratiometric cryoCLEM of these strains.

5.2.6 MatryoshCaMP6s loses its calcium sensitivity at 77 K

Another crucial ion in cell biology is calcium (Ca^{2+}). It plays important roles in signaling, cell division, cell motility, cell differentiation, and virulence, among others [281, 302,303]. For this reason, genetically encoded calcium indicators (GECIs) are often used to monitor Ca^{2+} dynamics and subcellular localization, especially in the context of neuronal activity [196, 304, 305]. The prevalence of Ca^{2+} in biological processes makes it a prime target for biosensor cryoCLEM. To identify a suitable Ca^{2+} biosensor for cryoCLEM, we tested two ratiometric sensors with distinct mechanisms and emission profiles.

First we tested MatryoshCaMP6s, a GCaMP-based biosensor with a nested reference reporter geometry [306]. This design includes a calcium reporting module GCamP6s, composed of a calmodulin domain, an M13 peptide, and a circularly permuted Enhanced GFP (cpEGFP), along with a nested large Stokes Shift (LSS) mOrange as a reference fluorescent protein (Fig. 5.8a). Both fluorescent proteins have overlapping excitation at 440 nm and emit at 510 nm and 570 nm, respectively, allowing for ratiometric readouts. Upon binding to calcium, the calmodulin domain binds the M13 peptide, which in turn makes the cpEGFP more compact. This structural change stabilizes the environment around the EGFP chromophore, enhancing its fluorescence emission.

We collected emission spectra of MatryoshCaMP6s to verify its behavior at RT and 77 K. At RT, the GCaMP6s emission was 10% of the reference emission in the absence of Ca^{2+}; upon addition of Ca^{2+}, we observed a 10-fold enhancement in GCaMP6s emission (Fig. 5.8b). Surprisingly, at 77 K, the GCaMP6s emission was 90% of the reference emission in the absence of Ca^{2+}, a massive increase compared to RT. In the presence of Ca2+, the GCaMP6s emission was identical to RT.

We hypothesize that the high emission of GCaMP6s in the absence of Ca^{2+} at 77 K is due to a temperature-imposed steric hinderance on the chromophore. This phenomenon was previously reported for model compounds of the GFP chromophore, which were non-fluorescent in solution due to the lack of constraints imposed by the protein (Maddalo and Zimmer, 2006). Upon freezing of the chromophore to 77 K, fluorescence was achieved by steric barriers to chromophore rotation. Given the reduced dynamic range of MatryoshCaMP6s at 77 K, we find it unsuitable as a biosensor for cryoCLEM.

5.2.7 jREX-GECO1 preserves its calcium sensing at cryogenic temperatures

The continuous development of GCaMP sensors has led to an expanded color palette. Among these are red GECIs, which are more desirable due to their red-shifted excitation wavelengths, making them more suitable for deep-tissue imaging and reducing photo-

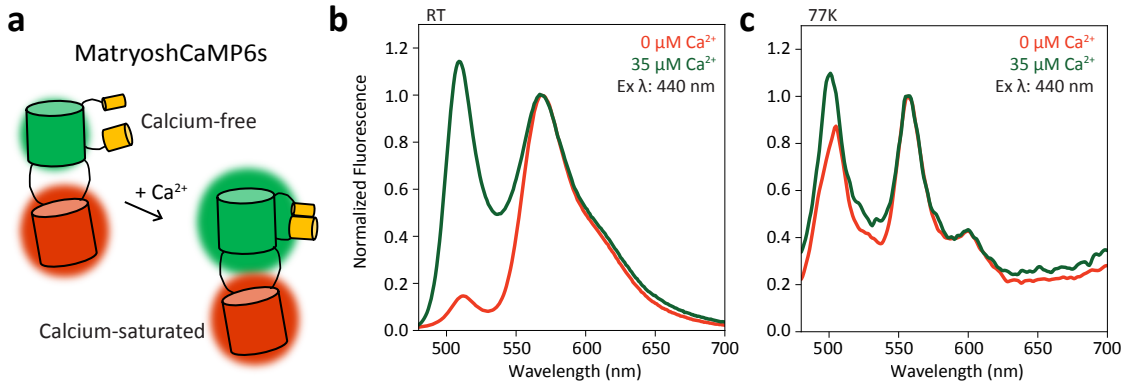


Figure 5.8: MatryoshCaMP does not sense calcium at cryogenic temperature. a. MatryoshCaMP6s is a nested calmodulin based ratiometric sensor. Upon calcium binding the calmodulin domain (yellow) undergoes a conformation change that rigidifies the cpEGFP (green) chromophore, increasing its emission. A large Stokes shift mOrange (LSSmOrange) is used as a reference fluorescent protein. **b-c**. Emission spectra of MatryoshCaMP6s at (**b**) RT and (**c**) 77 K with and without calcium. Samples were excited with 440 nm light. Each spectrum was normalized to the emission peak of LSSmOrange: 568 nm for RT and 556 nm for 77 K.

damage and cellular autofluorescence [307, 308]. We tested the red GECI jREX-GECO1, an engineered descendant of the fluorescent protein mApple (Fig. 5.9a) [309, 310]. In its calcium-free form, jREX-GECO1 behaves like a red fluorescent protein, with excitation and emission maxima at 577 nm and 585 nm, respectively. When saturated with calcium, jREX-GECO1 switches to a large Stokes shift form with excitation and emission at 480 nm and 600 nm, respectively.

Consistent with its reported mechanism, the excitation maxima of jREX-GECO1 shifted from approximately 575 nm to 480 nm in Ca^{2+}-saturating conditions (Fig. 5.9b). This behavior is preserved at 77 K (Fig. 5.9c). Calibration of high-pressure frozen jREX-GECO1 displayed its wide dynamic range, capturing typical intracellular Ca^{2+} concentrations of 100 nM and differentiating levels up to 10 µM (Fig. 5.9d), demonstrating the potential for jREX-GECO1 as a calcium sensor in cryoCLEM.

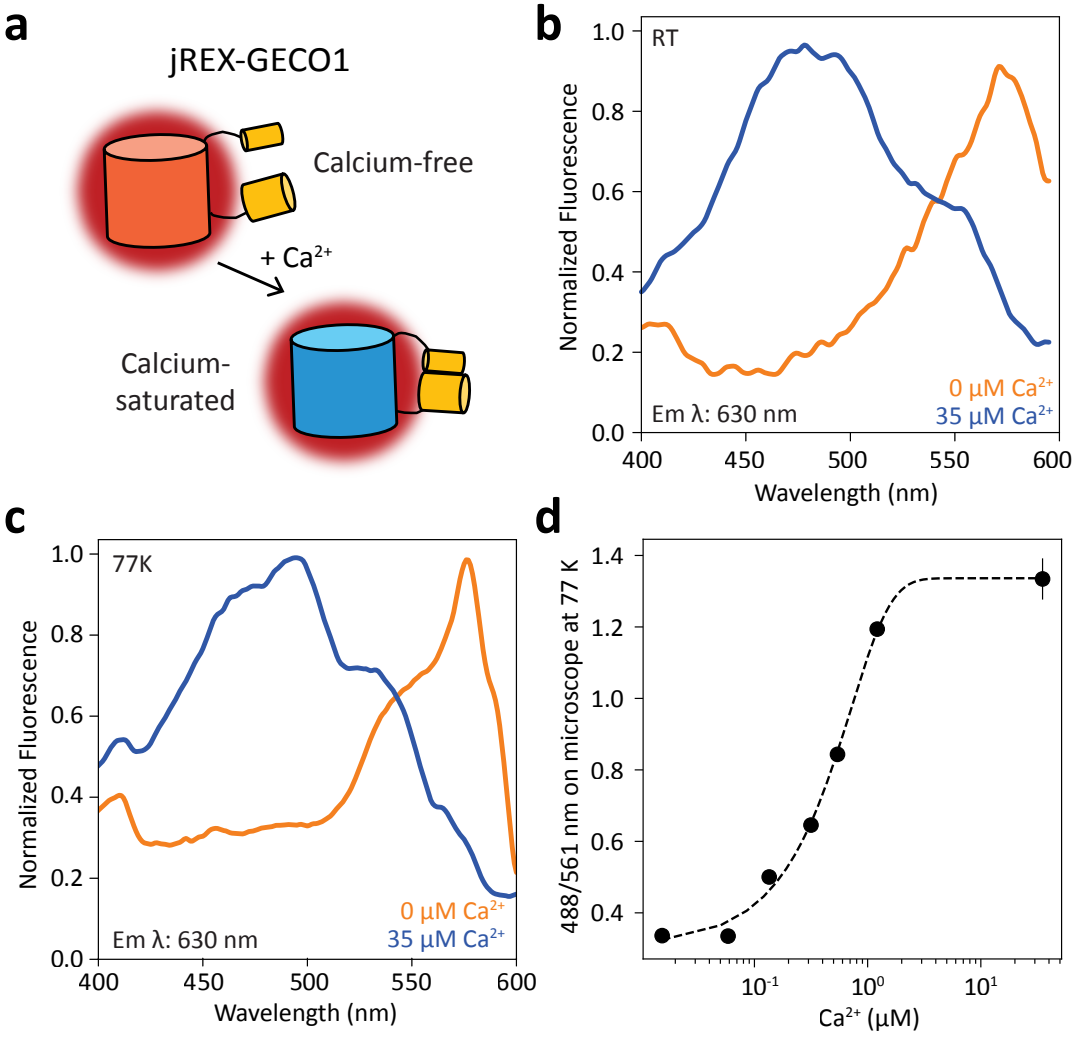


Figure 5.9: jREX-GECO1 maintains its calcium-sending properties at cryogenic temperatures. a. jREX-GECO1 is a calmodulin based ratiometric biosensor. Upon calcium binding, the calmodulin domain undergoes a conformational change the results in a blue-shifted excitation spectrum. **b-c**. Excitation spectra of jREX-GECO1 at (**b**) RT and (**c**) 77 K with and without calcium. Emission was collected a 630 nm. Each spectrum was normalized independently. **d**. Calibration curve of vitrified jREX-GECO1 measured on a microscope at 77 K. Each point on the calibration is the average of at least 5 ratiometric measurements for each condition. The error bars represent the standard error on the mean. The dashed line represents the fit of a continuous logistic function.

5.3 Discussion

In this work, we have identified fluorescent biosensors for monitoring molecular crowding, pH, and calcium, respectively, in cryoCLEM. We demonstrated that SED1 preserves its ability to report on osmotic stress through molecular crowding sensing at cryogenic temperature. Further, we illustrated the efficacy of SED1 in cryoCLEM by revealing structural perturbations in *S. cerevisiae* in response to osmotic stress. We also identified pHRed, pHluorin2, and pHmScarlet as pH sensors that preserve their function at cryogenic temperatures. Finally, we found that MatryoshCaMP6s, a GCaMP-based fluorescent calcium reporter, is unsuitable for cryoCLEM, but demonstrated that jREX-GECO1 is a viable red-emitting alternative for calcium sensing. We believe that identifying and applying fluorescent biosensors for cryoCLEM enhances an already powerful tool to understand the local chemical environments of subcellular structures and provide insight into the heterogeneities observed in structural investigations.

Our exploration of diverse fluorescent biosensors also provides guiding principles into the future selection of biosensors for cryoCLEM. For example, our demonstration of SED1 as an molecular crowding sensor highlights the potential for FRET-based sensors that use an intrinsically disordered linker as the sensing unit to be applied in cryoCLEM. Intrinsically disordered protein regions (IDRs) are highly sensitive to their physicochemical environment, resulting in conformational biases due to varying pH, salt, temperatures, and metabolites [311]. This property suggests that IDRs can be further engineered for specificity and sensitivity, and when coupled with FRET-compatible fluorescent proteins, IDRs can be exploited as biological sensors. Conversely, the loss of dynamic range by MatryoshCaMP6s at 77 K highlights a sensing mechanism that should be avoided in future studies. Sensors that rely on the flexibility or rigidity of their chromophores for quenching or enhancing fluorescence are not suitable for cryogenic studies, as cold temperatures heavily impact these photophysical dynamics. Additionally, this finding underscores the importance of validating fluorescent biosensors at cryogenic temperature prior to their

implementation for cellular cryoCLEM.

The data presented here builds on the original proof-of-principle demonstration of roGFP2 as a redox state sensor in cryoCLEM. We anticipate that future development of the approach will include its coupling to subtomogram averaging. Molecular structures can be binned by their local chemical environment to generate high-resolution structure classes that correspond to a specific chemical state. Such classifications may require the transition from cryogenic ensemble fluorescence measurements to cryogenic super-resolution imaging, an area of active research [177]. With such developments, biosensor cryoCLEM has the potential to couple specific chemical information to high-resolution structures *in situ*.

5.4 Materials and Methods

5.4.1 Protein Purification

An overnight culture DH5α *E. coli* cells expressing N-terminal His-tagged pHRed of a pRsetB-pHRed plasmid (AddGene Plasmid 31472) was inoculated (1:100) into a one-L culture of LB + carbenicillin (100 μg/ml) and grown at 37 °C with shaking until OD_{600} 1 – 1.2. Cells were pelleted and stored at -80 °C. Bacterial pellets were resuspended in 40 mL lysis buffer [100 mM MOPS pH 7.4; 50 mM KCl; 5 mM NaCl; 0.5 mM MgCl2; 20 mM Imidazole pH 7.4; 10% glycerol; 0.05 mg/ml Lysozyme (Thermo Fisher); protease inhibitor tablet (Thermo Fisher)], sonicated with cycles of 10 s on, 20 s off at 50% power for 6 min. Lysates were clarified via centrifugation at 13,000 rpm at 4 °C for 30 min. Clarified lysates were passed through a 0.45-μm filter a loaded onto a 1-ml HisTrap HP (Cytiva) equilibrated in buffer A [100 mM MOPS pH 7.4; 50 mM KCl; 5 mM NaCl; 0.5 mM MgCl2; 20 mM Imidazole pH 7.4; 10% glycerol; 5 mM 2-Mercaptoethanol (BME)]. Columns were washed with 5 column volumes of 5% buffer A. Elution was performed using a 5-100% gradient of buffer B [100 mM MOPS pH 7.4; 50 mM KCl; 5 mM NaCl; 0.5 mM MgCl2; 500 mM Imidazole pH

Table 5.1: Plasmids used in this study

Supplementary Table 5.1 Plasmids used in this study

Plasmid	Description	Source
pDEST-HisMBP-SED1	Bacterial expression of SED1	Cuevas-Velazquez et al., 2021
pRsetB-pHRed	Bacterial expression of pHRed	Tantama et al., 2010
RpHluorin2	Bacterial expression of pHluorin2	Linders et al., 2022
pBAD-pHScarlet	Bacterial expression of pHmScarlet	Campbell Lab
pET15b-eGO-Matryoshka-LE-LP	Bacterial expression of MatryoshCaMP6s	Ast et al., 2017
pTorPE-jREX-GECO1	Bacterial expression of jREX-GECO1	Molina et al., 2019
cbbS-pHRed	For chromosomal replacement of the native *cbbS* gene in *H. neapolitanus*	This study
cbbS-pHmScarlet	For chromosomal replacement of the native *cbbS* gene in *H. neapolitanus*	This study
cbbS-pHluorin2	For chromosomal replacement of the native *cbbS* gene in *H. neapolitanus*	This study

7.4; 10% glycerol; 5 mM BME] via an AKTA Pure system (Cytiva). Fractions with the highest yield were pooled, concentrated, passed through a 0.45-µM filter, and passed through a size exclusion column. Peak fractions were pooled, concentrated in storage buffer [10 mM HEPES pH 7.4; 120 mM KCl; 10 mM NaCl; 0.5 mM MgCl2, 10% glycerol], and stored at -80 °C.

Purification of other fluorescent biosensors was performed according to Cranfill et al. with minor adjustments [312]. Top10 chemically competent or BL21 *E. coli* cells (Thermo Fisher, Cat. C404003) were transformed with the appropriate plasmid (see Table 5.1 for plasmids used in this study) and grown to OD_{600} 0.6 in LB medium containing the appropriate antibiotic at 37 °C. Heterologous protein expression was then initiated with 0.02% w/v L-arabinose (Sigma A3256) or 0.5 mM IPTG overnight at 30 °C. Cells were collected by centrifugation (4000 g, 10 min) and stored at -80 °C. For purification, cells were resuspended and lysed in BugBuster Master Mix Protein Extraction Reagent (MilliporeSigma, Cat. 71456) at room temperature following the manufacturer's recommendation. Lysate was cleared by centrifugation (15000 g, 10 min) and the soluble fraction of His-tagged proteins was purified using His SpinTrap columns (Cytiva, Cat. 28401353) following the manufacturer's protocol. The eluate protein from NiNTA columns was buffered exchanged into PBS pH 7.4 and concentrated with 3 kDa Amicon Ultra-4 centrifugal filter units (Mil-

liporeSigma Cat. UFC800308). Proteins were frozen and stored at -80 °C.

5.4.2 Fluorescence spectroscopy

Purified SED1 was added to a solution of 20 mM PBS pH 7.4 with and without 10% PEG4000 (w/v. Emission spectra of both solutions were collected a room temperature by exciting at 410 nm (5 nm slit width) and collecting emission from 425-700 nm (2 nm slit width), with an exposure time of 0.1 s. The same cuvette was then dunked in liquid nitrogen and data collection was repeated using the same conditions.

Purified pHRed was added into buffers of pH 5.5 (50 mM MES-NaOH, 300 mM NaCl) and pH 9.0 (50 mM Tris-HCl, 300 mM NaCl) in a cuvette and loaded in a fluorimeter (Horiba Fluorolog 3). Excitation spectra of both solutions were collected from 400-590 nm (5 nm slit width) excitation and emission at 630 nm (20 nm slit width), with an exposure time of 0.5 s. A 594 nm long-pass filter was added before the detector to reduce scattered light detection. Excitation spectra of the frozen samples were collected as above, except the exposure time was changed to 0.1 s and five spectra collected in succession were averaged together.

Purified pHmScarlet was added to buffers of pH 5.5 (50 mM MES-NaOH, 300 mM NaCl) and pH 8 (50 mM Tris-HCl, 300 mM NaCl). Excitation spectra of both solutions at RT and freezing were collected with 400-585 nm excitation and emission at 612 nm, with an exposure time of 0.1 s.

Purified pHluorin2 was added to buffers of pH 5.5 (50 mM MES-NaOH, 300 mM NaCl) and pH 7.5 (50 mM MOPS-HCl, 300 mM NaCl). Excitation spectra of both solutions at RT and freezing were collected with 350-500 nm excitation and emission at 520 nm, with an exposure time of 0.1 s.

Purified MatryoshCaMP6s and jREX-GECO1 were added to a buffer solution with 35 μM Ca^{2+} and absent of Ca^{2+} (Invitrogen, Cat. C3008MP). RT and frozen MatryoshCaMP6s emission spectra were recorded by exciting at 440 nm and collecting emission from 480-

700 nm. The excitation spectra of RT and frozen jREX-GECO1 were recorded by exciting from 400-590 nm and collecting emission at 630 nm.

5.4.3 Cryogenic freezing of purified biosensors

Purified pHRed was added to buffer solutions with varying pH. The buffers contained 300 mM NaCl and 50 mM of one of the following buffers: MES for pH 5.5-6.0, MOPS for pH 6.5-8.0, and Tris for pH 8.5-9.0. Purified SED1 was added to a solution of 20 mM PBS pH 7.4 with various concentrations of PEG4000: 0, 2, 4, 8, 12, 16, 20% (w/v). Purified jREX-GECO1 was added to a buffer solution at various Ca^{2+} concentrations. The solutions were made using a commercially available calcium calibration buffer kit (Invitrogen, Cat. C3008MP) at the following concentrations: 0, 0.015, 0.058, 0.135, 0.316, 0.542, 1.215, and 35.0 μM.

A small aliquot (10-15 μL) of each sample was added to the 0.2 mm side of a glow-discharged Type A 6 mm gold carrier and sandwiched with the flat side of a Type B 6 mm gold carrier. The sandwich carrier was immediately transferred to a high-pressure freezer (Leica ICE, Leica Microsystems) to generate a thick layer (0.2 mm) of frozen protein. After cryogenic freezing, the gold carriers were stored in liquid nitrogen.

5.4.4 Production of strains

Production of CbbS-pHRed, CbbS-pHmScarlet, and CbbS-pHluorin2 *H. neapolitanus* strains: Construct cloning and transformation of *H. neapolitanus* was performed as described in MacCready and Tran et al. [131]. Briefly, the fusion constructs were generated using Gibson Assembly, verified by sequencing, and transformed into competent cells of *H. neapolitanus* (ATCC® 23641™) for homologous recombination into the native carboxysome (*cso*) operon. The sequence encoding the fluorescent protein was attached to the 3' region of the native *cbbS* coding sequence, separated by a GSGSGS linker. A kanamycin resistance cassette was inserted immediately downstream of the *cbbS* coding sequence. Transformants were selected by plating on S6 medium with kanamycin (50

Table 5.2: Strains used in this study

Supplementary Table 5.2. Strains used in this study

Strain	Description	Source
S. cerevisiae (SED1)	*S. cerevisiae* (BY4742) with *pDRFLIP38-SED1*	Cuevas-Velazquez et al., 2021
AGV_Hn_1	*H. neapolitanus*	ATCC
AGV_Hn_509	*H. neapolitanus cbbS::cbbS-pHRed*	This study
AGV_Hn_543	*H. neapolitanus cbbS::cbbS-pHluorin2*	This study
AGV_Hn_547	*H. neapolitanus cbbS::cbbS-pHmScarlet*	This study

µg/ml). Colonies were restreaked and subsequent colonies were verified for insertion by PCR and fluorescence microscopy. Colonies positive for the fusion and negative for the presence of plasmid were grown in S-6 medium and stored at -80 °C in 10% DMSO. All strains used in this study can be found in Table 5.2 .

5.4.5 Cell growth and sample preparation

Frozen *H. neapolitanus* cells were streaked onto an S-6 plate and incubated for 4-6 days at 30 °C in air supplemented with 5% CO_2. Single colonies were then inoculated in 4 mL of S-6 medium and incubated for 36-40 hr at 30 °C while shaken at 130 RPM in air supplemented with 5% CO_2. This culture was diluted (1:100) into 10 ml of fresh S-6 medium and grown for 24-30 hr. Cells were harvested by centrifugation at 5,000 rpm for 10 min and resuspended in 20 µl of spent S-6 medium. A 4 µl aliquot of the resuspension was mixed with 4 µL of a solution with 15-nm gold beads (EMS, Cat. 25489) and loaded on a glow-discharged carbon finder grids (EMS, Cat. cf-200-cu-50), blotted for 2 s, and plunge frozen in liquid ethane (Leica).

S. cerevisiae cells expressing SED1 were streaked onto a YNB SD-ura plate and incubated at 30 °C for 2-3 days. Single colonies were inoculated in 5 mL of YNB SD-ura medium and grown for 18-20 hrs at 30 °C, while shaken at 250 RPM. An aliquot of 1 ml of cells was harvested by centrifugation and resuspended in 100 µl of spent YNB SD-ura medium. To osmotically shock the cells, 1 M NaCl was added to 50 µl of the cell resuspension approximately 10 min before plunge freezing. A 3 µl aliquot of treated and untreated cells was

loaded on a glow-discharged carbon finder grids (EMS, Cat. cf-200-cu-50), blotted for 2 s, and plunge-frozen in liquid ethane (Gatan CP3).

5.4.6 Cryogenic fluorescence microscopy

Cryogenic fluorescence microscopy was conducted at 77 K on a home-built open cup cryostat described previously [313]. Liquid nitrogen was added to an insulated stainless-steel cup, cooling a mounted copper pedestal to near 77 K. The sample planchette or grid was then loaded onto the pedestal. The samples were imaged with a room-temperature Nikon CFI Plan Achromat LWD IMSI 100 XC (NA 0.85) through a 1 mm glass window. Appropriate excitation and emission filters (described below) were used for each biosensor, and emission was collected by an EMCCD (Andor iXon Ultra 897). For calibrations of cryogenic-frozen purified biosensors, 4-15 different regions on the gold carriers were imaged.

Purified and frozen SED1 was excited with 425 nm (Omicron LuxX) at 0.512 mW (at sample) passing through at 427/10 nm excitation filter. Fluorescence emission over the range 450-565 nm was distinguished from scattered excitation by a dichroic mirror, a 440 nm long pass filter, and two bandpass filters for CFP and YFP emission collection: 465/30 nm bandpass filter for 3-4 s and 545/40 nm bandpass filter for 3-4 s, respectively. Images were collected at 1 Hz with a gain input of 3. Plunge-frozen *S. cerevisiae* cells were excited with 425 nm (0.035 mW; at sample). Emission was collected as above but with a gain of 10.

Purified and frozen pHRed was excited with interleaved 425 nm (Omicron LuxX; 2.2 mW) and 561 nm (Crystalaser; 0.02 mW). Fluorescence emission was filtered with a dichroic mirror (Chroma 59003bs), and 594 nm long-pass filter (Semrock). Images were collected at 10 Hz with a gain input of 300. Plunge-frozen *H. neapolitanus* cells were imaged with interleaved 425 nm and 561 nm excitation at 50 Hz.

Purified and frozen jREX-GECO1 was excited with 488 nm (Coherent Sapphire; 0.335

mW) laser for 3-4 s and subsequentially excited with 561 nm (Crystalaser; 0.340 mW) for 3-4 s. Fluorescence emission was filtered with a dichroic mirror (Chroma ZT405/488/561rpc), and a bandpass filter (Semrock FF01-607/70-25). Images were collected at 1 Hz with a gain input of 3.

5.4.7 Fluorescence image analysis

Calibration data was analyzed with a custom Python script. The average intensity of a 150 x 150-pixel region at the center of the image was recorded across the entire movie. The first data point recorded at each excitation or emission condition was used for ratiometric measurements. Each data point was corrected for the intensity offset of the camera (100 counts) and the background emission collected from frozen buffer solutions without the biosensor with the corresponding excitation and emission conditions. The resulting mean ratiometric fluorescence values were fit to a continuous log function (Equation 5.1) by least-squares and weighted by the associated error of each data point. Fit parameters for each biosensor calibration curve can be found in Table 5.3 .

$$F_{\text{ratio}} = \frac{L}{1 + e^{-k(x-x_0)}} + b \tag{5.1}$$

F_{ratio} images of SED1 in *S. cerevisiae* were generated with a custom Python script. First, the camera intensity offset (100 counts) was subtracted from the CFP and YFP images. To prevent inaccurate F_{ratio} values from the background signal, pixel intensity values <300 were set to 300 in the YFP and CFP images such that the resulting F_{ratio} is 1. Corresponding processed YFP and CFP images were then divided to generate YFP/CFP ratiometric images.

F_{ratio} images of pHRed in *H. neapolitanus* were generated with a custom Python script. First, 425 nm and 561 nm excitation images were deinterleaved and the first 50 frames for each excitation were averaged. The averaged images were then background corrected using the white tophat function in scikit-image, with a radius of 5 pixels. To prevent inaccurate F_{ratio} values from the background signal, pixel intensity values <15 were set to

Table 5.3: Fit parameters for biosensor calibration curve fitting

Supplementary Table 3. Fit parameters for biosensor calibrations				
Biosensor	**L**	**k**	**x_0**	**b**
SED1	4.35	0.59	8.47	2.73
pHRed	9.04	1.27	8.17	1.6
jREX-GECO1	2.4	2	0.15	-1.07

15 in the average 425 nm and 561 nm images such that the resulting F_{ratio} is 1. Corresponding processed 425 nm and 561 nm images were then divided to generate the 425/561 ratiometric images.

5.4.8 Focused-ion beam milling

Focused ion beam milling was performed using a cryogenic dual-beam system (Aquilos 2 Thermo Fisher). Lamella targets in *S. cerevisiae* expressing SED1 were selected based on previously acquired ratiometric cryogenic fluorescence microscopy collected in the home-built instrument described above. Milling was performed with the assistance of autoTEM software to a target thickness of 200 nm.

5.4.9 Cryogenic electron tomography

Cryogenic electron tomographs were acquired on a 300-keV electron microscope (Titan Krios Thermo Fisher) with an energy filter and direct detector (Gatan K3). Tilt series were collected from bidirectionally from -30° to ± 48° in 2° steps. Total dose was 100 e-/Å2 with a pixel size of 4.63 Å and a defocus target of -10 μm. Alignment of the tilt series was achieved using selection of gold fiducials present on the grids located peripherally to *H. neapolitanus* cells or non-gold fiducials (small ice particles, grid hole defects) for *S. cerevisiae* cells and the Etomo package in IMOD [314]. Low-magnification (pixel size of 36.98 Å) micrographs were taken after the acquisition of tomography data. These low-magnification micrographs are used to register optical and electron microscopy data sets. Tomogram reconstructions were annotated in EMAN2 [315,316]. In the low-magnification micrographs, 10-15 grid holes were used for registration to the fluorescence data.

CHAPTER VI

Conclusions and Future Directions

6.1 Introduction

In this dissertation, I have described my contributions to the field of bacterial subcellular organization. Using quantitative fluorescence microscopy, super-resolution imaging, single-particle tracking, and cryogenic correlative light and electron microscopy (cryoCLEM), I developed tools for the field and provided key insights into compartmentalization and active partitioning. My research has enhanced our understanding of bacterial biomolecular condensates, a novel and relatively unstudied organelle class in bacteria. Additionally, I revealed the mechanism of carboxysome distribution in *H. neapolitanus*. Furthermore, I expanded the set of fluorescent biosensors that can be used in cryoCLEM workflows to provide clearer views of the structure-function relationships in bacteria. In this final chapter, I summarize the conclusions from the works presented in the previous chapters, describe future research relevant to each of these areas, and briefly outline my contributions to other projects not covered in this dissertation.

6.2 Biomolecular condensates in bacteria

Chapter 3 describes an experimental framework developed to assess biomolecular condensates in bacteria. In collaboration with Dr. Y Hoang in the Vecchiarelli Lab, I con-

ducted a systematic study of a series of condensates and their behaviors. Specifically, we examined the conditions for condensate formation, their reversibility, and the dynamics of their components, and we discovered that IbpA, an established marker for insoluble aggregates, exhibits different colocalization patterns with condensates than with aggregates. Specifically, IbpA penetrates condensates but is excluded to the surface of aggregates. Importantly, our work distinguishes between the behaviors of condensates and aggregates, demonstrating that condensates can reversibly form despite having different material states. Responsiveness to concentration and environmental cues indicates the presence of a saturation concentration, supporting the formation of these condensates through a phase separation process. The approaches used here are highly accessible and probe several aspects of condensate assembly, maintenance, and dissolution.

The framework does have its limitations. For example, the condensates investigated were limited to single-component systems, even though many examples in bacteria comprise multiple proteins and nucleic acids. We anticipate that our framework remains highly applicable to multi-component condensates and will help assess the effects that each different protein in a multi-component system has on the condensates. For instance, in future work, we can investigate the effects that McdA and other carboxysome proteins have on the McdB condensates. I hypothesize that the introduction of McdA may result in McdB condensate positioning across the nucleoid, demonstrating one of the first examples of active partitioning of biomolecular condensates in any organism. If achievable, this system could be exploited to test how the material state of condensates affects their ability to be partitioned. Furthermore, core carboxysome proteins form multi-component condensates together, implying that phase separation may be involved in carboxysome assembly [55–57]. Given that carboxysomes are responsive to environmental cues, it would be interesting to test how changes in pH or redox conditions affect condensate formation in an isolated *in vivo* system like ours.

The behavior of the investigated condensates supports their formation via a phase

separation process. However, the exact phase transitions and the emergent viscoelastic properties of these condensates remain unknown. One approach to studying the material properties of condensates is passive rheology, where the diffusion of an extrinsic probe, such as a protein nanocage [317], can provide viscosity measurements of the condensates. This approach has been used to measure the properties of the bacterial cytoplasm, revealing its glass-like behavior [239], and is currently being used in the Biteen Lab to investigate the viscoelasticity of the *E. coli* nucleoid.

Finally, our discovery of differential localization patterns by the molecular chaperone IbpA has broader implications for their relationship with biomolecular condensates. Indeed, condensates have been shown to be more rapidly dispersed by chaperones compared to misfolded protein aggregates [221]. These findings warrant a re-evaluation of the function of chaperone systems in governing protein homeostasis and demonstrate the utility of IbpA, and potentially other chaperones, as molecular sensors for the material state of putative condensates in bacteria.

6.3 Spatial regulation of carboxysomes

Chapter 4 reports a mechanistic investigation of α-carboxysome distribution in *H. neapolitanus*. Single-particle tracking of carboxysomes revealed their equidistant distribution and subdiffusive behavior, consistent with regular positioning. Investigation of the biochemical properties of McdA demonstrated its deviation from typical ParA ATPases; unlike most ParA ATPases, the ATPase activity of McdA is not stimulated by its partner protein, McdB, but rather by its positioning matrix substrate, DNA. Intriguingly, McdB promotes the release of McdA from DNA with dissociation constants that are inconsistent with ATP hydrolysis. These results challenge the general notion in the ParA field that ATP hydrolysis and release from DNA are obligatorily coupled (Jalal and Le, 2020; Pulianmackal and Vecchiarelli; 2024). Finally, single-molecule tracking of nucleoid-bound McdA dimers unveiled their ability to diffuse on the nucleoid, an often-ignored property of

ParA ATPases. Altogether, my work supports Brownian-ratchet models as an explanation for McdA-mediated partitioning. Furthermore, this investigation extends the field of ParA ATPases by providing another model system outside of those that position genetic cargos and has broader implications for the spatial regulation of bacterial microcompartments.

While my results support Brownian-ratchet models, ongoing work is focused on testing the mechanochemical Brownian-ratchet model with the experimentally determined parameters of the α-carboxysome system. If the model aligns with our results, the next step will be to test model predictions. For instance, decreasing the number of carboxysomes in the cell to one copy would increase the diffusive length scale required for McdA to maintain regular positioning, potentially placing carboxysomes in the oscillatory regime of the model. This hypothesis can be tested by placing the carboxysome shell operon under an inducible promoter or riboswitch control to finely tune the carboxysome copy number [127]. Another accessible approach is to alter the biochemical or diffusive properties of McdA. In Chapter 4, I introduced the McdA mutant McdA[R158E/R200E], which retains the ATPase activity of the wildtype McdA but has reduced DNA-binding activity. The increased dissociation rate of this mutant would affect its diffusive length scale, potentially moving the carboxysomes into or near the oscillatory regime.

Another ongoing effort is dissecting how the ATPase cycle of McdA governs carboxysome distribution. A similar study in *S. elongatus* by the Vecchiarelli Lab [89] provided key insights that informed past and current investigations in *H. neapolitanus*. In Chapter 4, I presented several McdA mutants that modify the equilibrium between ATPase cycle states. The DNA-binding and ATPase activities of these and other mutants are currently being tested. These mutants have also been introduced into *H. neapolitanus*, resulting in carboxysome aggregates loaded onto the nucleoid despite changes in dimerization, DNA-binding, and ATPase activities. Although preliminary, these data suggest that the ATPase cycle of McdA is responsible for carboxysome distribution once they are loaded onto the nucleoid, but this initial loading may be strictly governed by McdA-McdB

interactions.

A thorough investigation of the correlated dynamics between McdA and carboxysomes can be extended to the β-system in *S. elongatus*, particularly as this McdA homolog is unique in sequence and ATPase activity among ParA ATPases [127]. Preliminary data suggest that β-carboxysomes are also regularly positioned. Since McdA oscillates in *S. elongatus*, an exciting avenue of future research is to quantitatively examine how the McdA gradient locally affects carboxysome dynamics. Additionally, we have observed heterogeneity in mNG-McdB signal on carboxysomes [127], indicating that a different amount of McdB localizes to each carboxysome. I hypothesize that the amount of McdB localized to a carboxysome correlates with its ability to 'feel' the McdA gradients, thereby affecting carboxysome dynamics.

Several other BMC operons encode their own McdAB-like sequences [131]. A long-term aim is to study the proteins encoded by these sequences and determine if McdAB function is conserved across BMC types. Intriguingly, other BMCs implicated in bacterial pathogenesis also exhibit localization phenotypes consistent with active partitioning [254–257], making their spatial organization regulators key targets for antibiotics.

6.4 Biosensor cryoCLEM

In Chapter 5, I described the current progress in identifying environmental fluorescent biosensors for cryoCLEM and demonstrating their use in biologically relevant systems. In collaboration with Dr. Peter Dahlberg, I identified biosensors for molecular crowding, pH, and calcium under cryogenic conditions. Implementation of the molecular crowding sensor, SED1 [286], revealed structural perturbations in *S. cerevisiae* as a result of osmotic shock treatment. Additionally, our work with pH and calcium sensors highlighted important considerations that improved our biosensor identification and implementation process. For instance, high cellular autofluorescence in the 400 – 500 nm wavelength range motivated the search for red-emitting biosensors. However, we found that sensor bright-

ness plays a more critical role given the technical limitations of cryogenic fluorescence imaging. Consequently, the green-emitting pHluorin2 (Mahon, 2011) proved to be a more suitable sensor than the red-emitting pHRed.

Furthermore, we discovered that MatryoshCaMP [306], a calcium sensor, does not function at cryogenic temperatures. This finding revealed a significant mechanistic limitation of GCaMP-derived biosensors and underscored the importance of cryogenic validation as a critical first step in our process.

Altogether, this work provides an optimized experimental workflow for identifying and implementing fluorescent biosensors for cryoCLEM. We anticipate that it will lead to the expansion of the biosensor suite for cryoCLEM studies, ultimately providing physiological context to the high-resolution cellular structures obtained through cryoET. In the context of bacterial subcellular organization, a short-term aim is to determine whether there is a correlation between the structure of carboxysomes and their internal pH and/or redox states, since these factors have been implicated in carboxysome function and homeostasis [296,318–320]. Subtomogram averaging of carboxysome particles binned by pH or redox state can be used to obtain high-resolution structural information [321].

6.5 Contributions to other work

In this section, I will briefly note my contributions to work done during my PhD but not presented in this thesis. Expanding on my work with biomolecular condensates, I performed single-molecule tracking experiments to reveal that Hfq, an RNA chaperone, forms condensates with polyphosphate in response to nitrogen starvation in *E. coli* (Unpublished). Important in this study was the implementation of a computational tool that classifies single-molecule tracks based on their localization within or outside of condensates. This tool was also applied to show the arrested dynamics of RNaseE, an RNA endonuclease, within *C. crescentus* BR-bodies upon stress induction [70].

Throughout my PhD, I have also developed several image processing tools

(https://github.com/BiteenMatlab) used to quantify cellular morphology and subcellular organization. These tools were used to quantify the cellular morphology of *Bacteroides thetaiotaomicron* in response to co-microbial growth [322], and to analyze carboxysome and McdA dynamics under different nutrient-deprivation conditions (Unpublished). Currently, these tools are being implemented to analyze the relationship between polyphosphate granules and carboxysomes, carboxysome localization in response to mutations to the McdA-McdB interaction, and the endowed partitioning of different bacterial organelles by an engineered ParA system (Unpublished).

6.6 Overarching Conclusions

In this thesis, I have demonstrated the value of high-resolution microscopy techniques and furthered our understanding of subcellular organization in bacteria. The application of quantitative fluorescence microscopy and single-molecule tracking to investigate bacterial organelles and their trafficking has revealed key details about the properties of biomolecular condensates and active partitioning systems. Fluorescence and electron microscopy remain the most important tools for observing the dynamics and structures of biomolecular machinery within their native systems. Their co-implementation through cryoCLEM opens new frontiers in acquiring specific, high-resolution structures with physiological information within bacteria.

BIBLIOGRAPHY

BIBLIOGRAPHY

[1] M. H. Saier Jr., "Microcompartments and Protein Machines in Prokaryotes", *Journal of Molecular Microbiology and Biotechnology* **23**, 243 (2013). DOI: 10.1159/000351625.

[2] I. V. Surovtsev, C. Jacobs-Wagner, "Subcellular Organization: A Critical Feature of Bacterial Cell Replication", *Cell* **172**, 1271 (2018). DOI: 10.1016/j.cell.2018.01.014. Publisher: Elsevier.

[3] A. H. Chen, A. Robinson-Mosher, D. F. Savage, P. A. Silver, J. K. Polka, "The Bacterial Carbon-Fixing Organelle Is Formed by Shell Envelopment of Preassembled Cargo", *PLOS ONE* **8**, e76127 (2013). DOI: 10.1371/journal.pone.0076127. Publisher: Public Library of Science.

[4] C. Greening, T. Lithgow, "Formation and function of bacterial organelles", *Nature Reviews Microbiology* **18**, 677 (2020). DOI: 10.1038/s41579-020-0413-0. Publisher: Nature Publishing Group.

[5] D. J. Murphy, "The biogenesis and functions of lipid bodies in animals, plants and microorganisms", *Progress in Lipid Research* **40**, 325 (2001). DOI: 10.1016/S0163-7827(01)00013-3.

[6] C. R. Grant, J. Wan, A. Komeili, "Organelle Formation in Bacteria and Archaea", *Annual Review of Cell and Developmental Biology* **34**, 217 (2018). DOI: 10.1146/annurev-cellbio-100616-060908. Publisher: Annual Reviews.

[7] R. Uebe, D. Schüler, "Magnetosome biogenesis in magnetotactic bacteria", *Nature Reviews Microbiology* **14**, 621 (2016). DOI: 10.1038/nrmicro.2016.99. Publisher: Nature Publishing Group.

[8] C. R. Grant, *et al.*, "Distinct gene clusters drive formation of ferrosome organelles in bacteria", *Nature* **606**, 160 (2022). DOI: 10.1038/s41586-022-04741-x. Publisher: Nature Publishing Group.

[9] K. M. Frain, D. Gangl, A. Jones, J. A. Z. Zedler, C. Robinson, "Protein translocation and thylakoid biogenesis in cyanobacteria", *Biochimica et Biophysica Acta (BBA) - Bioenergetics* **1857**, 266 (2016). DOI: 10.1016/j.bbabio.2015.08.010.

[10] J. Nickelsen, *et al.*, "Biogenesis of the cyanobacterial thylakoid membrane system – an update", *FEMS Microbiology Letters* **315**, 1 (2011). DOI: 10.1111/j.1574-6968.2010.02096.x.

[11] T. W. Giessen, "Encapsulins: microbial nanocompartments with applications in biomedicine, nanobiotechnology and materials science", *Current Opinion in Chemical Biology* **34**, 1 (2016). DOI: 10.1016/j.cbpa.2016.05.013.

[12] M. Sutter, *et al.*, "Structural basis of enzyme encapsulation into a bacterial nanocompartment", *Nature Structural & Molecular Biology* **15**, 939 (2008). DOI: 10.1038/nsmb.1473. Publisher: Nature Publishing Group.

[13] T. W. Giessen, P. A. Silver, "Widespread distribution of encapsulin nanocompartments reveals functional diversity", *Nature Microbiology* **2**, 1 (2017). DOI: 10.1038/nmicrobiol.2017.29. Publisher: Nature Publishing Group.

[14] C. A. Kerfeld, C. Aussignargues, J. Zarzycki, F. Cai, M. Sutter, "Bacterial microcompartments", *Nature Reviews Microbiology* **16**, 277 (2018). DOI: 10.1038/nrmicro.2018.10. Publisher: Nature Publishing Group.

[15] C. Chowdhury, S. Sinha, S. Chun, T. O. Yeates, T. A. Bobik, "Diverse Bacterial Microcompartment Organelles", *Microbiology and Molecular Biology Reviews* **78**, 438 (2014). DOI: 10.1128/mmbr.00009-14. Publisher: American Society for Microbiology.

[16] C. A. Kerfeld, *et al.*, "Protein Structures Forming the Shell of Primitive Bacterial Organelles", *Science* **309**, 936 (2005). DOI: 10.1126/science.1113397. Publisher: American Association for the Advancement of Science.

[17] M. Sutter, M. R. Melnicki, F. Schulz, T. Woyke, C. A. Kerfeld, "A catalog of the diversity and ubiquity of bacterial microcompartments", *Nature Communications* **12**, 3809 (2021). DOI: 10.1038/s41467-021-24126-4. Publisher: Nature Publishing Group.

[18] P. Flombaum, *et al.*, "Present and future global distributions of the marine Cyanobacteria Prochlorococcus and Synechococcus", *Proceedings of the National Academy of Sciences* **110**, 9824 (2013). DOI: 10.1073/pnas.1307701110. Publisher: Proceedings of the National Academy of Sciences.

[19] G. Drews, W. Niklowitz, "Beiträge zur Cytologie der Blaualgen", *Archiv für Mikrobiologie* **24**, 147 (1956). DOI: 10.1007/BF00408629.

[20] J. M. Shively, F. L. Ball, B. W. Kline, "Electron Microscopy of the Carboxysomes (Polyhedral Bodies) of Thiobacillus neapolitanus", *Journal of Bacteriology* **116**, 1405 (1973). DOI: 10.1128/jb.116.3.1405-1411.1973. Publisher: American Society for Microbiology.

[21] J. M. Shively, F. Ball, D. H. Brown, R. E. Saunders, "Functional Organelles in Prokaryotes: Polyhedral Inclusions (Carboxysomes) of Thiobacillus neapolitanus", *Science* **182**, 584 (1973). DOI: 10.1126/science.182.4112.584. Publisher: American Association for the Advancement of Science.

[22] J. N. Kinney, S. D. Axen, C. A. Kerfeld, "Comparative analysis of carboxysome shell proteins", *Photosynthesis Research* **109**, 21 (2011). DOI: 10.1007/s11120-011-9624-6.

[23] S. P. Long, A. Marshall-Colon, X.-G. Zhu, "Meeting the Global Food Demand of the Future by Engineering Crop Photosynthesis and Yield Potential", *Cell* **161**, 56 (2015). DOI: 10.1016/j.cell.2015.03.019. Publisher: Elsevier.

[24] H. Kirst, C. A. Kerfeld, "Bacterial microcompartments: catalysis-enhancing metabolic modules for next generation metabolic and biomedical engineering", *BMC Biology* **17**, 79 (2019). DOI: 10.1186/s12915-019-0691-z.

[25] J. M. McGrath, S. P. Long, "Can the Cyanobacterial Carbon-Concentrating Mechanism Increase Photosynthesis in Crop Species? A Theoretical Analysis", *Plant Physiology* **164**, 2247 (2014). DOI: 10.1104/pp.113.232611.

[26] T. Chen, *et al.*, "Engineering α-carboxysomes into plant chloroplasts to support autotrophic photosynthesis", *Nature Communications* **14**, 2118 (2023). DOI: 10.1038/s41467-023-37490-0. Publisher: Nature Publishing Group.

[27] T. O. Yeates, C. A. Kerfeld, S. Heinhorst, G. C. Cannon, J. M. Shively, "Protein-based organelles in bacteria: carboxysomes and related microcompartments", *Nature Reviews Microbiology* **6**, 681 (2008). DOI: 10.1038/nrmicro1913. Publisher: Nature Publishing Group.

[28] B. D. Rae, B. M. Long, M. R. Badger, G. D. Price, "Functions, Compositions, and Evolution of the Two Types of Carboxysomes: Polyhedral Microcompartments That Facilitate CO2 Fixation in Cyanobacteria and Some Proteobacteria", *Microbiology and Molecular Biology Reviews* **77**, 357 (2013). DOI: 10.1128/mmbr.00061-12. Publisher: American Society for Microbiology.

[29] C. A. Kerfeld, M. R. Melnicki, "Assembly, function and evolution of cyanobacterial carboxysomes", *Current Opinion in Plant Biology* **31**, 66 (2016). DOI: 10.1016/j.pbi.2016.03.009.

[30] L.-N. Liu, "Advances in the bacterial organelles for CO2 fixation", *Trends in Microbiology* **30**, 567 (2022). DOI: 10.1016/j.tim.2021.10.004. Publisher: Elsevier.

[31] S. F. Banani, H. O. Lee, A. A. Hyman, M. K. Rosen, "Biomolecular condensates: organizers of cellular biochemistry", *Nature Reviews Molecular Cell Biology* **18**, 285 (2017). DOI: 10.1038/nrm.2017.7. Publisher: Nature Publishing Group.

[32] C. P. Brangwynne, *et al.*, "Germline P Granules Are Liquid Droplets That Localize by Controlled Dissolution/Condensation", *Science* **324**, 1729 (2009). DOI: 10.1126/science.1172046. Publisher: American Association for the Advancement of Science.

[33] C. P. Brangwynne, T. J. Mitchison, A. A. Hyman, "Active liquid-like behavior of nucleoli determines their size and shape in Xenopus laevis oocytes", *Proceedings of the National Academy of Sciences* **108**, 4334 (2011). DOI: 10.1073/pnas.1017150108. Publisher: Proceedings of the National Academy of Sciences.

[34] P. Li, *et al.*, "Phase transitions in the assembly of multivalent signalling proteins", *Nature* **483**, 336 (2012). DOI: 10.1038/nature10879. Publisher: Nature Publishing Group.

[35] S. Elbaum-Garfinkle, *et al.*, "The disordered P granule protein LAF-1 drives phase separation into droplets with tunable viscosity and dynamics", *Proceedings of the National Academy of Sciences* **112**, 7189 (2015). DOI: 10.1073/pnas.1504822112. Publisher: Proceedings of the National Academy of Sciences.

[36] P. J. Flory, "Thermodynamics of High Polymer Solutions", *The Journal of Chemical Physics* **10**, 51 (1942). DOI: 10.1063/1.1723621.

[37] M. L. Huggins, "Solutions of Long Chain Compounds", *The Journal of Chemical Physics* **9**, 440 (1941). DOI: 10.1063/1.1750930.

[38] J.-M. Choi, A. S. Holehouse, R. V. Pappu, "Physical Principles Underlying the Complex Biology of Intracellular Phase Transitions", *Annual Review of Biophysics* **49**, 107 (2020). DOI: 10.1146/annurev-biophys-121219-081629. Publisher: Annual Reviews.

[39] M. C. Cohan, R. V. Pappu, "Making the Case for Disordered Proteins and Biomolecular Condensates in Bacteria", *Trends in Biochemical Sciences* **45**, 668 (2020).

[40] T. Mittag, R. V. Pappu, "A conceptual framework for understanding phase separation and addressing open questions and challenges", *Molecular Cell* **82**, 2201 (2022). DOI: 10.1016/j.molcel.2022.05.018.

[41] A. N. Semenov, M. Rubinstein, "Thermoreversible Gelation in Solutions of Associative Polymers. 1. Statics", *Macromolecules* **31**, 1373 (1998). DOI: 10.1021/ma970616h. Publisher: American Chemical Society.

[42] A. Molliex, *et al.*, "Phase Separation by Low Complexity Domains Promotes Stress Granule Assembly and Drives Pathological Fibrillization", *Cell* **163**, 123 (2015). DOI: 10.1016/j.cell.2015.09.015. Publisher: Elsevier.

[43] A. W. Fritsch, *et al.*, "Local thermodynamics govern formation and dissolution of Caenorhabditis elegans P granule condensates", *Proceedings of the National Academy of Sciences* **118**, e2102772118 (2021). DOI: 10.1073/pnas.2102772118. Publisher: Proceedings of the National Academy of Sciences.

[44] A. Bremer, *et al.*, "Deciphering how naturally occurring sequence features impact the phase behaviours of disordered prion-like domains", *Nature Chemistry* **14**, 196 (2022). DOI: 10.1038/s41557-021-00840-w. Publisher: Nature Publishing Group.

[45] S. C. Weber, C. P. Brangwynne, "Inverse Size Scaling of the Nucleolus by a Concentration-Dependent Phase Transition", *Current Biology* **25**, 641 (2015). DOI: 10.1016/j.cub.2015.01.012. Publisher: Elsevier.

[46] A. A. Hyman, C. A. Weber, F. Jülicher, "Liquid-Liquid Phase Separation in Biology", *Annual Review of Cell and Developmental Biology* **30**, 39 (2014). DOI: 10.1146/annurev-cellbio-100913-013325. Publisher: Annual Reviews.

[47] S. Roberts, *et al.*, "Injectable tissue integrating networks from recombinant polypeptides with tunable order", *Nature Materials* **17**, 1154 (2018). DOI: 10.1038/s41563-018-0182-6. Publisher: Nature Publishing Group.

[48] L. Jawerth, *et al.*, "Protein condensates as aging Maxwell fluids", *Science* **370**, 1317 (2020). DOI: 10.1126/science.aaw4951. Publisher: American Association for the Advancement of Science.

[49] Y. Shen, *et al.*, "Biomolecular condensates undergo a generic shear-mediated liquid-to-solid transition", *Nature Nanotechnology* **15**, 841 (2020). DOI: 10.1038/s41565-020-0731-4. Publisher: Nature Publishing Group.

[50] T. Kaur, *et al.*, "Sequence-encoded and composition-dependent protein-RNA interactions control multiphasic condensate morphologies", *Nature Communications* **12**, 872 (2021). DOI: 10.1038/s41467-021-21089-4. Publisher: Nature Publishing Group.

[51] A. Ghosh, D. Kota, H.-X. Zhou, "Shear relaxation governs fusion dynamics of biomolecular condensates", *Nature Communications* **12**, 5995 (2021). DOI: 10.1038/s41467-021-26274-z. Publisher: Nature Publishing Group.

[52] I. Alshareedah, M. M. Moosa, M. Pham, D. A. Potoyan, P. R. Banerjee, "Programmable viscoelasticity in protein-RNA condensates with disordered sticker-spacer polypeptides", *Nature Communications* **12**, 6620 (2021). DOI: 10.1038/s41467-021-26733-7. Publisher: Nature Publishing Group.

[53] S. Alberti, A. Gladfelter, T. Mittag, "Considerations and Challenges in Studying Liquid-Liquid Phase Separation and Biomolecular Condensates", *Cell* **176**, 419 (2019). DOI: 10.1016/j.cell.2018.12.035. Publisher: Elsevier.

[54] C. A. Azaldegui, A. G. Vecchiarelli, J. S. Biteen, "The emergence of phase separation as an organizing principle in bacteria", *Biophysical Journal* **120**, 1123 (2021). DOI: 10.1016/j.bpj.2020.09.023.

[55] H. Wang, *et al.*, "Rubisco condensate formation by CcmM in β-carboxysome biogenesis", *Nature* **566**, 131 (2019). DOI: 10.1038/s41586-019-0880-5. Publisher: Nature Publishing Group.

[56] L. M. Oltrogge, *et al.*, "Multivalent interactions between CsoS2 and Rubisco mediate α-carboxysome formation", *Nature Structural & Molecular Biology* **27**, 281 (2020). DOI: 10.1038/s41594-020-0387-7. Publisher: Nature Publishing Group.

[57] K. Zang, H. Wang, F. U. Hartl, M. Hayer-Hartl, "Scaffolding protein CcmM directs multiprotein phase separation in β-carboxysome biogenesis", *Nature Structural & Molecular Biology* **28**, 909 (2021). DOI: 10.1038/s41594-021-00676-5. Publisher: Nature Publishing Group.

[58] H. M. Swasthi, J. L. Basalla, C. E. Dudley, A. G. Vecchiarelli, M. R. Chapman, "Cell surface-localized CsgF condensate is a gatekeeper in bacterial curli subunit secretion", *Nature Communications* **14**, 2392 (2023). DOI: 10.1038/s41467-023-38089-1. Publisher: Nature Publishing Group.

[59] F. Beaufay, *et al.*, "Polyphosphate drives bacterial heterochromatin formation", *Science Advances* **7**, eabk0233 (2021). DOI: 10.1126/sciadv.abk0233. Publisher: American Association for the Advancement of Science.

[60] A.-M. Ladouceur, *et al.*, "Clusters of bacterial RNA polymerase are biomolecular condensates that assemble through liquid–liquid phase separation", *Proceedings of the National Academy of Sciences* **117**, 18540 (2020). DOI: 10.1073/pnas.2005019117. Publisher: Proceedings of the National Academy of Sciences.

[61] B. Monterroso, *et al.*, "Bacterial FtsZ protein forms phase-separated condensates with its nucleoid-associated inhibitor SlmA", *EMBO reports* **20**, e45946 (2019). DOI: 10.15252/embr.201845946. Publisher: John Wiley & Sons, Ltd.

[62] L. Babl, A. Merino-Salomón, N. Kanwa, P. Schwille, "Membrane mediated phase separation of the bacterial nucleoid occlusion protein Noc", *Scientific Reports* **12**, 17949 (2022). DOI: 10.1038/s41598-022-22680-5. Publisher: Nature Publishing Group.

[63] B. Ramm, *et al.*, "Biomolecular condensate drives polymerization and bundling of the bacterial tubulin FtsZ to regulate cell division", *Nature Communications* **14**, 3825 (2023). DOI: 10.1038/s41467-023-39513-2. Publisher: Nature Publishing Group.

[64] F. Heinkel, *et al.*, "Phase separation and clustering of an ABC transporter in Mycobacterium tuberculosis", *Proceedings of the National Academy of Sciences* **116**, 16326 (2019). DOI: 10.1073/pnas.1820683116. Publisher: Proceedings of the National Academy of Sciences.

[65] J. L. Basalla, *et al.*, "Dissecting the phase separation and oligomerization activities of the carboxysome positioning protein McdB", *eLife* **12**, e81362 (2023). DOI: 10.7554/eLife.81362. Publisher: eLife Sciences Publications, Ltd.

[66] N. Al-Husini, D. T. Tomares, O. Bitar, W. S. Childers, J. M. Schrader, "α-Proteobacterial RNA Degradosomes Assemble Liquid-Liquid Phase-Separated RNP Bodies", *Molecular Cell* **71**, 1027 (2018). DOI: 10.1016/j.molcel.2018.08.003. Publisher: Elsevier.

[67] N. Al-Husini, *et al.*, "BR-Bodies Provide Selectively Permeable Condensates that Stimulate mRNA Decay and Prevent Release of Decay Intermediates", *Molecular Cell* **78**, 670 (2020). DOI: 10.1016/j.molcel.2020.04.001. Publisher: Elsevier.

[68] S. W. Hardwick, V. S. Y. Chan, R. W. Broadhurst, B. F. Luisi, "An RNA degradosome assembly in Caulobacter crescentus", *Nucleic Acids Research* **39**, 1449 (2011). DOI: 10.1093/nar/gkq928.

[69] N. S. Muthunayake, D. T. Tomares, W. S. Childers, J. M. Schrader, "Phase-separated bacterial ribonucleoprotein bodies organize mRNA decay", *WIREs RNA* **11**, e1599 (2020). DOI: 10.1002/wrna.1599. _eprint: https://onlinelibrary.wiley.com/doi/pdf/10.1002/wrna.1599.

[70] L. A. Ortiz-Rodríguez, *et al.*, "Stress Changes the Bacterial Biomolecular Condensate Material State and Shifts Function from mRNA Decay to Storage" (2024), (Accessed: 2024-12-20). Pages: 2024.11.12.623272 Section: New Results.

[71] G. Ebersbach, A. Briegel, G. J. Jensen, C. Jacobs-Wagner, "A Self-Associating Protein Critical for Chromosome Attachment, Division, and Polar Organization in Caulobacter", *Cell* **134**, 956 (2008). DOI: 10.1016/j.cell.2008.07.016. Publisher: Elsevier.

[72] G. R. Bowman, *et al.*, "A Polymeric Protein Anchors the Chromosomal Origin/ParB Complex at a Bacterial Cell Pole", *Cell* **134**, 945 (2008). DOI: 10.1016/j.cell.2008.07.015.

[73] K. Lasker, *et al.*, "Selective sequestration of signalling proteins in a membraneless organelle reinforces the spatial regulation of asymmetry in Caulobacter crescentus", *Nature Microbiology* **5**, 418 (2020). DOI: 10.1038/s41564-019-0647-7. Number: 3.

[74] K. C. Quon, B. Yang, I. J. Domian, L. Shapiro, G. T. Marczynski, "Negative control of bacterial DNA replication by a cell cycle regulatory protein that binds at the chromosomeorigin", *Proceedings of the National Academy of Sciences* **95**, 120 (1998). DOI: 10.1073/pnas.95.1.120. Publisher: Proceedings of the National Academy of Sciences.

[75] S. K. Radhakrishnan, M. Thanbichler, P. H. Viollier, "The dynamic interplay between a cell fate determinant and a lysozyme homolog drives the asymmetric division cycle of Caulobacter crescentus", *Genes & Development* **22**, 212 (2008). DOI: 10.1101/gad.1601808. Company: Cold Spring Harbor Laboratory Press Distributor: Cold Spring Harbor Laboratory Press Institution: Cold Spring Harbor Laboratory Press Label: Cold Spring Harbor Laboratory Press Publisher: Cold Spring Harbor Lab.

[76] A. M. Perez, *et al.*, "A Localized Complex of Two Protein Oligomers Controls the Orientation of Cell Polarity", *mBio* **8**, 10.1128/mbio.02238 (2017). DOI: 10.1128/mbio.02238-16. Publisher: American Society for Microbiology.

[77] S. Saurabh, *et al.*, "ATP-responsive biomolecular condensates tune bacterial kinase signaling", *Science Advances* **8**, eabm6570 (2022). DOI: 10.1126/sciadv.abm6570. Publisher: American Association for the Advancement of Science.

[78] K. Lasker, *et al.*, "The material properties of a bacterial-derived biomolecular condensate tune biological function in natural and synthetic systems", *Nature Communications* **13**, 5643 (2022). DOI: 10.1038/s41467-022-33221-z. Publisher: Nature Publishing Group.

[79] Y. Hoang, *et al.*, "An experimental framework to assess biomolecular condensates in bacteria", *Nature Communications* **15**, 3222 (2024). DOI: 10.1038/s41467-024-47330-4. Publisher: Nature Publishing Group.

[80] L. T. Pulianmackal, A. G. Vecchiarelli, "Positioning of cellular components by the ParA/MinD family of ATPases", *Current Opinion in Microbiology* **79**, 102485 (2024). DOI: 10.1016/j.mib.2024.102485.

[81] L. T. Pulianmackal, *et al.*, "Multiple ParA/MinD ATPases coordinate the positioning of disparate cargos in a bacterial cell", *Nature Communications* **14**, 3255 (2023). DOI: 10.1038/s41467-023-39019-x. Publisher: Nature Publishing Group.

[82] J. C. Baxter, B. E. Funnell, "Plasmid Partition Mechanisms", *Microbiology Spectrum* **2**, 10.1128/microbiolspec.plas (2014). DOI: 10.1128/microbiolspec.plas-0023-2014. Publisher: American Society for Microbiology.

[83] J. Lutkenhaus, "The ParA/MinD family puts things in their place", *Trends in Microbiology* **20**, 411 (2012). DOI: 10.1016/j.tim.2012.05.002.

[84] A. Merino-Salomón, L. Babl, P. Schwille, "Self-organized protein patterns: The MinCDE and ParABS systems", *Current Opinion in Cell Biology* **72**, 106 (2021). DOI: 10.1016/j.ceb.2021.07.001.

[85] A. S. B. Jalal, T. B. K. Le, "Bacterial chromosome segregation by the ParABS system", *Open Biology* **10**, 200097 (2020). DOI: 10.1098/rsob.200097. Publisher: Royal Society.

[86] E. V. Koonin, "A Superfamily of ATPases with Diverse Functions Containing Either Classical or Deviant ATP-binding Motif", *Journal of Molecular Biology* **229**, 1165 (1993). DOI: 10.1006/jmbi.1993.1115.

[87] D. D. Leipe, Y. I. Wolf, E. V. Koonin, L. Aravind, "Classification and evolution of P-loop GTPases and related ATPases1", *Journal of Molecular Biology* **317**, 41 (2002). DOI: 10.1006/jmbi.2001.5378.

[88] B. A. Perez-Cheeks, *et al.*, "The product of tadZ, a new member of the parA/minD superfamily, localizes to a pole in Aggregatibacter actinomycetemcomitans", *Molecular Microbiology* **83**, 694 (2012). DOI: 10.1111/j.1365-2958.2011.07955.x. _eprint: https://onlinelibrary.wiley.com/doi/pdf/10.1111/j.1365-2958.2011.07955.x.

[89] P. Hakim, Y. Hoang, A. G. Vecchiarelli, "Dissection of the ATPase active site of McdA reveals the sequential steps essential for carboxysome distribution", *Molecular Biology of the Cell* **32**, ar11 (2021). DOI: 10.1091/mbc.E21-03-0151. Publisher: American Society for Cell Biology (mboc).

[90] T. D. Dunham, W. Xu, B. E. Funnell, M. A. Schumacher, "Structural basis for ADP-mediated transcriptional regulation by P1 and P7 ParA", *The EMBO Journal* **28**, 1792 (2009). DOI: 10.1038/emboj.2009.120. Num Pages: 1802 Publisher: John Wiley & Sons, Ltd.

[91] W. Wu, K.-T. Park, T. Holyoak, J. Lutkenhaus, "Determination of the structure of the MinD–ATP complex reveals the orientation of MinD on the membrane and the relative location of the binding sites for MinE and MinC", *Molecular Microbiology* **79**, 1515 (2011). DOI: 10.1111/j.1365-2958.2010.07536.x. _eprint: https://onlinelibrary.wiley.com/doi/pdf/10.1111/j.1365-2958.2010.07536.x.

[92] T. A. Leonard, P. J. Butler, J. Löwe, "Bacterial chromosome segregation: structure and DNA binding of the Soj dimer — a conserved biological switch", *The EMBO Journal* **24**, 270 (2005). DOI: 10.1038/sj.emboj.7600530. Num Pages: 282 Publisher: John Wiley & Sons, Ltd.

[93] D. Kiekebusch, K. A. Michie, L.-O. Essen, J. Löwe, M. Thanbichler, "Localized Dimerization and Nucleoid Binding Drive Gradient Formation by the Bacterial Cell Division Inhibitor MipZ", *Molecular Cell* **46**, 245 (2012). DOI: 10.1016/j.molcel.2012.03.004. Publisher: Elsevier.

[94] M. A. Schumacher, M. Henderson, H. Zhang, "Structures of maintenance of carboxysome distribution Walker-box McdA and McdB adaptor homologs", *Nucleic Acids Research* **47**, 5950 (2019). DOI: 10.1093/nar/gkz314.

[95] C. Machón, T. J. G. Fothergill, D. Barillà, F. Hayes, "Promiscuous Stimulation of ParF Protein Polymerization by Heterogeneous Centromere Binding Factors", *Journal of Molecular Biology* **374**, 1 (2007). DOI: 10.1016/j.jmb.2007.09.025.

[96] Y. Ah-Seng, F. Lopez, F. Pasta, D. Lane, J.-Y. Bouet, "Dual Role of DNA in Regulating ATP Hydrolysis by the SopA Partition Protein *", *Journal of Biological Chemistry* **284**, 30067 (2009). DOI: 10.1074/jbc.M109.044800. Publisher: Elsevier.

[97] H. Ghasriani, *et al.*, "Appropriation of the MinD protein-interaction motif by the dimeric interface of the bacterial cell division regulator MinE", *Proceedings of the National Academy of Sciences* **107**, 18416 (2010). DOI: 10.1073/pnas.1007141107. Publisher: Proceedings of the National Academy of Sciences.

[98] D. Schumacher, *et al.*, "The PomXYZ Proteins Self-Organize on the Bacterial Nucleoid to Stimulate Cell Division", *Developmental Cell* **41**, 299 (2017). DOI: 10.1016/j.devcel.2017.04.011. Publisher: Elsevier.

[99] T. H. Szeto, S. L. Rowland, L. I. Rothfield, G. F. King, "Membrane localization of MinD is mediated by a C-terminal motif that is conserved across eubacteria, archaea, and chloroplasts", *Proceedings of the National Academy of Sciences* **99**, 15693 (2002). DOI: 10.1073/pnas.232590599. Publisher: Proceedings of the National Academy of Sciences.

[100] C. M. Hester, J. Lutkenhaus, "Soj (ParA) DNA binding is mediated by conserved arginines and is essential for plasmid segregation", *Proceedings of the National Academy of Sciences* **104**, 20326 (2007). DOI: 10.1073/pnas.0705196105. Publisher: Proceedings of the National Academy of Sciences.

[101] J.-P. Castaing, J.-Y. Bouet, D. Lane, "F plasmid partition depends on interaction of SopA with non-specific DNA", *Molecular Microbiology* **70**, 1000 (2008). DOI: 10.1111/j.1365-2958.2008.06465.x. _eprint: https://onlinelibrary.wiley.com/doi/pdf/10.1111/j.1365-2958.2008.06465.x.

[102] T. Hatano, Y. Yamaichi, H. Niki, "Oscillating focus of SopA associated with filamentous structure guides partitioning of F plasmid", *Molecular Microbiology* **64**, 1198 (2007). DOI: 10.1111/j.1365-2958.2007.05728.x. _eprint: https://onlinelibrary.wiley.com/doi/pdf/10.1111/j.1365-2958.2007.05728.x.

[103] S. Ringgaard, J. van Zon, M. Howard, K. Gerdes, "Movement and equipositioning of plasmids by ParA filament disassembly", *Proceedings of the National Academy of Sciences* **106**, 19369 (2009). DOI: 10.1073/pnas.0908347106. Publisher: Proceedings of the National Academy of Sciences.

[104] I. V. Surovtsev, M. Campos, C. Jacobs-Wagner, "DNA-relay mechanism is sufficient to explain ParA-dependent intracellular transport and patterning of single and multiple cargos", *Proceedings of the National Academy of Sciences* **113**, E7268 (2016). DOI: 10.1073/pnas.1616118113. Publisher: Proceedings of the National Academy of Sciences.

[105] S. Adachi, K. Hori, S. Hiraga, "Subcellular Positioning of F Plasmid Mediated by Dynamic Localization of SopA and SopB", *Journal of Molecular Biology* **356**, 850 (2006). DOI: 10.1016/j.jmb.2005.11.088.

[106] M. Sengupta, H. J. Nielsen, B. Youngren, S. Austin, "P1 Plasmid Segregation: Accurate Redistribution by Dynamic Plasmid Pairing and Separation", *Journal of Bacteriology* **192**, 1175 (2010). DOI: 10.1128/jb.01245-09. Publisher: American Society for Microbiology.

[107] G. Ebersbach, *et al.*, "Regular cellular distribution of plasmids by oscillating and filament-forming ParA ATPase of plasmid pB171", *Molecular Microbiology* **61**, 1428 (2006). DOI: 10.1111/j.1365-2958.2006.05322.x. _eprint: https://onlinelibrary.wiley.com/doi/pdf/10.1111/j.1365-2958.2006.05322.x.

[108] V. S. Lioy, *et al.*, "ParAB Partition Dynamics in Firmicutes: Nucleoid Bound ParA Captures and Tethers ParB-Plasmid Complexes", *PLOS ONE* **10**, e0131943 (2015). DOI: 10.1371/journal.pone.0131943. Publisher: Public Library of Science.

[109] L. Hu, A. G. Vecchiarelli, K. Mizuuchi, K. C. Neuman, J. Liu, "Directed and persistent movement arises from mechanochemistry of the ParA/ParB system", *Proceedings of the National Academy of Sciences* **112**, E7055 (2015). DOI: 10.1073/pnas.1505147112. Publisher: Proceedings of the National Academy of Sciences.

[110] L. Hu, A. G. Vecchiarelli, K. Mizuuchi, K. C. Neuman, J. Liu, "Brownian ratchet mechanisms of ParA-mediated partitioning", *Plasmid* **92**, 12 (2017). DOI: 10.1016/j.plasmid.2017.05.002.

[111] L. Hu, J. Rech, J.-Y. Bouet, J. Liu, "Spatial control over near-critical-point operation ensures fidelity of ParABS-mediated DNA partition", *Biophysical Journal* **120**, 3911 (2021). DOI: 10.1016/j.bpj.2021.08.022. Publisher: Elsevier.

[112] H. C. Lim, *et al.*, "Evidence for a DNA-relay mechanism in ParABS-mediated chromosome segregation", *eLife* **3**, e02758 (2014). DOI: 10.7554/eLife.02758. Publisher: eLife Sciences Publications, Ltd.

[113] L. Jindal, E. Emberly, "Operational Principles for the Dynamics of the In Vitro ParA-ParB System", *PLOS Computational Biology* **11**, e1004651 (2015). DOI: 10.1371/journal.pcbi.1004651. Publisher: Public Library of Science.

[114] R. Ietswaart, F. Szardenings, K. Gerdes, M. Howard, "Competing ParA Structures Space Bacterial Plasmids Equally over the Nucleoid", *PLOS Computational Biology* **10**, e1004009 (2014). DOI: 10.1371/journal.pcbi.1004009. Publisher: Public Library of Science.

[115] T. Sugawara, K. Kaneko, "Chemophoresis as a driving force for intracellular organization: Theory and application to plasmid partitioning", *Biophysics* **7**, 77 (2011). DOI: 10.2142/biophysics.7.77.

[116] T. Sugawara, K. Kaneko, "Chemophoresis engine: A general mechanism of ATPase-driven cargo transport", *PLOS Computational Biology* **18**, e1010324 (2022). DOI: 10.1371/journal.pcbi.1010324. Publisher: Public Library of Science.

[117] C. S. Peskin, G. M. Odell, G. F. Oster, "Cellular motions and thermal fluctuations: the Brownian ratchet", *Biophysical Journal* **65**, 316 (1993). DOI: 10.1016/S0006-3495(93)81035-X. Publisher: Elsevier.

[118] L. Hu, A. G. Vecchiarelli, K. Mizuuchi, K. C. Neuman, J. Liu, "Brownian ratchet mechanisms of ParA-mediated partitioning", *Plasmid* **92**, 12 (2017). DOI: 10.1016/j.plasmid.2017.05.002.

[119] L. C. Hwang, *et al.*, "ParA-mediated plasmid partition driven by protein pattern self-organization", *The EMBO Journal* **32**, 1238 (2013). DOI: 10.1038/emboj.2013.34. Num Pages: 1249 Publisher: John Wiley & Sons, Ltd.

[120] A. G. Vecchiarelli, L. C. Hwang, K. Mizuuchi, "Cell-free study of F plasmid partition provides evidence for cargo transport by a diffusion-ratchet mechanism", *Proceedings of the National Academy of Sciences* **110**, E1390 (2013). DOI: 10.1073/pnas.1302745110. Publisher: Proceedings of the National Academy of Sciences.

[121] A. G. Vecchiarelli, Y. Seol, K. C. Neuman, K. Mizuuchi, "A moving ParA gradient on the nucleoid directs subcellular cargo transport via a chemophoresis force", *BioArchitecture* **4**, 154 (2014). DOI: 10.4161/19490992.2014.987581. Publisher: Taylor & Francis _eprint: https://doi.org/10.4161/19490992.2014.987581.

[122] A. G. Vecchiarelli, K. C. Neuman, K. Mizuuchi, "A propagating ATPase gradient drives transport of surface-confined cellular cargo", *Proceedings of the National Academy of Sciences* **111**, 4880 (2014). DOI: 10.1073/pnas.1401025111. Publisher: Proceedings of the National Academy of Sciences.

[123] A. Le Gall, *et al.*, "Bacterial partition complexes segregate within the volume of the nucleoid", *Nature Communications* **7**, 12107 (2016). DOI: 10.1038/ncomms12107. Publisher: Nature Publishing Group.

[124] R. Köhler, E. Kaganovitch, S. M. Murray, "High-throughput imaging and quantitative analysis uncovers the nature of plasmid positioning by ParABS", *eLife* **11**, e78743 (2022). DOI: 10.7554/eLife.78743. Publisher: eLife Sciences Publications, Ltd.

[125] R. Köhler, S. M. Murray, "Plasmid partitioning driven by collective migration of ParA between nucleoid lobes", *Proceedings of the National Academy of Sciences* **121**, e2319205121 (2024). DOI: 10.1073/pnas.2319205121. Company: National Academy of Sciences Distributor: National Academy of Sciences Institution: National Academy of Sciences Label: National Academy of Sciences Publisher: Proceedings of the National Academy of Sciences.

[126] D. F. Savage, B. Afonso, A. H. Chen, P. A. Silver, "Spatially Ordered Dynamics of the Bacterial Carbon Fixation Machinery", *Science* **327**, 1258 (2010). DOI: 10.1126/science.1186090. Publisher: American Association for the Advancement of Science.

[127] J. S. MacCready, *et al.*, "Protein gradients on the nucleoid position the carbon-fixing organelles of cyanobacteria", *eLife* **7**, e39723 (2018). DOI: 10.7554/eLife.39723. Publisher: eLife Sciences Publications, Ltd.

[128] R. Rillema, Y. Hoang, J. S. MacCready, A. G. Vecchiarelli, "Carboxysome Mispositioning Alters Growth, Morphology, and Rubisco Level of the Cyanobacterium Synechococcus elongatus PCC 7942", *mBio* **12**, 10.1128/mbio.02696 (2021). DOI: 10.1128/mbio.02696-20. Publisher: American Society for Microbiology.

[129] J. L. Ptacin, *et al.*, "A spindle-like apparatus guides bacterial chromosome segregation", *Nature Cell Biology* **12**, 791 (2010). DOI: 10.1038/ncb2083. Publisher: Nature Publishing Group.

[130] J. S. MacCready, J. L. Basalla, A. G. Vecchiarelli, "Origin and Evolution of Carboxysome Positioning Systems in Cyanobacteria", *Molecular Biology and Evolution* **37**, 1434 (2020).

[131] J. S. MacCready, L. Tran, J. L. Basalla, P. Hakim, A. G. Vecchiarelli, "The McdAB system positions α-carboxysomes in proteobacteria", *Molecular Microbiology* **116**, 277 (2021). DOI: 10.1111/mmi.14708. _eprint: https://onlinelibrary.wiley.com/doi/pdf/10.1111/mmi.14708.

[132] J. S. MacCready, A. G. Vecchiarelli, "Positioning the Model Bacterial Organelle, the Carboxysome", *mBio* **12**, 10.1128/mbio.02519 (2021). DOI: 10.1128/mbio.02519-19. Publisher: American Society for Microbiology.

[133] G. C. Cannon, *et al.*, "Microcompartments in Prokaryotes: Carboxysomes and Related Polyhedra", *Applied and Environmental Microbiology* **67**, 5351 (2001). DOI: 10.1128/AEM.67.12.5351-5361.2001. Publisher: American Society for Microbiology.

[134] E. Abbe, "Beiträge zur Theorie des Mikroskops und der mikroskopischen Wahrnehmung", *Archiv für Mikroskopische Anatomie* **9**, 413 (1873). DOI: 10.1007/BF02956173.

[135] J. R. Maddock, L. Shapiro, "Polar Location of the Chemoreceptor Complex in the Escherichia coli Cell", *Science* **259**, 1717 (1993). DOI: 10.1126/science.8456299. Publisher: American Association for the Advancement of Science.

[136] K. Pogliano, E. Harry, R. Losick, "Visualization of the subcellular location of sporulation proteins in Bacillus subtilis using immunofluorescence microscopy", *Molecular Microbiology* **18**, 459 (1995). DOI: 10.1111/j.1365-2958.1995.mmi_18030459.x. _eprint: https://onlinelibrary.wiley.com/doi/pdf/10.1111/j.1365-2958.1995.mmi_18030459.x.

[137] C. A. Hoelzel, X. Zhang, "Visualizing and Manipulating Biological Processes by Using HaloTag and SNAP-Tag Technologies", *ChemBioChem* **21**, 1935 (2020). DOI: 10.1002/cbic.202000037. _eprint: https://onlinelibrary.wiley.com/doi/pdf/10.1002/cbic.202000037.

[138] A. F. L. Schneider, C. P. R. Hackenberger, "Fluorescent labelling in living cells", *Current Opinion in Biotechnology* **48**, 61 (2017). DOI: 10.1016/j.copbio.2017.03.012.

[139] E. Kozma, P. Kele, "Bioorthogonal Reactions in Bioimaging", *Topics in Current Chemistry* **382**, 7 (2024). DOI: 10.1007/s41061-024-00452-1.

[140] R. Y. Tsien, "THE GREEN FLUORESCENT PROTEIN", *Annual Review of Biochemistry* **67**, 509 (1998). DOI: 10.1146/annurev.biochem.67.1.509. Publisher: Annual Reviews.

[141] E. A. Rodriguez, *et al.*, "The Growing and Glowing Toolbox of Fluorescent and Photoactive Proteins", *Trends in Biochemical Sciences* **42**, 111 (2017). DOI: 10.1016/j.tibs.2016.09.010.

[142] C. P. Toseland, "Fluorescent labeling and modification of proteins", *Journal of Chemical Biology* **6**, 85 (2013). DOI: 10.1007/s12154-013-0094-5.

[143] G. Airy, "On the diffraction of an object-glass with circular aperture", *SPIE milestone series* (1835).

[144] W. E. Moerner, L. Kador, "Optical detection and spectroscopy of single molecules in a solid", *Physical Review Letters* **62**, 2535 (1989). DOI: 10.1103/PhysRevLett.62.2535. Publisher: American Physical Society.

[145] F. Güttler, T. Irngartinger, T. Plakhotnik, A. Renn, U. P. Wild, "Fluorescence microscopy of single molecules", *Chemical Physics Letters* **217**, 393 (1994). DOI: 10.1016/0009-2614(94)87003-9.

[146] A. M. van Oijen, J. Köhler, J. Schmidt, M. Müller, G. J. Brakenhoff, "3-Dimensional super-resolution by spectrally selective imaging", *Chemical Physics Letters* **292**, 183 (1998). DOI: 10.1016/S0009-2614(98)00673-3.

[147] R. E. Thompson, D. R. Larson, W. W. Webb, "Precise Nanometer Localization Analysis for Individual Fluorescent Probes", *Biophysical Journal* **82**, 2775 (2002). DOI: 10.1016/S0006-3495(02)75618-X. Publisher: Elsevier.

[148] M. Heilemann, *et al.*, "High-Resolution Colocalization of Single Dye Molecules by Fluorescence Lifetime Imaging Microscopy", *Analytical Chemistry* **74**, 3511 (2002). DOI: 10.1021/ac025576g. Publisher: American Chemical Society.

[149] M. P. Gordon, T. Ha, P. R. Selvin, "Single-molecule high-resolution imaging with photobleaching", *Proceedings of the National Academy of Sciences* **101**, 6462 (2004). DOI: 10.1073/pnas.0401638101. Publisher: Proceedings of the National Academy of Sciences.

[150] X. Qu, D. Wu, L. Mets, N. F. Scherer, "Nanometer-localized multiple single-molecule fluorescence microscopy", *Proceedings of the National Academy of Sciences* **101**, 11298 (2004). DOI: 10.1073/pnas.0402155101. Publisher: Proceedings of the National Academy of Sciences.

[151] K. A. Lidke, B. Rieger, T. M. Jovin, R. Heintzmann, "Superresolution by localization of quantum dots using blinking statistics", *Optics Express* **13**, 7052 (2005). DOI: 10.1364/OPEX.13.007052. Publisher: Optica Publishing Group.

[152] M. J. Rust, M. Bates, X. Zhuang, "Sub-diffraction-limit imaging by stochastic optical reconstruction microscopy (STORM)", *Nature Methods* **3**, 793 (2006). DOI: 10.1038/nmeth929. Publisher: Nature Publishing Group.

[153] E. Betzig, *et al.*, "Imaging Intracellular Fluorescent Proteins at Nanometer Resolution", *Science* **313**, 1642 (2006). DOI: 10.1126/science.1127344. Publisher: American Association for the Advancement of Science.

[154] S. T. Hess, T. P. K. Girirajan, M. D. Mason, "Ultra-High Resolution Imaging by Fluorescence Photoactivation Localization Microscopy", *Biophysical Journal* **91**, 4258 (2006). DOI: 10.1529/biophysj.106.091116.

[155] A. Sharonov, R. M. Hochstrasser, "Wide-field subdiffraction imaging by accumulated binding of diffusing probes", *Proceedings of the National Academy of Sciences*

103, 18911 (2006). DOI: 10.1073/pnas.0609643104. Publisher: Proceedings of the National Academy of Sciences.

[156] J. S. Biteen, M. A. Thompson, N. K. Tselentis, L. Shapiro, W. E. Moerner, *Conference on Lasers and Electro-Optics/Quantum Electronics and Laser Science Conference and Photonic Applications Systems Technologies (2008), paper CFT2* (Optica Publishing Group, 2008), p. CFT2.

[157] H. H. Tuson, J. S. Biteen, "Unveiling the Inner Workings of Live Bacteria Using Super-Resolution Microscopy", *Analytical Chemistry* **87**, 42 (2015). DOI: 10.1021/ac5041346. Publisher: American Chemical Society.

[158] J. Biteen, "Moving toward the future of single-molecule-based super-resolution imaging", *Biopolymers* **95**, 287 (2011). DOI: 10.1002/bip.21592. _eprint: https://onlinelibrary.wiley.com/doi/pdf/10.1002/bip.21592.

[159] J. Lippincott-Schwartz, G. H. Patterson, "Photoactivatable fluorescent proteins for diffraction-limited and super-resolution imaging", *Trends in Cell Biology* **19**, 555 (2009). DOI: 10.1016/j.tcb.2009.09.003. Publisher: Elsevier.

[160] S. Wang, J. R. Moffitt, G. T. Dempsey, X. S. Xie, X. Zhuang, "Characterization and development of photoactivatable fluorescent proteins for single-molecule–based superresolution imaging", *Proceedings of the National Academy of Sciences* **111**, 8452 (2014). DOI: 10.1073/pnas.1406593111. Publisher: Proceedings of the National Academy of Sciences.

[161] M. Heilemann, P. Dedecker, J. Hofkens, M. Sauer, "Photoswitches: Key molecules for subdiffraction-resolution fluorescence imaging and molecular quantification", *Laser & Photonics Reviews* **3**, 180 (2009). DOI: 10.1002/lpor.200810043. _eprint: https://onlinelibrary.wiley.com/doi/pdf/10.1002/lpor.200810043.

[162] R. M. Dickson, A. B. Cubitt, R. Y. Tsien, W. E. Moerner, "On/off blinking and switching behaviour of single molecules of green fluorescent protein", *Nature* **388**, 355 (1997). DOI: 10.1038/41048. Publisher: Nature Publishing Group.

[163] W. E. Moerner, "Single-molecule mountains yield nanoscale cell images", *Nature Methods* **3**, 781 (2006). DOI: 10.1038/nmeth1006-781. Publisher: Nature Publishing Group.

[164] J. Gelles, B. J. Schnapp, M. P. Sheetz, "Tracking kinesin-driven movements with nanometre-scale precision", *Nature* **331**, 450 (1988). DOI: 10.1038/331450a0. Publisher: Nature Publishing Group.

[165] R. J. Ober, S. Ram, E. S. Ward, "Localization Accuracy in Single-Molecule Microscopy", *Biophysical Journal* **86**, 1185 (2004). DOI: 10.1016/S0006-3495(04)74193-4. Publisher: Elsevier.

[166] H. Deschout, *et al.*, "Precisely and accurately localizing single emitters in fluorescence microscopy", *Nature Methods* **11**, 253 (2014). DOI: 10.1038/nmeth.2843. Publisher: Nature Publishing Group.

[167] A. Gahlmann, W. E. Moerner, "Exploring bacterial cell biology with single-molecule tracking and super-resolution imaging", *Nature Reviews Microbiology* **12**, 9 (2014). DOI: 10.1038/nrmicro3154. Publisher: Nature Publishing Group.

[168] F. V. Subach, *et al.*, "Photoactivatable mCherry for high-resolution two-color fluorescence microscopy", *Nature Methods* **6**, 153 (2009). DOI: 10.1038/nmeth.1298. Publisher: Nature Publishing Group.

[169] C. H. Bohrer, J. Xiao, *Physical Microbiology*, G. Duménil, S. van Teeffelen, eds. (Springer International Publishing, Cham, 2020), pp. 15–43.

[170] H. Qian, M. P. Sheetz, E. L. Elson, "Single particle tracking. Analysis of diffusion and flow in two-dimensional systems", *Biophysical Journal* **60**, 910 (1991). DOI: 10.1016/S0006-3495(91)82125-7.

[171] A. J. Berglund, "Statistics of camera-based single-particle tracking", *Physical Review E* **82**, 011917 (2010). DOI: 10.1103/PhysRevE.82.011917. Publisher: American Physical Society.

[172] X. Michalet, "Mean square displacement analysis of single-particle trajectories with localization error: Brownian motion in an isotropic medium", *Physical Review E* **82**, 041914 (2010). DOI: 10.1103/PhysRevE.82.041914. Publisher: American Physical Society.

[173] M. J. Saxton, "Anomalous diffusion due to binding: a Monte Carlo study", *Biophysical Journal* **70**, 1250 (1996). DOI: 10.1016/S0006-3495(96)79682-0. Publisher: Elsevier.

[174] L. Bruno, V. Levi, M. Brunstein, M. A. Despósito, "Transition to superdiffusive behavior in intracellular actin-based transport mediated by molecular motors", *Physical Review E* **80**, 011912 (2009). DOI: 10.1103/PhysRevE.80.011912. Publisher: American Physical Society.

[175] S. C. Weber, A. J. Spakowitz, J. A. Theriot, "Bacterial Chromosomal Loci Move Subdiffusively through a Viscoelastic Cytoplasm", *Physical Review Letters* **104**, 238102 (2010). DOI: 10.1103/PhysRevLett.104.238102. Publisher: American Physical Society.

[176] G. J. Schütz, H. Schindler, T. Schmidt, "Single-molecule microscopy on model membranes reveals anomalous diffusion", *Biophysical Journal* **73**, 1073 (1997). DOI: 10.1016/S0006-3495(97)78139-6. Publisher: Elsevier.

[177] P. D. Dahlberg, W. E. Moerner, "Cryogenic Super-Resolution Fluorescence and Electron Microscopy Correlated at the Nanoscale", *Annual Review of Physical Chemistry*

72, 253 (2021). DOI: 10.1146/annurev-physchem-090319-051546. Publisher: Annual Reviews.

[178] D. Elmlund, H. Elmlund, "Cryogenic Electron Microscopy and Single-Particle Analysis", *Annual Review of Biochemistry* **84**, 499 (2015). DOI: 10.1146/annurev-biochem-060614-034226. Publisher: Annual Reviews.

[179] Y. Cheng, N. Grigorieff, P. A. Penczek, T. Walz, "A Primer to Single-Particle Cryo-Electron Microscopy", *Cell* **161**, 438 (2015). DOI: 10.1016/j.cell.2015.03.050. Publisher: Elsevier.

[180] W. Baumeister, R. Grimm, J. Walz, "Electron tomography of molecules and cells", *Trends in Cell Biology* **9**, 81 (1999). DOI: 10.1016/S0962-8924(98)01423-8. Publisher: Elsevier.

[181] S. Asano, B. D. Engel, W. Baumeister, "*In Situ* Cryo-Electron Tomography: A Post-Reductionist Approach to Structural Biology", *Journal of Molecular Biology* **428**, 332 (2016). DOI: 10.1016/j.jmb.2015.09.030.

[182] J. Dubochet, *et al.*, "Cryo-electron microscopy of vitrified specimens", *Quarterly Reviews of Biophysics* **21**, 129 (1988). DOI: 10.1017/S0033583500004297.

[183] A. Rigort, *et al.*, "Focused ion beam micromachining of eukaryotic cells for cryoelectron tomography", *Proceedings of the National Academy of Sciences* **109**, 4449 (2012). DOI: 10.1073/pnas.1201333109. Publisher: Proceedings of the National Academy of Sciences.

[184] M. Marko, C. Hsieh, R. Schalek, J. Frank, C. Mannella, "Focused-ion-beam thinning of frozen-hydrated biological specimens for cryo-electron microscopy", *Nature Methods* **4**, 215 (2007). DOI: 10.1038/nmeth1014. Publisher: Nature Publishing Group.

[185] D. Perez, *et al.*, "Identification and demonstration of roGFP2 as an environmental sensor for cryogenic correlative light and electron microscopy", *Journal of Structural Biology* **214**, 107881 (2022). DOI: 10.1016/j.jsb.2022.107881.

[186] C. L. Schwartz, V. I. Sarbash, F. I. Ataullakhanov, J. R. Mcintosh, D. Nicastro, "Cryo-fluorescence microscopy facilitates correlations between light and cryo-electron microscopy and reduces the rate of photobleaching", *Journal of Microscopy* **227**, 98 (2007). DOI: 10.1111/j.1365-2818.2007.01794.x. _eprint: https://onlinelibrary.wiley.com/doi/pdf/10.1111/j.1365-2818.2007.01794.x.

[187] K. Höhn, *et al.*, "Preservation of protein fluorescence in embedded human dendritic cells for targeted 3D light and electron microscopy", *Journal of Microscopy* **259**, 121 (2015). DOI: 10.1111/jmi.12230. _eprint: https://onlinelibrary.wiley.com/doi/pdf/10.1111/jmi.12230.

[188] A. Kremer, S. Lippens, C. J. Guérin, *eLS* (John Wiley & Sons, Ltd, 2016), pp. 1–10. _eprint: https://onlinelibrary.wiley.com/doi/pdf/10.1002/9780470015902.a0025983.

[189] Y.-W. Chang, *et al.*, "Correlated cryogenic photoactivated localization microscopy and cryo-electron tomography", *Nature Methods* **11**, 737 (2014). DOI: 10.1038/nmeth.2961. Publisher: Nature Publishing Group.

[190] B. Liu, *et al.*, "Three-dimensional super-resolution protein localization correlated with vitrified cellular context", *Scientific Reports* **5**, 13017 (2015). DOI: 10.1038/srep13017. Publisher: Nature Publishing Group.

[191] M. W. Tuijtel, A. J. Koster, S. Jakobs, F. G. A. Faas, T. H. Sharp, "Correlative cryo super-resolution light and electron microscopy on mammalian cells using fluorescent proteins", *Scientific Reports* **9**, 1369 (2019). DOI: 10.1038/s41598-018-37728-8. Publisher: Nature Publishing Group.

[192] P. D. Dahlberg, *et al.*, "Cryogenic single-molecule fluorescence annotations for electron tomography reveal in situ organization of key proteins in Caulobacter", *Proceedings of the National Academy of Sciences* **117**, 13937 (2020). DOI: 10.1073/pnas.2001849117. Publisher: Proceedings of the National Academy of Sciences.

[193] G.-H. Wu, *et al.*, "Multi-scale 3D Cryo-Correlative Microscopy for Vitrified Cells", *Structure* **28**, 1231 (2020). DOI: 10.1016/j.str.2020.07.017. Publisher: Elsevier.

[194] K. A. Sochacki, G. Shtengel, S. B. van Engelenburg, H. F. Hess, J. W. Taraska, "Correlative super-resolution fluorescence and metal-replica transmission electron microscopy", *Nature Methods* **11**, 305 (2014). DOI: 10.1038/nmeth.2816. Publisher: Nature Publishing Group.

[195] B. G. Kopek, *et al.*, "Diverse protocols for correlative super-resolution fluorescence imaging and electron microscopy of chemically fixed samples", *Nature Protocols* **12**, 916 (2017). DOI: 10.1038/nprot.2017.017. Publisher: Nature Publishing Group.

[196] E. C. Greenwald, S. Mehta, J. Zhang, "Genetically Encoded Fluorescent Biosensors Illuminate the Spatiotemporal Regulation of Signaling Networks", *Chemical Reviews* **118**, 11707 (2018). DOI: 10.1021/acs.chemrev.8b00333. Publisher: American Chemical Society.

[197] S. Boeynaems, *et al.*, "Protein Phase Separation: A New Phase in Cell Biology", *Trends in Cell Biology* **28**, 420 (2018). DOI: 10.1016/j.tcb.2018.02.004.

[198] B. R. Sabari, A. Dall'Agnese, R. A. Young, "Biomolecular Condensates in the Nucleus", *Trends in Biochemical Sciences* **45**, 961 (2020). DOI: 10.1016/j.tibs.2020.06.007.

[199] S. Alberti, D. Dormann, "Liquid–Liquid Phase Separation in Disease", *Annual Review of Genetics* **53**, 171 (2019). DOI: 10.1146/annurev-genet-112618-043527.

[200] A. S. Lyon, W. B. Peeples, M. K. Rosen, "A framework for understanding the functions of biomolecular condensates across scales", *Nature Reviews Molecular Cell Biology* **22**, 215 (2021). DOI: 10.1038/s41580-020-00303-z.

[201] D. Bracha, *et al.*, "Mapping Local and Global Liquid Phase Behavior in Living Cells Using Photo-Oligomerizable Seeds", *Cell* **175**, 1467 (2018). DOI: 10.1016/j.cell.2018.10.048.

[202] D. W. Sanders, *et al.*, "Competing Protein-RNA Interaction Networks Control Multiphase Intracellular Organization", *Cell* **181**, 306 (2020). DOI: 10.1016/j.cell.2020.03.050.

[203] J. Guillén-Boixet, *et al.*, "RNA-Induced Conformational Switching and Clustering of G3BP Drive Stress Granule Assembly by Condensation", *Cell* **181**, 346 (2020). DOI: 10.1016/j.cell.2020.03.049.

[204] A. Klosin, *et al.*, "Phase separation provides a mechanism to reduce noise in cells", *Science* **367**, 464 (2020). DOI: 10.1126/science.aav6691.

[205] Y. Shin, *et al.*, "Spatiotemporal Control of Intracellular Phase Transitions Using Light-Activated optoDroplets", *Cell* **168**, 159 (2017). DOI: 10.1016/j.cell.2016.11.054. Publisher: Elsevier.

[206] B. Guilhas, *et al.*, "ATP-Driven Separation of Liquid Phase Condensates in Bacteria", *Molecular Cell* **79**, 293 (2020). DOI: 10.1016/j.molcel.2020.06.034. Number: 2.

[207] X. Jin, J.-E. Lee, C. Schaefer, "Membraneless organelles formed by liquid-liquid phase separation increase bacterial fitness", *Science Advances* **7**, eabh2929 (2021).

[208] J. McQuail, A. Switzer, L. Burchell, S. Wigneshweraraj, "The RNA-binding protein Hfq assembles into foci-like structures in nitrogen starved Escherichia coli", *Journal of Biological Chemistry* **295**, 12355 (2020). DOI: 10.1074/jbc.RA120.014107.

[209] M. Lieb, "Studies of heat-inducible lambda bacteriophage: I. Order of genetic sites and properties of mutant prophages", *Journal of Molecular Biology* **16**, 149 (1966).

[210] S. K. Govers, J. Mortier, A. Adam, A. Aertsen, "Protein aggregates encode epigenetic memory of stressful encounters in individual Escherichia coli cells", *PLOS Biology* **16**, e2003853 (2018). DOI: 10.1371/journal.pbio.2003853.

[211] P. S. Maddox, N. Portier, A. Desai, K. Oegema, "Molecular analysis of mitotic chromosome condensation using a quantitative time-resolved fluorescence microscopy assay", *Proceedings of the National Academy of Sciences* **103**, 15097 (2006). DOI: 10.1073/pnas.0606993103.

[212] D. T. McSwiggen, M. Mir, X. Darzacq, R. Tjian, "Evaluating phase separation in live cells: diagnosis, caveats, and functional consequences", *Genes & Development* **33**, 1619 (2019). DOI: 10.1101/gad.331520.119.

[213] J. Berry, S. C. Weber, N. Vaidya, M. Haataja, C. P. Brangwynne, "RNA transcription modulates phase transition-driven nuclear body assembly", *Proceedings of the National Academy of Sciences* **112** (2015). DOI: 10.1073/pnas.1509317112.

[214] C. F. Lee, "Scaling law and universal drop size distribution of coarsening in conversion-limited phase separation", *Physical Review Research* **3**, 043081 (2021). DOI: 10.1103/PhysRevResearch.3.043081.

[215] W. M. Śmigiel, *et al.*, "Protein diffusion in Escherichia coli cytoplasm scales with the mass of the complexes and is location dependent", *Science Advances* **8**, eabo5387 (2022). DOI: 10.1126/sciadv.abo5387. Publisher: American Association for the Advancement of Science.

[216] F. Baneyx, M. Mujacic, "Recombinant protein folding and misfolding in Escherichia coli", *Nature Biotechnology* **22**, 1399 (2004). DOI: 10.1038/nbt1029.

[217] Y. Zhou, J. M. Su, C. E. Samuel, D. Ma, "Measles Virus Forms Inclusion Bodies with Properties of Liquid Organelles", *Journal of Virology* **93**, e00948 (2019).

[218] S. Cheng, Y. Liu, C. S. Crowley, T. O. Yeates, T. A. Bobik, "Bacterial microcompartments: their properties and paradoxes", *BioEssays* **30**, 1084 (2008). DOI: 10.1002/bies.20830. _eprint: https://onlinelibrary.wiley.com/doi/pdf/10.1002/bies.20830.

[219] S. Ungelenk, *et al.*, "Small heat shock proteins sequester misfolding proteins in near-native conformation for cellular protection and efficient refolding", *Nature Communications* **7**, 13673 (2016). DOI: 10.1038/ncomms13673.

[220] S. Żwirowski, *et al.*, "Hsp70 displaces small heat shock proteins from aggregates to initiate protein refolding", *The EMBO Journal* **36**, 783 (2017). DOI: 10.15252/embj.201593378.

[221] H. Yoo, J. A. M. Bard, E. V. Pilipenko, D. A. Drummond, "Chaperones directly and efficiently disperse stress-triggered biomolecular condensates", *Molecular Cell* **82**, 741 (2022). DOI: 10.1016/j.molcel.2022.01.005. Publisher: Elsevier.

[222] D. G. Gibson, *et al.*, "Enzymatic assembly of DNA molecules up to several hundred kilobases", *Nature Methods* **6**, 343 (2009). DOI: 10.1038/nmeth.1318.

[223] P. R. Jensen, H. V. Westerhoff, O. Michelsen, "The use of lac-type promoters in control analysis", *European Journal of Biochemistry* **211**, 181 (1993). DOI: 10.1111/j.1432-1033.1993.tb19885.x.

[224] B. P. Isaacoff, Y. Li, S. A. Lee, J. S. Biteen, "SMALL-LABS: Measuring Single-Molecule Intensity and Position in Obscuring Backgrounds", *Biophysical Journal* **116**, 975 (2019). DOI: 10.1016/j.bpj.2019.02.006. Publisher: Elsevier.

[225] J. Munkres, "Algorithms for the Assignment and Transportation Problems", *Journal of the Society for Industrial and Applied Mathematics* **5**, 32 (1957). DOI: 10.1137/0105003. Publisher: Society for Industrial and Applied Mathematics.

[226] Y. Liao, J. W. Schroeder, B. Gao, L. A. Simmons, J. S. Biteen, "Single-molecule motions and interactions in live cells reveal target search dynamics in mismatch repair", *Proceedings of the National Academy of Sciences* **112** (2015). DOI: 10.1073/pnas.1507386112.

[227] N. L. Fernandez, *et al.*, "DNA Methylation and RNA-DNA Hybrids Regulate the Single-Molecule Localization of a DNA Methyltransferase on the Bacterial Nucleoid", *mBio* **14**, e03185 (2023). DOI: 10.1128/mbio.03185-22.

[228] T. Photometrics, "Teledyne Photometrics Technical note on camera test protocol" (2019).

[229] M. Newberry, "Mirametrics Technical note on pixel response effects on CCD camera gain calibration" (1996).

[230] W. W. Baldwin, P. W. Bankston, "Measurement of live bacteria by Nomarski interference microscopy and stereologic methods as tested with macroscopic rod-shaped models", *Applied and Environmental Microbiology* **54**, 105 (1988). DOI: 10.1128/aem.54.1.105-109.1988.

[231] C. Stringer, T. Wang, M. Michaelos, M. Pachitariu, "Cellpose: a generalist algorithm for cellular segmentation", *Nature Methods* **18**, 100 (2021). DOI: 10.1038/s41592-020-01018-x.

[232] K. J. Cutler, *et al.*, "Omnipose: a high-precision morphology-independent solution for bacterial cell segmentation", *Nature Methods* **19**, 1438 (2022). DOI: 10.1038/s41592-022-01639-4. Number: 11 Publisher: Nature Publishing Group.

[233] C. Hult, *et al.*, "Enrichment of dynamic chromosomal crosslinks drive phase separation of the nucleolus", *Nucleic Acids Research* **45**, 11159 (2017). DOI: 10.1093/nar/gkx741.

[234] J.-Y. Tinevez, *et al.*, "TrackMate: An open and extensible platform for single-particle tracking", *Methods* **115**, 80 (2017). DOI: 10.1016/j.ymeth.2016.09.016.

[235] B. D. Rae, *et al.*, "Cyanobacterial Carboxysomes: Microcompartments that Facilitate CO_2 Fixation", *Journal of Molecular Microbiology and Biotechnology* **23**, 300 (2013). DOI: 10.1159/000351342.

[236] J. L. Basalla, M. Ghalmi, Y. Hoang, R. E. Dow, A. G. Vecchiarelli, "An invariant C-terminal tryptophan in McdB mediates its interaction and positioning function with carboxysomes", *Molecular Biology of the Cell* **35**, ar107 (2024). DOI: 10.1091/mbc.E23-11-0443. Publisher: American Society for Cell Biology (mboc).

[237] A. Javer, *et al.*, "Short-time movement of E. coli chromosomal loci depends on coordinate and subcellular localization", *Nature Communications* **4**, 3003 (2013). DOI: 10.1038/ncomms3003. Publisher: Nature Publishing Group.

[238] A. Javer, *et al.*, "Persistent super-diffusive motion of Escherichia coli chromosomal loci", *Nature Communications* **5**, 3854 (2014). DOI: 10.1038/ncomms4854. Publisher: Nature Publishing Group.

[239] B. R. Parry, *et al.*, "The Bacterial Cytoplasm Has Glass-like Properties and Is Fluidized by Metabolic Activity", *Cell* **156**, 183 (2014). DOI: 10.1016/j.cell.2013.11.028.

[240] Y. Sun, A. J. M. Wollman, F. Huang, M. C. Leake, L.-N. Liu, "Single-Organelle Quantification Reveals Stoichiometric and Structural Variability of Carboxysomes Dependent on the Environment", *The Plant Cell* **31**, 1648 (2019). DOI: 10.1105/tpc.18.00787.

[241] W. B. Schofield, H. C. Lim, C. Jacobs-Wagner, "Cell cycle coordination and regulation of bacterial chromosome segregation dynamics by polarly localized proteins", *The EMBO Journal* (2010). DOI: 10.1038/emboj.2010.207. Publisher: John Wiley & Sons, LtdChichester, UK.

[242] F. O. Bendezú, C. A. Hale, T. G. Bernhardt, P. A. J. de Boer, "RodZ (YfgA) is required for proper assembly of the MreB actin cytoskeleton and cell shape in E. coli", *The EMBO Journal* **28**, 193 (2009). DOI: 10.1038/emboj.2008.264. Num Pages: 204 Publisher: John Wiley & Sons, Ltd.

[243] D. A. Moore, Z. N. Whatley, C. P. Joshi, M. Osawa, H. P. Erickson, "Probing for Binding Regions of the FtsZ Protein Surface through Site-Directed Insertions: Discovery of Fully Functional FtsZ-Fluorescent Proteins", *Journal of Bacteriology* **199**, 10.1128/jb.00553 (2016). DOI: 10.1128/jb.00553-16. Publisher: American Society for Microbiology.

[244] A. W. Bisson-Filho, *et al.*, "Treadmilling by FtsZ filaments drives peptidoglycan synthesis and bacterial cell division", *Science* **355**, 739 (2017). DOI: 10.1126/science.aak9973. Publisher: American Association for the Advancement of Science.

[245] T. A. Cameron, W. Margolin, "Construction and Characterization of Functional FtsA Sandwich Fusions for Studies of FtsA Localization and Dynamics during Escherichia coli Cell Division", *Journal of Bacteriology* **205**, e00373 (2023). DOI: 10.1128/jb.00373-22. Publisher: American Society for Microbiology.

[246] Y. Ah-Seng, J. Rech, D. Lane, J.-Y. Bouet, "Defining the Role of ATP Hydrolysis in Mitotic Segregation of Bacterial Plasmids", *PLOS Genetics* **9**, e1003956 (2013). DOI: 10.1371/journal.pgen.1003956. Publisher: Public Library of Science.

[247] A. G. Vecchiarelli, *et al.*, "ATP control of dynamic P1 ParA–DNA interactions: a key role for the nucleoid in plasmid partition", *Molecular Microbiology* **78**, 78 (2010). DOI: 10.1111/j.1365-2958.2010.07314.x. _eprint: https://onlinelibrary.wiley.com/doi/pdf/10.1111/j.1365-2958.2010.07314.x.

[248] D. Kuo, M. Nie, A. J. Courey, *Protein Affinity Tags: Methods and Protocols*, R. J. Giannone, A. B. Dykstra, eds. (Springer, New York, NY, 2014), pp. 71–80.

[249] M. A. Davis, K. A. Martin, S. J. Austin, "Biochemical activities of the ParA partition protein of the P1 plasmid", *Molecular Microbiology* **6**, 1141 (1992). DOI: 10.1111/j.1365-2958.1992.tb01552.x. _eprint: https://onlinelibrary.wiley.com/doi/pdf/10.1111/j.1365-2958.1992.tb01552.x.

[250] A. G. Vecchiarelli, *et al.*, "Dissection of the ATPase Active Site of P1 ParA Reveals Multiple Active Forms Essential for Plasmid Partition *", *Journal of Biological Chemistry* **288**, 17823 (2013). DOI: 10.1074/jbc.M113.469981. Publisher: Elsevier.

[251] S. Manley, *et al.*, "High-density mapping of single-molecule trajectories with photoactivated localization microscopy", *Nature Methods* **5**, 155 (2008). DOI: 10.1038/nmeth.1176. Number: 2 Publisher: Nature Publishing Group.

[252] S. M. Murray, M. Howard, "Center Finding in *E. coli* and the Role of Mathematical Modeling: Past, Present and Future", *Journal of Molecular Biology* **431**, 928 (2019). DOI: 10.1016/j.jmb.2019.01.017.

[253] I. V. Surovtsev, H. C. Lim, C. Jacobs-Wagner, "The Slow Mobility of the ParA Partitioning Protein Underlies Its Steady-State Patterning in Caulobacter", *Biophysical Journal* **110**, 2790 (2016). DOI: 10.1016/j.bpj.2016.05.014. Publisher: Elsevier.

[254] S. Cheng, S. Sinha, C. Fan, Y. Liu, T. A. Bobik, "Genetic Analysis of the Protein Shell of the Microcompartments Involved in Coenzyme B12-Dependent 1,2-Propanediol Degradation by Salmonella", *Journal of Bacteriology* **193**, 1385 (2011). DOI: 10.1128/jb.01473-10. Publisher: American Society for Microbiology.

[255] M. Yang, *et al.*, "Decoding the stoichiometric composition and organisation of bacterial metabolosomes", *Nature Communications* **11**, 1976 (2020). DOI: 10.1038/s41467-020-15888-4. Publisher: Nature Publishing Group.

[256] C. E. Mills, *et al.*, "Vertex protein PduN tunes encapsulated pathway performance by dictating bacterial metabolosome morphology", *Nature Communications* **13**, 3746 (2022). DOI: 10.1038/s41467-022-31279-3. Publisher: Nature Publishing Group.

[257] M. Yang, *et al.*, "Biogenesis of a bacterial metabolosome for propanediol utilization", *Nature Communications* **13**, 2920 (2022). DOI: 10.1038/s41467-022-30608-w. Publisher: Nature Publishing Group.

[258] D. A. Garsin, "Ethanolamine utilization in bacterial pathogens: roles and regulation", *Nature Reviews Microbiology* **8**, 290 (2010). DOI: 10.1038/nrmicro2334. Publisher: Nature Publishing Group.

[259] M. B. Prentice, "Bacterial microcompartments and their role in pathogenicity", *Current Opinion in Microbiology* **63**, 19 (2021). DOI: 10.1016/j.mib.2021.05.009.

[260] M. Hutchinson, K. I. Johnstone, D. White, "The Taxonomy of certain Thiobacilli", *Microbiology* **41**, 357 (1965). DOI: 10.1099/00221287-41-3-357. Publisher: Microbiology Society,.

[261] M. Mirdita, *et al.*, "ColabFold: making protein folding accessible to all", *Nature Methods* **19**, 679 (2022). DOI: 10.1038/s41592-022-01488-1. Publisher: Nature Publishing Group.

[262] J. Jumper, *et al.*, "Highly accurate protein structure prediction with AlphaFold", *Nature* **596**, 583 (2021). DOI: 10.1038/s41586-021-03819-2. Publisher: Nature Publishing Group.

[263] S. Van Der Walt, *et al.*, "scikit-image: image processing in Python", *PeerJ* **2**, e453 (2014). DOI: 10.7717/peerj.453.

[264] J. H. Smit, Y. Li, E. M. Warszawik, A. Herrmann, T. Cordes, "ColiCoords: A Python package for the analysis of bacterial fluorescence microscopy data", *PLOS ONE* **14**, e0217524 (2019). DOI: 10.1371/journal.pone.0217524. Publisher: Public Library of Science.

[265] J.-C. Yen, F.-J. Chang, S. Chang, "A new criterion for automatic multilevel thresholding", *IEEE Transactions on Image Processing* **4**, 370 (1995). DOI: 10.1109/83.366472. Conference Name: IEEE Transactions on Image Processing.

[266] Y. Liao, Y. Li, J. W. Schroeder, L. A. Simmons, J. S. Biteen, "Single-Molecule DNA Polymerase Dynamics at a Bacterial Replisome in Live Cells", *Biophysical Journal* **111**, 2562 (2016). DOI: 10.1016/j.bpj.2016.11.006.

[267] C. A. Schneider, W. S. Rasband, K. W. Eliceiri, "NIH Image to ImageJ: 25 years of image analysis", *Nature Methods* **9**, 671 (2012). DOI: 10.1038/nmeth.2089. Publisher: Nature Publishing Group.

[268] F. Pedregosa, *et al.*, "Scikit-learn: Machine Learning in Python", *J. Mach. Learn. Res.* **12**, 2825 (2011).

[269] J. D. Hunter, "Matplotlib: A 2D Graphics Environment", *Computing in Science & Engineering* **9**, 90 (2007). DOI: 10.1109/MCSE.2007.55. Conference Name: Computing in Science & Engineering.

[270] P. Virtanen, *et al.*, "SciPy 1.0: fundamental algorithms for scientific computing in Python", *Nature Methods* **17**, 261 (2020). DOI: 10.1038/s41592-019-0686-2. Publisher: Nature Publishing Group.

[271] M. L. Waskom, "seaborn: statistical data visualization", *Journal of Open Source Software* **6**, 3021 (2021). DOI: 10.21105/joss.03021.

[272] W. McKinney, "Data Structures for Statistical Computing in Python", *scipy* (2010). DOI: 10.25080/Majora-92bf1922-00a.

[273] M. Newville, T. Stensitzki, D. B. Allen, A. Ingargiola, "LMFIT: Non-Linear Least-Square Minimization and Curve-Fitting for Python" (2014), (Accessed: 2024-11-04).

[274] Y. S. Bykov, M. Cortese, J. A. G. Briggs, R. Bartenschlager, "Correlative light and electron microscopy methods for the study of virus–cell interactions", *FEBS Letters* **590**, 1877 (2016). DOI: 10.1002/1873-3468.12153. _eprint: https://onlinelibrary.wiley.com/doi/pdf/10.1002/1873-3468.12153.

[275] D. P. Hoffman, *et al.*, "Correlative three-dimensional super-resolution and block-face electron microscopy of whole vitreously frozen cells", *Science* **367**, eaaz5357 (2020). DOI: 10.1126/science.aaz5357. Publisher: American Association for the Advancement of Science.

[276] M. Wang, Y. Da, Y. Tian, "Fluorescent proteins and genetically encoded biosensors", *Chemical Society Reviews* **52**, 1189 (2023). DOI: 10.1039/D2CS00419D. Publisher: The Royal Society of Chemistry.

[277] L. A. Metskas, J. A. G. Briggs, "Fluorescence-Based Detection of Membrane Fusion State on a Cryo-EM Grid using Correlated Cryo-Fluorescence and Cryo-Electron Microscopy", *Microscopy and Microanalysis* **25**, 942 (2019). DOI: 10.1017/S1431927619000606.

[278] P. C. Hoffmann, *et al.*, "Tricalbins Contribute to Cellular Lipid Flux and Form Curved ER-PM Contacts that Are Bridged by Rod-Shaped Structures", *Developmental Cell* **51**, 488 (2019). DOI: 10.1016/j.devcel.2019.09.019. Publisher: Elsevier.

[279] J. Spitzer, B. Poolman, "The Role of Biomacromolecular Crowding, Ionic Strength, and Physicochemical Gradients in the Complexities of Life's Emergence", *Microbiology and Molecular Biology Reviews* **73**, 371 (2009). DOI: 10.1128/mmbr.00010-09. Publisher: American Society for Microbiology.

[280] J. R. Casey, S. Grinstein, J. Orlowski, "Sensors and regulators of intracellular pH", *Nature Reviews Molecular Cell Biology* **11**, 50 (2010). DOI: 10.1038/nrm2820. Publisher: Nature Publishing Group.

[281] M. J. Berridge, P. Lipp, M. D. Bootman, "The versatility and universality of calcium signalling", *Nature Reviews Molecular Cell Biology* **1**, 11 (2000). DOI: 10.1038/35036035. Publisher: Nature Publishing Group.

[282] P. H. Yancey, "Organic osmolytes as compatible, metabolic and counteracting cytoprotectants in high osmolarity and other stresses", *Journal of Experimental Biology* **208**, 2819 (2005). DOI: 10.1242/jeb.01730.

[283] S. M. Hosseiniyan Khatibi, *et al.*, "Osmolytes resist against harsh osmolarity: Something old something new", *Biochimie* **158**, 156 (2019). DOI: 10.1016/j.biochi.2019.01.002.

[284] M. T. R. Jr, E. S. Courtenay, D. S. Cayley, H. J. Guttman, "Responses of E. coli to osmotic stress: large changes in amounts of cytoplasmic solutes and water", *Trends in Biochemical Sciences* **23**, 143 (1998). DOI: 10.1016/S0968-0004(98)01196-7. Publisher: Elsevier.

[285] S. Sukenik, P. Ren, M. Gruebele, "Weak protein–protein interactions in live cells are quantified by cell-volume modulation", *Proceedings of the National Academy of Sciences* **114**, 6776 (2017). DOI: 10.1073/pnas.1700818114. Publisher: Proceedings of the National Academy of Sciences.

[286] C. L. Cuevas-Velazquez, *et al.*, "Intrinsically disordered protein biosensor tracks the physical-chemical effects of osmotic stress on cells", *Nature Communications* **12**, 5438 (2021). DOI: 10.1038/s41467-021-25736-8. Publisher: Nature Publishing Group.

[287] R. Zondervan, F. Kulzer, M. A. Kol'chenk, M. Orrit, "Photobleaching of Rhodamine 6G in Poly(vinyl alcohol) at the Ensemble and Single-Molecule Levels", *The Journal of Physical Chemistry A* **108**, 1657 (2004). DOI: 10.1021/jp037222e. Publisher: American Chemical Society.

[288] M. Le Gros, G. McDERMOTT, M. Uchida, C. Knoechel, C. Larabell, "High-aperture cryogenic light microscopy", *Journal of Microscopy* **235**, 1 (2009). DOI: 10.1111/j.1365-2818.2009.03184.x. _eprint: https://onlinelibrary.wiley.com/doi/pdf/10.1111/j.1365-2818.2009.03184.x.

[289] R. Kaufmann, *et al.*, "Super-Resolution Microscopy Using Standard Fluorescent Proteins in Intact Cells under Cryo-Conditions", *Nano Letters* **14**, 4171 (2014). DOI: 10.1021/nl501870p. Publisher: American Chemical Society.

[290] C. N. Hulleman, W. Li, I. Gregor, B. Rieger, J. Enderlein, "Photon Yield Enhancement of Red Fluorophores at Cryogenic Temperatures", *ChemPhysChem* **19**, 1774 (2018). DOI: 10.1002/cphc.201800131. _eprint: https://onlinelibrary.wiley.com/doi/pdf/10.1002/cphc.201800131.

[291] P. D. Dahlberg, *et al.*, "Identification of PAmKate as a Red Photoactivatable Fluorescent Protein for Cryogenic Super-Resolution Imaging", *Journal of the American Chemical Society* **140**, 12310 (2018). DOI: 10.1021/jacs.8b05960. Publisher: American Chemical Society.

[292] M. Obara, M. Szeliga, J. Albrecht, "Regulation of pH in the mammalian central nervous system under normal and pathological conditions: Facts and hypotheses", *Neurochemistry International* **52**, 905 (2008). DOI: 10.1016/j.neuint.2007.10.015.

[293] R. D. Vaughan-Jones, K. W. Spitzer, P. Swietach, "Intracellular pH regulation in heart", *Journal of Molecular and Cellular Cardiology* **46**, 318 (2009). DOI: 10.1016/j.yjmcc.2008.10.024.

[294] M. Pérez-Sayáns, A. García-García, M. D. Reboiras-López, P. Gándara-Vila, "Role of V-ATPases in solid tumors: Importance of the subunit C (Review)", *International*

Journal of Oncology **34**, 1513 (2009). DOI: 10.3892/ijo_00000280. Publisher: Spandidos Publications.

[295] B. B. Menon, S. Heinhorst, J. M. Shively, G. C. Cannon, "The Carboxysome Shell Is Permeable to Protons", *Journal of Bacteriology* **192**, 5881 (2010). DOI: 10.1128/jb.00903-10. Publisher: American Society for Microbiology.

[296] N. M. Mangan, A. Flamholz, R. D. Hood, R. Milo, D. F. Savage, "pH determines the energetic efficiency of the cyanobacterial CO2 concentrating mechanism", *Proceedings of the National Academy of Sciences* **113**, E5354 (2016). DOI: 10.1073/pnas.1525145113. Publisher: Proceedings of the National Academy of Sciences.

[297] J. Huang, *et al.*, "Probing the Internal pH and Permeability of a Carboxysome Shell", *Biomacromolecules* **23**, 4339 (2022). DOI: 10.1021/acs.biomac.2c00781. Publisher: American Chemical Society.

[298] M. Tantama, Y. P. Hung, G. Yellen, "Imaging Intracellular pH in Live Cells with a Genetically Encoded Red Fluorescent Protein Sensor", *Journal of the American Chemical Society* **133**, 10034 (2011). DOI: 10.1021/ja202902d. Publisher: American Chemical Society.

[299] L. A. Metskas, *et al.*, "Rubisco forms a lattice inside alpha-carboxysomes", *Nature Communications* **13**, 4863 (2022). DOI: 10.1038/s41467-022-32584-7. Publisher: Nature Publishing Group.

[300] T. Ni, *et al.*, "Structure and assembly of cargo Rubisco in two native α-carboxysomes", *Nature Communications* **13**, 4299 (2022). DOI: 10.1038/s41467-022-32004-w. Publisher: Nature Publishing Group.

[301] A. Liu, *et al.*, "pHmScarlet is a pH-sensitive red fluorescent protein to monitor exocytosis docking and fusion steps", *Nature Communications* **12**, 1413 (2021). DOI: 10.1038/s41467-021-21666-7. Publisher: Nature Publishing Group.

[302] C. Giorgi, A. Danese, S. Missiroli, S. Patergnani, P. Pinton, "Calcium Dynamics as a Machine for Decoding Signals", *Trends in Cell Biology* **28**, 258 (2018). DOI: 10.1016/j.tcb.2018.01.002. Publisher: Elsevier.

[303] C. Giorgi, S. Marchi, P. Pinton, "The machineries, regulation and cellular functions of mitochondrial calcium", *Nature Reviews Molecular Cell Biology* **19**, 713 (2018). DOI: 10.1038/s41580-018-0052-8. Publisher: Nature Publishing Group.

[304] A. Miyawaki, *et al.*, "Fluorescent indicators for Ca2+based on green fluorescent proteins and calmodulin", *Nature* **388**, 882 (1997). DOI: 10.1038/42264. Publisher: Nature Publishing Group.

[305] H. Dana, *et al.*, "High-performance calcium sensors for imaging activity in neuronal populations and microcompartments", *Nature Methods* **16**, 649 (2019). DOI: 10.1038/s41592-019-0435-6. Publisher: Nature Publishing Group.

[306] C. Ast, *et al.*, "Ratiometric Matryoshka biosensors from a nested cassette of green- and orange-emitting fluorescent proteins", *Nature Communications* **8**, 431 (2017). DOI: 10.1038/s41467-017-00400-2. Publisher: Nature Publishing Group.

[307] Y. Zhao, *et al.*, "An Expanded Palette of Genetically Encoded Ca2+ Indicators", *Science* **333**, 1888 (2011). DOI: 10.1126/science.1208592. Publisher: American Association for the Advancement of Science.

[308] N. Deliolanis, *et al.*, "Performance of the red-shifted fluorescent proteins in deep-tissue molecular imaging applications", *Journal of Biomedical Optics* **13**, 044008 (2008). DOI: 10.1117/1.2967184. Publisher: SPIE.

[309] R. S. Molina, *et al.*, "Understanding the Fluorescence Change in Red Genetically Encoded Calcium Ion Indicators", *Biophysical Journal* **116**, 1873 (2019). DOI: 10.1016/j.bpj.2019.04.007.

[310] J. Wu, *et al.*, "A long Stokes shift red fluorescent Ca2+ indicator protein for two-photon and ratiometric imaging", *Nature Communications* **5**, 5262 (2014). DOI: 10.1038/ncomms6262. Publisher: Nature Publishing Group.

[311] D. Moses, G. M. Ginell, A. S. Holehouse, S. Sukenik, "Intrinsically disordered regions are poised to act as sensors of cellular chemistry", *Trends in Biochemical Sciences* **48**, 1019 (2023). DOI: 10.1016/j.tibs.2023.08.001. Publisher: Elsevier.

[312] P. J. Cranfill, *et al.*, "Quantitative assessment of fluorescent proteins", *Nature Methods* **13**, 557 (2016). DOI: 10.1038/nmeth.3891. Publisher: Nature Publishing Group.

[313] D. Perez, P. D. Dahlberg, W. E. Moerner, "Advanced Cryogenic Light Microscopy Stage to Enable 3D Super-resolved Cryogenic Correlative Light and Electron Microscopy", *Microscopy and Microanalysis* **29**, 1941 (2023). DOI: 10.1093/micmic/ozad067.1005.

[314] J. R. Kremer, D. N. Mastronarde, J. R. McIntosh, "Computer Visualization of Three-Dimensional Image Data Using IMOD", *Journal of Structural Biology* **116**, 71 (1996). DOI: 10.1006/jsbi.1996.0013.

[315] G. Tang, *et al.*, "EMAN2: An extensible image processing suite for electron microscopy", *Journal of Structural Biology* **157**, 38 (2007). DOI: 10.1016/j.jsb.2006.05.009.

[316] M. Chen, *et al.*, "A complete data processing workflow for cryo-ET and subtomogram averaging", *Nature Methods* **16**, 1161 (2019). DOI: 10.1038/s41592-019-0591-8. Publisher: Nature Publishing Group.

[317] Y. Hsia, *et al.*, "Design of a hyperstable 60-subunit protein icosahedron", *Nature* **535**, 136 (2016). DOI: 10.1038/nature18010. Publisher: Nature Publishing Group.

[318] K. L. Peña, S. E. Castel, C. de Araujo, G. S. Espie, M. S. Kimber, "Structural basis of the oxidative activation of the carboxysomal γ-carbonic anhydrase, CcmM", *Proceedings of the National Academy of Sciences* **107**, 2455 (2010). DOI: 10.1073/pnas.0910866107. Publisher: Proceedings of the National Academy of Sciences.

[319] B. M. Long, B. Förster, S. B. Pulsford, G. D. Price, M. R. Badger, "Rubisco proton production drives the elevation of CO $_2$ within condensates and carboxysomes", *preprint*, Plant Biology (2020).

[320] W. B. Carpenter, *et al.*, "Ratiometric Sensing of Redox Environments Inside Individual Carboxysomes Trapped in Solution", *The Journal of Physical Chemistry Letters* **13**, 4455 (2022). DOI: 10.1021/acs.jpclett.2c00782. Publisher: American Chemical Society.

[321] W. Wan, J. A. G. Briggs, *Methods in Enzymology*, R. A. Crowther, ed. (Academic Press, 2016), vol. 579 of *The Resolution Revolution: Recent Advances In cryoEM*, pp. 329–367.

[322] A. A. Rangarajan, *et al.*, "Ruminococcus bromii enables the growth of proximal Bacteroides thetaiotaomicron by releasing glucose during starch degradation", *Microbiology* **168**, 001180 (2022). DOI: 10.1099/mic.0.001180. Publisher: Microbiology Society,.